



**HAL**  
open science

# Tuning forks in photoacoustic spectroscopy : Comparative study and new developments

Maxime Duquesnoy

► **To cite this version:**

Maxime Duquesnoy. Tuning forks in photoacoustic spectroscopy : Comparative study and new developments. General Physics [physics.gen-ph]. Université Paris-Saclay, 2021. English. NNT : 2021UP-ASP022 . tel-03198755

**HAL Id: tel-03198755**

**<https://theses.hal.science/tel-03198755>**

Submitted on 15 Apr 2021

**HAL** is a multi-disciplinary open access archive for the deposit and dissemination of scientific research documents, whether they are published or not. The documents may come from teaching and research institutions in France or abroad, or from public or private research centers.

L'archive ouverte pluridisciplinaire **HAL**, est destinée au dépôt et à la diffusion de documents scientifiques de niveau recherche, publiés ou non, émanant des établissements d'enseignement et de recherche français ou étrangers, des laboratoires publics ou privés.

Mise en œuvre de diapasons en  
spectroscopie photoacoustique  
: Étude comparative et  
nouveaux développements

*Tuning forks in photoacoustic spectroscopy:  
Comparative study and new developments*

**Thèse de doctorat de l'université Paris-Saclay**

École doctorale n° 572, Ondes et Matière (EDOM)  
Spécialité de doctorat : Physique  
Unité de recherche : Université Paris-Saclay, ONERA, Physique,  
Instrumentation, Environnement, Espace, 92322, Châtillon, France.  
Réfèrent : Faculté des sciences

**Thèse présentée et soutenue à Paris-Saclay, le  
30/03/2021, par**

**Maxime Duquesnoy**

**Composition du jury :**

<b>Delphine Marris-Morini</b> Professeur, C2N Paris-Saclay	Présidente
<b>Aurore Vicet</b> Maître de conférence, IES Montpellier	Rapporteur & Examinatrice
<b>Virginie Zéninari</b> Professeur, GSMA Reims	Rapporteur & Examinatrice
<b>Guillaume Aoust</b> Ingénieur-chercheur, Mirsense	Examineur & tuteur entreprise
<b>Wolfgang Schade</b> Professeur, IEPT Clausthal University of Technology & Fraunhofer HHI	Examineur
<b>Antoine Godard</b> Maître de recherche, ONERA	Directeur de thèse
<b>Jean-Michel Melkonian</b> Maître de recherche, ONERA	Co-Encadrant
<b>Raphaël Levy</b> Ingénieur-chercheur, ONERA	Co-Encadrant





# Tuning forks in photoacoustic spectroscopy: Comparative study and new developments

PhD Thesis Paris-Saclay University

Maxime DUQUESNOY

This thesis was hosted by Mirsense and Onera.





*A mes parents et Filou,*



# Résumé en Français

## (French summary)

La spectroscopie photoacoustique est une technique offrant un fort potentiel de détection multi-gaz. La détection est effectuée dans le domaine acoustique au moyen de microphones plutôt que dans le domaine optique à l'aide de photodétecteurs, rendant la détection indépendante de la longueur d'onde optique. En vue d'améliorer la détection acoustique, des résonateurs mécaniques de géométries très diverses peuvent être couplés à des résonateurs acoustiques. Le but de cette thèse est d'étudier l'utilisation de ces résonateurs en vue de comprendre les phénomènes physiques mis en jeu. Plus particulièrement, l'objectif est d'estimer la limite de sensibilité de diapasons en quartz seuls ou couplés à des résonateurs acoustiques et de les comparer aux autres capteurs photoacoustiques existants.

Dans ce manuscrit, un état de l'art exhaustif des différentes techniques photoacoustiques est mené, incluant les travaux ayant déjà été effectués à l'ONERA : la MPAS (*Microphone based PhotoAcoustic Spectroscopy*) qui utilise des microphones pour la détection, la CEPAS (*Cantilever-Enhanced PhotoAcoustic Spectroscopy*) qui utilise des poutres et la QEPAS (*Quartz-Enhanced PhotoAcoustic Spectroscopy*) qui utilise des diapasons en Quartz. Les limites de détection rapportées dans la littérature sont calculées et comparées. La technique QEPAS y est présentée de manière plus détaillée à travers une description des différents diapasons, résonateurs acoustiques et méthodes de détection utilisés dans la littérature.

Un modèle analytique et éléments finis pouvant décrire les différents résonateurs acoustiques ou mécaniques est présenté. Ce modèle est validé expérimentalement pour les différentes techniques (MPAS, CEPAS et QEPAS). Notamment, pour chacune, les systèmes présentant une sensibilité à l'état de l'art sont analysés. Ainsi, en MPAS et CEPAS, les constantes de cellule sont dérivées ainsi que le rapport signal-à-bruit normalisé des détecteurs. En QEPAS, la sensibilité de plusieurs diapasons est évaluée et comparée expérimentalement. Pour chaque système les modèles analytiques et éléments finis démontrent un bon accord sur les nombreux systèmes évalués.

Cependant, les phénomènes menant à la sensibilité de chaque technique restent peu clairs. Notamment, la sensibilité ultime de la QEPAS est dégradée d'un ordre de grandeur par rapport aux autres techniques. Afin de comprendre cette limitation, un nouveau modèle unifié est décrit. Ce modèle introduit différents facteurs tels que la chaleur générée, le recouvrement de l'onde de pression sur le détecteur ou le rapport signal-à-bruit normalisé.

Grâce à l'évaluation de ces facteurs, nous avons déterminé l'origine des limitations de sensibilité actuelles de chaque technique. Pour la MPAS, les microphones sont sensibles au fond ambiant, qui varie et empêche sa suppression. Pour la CEPAS, les cellules utilisées dans la littérature sont non-résonnantes entraînant une pression plus basse qu'en MPAS avec des cellules similaires. Pour la QEPAS enfin, le recouvrement de l'onde de pression acoustique sur le diapason est en général mauvais, de plus le couplage de cellules de faible facteur de qualité à des diapasons possédant un fort facteur de qualité induit une réduction intrinsèque du rapport signal-à-bruit normalisé. Afin de compenser ces limitations en QEPAS, deux nouveaux développements sont présentés. Le premier est la configuration "in-plane" permettant de maximiser le recouvrement acoustique-mécanique. Cette configuration est testée à l'aide d'un diapason ONERA en double passage dans l'interbranche et démontre une sensibilité de l'ordre de l'état de l'art. Le deuxième est l'utilisation d'un résonateur radial couplé à un diapason, améliorant le recouvrement acoustique-mécanique. Ce système démontre une sensibilité similaire à l'état de l'art



avec des contraintes de mises en oeuvre fortement réduites. Enfin, à l'aune de ces nouveaux développements, un positionnement des techniques photoacoustiques est extrait, permettant de déterminer l'intérêt respectif de chaque technique et les perspectives d'améliorations.

Pour terminer, un schéma de détection innovant en boucle fermée est décrit et modélisé. Le diapason est mis en oscillation à l'aide d'un circuit électrique. La force photoacoustique appliquée sur le diapason engendre un décalage de la fréquence de l'oscillateur que l'on mesure. Un déphasage contrôlé dans la boucle oscillatrice permet la mise en place d'une mesure différentielle en un temps nettement inférieur aux schémas conventionnels. Ce différentiel serait alors utile pour réduire les fonds sonores et vibratoires ambiants ainsi que pour compenser les dérives du capteur. Les performances de cette nouvelle méthode sont mesurées expérimentalement : facteur d'échelle, linéarité, et sensibilité. Nous avons alors démontré que sa sensibilité n'était pas dégradée par rapport à la mesure traditionnelle. Cette méthode devra par la suite être étudiée plus en profondeur pour l'intégrer au sein de capteurs industriels. On devra notamment démontrer l'amélioration de la compensation des dérives, de la réduction des fonds et la possibilité de calibrage du capteur en temps réel.

# Remerciements

## (Acknowledgments)

Un peu plus de trois années de travail se sont enfin concrétisées. Mon travail n'aurait pas été possible sans beaucoup de personnes ni aussi agréable sans beaucoup d'autres. Je tenais donc à tous vous remercier !

Tout d'abord merci à toi Antoine pour avoir toujours suivi l'avancement de mes travaux et les avoir réorientés au besoin. Tu m'as aidé à m'améliorer grâce à ta grande rigueur et ta vision plus générale de directeur scientifique. Je réalise avoir eu beaucoup de chance de t'avoir eu comme directeur de thèse. Tu t'es vraiment impliqué dans ma thèse et toujours avec le sourire.

Je tenais également à remercier l'équipe de mes encadrants qui était une véritable famille recomposée.

Tout d'abord Jean-Michel, tu m'as aidé dès le début pendant mon stage à comprendre les choses et à mettre les mains dans les expériences. Dès que j'avais le moindre soucis je venais te voir et tu laissais tout tomber pour venir m'aider ou m'expliquer quelque chose et encore une fois j'étais chanceux de t'avoir comme encadrant. Tes capacités de bricoleur ont bien servi, même si parfois j'avais peur que tu démontes tout quand tu arrivais avec tes tournevis ! Je me souviendrai aussi t'avoir rendu malade avec des fraises Tagada<sup>®</sup>, du coup je te ferai moins de gâteaux cette année !

Ensuite merci à Raphaël, tu m'as expliqué beaucoup de choses au tableau malgré la malédiction des feutres qui ne fonctionnent jamais. A chaque fois que je venais à Châtillon tu avais de nouvelles idées de brevets. Bon il y en a très peu qui ont abouti mais on voit bien que tu t'es beaucoup impliqué dans la photoacoustique et que tu sais même faire toutes les simulations maintenant. Merci aussi de m'avoir aidé en électronique et d'avoir ensemble démontré et étudié le principe de la détection active. Merci aussi pour les nombreux fous rires nerveux à chaque fois que tu m'expliquais quelque chose. Enfin je tiens à te féliciter pour ta fibre écologique, puisque tu finis toujours les gâteaux qui traînent en salle de pause et ça empêche le gâchis !

Enfin, merci à toi Guillaume de m'avoir accueilli chez Mirsense. Tu m'as poussé à me dépasser à chaque fois pour améliorer ma rigueur scientifique et je pense avoir progressé même si ça n'a pas toujours été facile. Tu as également dès le début eu de bonnes idées pour comprendre la photoacoustique, ce qui a permis à la fin l'obtention des supers résultats présentés dans cette thèse. Enfin merci pour m'avoir fait découvrir la MPAS et j'espère que tu te souviendras du jour où je t'ai fais entendre à l'oreille l'effet photoacoustique avec la cellule Mirsense ! J'ai aussi beaucoup appris à bricoler chez Mirsense avec toi, le scotch double face et la perceuse sont nos amis.

Je tenais également à remercier mes deux rapporteurs Aurore Vicet et Virginie Zéninari. C'était un plaisir d'avoir votre avis sur mon travail à travers vos rapports très détaillés et nos discussions. J'espère que nous pourrons de nouveau nous rencontrer pour échanger sur la photoacoustique !

Merci également aux autres membres du jury qui ont accepté d'évaluer mon travail. Merci à Delphine Marris-Morini d'avoir présidé mon jury et d'avoir été si agréable. Special thanks to Wolfgang Schade as well as to Ulrike Willer for agreeing to review my work. Your participation was important for us. I hope we will have the pleasure to talk again together.

Enfin, il me reste à remercier tous mes collègues et ce sera long ! Mais avant cela, il me reste quelques

mentions spéciales.

Merci à Olivier Le Traon, pour l'intérêt que tu as mis dans mes travaux et mes présentations aussi longues soit elles. Merci aussi d'avoir voulu me garder et de m'avoir soutenu dans la création de mon projet SATT. Tu es notre gourou des résonateurs en quartz et plus particulièrement des gyros, j'attends donc avec impatience tes nouveaux résultats.

Merci à Svetlana et toute l'équipe de la SATT Paris-Saclay pour m'avoir accompagné dans la création de mon dossier jusqu'à son acceptation !

Merci à Weidong pour votre gentillesse et pour nos discussions.

Merci également à Roman Rousseau, nous avons passé nos thèses en même temps sur le même sujet et c'était très agréable de pouvoir discuter avec toi. Tu possèdes une grande rigueur scientifique et je te souhaite tout le meilleur pour la suite.

Merci également à tous ceux qui sont venus assister à ma soutenance. De Dunkerque, Reims, Paris, Grenoble et Montpellier, la France a de la chance de posséder tant d'experts dans ce domaine ! J'espère que nous nous croiserons plus tard et bon courage à tous les doctorants qui fournirez, j'en suis sûr, des travaux très intéressants. Enfin merci à ma famille qui m'a soutenu pendant tout ce temps et ces périodes plus ou moins difficiles et à mon chien qui me rend toujours de bonne humeur.

Passons dorénavant à mes collègues de Mirsense ! Merci à Françoise qui est la première personne à m'avoir accueilli et qui était notre maman à tous. Merci à Mathieu d'avoir suivi ma thèse et de m'avoir soutenu dans ma démarche de projet SATT. Je tiens également à remercier Greg, c'était vraiment très agréable de travailler avec toi. Merci Ali, tu m'as vraiment bien aidé dès le moment où j'ai dû manipuler des lasers. Ta grande expérience en industrie optique m'a permis de réapprendre les bases pour construire des beaux bancs bien alignés, et aussi les bases du taraudage et de la mécanique. Ça me servira très longtemps ! Merci à Maxime G. Faire nos thèses en parallèle était une bonne occasion pour nous de discuter et c'était agréable de pouvoir partager nos expériences à la pause café. Merci à tous les autres, Matthieu pour tes bières même si j'aime pas vraiment ça, Laureline pour avoir illuminé le labo dès ton arrivée, Johan pour ta gentillesse, Viktoriya pour ton aide, Adrien pour tes blagues pas toujours drôles, Ludo pour ton incroyable sympathie et beaucoup d'autres que j'ai peut être moins côtoyé ; Fahem, Mickael, Florian, Paula, David, Pierre, Zheng, Bilal, Olivier, Sullivan ainsi que les très nombreux stagiaires que j'ai vu passer. Enfin, je retiendrai les activités de groupes ! Le karting et les quelques bleus, l'accrobranche que je n'aurais jamais fait tout seul et où j'ai battu mon vertige. Enfin et surtout le laser game qui était génial ainsi que le restaurant après dans lequel j'ai réussi à manger pour la première fois depuis très longtemps.

Au tour de mes collègues de l'ONERA à Palaiseau. Merci à Myriam pour avoir suivi mes travaux et avoir cherché des idées novatrices. Merci à Alex, notre chef sympa qui rigole tout le temps, c'est à chaque fois un plaisir de venir te voir. Jean-Pierre, que dire ? Je ne vais pas t'envoyer un mail pour te remercier, j'aurais trop peur de déclencher des virus sur ton pc ! Merci pour m'avoir aidé pour la mécanique et les bouteilles de gaz (ouf nous sommes toujours vivants). C'était très agréable de pouvoir discuter avec toi tous les jours, tu es un peu devenu mon papi. Ça y est, j'ai passé ma thèse tu peux prendre ta retraite si tu veux. Merci à mes quelques stagiaires, Guillaume, Hugo et Julien qui m'avez aidé. Il y a encore beaucoup de personnes à remercier ; JB, Nelly, Quentin, Rosa, Christophe, Cedric, Philippe, Hélène, Gautier, Alexis, Nassim, Mickael, Yannick, Sylvain, Marie, Florence... mais j'aurais encore le temps de vous le dire en personne ! Enfin mention spéciale aux doctorants. Les anciens ; Julie et les éléments perturbateurs Thomas, Vincent, Jérèmy et Guillaume qui mangeait des sandwiches beurre harrissa tous les midis, quelle horreur. Et les nouveaux doctorants plus sympas les uns que les autres (il ne faut pas se faire d'ennemis) ; Jonas, Elodie, Jeanne, Pier-Henri et la ptite dernière Eve-Line, je vous soutiendrai pendant vos années de thèse restantes.

On en vient enfin à mes collègues de l'ONERA à Châtillon. Les meilleurs pour la fin ? Merci à Thomas, tu es le grand frère que je n'ai jamais eu. Derrière tes apparences ronchonnes tu es un nounours. Tu m'as bien

aidé pour les simulations, pour les scripts Python, et beaucoup d'autres choses alors merci encore. J'espère te voir un peu plus malgré le confinement et aussi que tu iras mieux, je pense à qui tu sais. Merci à Marc, Claude et Vincent pour avoir réalisé les résonateurs que j'ai utilisé pendant ma thèse, de l'usinage au câblage. Votre travail est la base de nos résultats et vous le faites toujours dans la bonne humeur ! Merci également à Andrea et Jean d'avoir travaillé avec nous sur la programmation FPGA. Pour terminer avec les permanents, je n'oublierai pas Paul, le maître pâtissier de l'unité, Pierre, le jumeau maléfique de Raphaël finisseur de gâteaux, Amandine qui nous illumine tous par son sourire et Béatrice qui m'a aidé au début de ma thèse. Je me souviendrai des anciens doctorants, Lucas, Léopold et Amina, j'espère que vous trouverez un emploi qui vous convienne. Pour terminer, les plus jeunes, les cyclistes Vincent et Charles que j'apprécie beaucoup même si je ne vous vois pas souvent et Margot qui je l'espère m'apprendra des choses sur le HF2LI. Tout cela sans compter les nombreux stagiaires avec qui j'ai pu travailler et Lucie qui je l'espère appréciera son stage.

Voilà je pense n'avoir oublié personne ! J'espère que vous avez apprécié ma compagnie durant tout ce temps et mes gâteaux. Je suis bien content de rester avec des équipes aussi sympathiques pendant encore un an. Nous ferons, je l'espère, des choses formidables. Alors à très bientôt !



# Contents

<b>Introduction</b>	<b>1</b>
<b>1 Photoacoustic state of the art</b>	<b>17</b>
1.1 Microphone based photoacoustic spectroscopy: MPAS	17
1.1.1 Microphones	17
1.1.2 Acoustic amplification cells	19
1.1.2.1 Simple cylindrical cells	19
1.1.2.2 Differential cells	21
1.2 Cantilever enhanced photoacoustic spectroscopy: CEPAS	23
1.2.1 Cantilevers	23
1.2.2 Acoustic amplification cells	24
1.3 Quartz enhanced photoacoustic spectroscopy: QEPAS	25
1.3.1 Watch tuning forks	25
1.3.2 Custom tuning forks	26
1.3.3 Coupling of acoustic resonators with QTFs	29
1.4 Different signal processing methods	32
1.4.1 Background compensation: MOCAM	32
1.4.2 Electrical excitation for calibration and gas relaxation measurement	33
1.4.3 Beat-frequency QEPAS	34
1.5 In the industry	35
1.6 State of the art at ONERA	36
1.6.1 Modelling	36
1.6.2 Custom QTFs	37
1.6.3 Acoustic resonators	38
<b>2 Photoacoustic analytical and finite element modelling</b>	<b>39</b>
2.1 Analytical model description	39
2.1.1 Laser excitation	40
2.1.2 Absorption by the gas and heat generation	41
2.1.2.1 Gas absorption	41
2.1.2.2 Molecular relaxation	42
2.1.2.3 Heat source modulation	42
2.1.3 Acoustic pressure generation	44
2.1.3.1 In free space	45
2.1.3.2 In acoustic resonators	46
Pressure distribution	46
Resonance frequency	46
Acoustic quality factors	47
Cell constant	49
2.1.4 Acoustic pressure detection with mechanical resonators	50
2.1.4.1 Resonance frequency	51

2.1.4.2	Quality factors	51
2.1.4.3	Beam displacement	53
2.1.4.4	Photoacoustic force	54
2.1.4.5	Vibroacoustic coupling of acoustical and mechanical resonators	55
2.1.4.6	Brownian motion and SNR	56
2.1.5	The particular case of microphones	56
2.1.5.1	Microphone sensitivity	56
2.1.5.2	Microphone noise and SNR	57
2.1.6	Signal processing	58
2.1.6.1	Equivalent electric model	58
2.1.6.2	Signal amplification	58
2.1.6.3	Lock-in detection	59
2.1.7	NNEA	60
2.2	Modelling photoacoustics by FEM	61
2.2.1	Mechanical resonator modelling	61
2.2.1.1	Modal analysis	61
2.2.1.2	Harmonic analysis	62
2.2.2	Acoustic modelling	62
2.2.2.1	Acoustic source	62
2.2.2.2	Acoustic boundaries	63
2.2.2.3	Acoustic resonator quality factor	63
2.2.3	Vibroacoustic interaction modelling	64
2.2.4	Conclusion	64
2.3	Definition of a new unified modelling	65
2.3.1	Heat source $H$	65
2.3.2	Pressure generation: laser constant $C_L$	65
2.3.3	Pressure amplification and cell constant: amplification factor $A_s$	66
2.3.4	Acoustic-mechanic overlap $\eta_s$	67
2.3.5	Vibroacoustic efficiency $\varepsilon_{va}$	67
2.3.6	Normalised signal to noise ratio $SNR_{1Pa}$	68
2.3.7	SNR	68
2.4	Conclusion	69
<b>3</b>	<b>Comparison through experiments for representative cases</b>	<b>71</b>
3.1	Study of typical MPAS and CEPAS setups	71
3.1.1	Microphones and cantilevers analytical signal-to-noise ratio	71
3.1.1.1	Determination of the SNR at 1 Pa of commercial microphones	71
3.1.1.2	Determination of the SNR at 1 Pa of cantilevers	72
3.1.2	Analytical cell constant and sensitivity using simple cylinder shaped resonators	74
3.1.3	Comparison to experimental results	75
3.1.3.1	MPAS sensors from the literature	75
3.1.3.2	CEPAS sensors from the literature	77
3.1.4	Study of differential MPAS setups	79
3.1.4.1	Study cases parameters	79
3.1.4.2	Analytical cell constant and sensitivity	79
3.1.4.3	Comparison to experimental results	80
	In the literature	80
	Study of Mirsense's differential cell	82
3.1.5	Conclusion on MPAS and CEPAS	86

3.2	Study of QEPAS setups . . . . .	86
3.2.1	The case of bare QTFs . . . . .	86
3.2.1.1	QTFs characteristics . . . . .	86
3.2.1.2	Analytical and FEM results . . . . .	87
	Analytical determination of the frequency and quality factor . . . . .	87
	Determination of the sensitivity . . . . .	90
3.2.1.3	Experimental comparison . . . . .	90
	Experimental setup . . . . .	90
	Modulation scheme . . . . .	92
	Determination of the system limiting noise . . . . .	93
	Experimental results for the on-beam configuration . . . . .	94
3.2.2	The case of QTFs coupled with acoustic resonators . . . . .	95
3.2.2.1	Watch QTF with longitudinal dual-tube microresonators . . . . .	95
	Problem definition . . . . .	95
	Theoretical study of the resonators coupling . . . . .	96
	Experimental validation . . . . .	99
3.2.2.2	Custom QTF C2 with an acoustic recovery cavity . . . . .	101
	Problem definition . . . . .	101
	Recovery of the acoustic waves . . . . .	102
	Determination of the sensitivity with the recovery cavity . . . . .	103
	Sensitivity enhancement with dual tube resonators . . . . .	105
3.3	Conclusion . . . . .	110
<b>4</b>	<b>Comparison of photoacoustic technologies through an unified modelling</b>	<b>113</b>
4.1	Determination of the model factors for the three photoacoustic techniques . . . . .	113
4.1.1	Determination of the model factors for MPAS and CEPAS . . . . .	113
4.1.2	Determination of the model factors for QEPAS . . . . .	115
4.1.2.1	Bare QTFs . . . . .	115
	Validation of $\eta_s$ values for limiting cases . . . . .	115
	Model factors for bare QTFs . . . . .	116
	FEM modelling in static operation . . . . .	118
	FEM modelling of the vibroacoustic interaction and discussion on $\epsilon_{va}$ . . . . .	119
4.1.2.2	QTF coupling with acoustic resonators . . . . .	121
	Computation of the normalised SNR at 1 Pa . . . . .	122
	Watch QTF with dual tubes microresonators . . . . .	122
	C2 with acoustic resonators . . . . .	124
4.2	New developments for QEPAS sensors . . . . .	125
4.2.1	In-plane configuration . . . . .	125
4.2.1.1	Analytical study . . . . .	125
4.2.1.2	In-plane double pass inside a custom QTF prong space . . . . .	126
4.2.2	A new radial resonator for QEPAS with C2 . . . . .	128
4.2.2.1	Design and analytical results . . . . .	128
	Problem definition . . . . .	128
	Theoretical study of the resonators coupling . . . . .	128
	Computation of the model factors . . . . .	131
4.2.2.2	Experimental study of the system . . . . .	132
	Measurement of the acoustic resonator quality factor . . . . .	132
	Determination of the system limiting noise . . . . .	133
	Photoacoustic measurement . . . . .	134



4.2.3	Conclusion	135
4.3	Comparison of existing photoacoustic techniques	136
4.3.1	Study of the limit of sensitivity	136
4.3.1.1	Ultimate sensitivity of the mechanical pressure detector	137
4.3.1.2	Sensitivity enhancement with acoustic resonators	137
4.3.1.3	Overall sensitivity enhancement	138
4.3.1.4	Perspectives	139
	MPAS sensors	139
	CEPAS sensors	139
	QEPAS sensors	140
4.3.2	Frequency	141
4.3.3	Sensitivity to the environment	141
4.3.4	Compactness	143
4.4	Conclusion	144

**5 Study of a new signal processing method for time stable and background-free photoacoustic measurements 147**

5.1	Motivation and principle	147
5.1.1	Motivation	147
5.1.2	Principle	148
5.2	Theoretical analysis of the method	149
5.2.1	Signal generation	149
5.2.1.1	Variation of frequency with phase	149
5.2.1.2	Phase variation induced by force application	151
5.2.1.3	Frequency variation induced by force application	152
5.2.2	Frequency noise description using Leeson's equation	153
5.3	Experimental validation of the analytical model	155
5.3.1	Implementation	155
5.3.1.1	Proximity electronics	155
5.3.1.2	Oscillator	156
5.3.2	Noise measurements	156
5.3.2.1	Experimental setup	156
5.3.2.2	Determination of the limiting noise	157
5.3.2.3	Influence of excitation voltage	158
5.3.2.4	Influence of motional resistance	159
5.3.3	Photoacoustic measurements	160
5.3.3.1	Experimental setup	160
5.3.3.2	Principle validation	161
5.3.3.3	Influence of excitation voltage	163
5.3.3.4	Influence of motional resistance	165
5.3.3.5	Linearity with gas concentration	165
5.3.3.6	Comparison with open loop detection	166
5.4	Conclusion and perspectives	167

<b>Conclusion</b>	<b>169</b>
<b>Bibliography</b>	<b>185</b>
<b>List of publications</b>	<b>187</b>
<b>Appendices</b>	<b>195</b>
<b>A Material parameters</b>	<b>196</b>
<b>B Determination of microphone parameters from datasheets</b>	<b>199</b>
<b>C Realisation of custom quartz resonators at ONERA</b>	<b>205</b>



# Introduction

After two centuries of constant development and industrialisation, needs to control and regulate the impact of Human activity on the environment have emerged. As market studies suggest, sales of gas detection systems are increasing, representing several billion dollars a year (Frost and Sullivan 2013). Whilst technologies such as absorption spectroscopy have spread across the industry, none has yet demonstrated a good compromise, in terms of cost, sensitivity, size, etc., enabling to address the consumer market. This thesis aims at studying photoacoustic technologies that, through unique advantages, could spread over the entire gas detection market. More particularly we will focus our interest on quartz enhanced photoacoustic spectroscopy.

## Needs and applications

### Applications and needs for gas detection

From the industrial use to the consumer market, the range of applications is wide. However, the requirements are quite similar: a sensitive detection to quantify chemical species at the state of trace in a gas matrix. Needs and typical applications are presented in Figure 1.

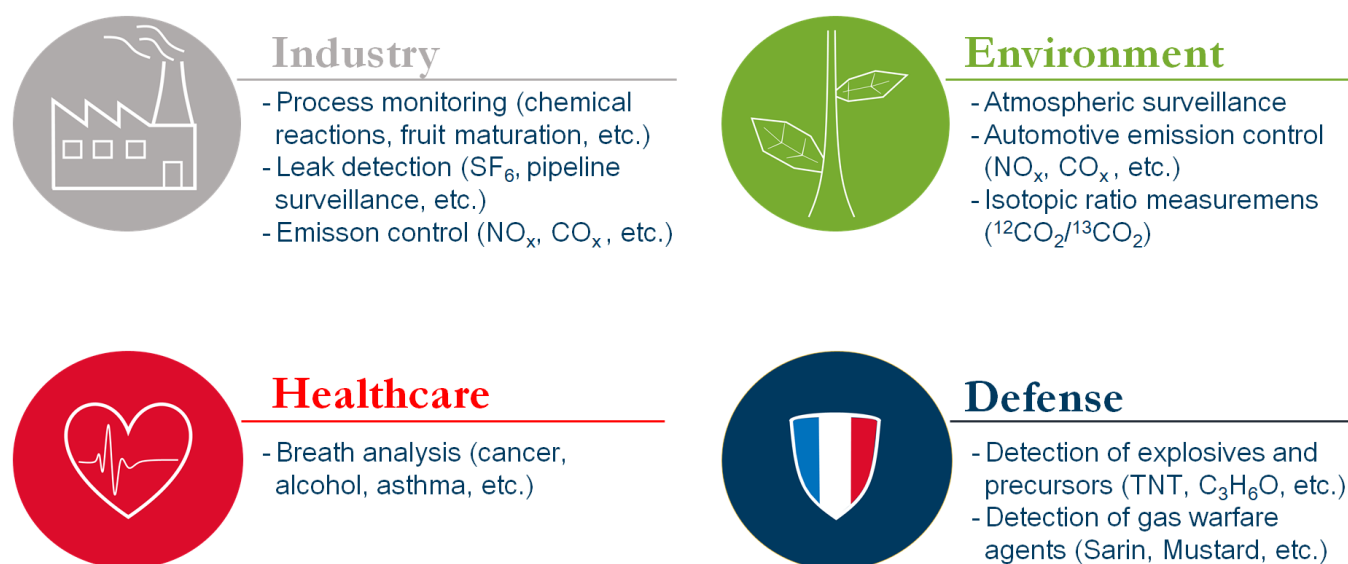


Figure 1: Needs for gas detection in the main areas.

The main areas requiring gas detection are the industry and the environment. Typical applications are: atmospheric monitoring [1, 2] (emissions from factories, cars, etc.), process optimisation, in which quantifying a gas resulting from a chemical reaction allows to adjust and increase the yields (surveillance of fruit maturation [3], etc.) or also the detection of leaks from electric power generators cooling systems [4].

Needs for Defense, such as the detection of explosives and precursors [5], are of great importance in order to

prevent terrorist attempts in a tense international environment (airports, train stations surveillance, etc.). One could also quote the necessity for detecting gas warfare agents [5, 6], although their use was prohibited in 1997 by the Chemical Weapons Convention. The need to protect infantry and populations is still present as it is necessary to detect and to prove the use of these chemical agents, as it was recently the case in Syria in 2013 and 2017 according to the United Nations.

Ultimately, very promising applications are foreseen in the medical area. In breath analysis, detection of biomarkers such as ethylene or nitrous oxide can lead to the early diagnosis of lung cancer, asthma or diabetes [1, 7]. The use of photoacoustics in medicine, not only for gases but also for liquids and solids, such as blood analysis, tumor detection [8] and vascular imaging, will undoubtedly rise in the years to come, as the tremendous number of publications on the subject indicates.

## Market requirements

In order to access the actual market, our aim is to study the most generic and simplest sensors. In this context, the instruments will have to satisfy as many of the following requirements as possible:

- ability to measure simultaneously several gases
- sensitivity, in the order of the part per billion range for most molecules
- excellent selectivity, so as to increase the sensor accuracy and decrease false alarms rates
- reduced volume
- affordability
- assembly simplicity, to allow for mass production and cost reductions

As such, good compromises will have to be found and are part of the present work philosophy. After having summed up all of the requirements for the actual gas detection market, we now have to choose the most adapted technology.

## Existing technologies

In order to meet the global market demands, a lot of technologies are used nowadays.

However, to clarify our speech we need to make some distinctions. Let us specify that we distinguish laboratory instruments from embedded ones. Indeed, while laboratory instruments such as mass spectrometers present the highest sensitivities, they are, in contrast, completely inconsistent with field deployment because of their lack of compactness and their high cost. Furthermore, a distinction can be made between standoff and local detection. In this manuscript we focus on local detection only, through the use of embedded systems.

The most common embedded and local detection instruments rest upon different technologies, the main ones being:

- Tunable diode laser absorption spectroscopy (TDLAS) is the most straightforward laser absorption technique. After passing through the sample once, the laser power is measured. Beer-Lambert-Bouguer's law then allows to identify the sample by analysing the light extinction over wavelength and quantifying its concentration [9, 10].
- Non dispersive infrared spectroscopy (NDIR) is similar to TDLAS. Instead of using a tunable laser, a wide band light source is used and filtered to select the desired wavelength, for which the absorption is measured [11].

- Cavity enhanced absorption spectroscopy (CEAS) [12], cavity ring-down spectroscopy (CRDS) [13], and multipass absorption spectroscopy [14], which relate to a family of laser spectroscopy techniques where an optical cavity or a multipass cell is used to enhance the absorption of a laser light by the sample. Beer-Lambert-Bouguer's law or more specifically the optical cavity decay time for CRDS enable to analyse the sample.
- Fourier transform infrared spectroscopy (FT-IR) which is similar to the above mentioned techniques, however the source is usually not a laser, and the analysis is made through a Fourier transform of the sample absorption [15].
- Chemical sensors, using electrochemistry are the most widespread. One example of the future generation of these is Graphene sensors [16]. Gas composition is then determined by measuring conductivity modifications of an atomic size film specialised to adsorb specific molecules.
- Flame spectrophotometry, which consists in the analysis of the sample combustion emitted light [17].
- Ion mobility spectroscopy (IMS), consisting in the ionisation and separation of gas components [18]. The gas identification is then made by measuring the ions mobility in a carrier buffer gas.
- Gas chromatography, which uses the elution time of the gas components in a column [19, 20].
- Photoacoustics based on microphone photoacoustic spectroscopy (MPAS) [21]. It is the most widespread photoacoustic technique in the industry, that we will extensively describe and investigate in this manuscript.

A comparison of these technologies over criteria of sensitivity, selectivity, multi-gas capacity, compactness and cost is presented in Table 1. Concerning the sensitivity, a more complete study can be found in [22].

Technology	Sensitivity	Selectivity	Multi-gas capacity	Compactness	Cost
<b>Chemical</b>	Good	Very bad	Bad	Very good	Very Low
<b>Flame spectrophotometry</b>	Very good	Very bad	Very good	Good	Average
<b>IMS</b>	Very good	Average	Bad	Average	Average
<b>Gas chromatography</b>	Very good	Good	Very good	Bad	High
<b>TDLAS</b>	Good	Very good	Average	Average	Average
<b>NDIR</b>	Average	Average	Good	Very good	Very low
<b>CRDS</b>	Very good	Good	Bad	Bad	High
<b>FT-IR</b>	Good	Average	Very good	Average	High
<b>Photoacoustics</b>	Good	Very good	Very good	Good	Low

Table 1: Qualitative comparison of different gas detection methods for embedded instruments over criteria of sensitivity, selectivity, multi-gas measurement capacity, compactness and cost.

While these technologies are able to demonstrate very good sensitivities, only laser based techniques allow for good selectivity. Even fewer techniques enable good compactness and low cost applications. Among them, we take particular interest in laser based spectroscopy, especially photoacoustic spectroscopy (PAS) which, as we prove in this manuscript, is capable of meeting good compromises between the previously stated criteria.

## Laser spectroscopy

Laser based spectroscopy relies on the principle of energy quantification. Each and every molecular species can be described by its spectrum, i.e. the quantization of its energy transitions distributed over an energy scale. One is then able to identify species in a molecular mix by analysing their energy distribution. These transitions can be achieved by the absorption of an external source of matching energy, such as a laser photon. Lasers are coherent electromagnetic sources that enable the change of their emission spectrum with a high precision, given their narrow emission bandwidth in wavelength. The most common method for quantification is direct absorption spectroscopy such as TDLAS. The principle is to measure the difference of laser power before and after the sample to be analysed. The identification of the molecular species is accomplished by sweeping the laser wavelength. The absorbed power is directly linked to the line strength of the targeted transition.

### The molecular fingerprint region

Most molecular species present strong absorption lines in the infrared region of the spectrum, reason why it is called the "molecular fingerprint region". In particular, in the mid-infrared, the region from 3 to 12  $\mu\text{m}$  is very interesting. Indeed, many species present rovibrational transitions in this region as shown in Figure 2.

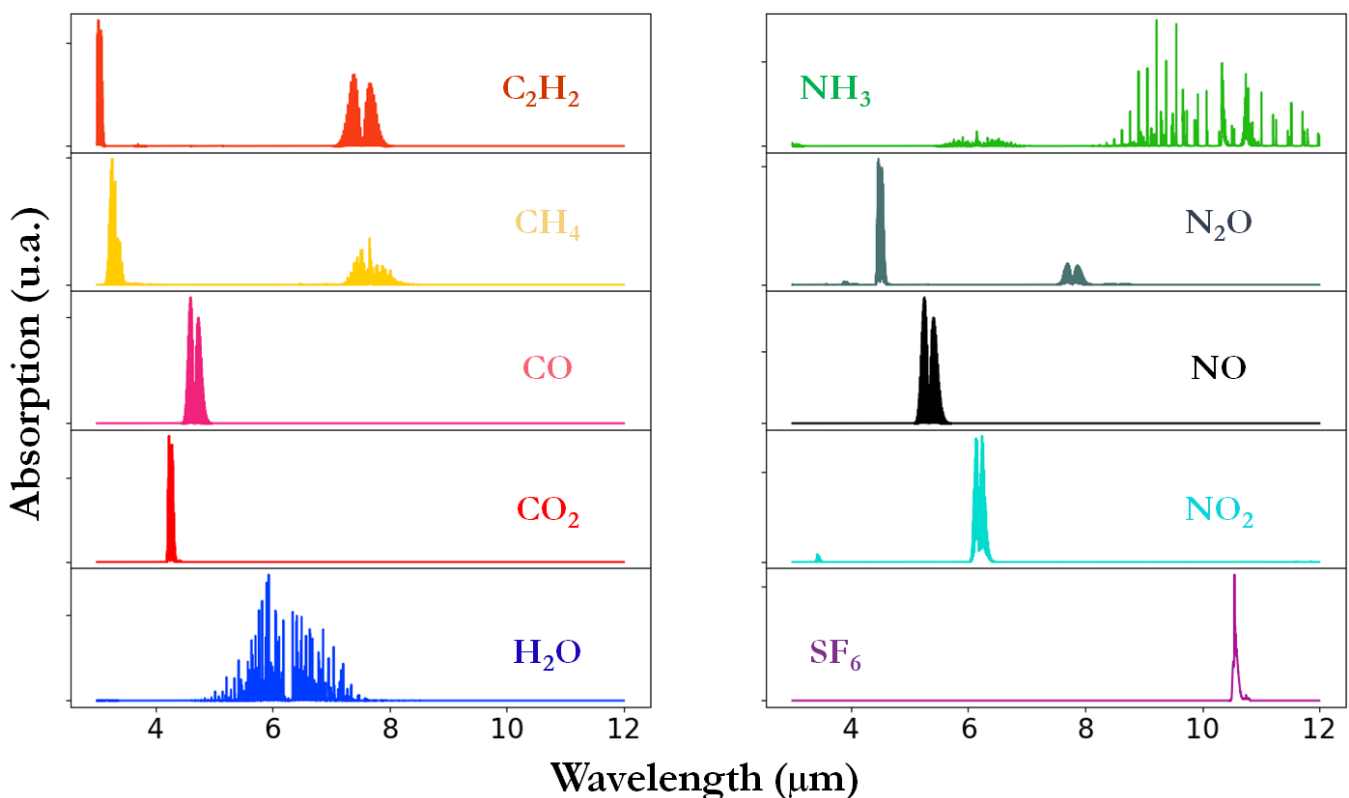


Figure 2: Absorption spectra for different target molecules in the mid-infrared region.

### Available sources

To widely access the MIR several technologies exist, among which: quantum cascade lasers (QCL) and optical parametric oscillators (OPO), which principles are presented in Figure 3.

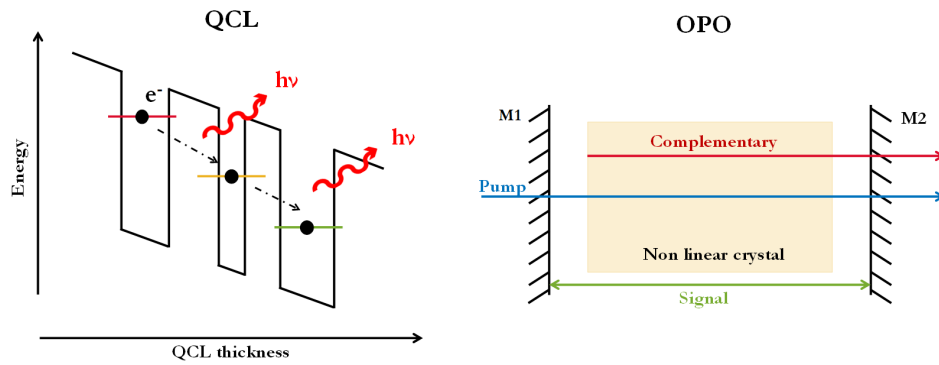


Figure 3: Schematic principle of QCLs (left) and of a single signal-resonant OPO (right).

QCLs are semiconductor lasers using intersubband transitions. When a current is applied, electrons from the conduction band pass from one internal band to another, generating photons of matched energy. To increase the laser emission, this transition is repeated by design and so the electrons pass from one quantum well to another, provoking the "cascade effect". Their main advantages are their compactness, robustness and possibility to be produced at a large scale.

OPOs use optical non linearity allowing transformation of a wavelength into two complementary ones. A pump laser beam is introduced inside a cavity containing a non linear crystal. When the condition of quasi-phase-matching is met, the pump laser is partly converted into two coherent radiations, referred as signal and idler, satisfying the energy conservation principle. OPOs allow for a continuous tuning of the wavelength to access a wide spectral band.

## The principle of photoacoustics

Part of the laser spectroscopy techniques, photoacoustics is the one we investigate in this manuscript.

In 1880, A.G. Bells discovers the photoacoustic effect in solids by exciting a Selenium sheet with the sun modulated light and by listening to the generated sound with his very ears [23]. Later on, the experiment was extended to liquids and gases. Five years after the telephone, the photophone was born, which Bell considered far greater. From this invention, Bell considered the selective detection of chemical species. It is only one century later, with the maturation of microphones and the invention of lasers in 1960 that the photoacoustic effect truly began to be exploited [24].

### Principle

The principle of photoacoustics is presented in Figure 4.

First, a light source is time modulated, in amplitude or wavelength, at a frequency  $f$ . Then, the source passes through the gas to be analysed. Molecular species possessing an absorption line matching the light energy will absorb the light radiation leading to an unstable state. The excited molecules return into their fundamental level of energy after a rotation, translation or vibration. When working in the infrared at low pressure, the desexcitation through translations is the most probable [25, 26]. The periodic relaxation through translations then induces the creation of a periodic heating of the medium, at the frequency  $f$ , giving rise to acoustic waves of same period. A detector, such as a microphone, a cantilever beam or a tuning fork, will be set into vibration by the acoustic waves and operate the transduction towards an electric signal. Finally, this signal is processed, usually by demodulating it at the excitation modulation frequency.



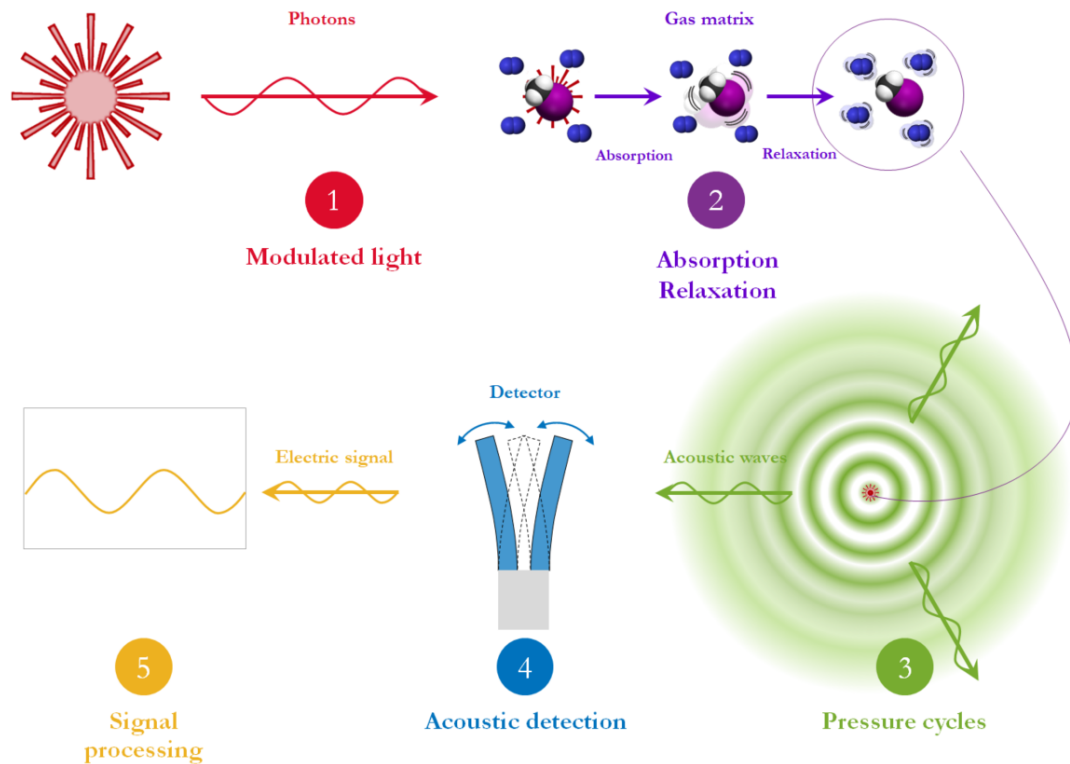


Figure 4: Principle of photoacoustics.

While the firsts historically developed photoacoustic instruments used microphone enhanced technology (MPAS), new techniques based on the use of cantilevers (CEPAS) [27] and quartz tuning forks (QEPAS) [28] arose, leading to new possibilities in the area.

### Advantages and drawbacks of this method

Photoacoustic spectroscopy benefits from several advantages: a very good selectivity, the possibility to enhance the signal by increasing laser mean power or the light-gas interaction path. Also, because we detect the sound and not the light, the method is totally achromatic, allowing to use any laser source with the same detector, whatever the light spectral range.

Other benefits are the wide linearity range of the signal with the gas concentration and a wide dynamic range from parts per billion to percents. Also, the technique is said to be a background-free technique, meaning that the signal must not be extracted from an existing background as in direct absorption spectroscopy. Lastly, the sensitivity does not depend on the volume, as first approximation, rendering possible compromises between sensitivity and compactness of the sensor.

However, PAS presents drawbacks such as the dependence to the gas matrix. The sound is generated thanks to the gas relaxation which in turn depends on the gas matrix (collision partners, pressure, etc...). Another drawback is its sensitivity to external acoustic and vibratory background noises, even though methods are developed to reduce it.

### Problematic

Recently, quartz tuning forks have been introduced in PAS with the promise of enabling smaller and more sensitive sensors. While many research teams worked with watch tuning forks, fewer, including ONERA, focused

their research on the modelling and design of custom QTFs. The sensitivities of custom QTFs and watch QTFs are heterogeneous and hard to read. Besides, both present similar sensitivities which may suggest a physical limitation.

Also, to enhance their sensitivities, QTFs have been coupled to acoustic resonators. These resonators are usually tubes of small radius in which the laser beam passes, making the alignment difficult. Very few variations are found in the literature and the analysis of such coupled resonators is complex. It is thus difficult to determine if the design of more convenient or more sensitive resonators is possible.

Finally, a question resides, which is the one of the interest of using tuning forks in PAS or spectroscopy in general. Often, the use of QTFs is promoted over other detectors such as microphones but we will show through the literature that there is no clear evidence of their superiority.

Based on these observations we propose to study the use of quartz tuning forks in photoacoustic spectroscopy and possible improvements.

## Context

Since 2013 ONERA showed its interest towards photoacoustic spectroscopy. A previous PhD thesis focused on the development of infrared laser sources and quartz tuning forks for photoacoustics, leading to founding material in the field [26]. Results of the previous work are detailed in Section 1.6.

In the dynamic, my PhD thesis was held thanks to a special PhD convention allowing shared time between a company and a laboratory. This thesis was held at Mirsense and at ONERA.

Mirsense is a company born in 2015, composed of a team of nearly 20 persons, including 9 doctors and 3 PhD students. Mirsense's business plan rests upon two main areas. First, the production and driving of custom QCLs for spectroscopy [29], emitting from 3 to 20  $\mu\text{m}$ , or Defense applications [30]. Second, the development of custom photoacoustic solutions based on QCL photoacoustic spectroscopy. These products are shown in the following figure.

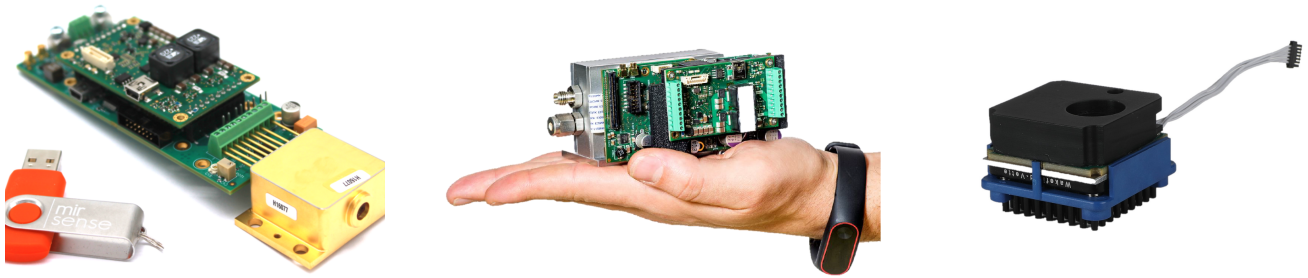


Figure 5: Mirsense's products. Packaged QCL for power application with its driving solution (left). Photoacoustic QCL based gas analyser called "Multisense V1" that we will use in this manuscript. A new version is now commercialised. (Middle). Miniature photoacoustic gas analyser "Mirchip" (Right).

ONERA is a laboratory working under the supervision of the French Ministry of the Armed Forces, whose researches are focused on aeronautics and aerospace. This work took place between two research teams, "Sensors and Micro/Nano technologies" and "Laser sources and metrology". The first one is specialised in the development of quartz based resonators for applications such as accelerometry [31], gyrometry [32], magnetometry [33], etc. The second one is specialised in the development of infrared sources, mainly OPOs [34], and advanced instrumentation for field spectroscopy using light detection and ranging (LIDAR) technologies [35].

This context was favorable to research on photoacoustic spectroscopy while understanding the constraints of field applications and market requirements.

## Approach

To answer the different problems we highlighted, our study revolves around different axis.

To have a good overview of the many systems used in PAS, we first describe the state-of-the-art of photoacoustic spectroscopy, in particular by investigating the reported performances of the three main variants: MPAS, CEPAS and QEPAS.

Secondly, a complete modelling of photoacoustics, from the light source to the detector and signal processing, is detailed. It has been developed to lay common foundations for the comparison between MPAS, CEPAS and QEPAS. Hypotheses, upon which the analytical and finite element simulations are based, are explained.

The third chapter is dedicated to the model validation through photoacoustic measurements. Experiments implementing the different photoacoustic techniques from literature are analysed. We also present our results using different setups and detectors. We first study Mirsense's first differential acoustic cell with one of their QCLs. Secondly, we present experiments on ONERA's quartz tuning forks and acoustic resonators.

The fourth chapter presents a comparison of the different photoacoustic techniques. Using a new unified modelling, a sensitivity comparison is achieved, with associated advantages and drawbacks.

The last chapter focuses on a promising new signal processing method for quartz tuning fork based photoacoustic sensors. The first part focuses on the theory behind this method while the second part presents experimental results and interpretation.

Eventually, we conclude on the interest of using the different photoacoustic techniques, with a focus on the interest of using quartz tuning forks in photoacoustic spectroscopy. Outlooks are drawn for possible future improvements.





# Abbreviations

AFM	atomic force microscopy
AM	amplitude modulation
BF-QEPAS	beat-frequency quartz enhanced photoacoustic spectroscopy
CAD	computer aided design
CEAS	cavity enhanced absorption spectroscopy
CEPAS	cantilever enhanced photoacoustic spectroscopy
CRDS	cavity ring down spectroscopy
CW	continuous wavelength
DFB	distributed feedback
EIN	equivalent input noise
ENBW	equivalent noise bandwidth
FEM	finite element method
FFT	fast Fourier transform
FPGA	field programmable gate array
FTIR	Fourier transform infrared spectrometer
FWHM	full width at half maximum
ICL	interband cascade laser
IMS	ion mobility spectrometry
LASER	light amplification by stimulated emission of radiation
LED	light-emitting diode
LIA	lock-in amplifier
LIDAR	light detection and ranging
LOD	limit of detection
MEMS	micro electro mechanical systems
MOCAM	modulation cancellation method
MPAS	microphone based photoacoustic spectroscopy
MIR	mid-infrared
NEA	noise equivalent absorption
NDIR	non-dispersive infrared absorption spectroscopy
NEC	noise equivalent concentration
NEP	noise equivalent power
NNEA	normalised noise equivalent absorption
OPO	optical parametric oscillator
PAS	photoacoustic spectroscopy
PID	proportional–integral–derivative controller
PLL	phase-locked loop
PML	perfectly matched layer
PPBV	part per billion in volume
PPMV	part per million in volume
PSD	power spectral density
PYRATS	Python resonators analytical simulator
QCL	quantum cascade laser
QCW	quasi continuous wavelength
QEPAS	quartz enhanced photoacoustic spectroscopy
QTF	quartz tuning fork
RMS	root mean square
SNR	signal-to-noise ratio
SPL	standard pressure level
TDLAS	tunable diode laser absorption spectroscopy
VCO	voltage control oscillator
WM	wavelength modulation



# List of Symbols

## General

Symbol	Description	Unit
$k_B$	Boltzmann constant	$J.K^{-1}$
$T$	Temperature	K

## Optics

Symbol	Description	Unit
$I_L$	Laser intensity	$W.m^{-2}$
$r$	Distance to laser axis	m
$P_L$	Laser mean power before modulation	W
$w_L$	Laser waist	m
$\lambda_L$	Wavelength	m
$\sigma_L$	Wavenumber	$cm^{-1}$
$\delta$	Wavelength modulation amplitude	$cm^{-1}$
$L_{source}$	Laser source length in FEM	m

## Fluid

Symbol	Description	Unit
$\rho_f$	Gas volumetric mass density	$kg.m^{-3}$
$\alpha_G$	Gas maximal linear absorption	$cm^{-1}$
$\alpha_{min}$	Gas minimal detectable linear absorption	$cm^{-1}$
FWHM	Absorption line full width at half maximum	$cm^{-1}$
$\tau_{V-T}$	Vibrational-translational relaxation rate	s
$\gamma$	Heat capacity ratio	-
$\mu$	Dynamic viscosity	Pa.s
$\kappa$	Thermal conductivity	$W.m^{-1}.K^{-1}$
$C_p$	Specific heat capacity	$J.m^{-3}.K^{-1}$



# Acoustics

Symbol	Description	Unit
$\lambda_{ac}$	Acoustic wavelength	m
$k_{ac}$	Acoustic wave vector	$m^{-1}$
$A$	Pressure mode amplitude	-
$P$	Pressure	Pa
$v$	Sound speed	$m.s^{-1}$
$L_c$	Cell length	m
$L_{eff}$	Cell effective length	m
$R_c$	Cell radius	m
$V_c$	Cell volume	$m^3$
$C$	Cell constant	$Pa.W^{-1}.cm$
$L_{cha}$	Differential cell chamber length	m
$L_{cap}$	Differential cell capillary length	m
$R_{cha}$	Differential cell chamber radius	m
$R_{cap}$	Differential cell capillary radius	m
$A_0$	Differential cell capillary area	$m^2$
$A_{eff}$	Differential cell effective capillary area	$m^2$
$V_{1/2}$	Differential cell chamber volume	$m^3$
$V_{eff}$	Differential cell effective volume	$m^3$
$L_{mr}$	Acoustic micro resonator length	m
$R_I$	Acoustic micro resonator internal radius	m
$R_O$	Acoustic micro resonator external radius	m
$h_{mr}$	Acoustic micro resonator height compared to QTF stem	m
$e_{mr}$	Acoustic micro resonator penetration depth to QTF face	m
$l_{\mu}$	Viscous characteristic length	m
$l_{\kappa}$	Thermal characteristic length	m
$d_{\mu}$	Viscous boundary layer length	m
$d_{\kappa}$	Thermal boundary layer length	m
$Q_{ac}$	Acoustic total quality factor	-
$Q_{ac,radiation}$	Acoustic radiative quality factor	-
$Q_{ac,viscous}$	Acoustic viscous quality factor	-
$Q_{ac,thermal}$	Acoustic thermal quality factor	-
$Q_{ac,volume}$	Acoustic volumic quality factor	-

## Mechanics

Symbol	Description	Unit
$W$	Beam displacement	m
$\xi$	Damping ratio	-
$E$	Young modulus	Pa
$\rho_q$	Quartz volumetric mass density	$\text{kg}\cdot\text{m}^{-3}$
$\alpha$	Linear thermal expansion	$\text{K}^{-1}$
$e$	Beam vibrating width	m
$l$	Beam vibrating thickness	m
$L$	Beam length	m
$g$	QTF gap	m
$f_0$	Resonance frequency	Hz
$\omega_0$	Resonance pulsation	rad.Hz
$K$	Stiffness	$\text{kg}\cdot\text{s}^{-2}$
$\eta$	Damping ratio	$\text{kg}\cdot\text{s}^{-1}$
$M$	Equivalent mass	kg
$\phi$	Beam deformation	-
$R_m$	Motional resistance	$\Omega$
$L_m$	Motional inductance	H
$C_m$	Motional capacitance	F
$C_0$	Parasitic capacitance	F
$Q$	Quality factor	-
$Q_{\text{thermo}}$	Thermoelastic quality factor	-
$Q_{\text{struct}}$	Structural quality factor	-
$Q_{\text{electrode}}$	Electrode quality factor	-
$Q_{\text{vac}}$	Vacuum quality factor	-
$Q_{\text{viscousfrontal}}$	Frontal viscous quality factor	-
$Q_{\text{viscouslateral}}$	Lateral viscous quality factor	-
$Q_{\text{squeeze}}$	Squeeze damping quality factor	-
$Q_{\text{Couette}}$	Couette damping quality factor	-
$Q_{\text{acoustic}}$	Acoustic radiation quality factor of a QTF	-
$Q^*$	Coupled system quality factor	-
$F_B$	Noise equivalent force	N
$d$	Distance to the wall for squeeze damping	m

## Electronics

### General

Symbol	Description	Unit
$\varphi$	Phase	rad
$\Delta f$	Bandwidth	Hz
$\tau_{\text{LIA}}$	Lock-in amplifier integration time	s
$R_M$	Microphone sensitivity	$\text{mV}\cdot\text{Pa}^{-1}$
$S$	Photoacoustic signal	mV
$S_{\text{diff}}$	Differential photoacoustic signal	mV
$\sigma_{\text{RMS}}$	RMS noise level	$V_{\text{RMS}}$

## Oscillator

Symbol	Description	Unit
$\varphi$	Phase	rad
$\varphi_{\text{laser}}$	Phase shift due to laser propagation	rad
$\varphi_{\text{PA}}$	Photoacoustic phase shift	rad
$\varphi_{\text{elec}}$	Electronic phase shift	rad
$\varphi_{\text{PS}}$	Varying phase shift	rad
$\varphi_{\text{PS,min/max}}$	Phase shift minimising/maximising the frequency shift	rad
$\Delta\varphi$	Phase shift variation	rad
$\Delta f_0$	Frequency shift around resonance	Hz
$\Delta f_{0,\text{diff}}$	Differential frequency shift around resonance	Hz
$F_X$	Piezoelectric force	N
$d$	Distance between laser and tuning fork	m
$S_\phi$	Phase noise spectral density	$\text{rad}^2 \cdot \text{Hz}^{-1}$
$S_F$	Frequency noise spectral density	$\text{Hz}^2 \cdot \text{Hz}^{-1}$
$F$	Oscillator noise factor	-
$f_c$	Flicker corner frequency	Hz
$f_L$	Leeson frequency	Hz
$P_0$	Oscillator power	W
$\delta f$	Distance from carrier	Hz
$f_H$	High corner frequency	Hz
$\sigma$	Allan deviation	-
$\sigma_F$	Allan frequency deviation	Hz
$V_X$	Excitation voltage	V
$c_X$	Piezoelectric actuation force equivalent voltage	$\text{N} \cdot \text{V}^{-1}$

## Photoacoustics

Symbol	Description	Unit
$F_{\text{PA}}$	Photoacoustic force	N
$H$	Heat deposition	$\text{W} \cdot \text{cm}^{-1}$
$C_L$	Maximal generated pressure amplitude	$\text{Pa} \cdot \text{W}^{-1} \cdot \text{cm}$
$A_s$	Static pressure amplification	-
$\eta_s$	Static acoustical-mechanical overlap	-
$\varepsilon_{\text{va}}$	Vibroacoustic efficiency	-
$SNR$	Signal-to-noise ratio	-
$SNR_{1\text{Pa}}$	Signal-to-noise ratio for 1 Pa pressure on one face	$\text{dB} \cdot \text{Pa}^{-1}$
$NNEA$	Normalised noise equivalent absorption	$\text{W} \cdot \text{cm}^{-1} \cdot \text{Hz}^{-1/2}$





# Chapter 1

## Photoacoustic state of the art

### Objectives:

The aim of this first chapter is to describe the main technologies and techniques used in photoacoustic spectroscopy. A state-of-the-art review is presented concerning the different sensors employed in PAS with a special focus on quartz enhanced photoacoustic spectroscopy. In particular, a summary of the previous PhD student's work at ONERA on photoacoustics is provided. A review of different industrial sensors is also provided, describing the maturity of these technologies in the area of gas detection.

### 1.1 Microphone based photoacoustic spectroscopy: MPAS

We choose to call microphone based photoacoustic spectroscopy (MPAS) the photoacoustic technique developed in the late forties [36]. It historically takes advantage of the development of microphones as quantitative acoustic detectors which was a huge improvement in comparison with the previously used human hearing.

#### 1.1.1 Microphones

The basic principle of a microphone consists in the movement of a membrane, excited by acoustic waves, and the reading of this membrane displacement. One can distinguish several types of microphones: carbon, ribbon, piezoelectric or more recently laser based optoacoustic microphones. However, we will describe here the most common type of microphone which is the condenser microphone.

Condenser microphones rely on the same principle as other microphones, a thin film membrane, usually made of gold coated Mylar<sup>®</sup>, Silicon or stainless steel, is forced into oscillation by an external acoustic force. The reading of its displacement is based on the principle of condensers, as its name suggests. The condenser consists of two conductor plates (here the membrane and the backplate) separated by a dielectric medium (in our case air or gas). For this purpose, the backplate is polarised by an electrical circuit or can be permanently magnetised, we then talk about "electret microphones". Its capacitance changes with the modification of the distance between the conductor plates. The sensitivity depends mainly on the area of the plates and the distance from each other as well as the membrane material and thickness. Capacitance value is converted into an analog or digital signal through proximity electronics, giving the measured pressure. A schematic diagram of a condenser microphone is presented in Figure 1.1.

From the acoustical point of view, the microphone is made of two gas volumes separated by the membrane. The membrane is usually perforated in order to balance the low frequency pressure waves between the two

volumes. In addition, a vent is sometimes made in the back volume of the microphone to equalise pressure with ambient air. By carefully designing the microphone it is possible to reduce acoustic damping due to the existence of the back volume [37, 38].

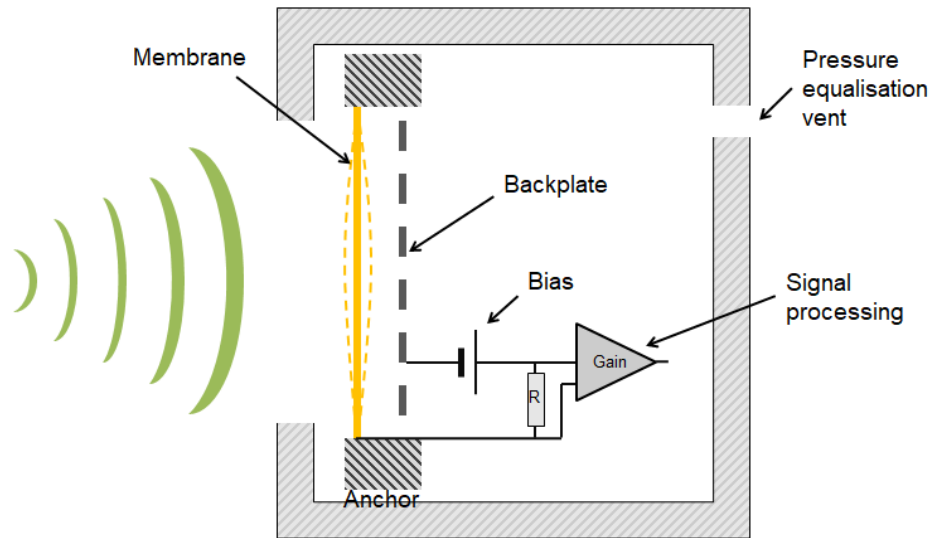


Figure 1.1: Schematic of a condenser microphone.

A further distinction has to be made, between the different condenser microphones. Indeed, with the development of the Internet of Things and the need for compact solutions, Microelectromechanical systems (MEMS) were developed. In comparison with classical microphones these are smaller and adapted to the use in portable applications, such as audio systems for smartphones, through low power consumption, low cost, and durability. An example of state-of-the-art MEMS and classic microphones is presented in Figure 1.2.

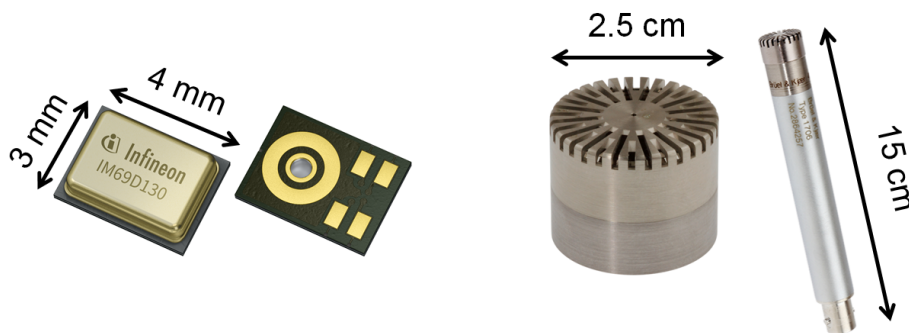


Figure 1.2: Examples of condenser microphones. On the left: Infineon digital IM69D130 MEMS microphone [39, 40]. On the right: Bruel&Kjaer BK4144 1 inch microphone and its preamplifier [41].

Microphones used in PAS are usually designed for the human hearing audio band from 20 Hz to 20 kHz. Therefore their first mode of resonance is generally beyond 20 kHz in order to present a flat response over the audio band. In photoacoustics they are generally used in that spectral band because of the limitations due to molecular relaxation rates as we will see in Section 2.1.2. However, they could also be used at their resonance frequency so as to make sure that the noise of the microphone is limiting compared to the electronic noise of the signal processing unit (preamplifier and lock-in detection). It can be noted that microphones working at higher frequencies exist, for example for non-destructive control in the industry or for medical applications.

In photoacoustics, only a part of their spectral response is used and selected by employing a lock-in detection scheme (which principle is detailed in Section 2.1.6) in order to reduce the system noise.

Even though developments are still in progress, particularly for piezoelectric MEMS microphones, these technologies have already reached their fundamental limits in terms of material losses and SNR. Indeed, the membrane losses are well known, the thermal noise is usually limiting [42], and the acoustic design is controlled to limit membrane damping [38, 37]. Nevertheless, using a microphone alone does not allow for meeting the needs required for most gas detection applications in terms of sensitivity. That is why they are generally used with acoustic resonators as we describe in the next paragraph.

## 1.1.2 Acoustic amplification cells

In order to increase the acoustic pressure detected by the microphone, acoustic resonators are used. They consist in acoustic cavities containing the gas to be detected and inside which the laser beam passes. The microphone is placed where pressure amplitude is the highest.

In order to compare cells, their capacity to amplify acoustic pressure waves is evaluated. The figure of merit giving the pressure generated for a normalised heat deposition in the medium is called the cell constant  $C$  and is expressed in  $\text{Pa}\cdot\text{W}^{-1}\cdot\text{cm}$ . Also, a figure of merit called normalised noise equivalent absorption (NNEA) is used so as to compare sensors sensitivity. NNEA is directly related to the cell constant but additionally takes into account the microphone sensitivity. It is the sensor signal-to-noise ratio normalised by the laser power, gas absorption and measurement bandwidth expressed in  $\text{W}\cdot\text{cm}^{-1}\cdot\text{Hz}^{-1/2}$ . These figures of merit are presented extensively in Chapter 2.

Main cell geometries employed in laboratories are presented in the next paragraphs as well as reached performances.

### 1.1.2.1 Simple cylindrical cells

Cells used in photoacoustic spectroscopy generally present a simple cylinder shaped geometry resonating at their first longitudinal, radial or azimuthal eigenmode as illustrated in Figure 1.3. Several groups demonstrated the use of acoustic resonators since approximately 1940 [43, 44, 45]. Amongst them, Dewey et al. demonstrated an enhancement of a factor 100 of the generated pressure compared to free space absorption when detecting n-butane by means of a radial resonator [44].

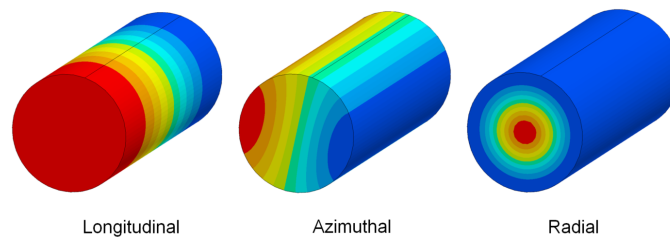


Figure 1.3: First pressure modes of a cylindrical acoustic resonator. The positive relative pressure is represented in red, the negative in blue.

The cell constant mainly depends on its geometry, quality factor, and on the overlap integral between the acoustic mode and the laser beam intensity distribution. Analytical models exist in order to predict the cell resonance frequency, quality factor and constant [21, 46] for simple cell geometries (see Section 2.1.3.2).

As such, cells have been designed to have quality factors as high as 1,000 up to 10,000 [47, 48]. However, it has been shown that the optimal cell constant is obtained for cells with increased interaction length between the laser beam and the gas while keeping a small volume [21]. As a result, the optimal cell reported to date for



photoacoustics, in terms of sensitivity, is a cylinder of small radius and long length to maximise the pressure, even though its quality factor is low (Figure 1.4(a)). For example, while a high quality factor cell demonstrated a cell constant of  $200 \text{ Pa}\cdot\text{W}^{-1}\cdot\text{cm}$  [21], a 30 quality factor cylinder of 3 mm radius and 170 mm length demonstrated a cell constant of  $8,615 \text{ Pa}\cdot\text{W}^{-1}\cdot\text{cm}$  [49].

A consequence of the use of cylindrical geometry and the need for low frequencies, due to photoacoustic relaxation processes, is the common use of the first longitudinal mode. However, radial and azimuthal resonators also demonstrate good performances [50].

It should be noted that cells used in PAS are usually not simple cylinders. Actually, by using laser amplitude modulation (AM), a part of the laser power is absorbed by the cell windows or by the cell walls, generating an acoustic signal background at the same frequency as the detection [21]. The presence of this signal background is undesirable because it could degrade the dynamic range of the lock-in detection. So usually cells are equipped with buffer volumes as can be seen in Figure 1.4(b). These additional volumes act as acoustic filters attenuating the sound background detected by the microphone [51].

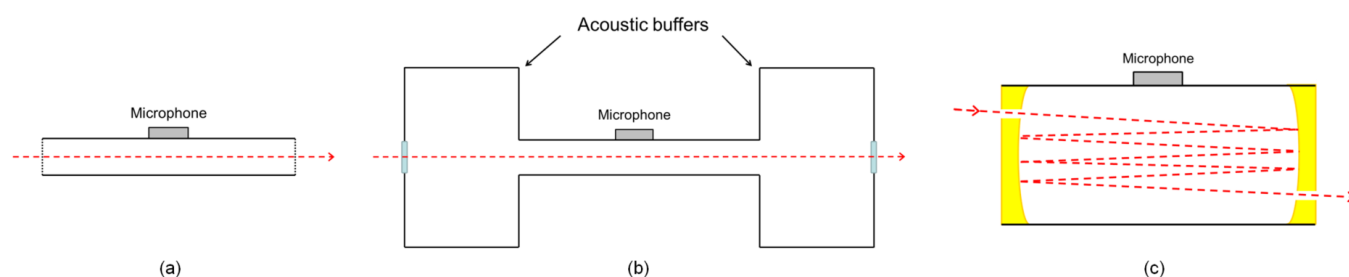


Figure 1.4: Slice view schematic of simple cylinder shaped resonators used in photacoustic gas spectroscopy (a). Used with acoustic buffers (b). Schematic of a multipass cell (c).

Such carefully designed cells equipped with state-of-the-art microphones can reach NNEA ranging from  $10^{-9} \text{ W}\cdot\text{cm}^{-1}\cdot\text{Hz}^{-1/2}$  [52, 53] to  $10^{-11} \text{ W}\cdot\text{cm}^{-1}\cdot\text{Hz}^{-1/2}$  [54]. The NNEA can be further improved by increasing the optical path through using multipass absorption cells (Figure 1.4(c)), such as a Herriott cell. The cylinder cell is then closed by two mirrors carefully designed so as to generate the maximal number of laser passes while avoiding beam interference. Typically, the number of passes generated by such cells is close to 30 [55]. Zhang et al. reported a NNEA of  $1.4 \cdot 10^{-9} \text{ W}\cdot\text{cm}^{-1}\cdot\text{Hz}^{-1/2}$  by using such a cell with 17 passes [56].

However, the use of the NNEA may be questionable for such systems because laser power absorption may not be linear anymore due to the long path lengths (the linear approximation of Beer-Lambert-Bouguer's law may no longer hold). In these cases, the NNEA should be computed in the linear mode of the sensor, otherwise, other figures of merit should be used <sup>1</sup>.

One could expect that the increase of sensitivity generated by the multipass technique could benefit to state-of-the-art single pass cells. However, the limits of detection for multipass techniques reach the same order of magnitude as single-pass cells ones. This can be explained by the technical constraints needed to set multipass cavities. In order for the reflected beams not to interfere, the cavity radius should be increased, degrading both the acoustic pressure generation (inversely proportional to the squared cell radius (see Section 2.1.3.2)) and the overlap of the acoustic waves with the microphone. A compromise may be found between the number of passes and the cell constant by reducing the multipass cell radius. It is also possible to keep a small cell radius (some

<sup>1</sup>In the case in which Beer-Lambert-Bouguer's law linear approximation does not hold it is preferable to use the NEA (noise equivalent absorption). It is defined in the same way as the NNEA except that it is not normalised by laser power. A NEA of  $2.1 \cdot 10^{-11} \text{ cm}^{-1}\cdot\text{Hz}^{-1/2}$  can be derived from [56].

millimeters) and to employ right angle prisms to increase up to 4 times the number of passes [57, 58].

In order to improve the cell constant a minimal radius should be chosen, however this radius cannot be infinitely decreased. The optimal radius should be chosen as the minimal radius allowing for the laser beam not to touch the cell walls, otherwise a signal background will be generated (especially at high wavelengths such as in the mid-infrared).

Although photoacoustic spectroscopy is an optical background free technique it is very sensitive to acoustic background which cannot always be avoided [54], especially out of the lab. As we have seen, background signal can be generated by the laser beam absorption, but it can also come from the acoustic or electromagnetic environment, vibrations or gas flow. A solution to reduce these backgrounds consists in the use of differential measurement as we will describe in the next paragraph.

### 1.1.2.2 Differential cells

The first differential cell was presented in 1975 [45], it consists in the use of two cylinder volumes, in which the laser beam passes. In each volume a microphone measures the acoustic pressure and a differential signal is obtained allowing to reduce signal background. This configuration was improved later on by adding buffer volumes [21], and by carefully placing the gas inlet and outlet (Figure 1.5(a,b)), achieving a NNEA of the order of  $10^{-9} \text{ W.cm}^{-1}.\text{Hz}^{-1/2}$  [59].

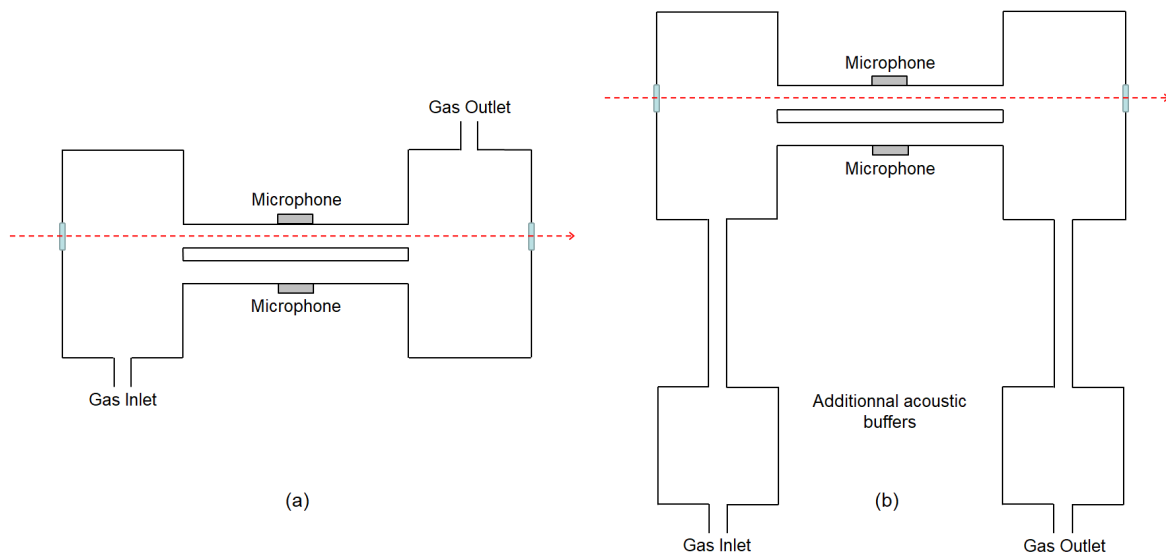


Figure 1.5: Schematic of differential resonators used in photoacoustic spectroscopy. (a) is similar to classic cells presented before with an additional microphone. (b) Differential cell with supplementary buffers to shield from signal background coming from the gas circuit.

Another possibility is to make the entire differential cell resonant as shown in Figure 1.6. The resonator is then composed of two chambers in which the laser beam passes and of two capillaries connecting them. The resonator can be assimilated as a mass-spring system with the chambers being the masses and the air volume in the capillaries being the spring. At the first anti-symmetric acoustic mode, pressure amplitude oscillates in time between the two chambers while the middle of the capillaries presents a pressure amplitude node. Placing the gas connectors in the capillaries allows for reducing the sound background coming from the gas circuit seen by the microphones.

State-of-the-art sensitivity of such cells has reached  $2.4 \cdot 10^{-10} \text{ W.cm}^{-1}.\text{Hz}^{-1/2}$  [46] employing Helmholtz resonance. Miniaturised cells based on the same kind of resonators have also been designed [60] reaching a NNEA of  $4.3 \cdot 10^{-9} \text{ W.cm}^{-1}.\text{Hz}^{-1/2}$ .

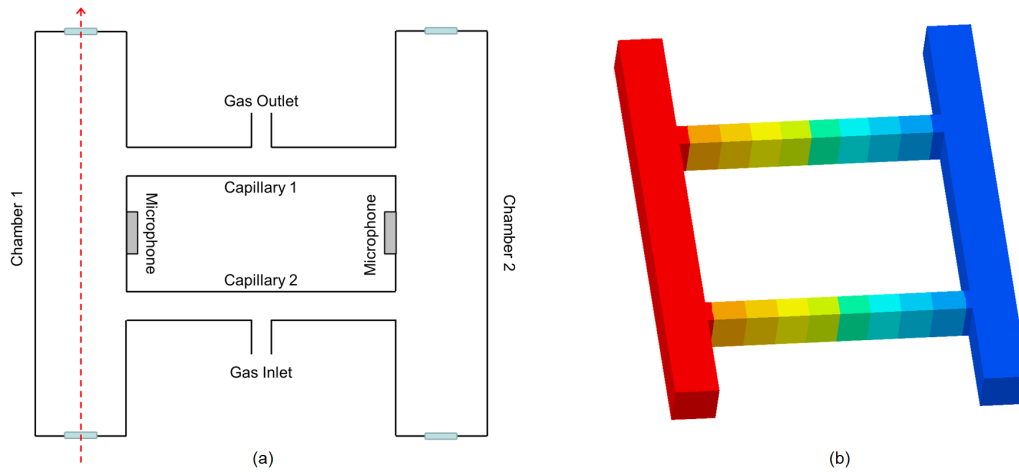


Figure 1.6: Schematic of Helmholtz type differential resonators used in photoacoustic spectroscopy. (a) Helmholtz type resonator. (b) Resonator anti-symmetric acoustic mode. The positive relative pressure is represented in red, the negative in blue.

A sum up of the detection limits reached by MPAS type sensors is given in Table 1.1.

Gas	Wavenumber (cm <sup>-1</sup> )	Laser power (mW)	Integration time (s)	LOD (1σ)	α <sub>min</sub> (cm <sup>-1</sup> )	NNEA (W.cm <sup>-1</sup> .Hz <sup>-1/2</sup> )	Ref.
CO <sub>2</sub>	6,362.5	2	60	114 ppmv	2 10 <sup>-7</sup>	3.1 10 <sup>-9</sup>	[52]
O <sub>2</sub>	13,091.71	3		100 ppmv	1.3 10 <sup>-7</sup>		
C <sub>2</sub> H <sub>2</sub>	6,529.17	15.1	100	8.4 ppbv	9.6 10 <sup>-9</sup>	1.4 10 <sup>-9</sup>	[56]
NO <sub>2</sub>	22,371.36	1,300	1	54 pptv	6 10 <sup>-10</sup>	1.58 10 <sup>-9</sup>	[59]
CH <sub>4</sub>	6,046	0.7	1	5 ppmv	1.8 10 <sup>-6</sup>	1.3 10 <sup>-9</sup>	[46]
	6,046	0.7		1 ppmv	3.4 10 <sup>-7</sup>	2.4 10 <sup>-10</sup>	
	6,056	2		0.3 ppmv	1.2 10 <sup>-7</sup>	2.4 10 <sup>-10</sup>	
CH <sub>4</sub>	2,979	2.2	1	92 ppbv	1.7 10 <sup>-6</sup>	4.3 10 <sup>-9</sup>	[60]
NO	1,857.27	2.8	1	20 ppbv	2.6 10 <sup>-7</sup>	3.3 10 <sup>-10</sup>	[61]
DMMP	1,053	12	1	3 ppbv	1.8 10 <sup>-7</sup>	4.2 10 <sup>-9</sup>	[62]
NO <sub>2</sub>	1,614.7	5	2	80 ppbv	2.5 10 <sup>-6</sup>	2.5 10 <sup>-8</sup>	[63]
	N <sub>2</sub> O	1,254.5		10	84 ppbv	5 10 <sup>-7</sup>	
NH <sub>3</sub>	6,528.7	1,000	40	6 ppbv	1.4 10 <sup>-9</sup>	1.5 10 <sup>-9</sup>	[53]
CH <sub>4</sub>	6,057.1	10	4	0.5 ppmv	2.2 10 <sup>-7</sup>	4.4 10 <sup>-9</sup>	[49]
C <sub>2</sub> H <sub>4</sub>	949.49	2,000	2	6 pptv	2.5 10 <sup>-10</sup>	6.7 10 <sup>-11</sup>	[54]

Table 1.1: Sensitivities and limits of detection reported for MPAS.

## 1.2 Cantilever enhanced photoacoustic spectroscopy: CEPAS

The second technique, called cantilever enhanced photoacoustic spectroscopy (CEPAS), was introduced in 2003 [64, 65]. In a very similar way to MPAS, CEPAS uses a cantilever beam to detect the acoustic pressure waves generated inside an acoustic cavity.

### 1.2.1 Cantilevers

In order to enhance the sensitivity of photoacoustic detectors, cantilevers were designed to replace microphones [64]. While microphones are designed to present a resonance frequency near 20 kHz, allowing their use in a wide audio band (usually 20 Hz - 20 kHz), cantilevers are designed to present lower resonance frequencies (usually below 1 kHz). They take advantage of the higher pressure amplitude at lower frequencies in acoustic resonators. Moreover, working at low frequencies also allows for detecting gases with slower relaxation rates. Another benefit of working at a detection frequency close to the detector resonance frequency is to take advantage from the higher level of the Brownian noise in order to raise this noise out of the system other noises.

Different types of cantilevers have been used. The main ones are machined from Silicon wafers [66, 67] or from stainless steel films [68] (Figure 1.7). They usually present low quality factors inferior to 100, and a resonance frequency below 1 kHz. Their thickness is chosen to be as thin as possible in order to enhance their stiffness and displacement and thus to facilitate the detection. As a consequence, the modelling of these detectors needs to take into account the influence of the gas on the beam displacement [66].

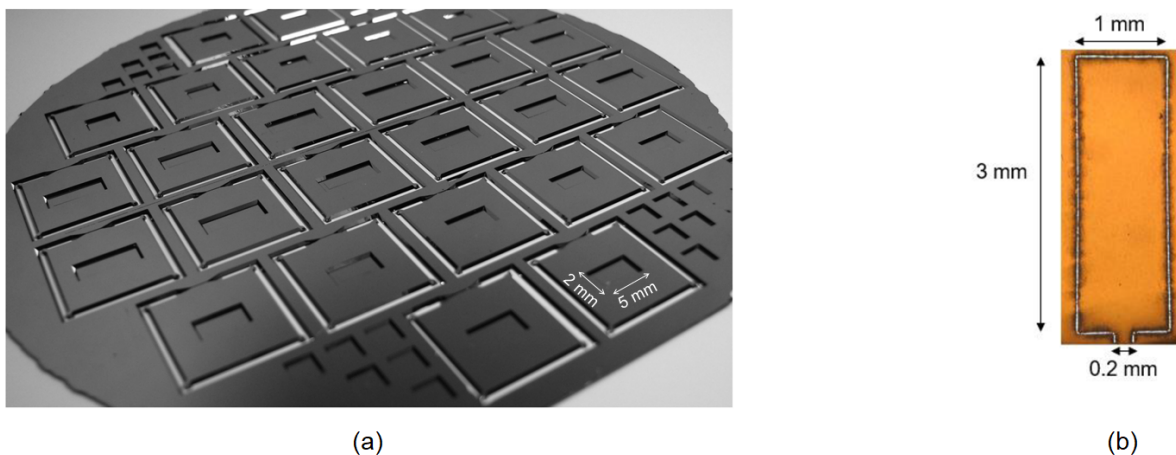


Figure 1.7: Examples of cantilevers from literature. (a) Photograph of a Silicon wafer with cantilevers of typical dimensions 5 mm long, 2 mm wide and 10  $\mu\text{m}$  thickness [66]. (b) Photograph of a cantilever laser cut from a stainless steel sheet with dimensions 3 mm long, 1 mm wide and 100  $\mu\text{m}$  thickness [68].

Detection of the displacement is mainly carried out optically through the use of an optical interferometer (such as a Michelson one) (Figure 1.8(a)). This method is generally sufficient to detect the Brownian noise of the cantilever [66]. Another method is to detect the stress generated by the beam displacement through the use of nano-gauges [69] (Figure 1.8(b)). Yet another method consists in using piezoelectricity by depositing a thin film on the cantilever and collecting the generated charges [70] (Figure 1.8(c)). One could also use quartz cantilever beams, although we have no example of a CEPAS sensor using these in the literature.

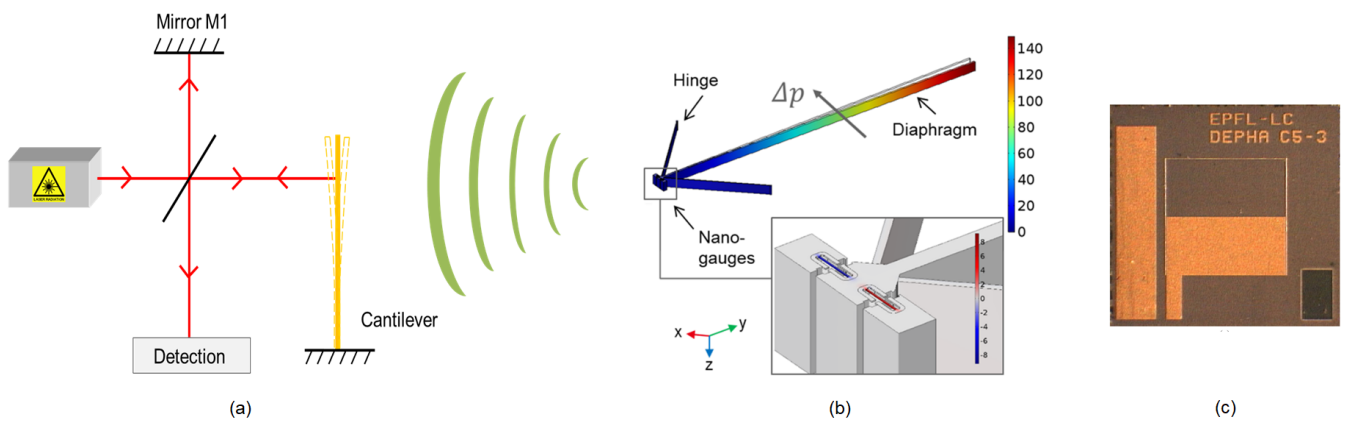


Figure 1.8: Scheme of the principle of cantilever enhanced photoacoustic spectroscopy detection. Cantilever displacement reading is made through a simple Michelson interferometer (a), through use of nano-gauges [69] (b) or through charge collection by depositing a piezoelectric film on the cantilever (c) [70].

## 1.2.2 Acoustic amplification cells

As for MPAS, usually cantilevers are combined to an acoustic amplification cell. The setup is similar to what is used in MPAS, the cell usually is a cylinder where the cantilever is positioned at a pressure antinode (Figure 1.4(b)).

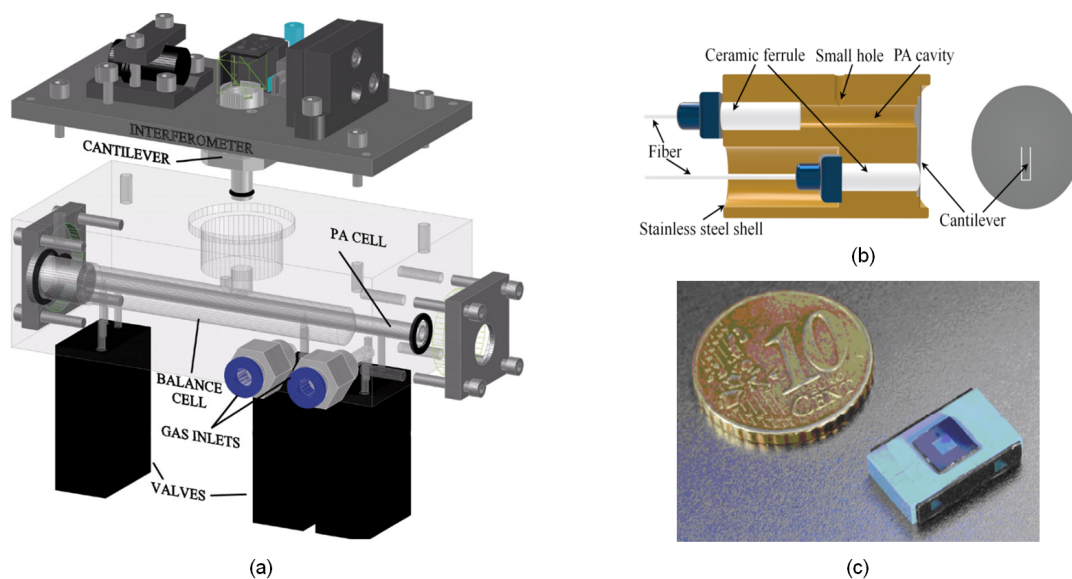


Figure 1.9: Example of a complete CEPAS setup reaching state-of-the-art NNEA (a). The cantilever is placed in the middle of the cylinder in which a laser beam passes. Displacement of the cantilever is read by using an interferometer placed above the cylinder [71]. (b) Example of a new kind of miniature CEPAS detector based on the use of optical fibers for excitation and readout [72]. (c) Photography of a miniature differential cell containing a Silicon cantilever [73].

The first to use cantilevers demonstrated a state-of-the-art sensitivity of  $1.7 \cdot 10^{-10} \text{ W.cm}^{-1} \cdot \text{Hz}^{-1/2}$  [74]. The cell they used was a 3 mm diameter and 95 mm length cylinder that should be resonating near 1.6 kHz. The Silicon cantilever dimensions are typically 4 mm long, 2 mm wide and 5 to 10  $\mu\text{m}$  thick [71] with a gap between

the frame and the cantilever of the order of the micrometer. The first resonance frequency of this cantilever is around 550 Hz and presents a quality factor in the range 10 to 100 under atmospheric pressure. Neither the cantilever nor the cell was used at its resonance frequency since the detection was operated near 10 Hz.

Such thin cantilevers can be easily excited by external sound or vibration, especially at low frequencies. In order to mitigate those effects, the quality factor can be increased as well as the resonance frequency through modification of the cantilever geometry. Also, a balance or differential cell is often used (Figure 1.8(a,c)), enabling to equalise pressure on each side of the cantilever and avoid acceleration noise [75], although special care should be taken when choosing the dimension of the gap between the cantilever and the frame [71].

Lately, in order to miniaturise CEPAS sensors, fiber optic interferometer and excitation laser have been used and cell size was decreased (Figure 1.9(a)). Chen et al. demonstrated  $2.3 \cdot 10^{-9} \text{ W.cm}^{-1}.\text{Hz}^{-1/2}$  using a 3 mm long, 1 mm wide and 10  $\mu\text{m}$  thick stainless steel cantilever [72]. By using such a cantilever to monitor the acoustic pressure generated with a cell presenting a higher cell constant (radius 4 mm, length 120 mm) the sensitivity was increased to  $4.2 \cdot 10^{-10} \text{ W.cm}^{-1}.\text{Hz}^{-1/2}$  [76], showing the importance in the design of the acoustic cell.

A sum up of the detection limits reached by CEPAS instruments is given in Table 1.2.

Gas	Wavenumber (cm <sup>-1</sup> )	Laser power (mW)	Integration time (s)	LOD (1 $\sigma$ )	$\alpha_{\text{min}}$ (cm <sup>-1</sup> )	NNEA (W.cm <sup>-1</sup> .Hz <sup>-1/2</sup> )	Ref.
C <sub>2</sub> H <sub>2</sub>	6,523.87	100	500	0.5 ppbv	$5.2 \cdot 10^{-10}$	$2.3 \cdot 10^{-9}$	[72]
CO <sub>2</sub>	6,361.25	30	100	300 ppbv	$5.5 \cdot 10^{-10}$	$1.7 \cdot 10^{-10}$	[74]
C <sub>2</sub> H <sub>2</sub>	6,523.88	1,000	200	27 pptv	$2.8 \cdot 10^{-11}$	$4.2 \cdot 10^{-10}$	[76]
				71 pptv	$7.5 \cdot 10^{-11}$	$1.1 \cdot 10^{-9}$	[77]
C <sub>2</sub> H <sub>2</sub>	6,534.37	24	230	3 ppbv	$3.5 \cdot 10^{-9}$	$1.3 \cdot 10^{-9}$	[78]
CO <sub>2</sub>	2,302.6	4.88	1	3 ppmv	$6.2 \cdot 10^{-5}$	$3 \cdot 10^{-7}$	[69]
C <sub>2</sub> H <sub>4</sub> CH <sub>4</sub>	915.6	4	20	45 ppmv	$3.6 \cdot 10^{-4}$	$4.7 \cdot 10^{-5}$	[67]
	6,046.94		600	242 ppmv	$9 \cdot 10^{-5}$		

Table 1.2: Sensitivities and detection limits reported for CEPAS.

### 1.3 Quartz enhanced photoacoustic spectroscopy: QEPAS

The last technique we describe is quartz enhanced photoacoustic spectroscopy (QEPAS). QEPAS consists in the detection of the acoustic waves by means of quartz tuning forks (QTF).

#### 1.3.1 Watch tuning forks

The first tuning forks employed for PAS were watch tuning forks (Figure 1.10(a)) because of their large availability in the industry, their low cost as well as compactness. For their original horological application, they are generally used under vacuum and their resonance frequency is chosen to be a power of 2 (32,768 Hz:  $2^{15}$ ).

Kosterev et al. were the first to use quartz tuning forks in photoacoustic spectroscopy [28]. The QTF was used in on-beam configuration (Figure 1.10(b)) where the laser beam is perpendicular to the prongs and focused between them. It can be noted that the laser beam height is optimised compared to the length of the prongs, giving a maximal signal around 85% of the prong length [79]. Typically watch QTFs present a prong length of 3.75 mm, width of 0.4 mm, thickness of 0.34 mm and gap between the prongs of 0.31 mm in which the laser

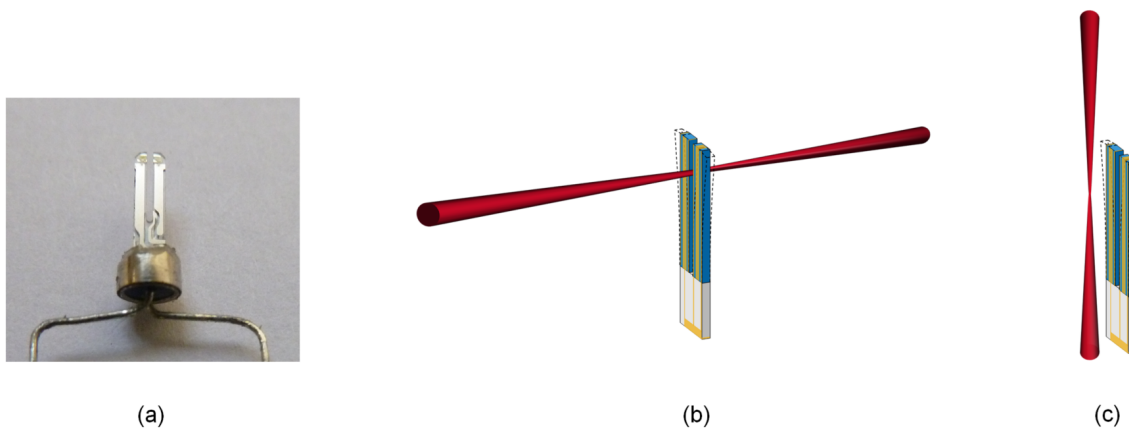


Figure 1.10: (a) Photography of a watch quartz tuning fork. (b) Schematic of on-beam configuration where the laser beam passes between the QTF prongs. (c) Schematic of in-plane configuration where the laser beam is parallel to the QTF and focused near the gap or inside it.

beam is focused.

Compared to microphones and cantilever beams, QTFs present high quality factors. While these QTFs were designed to work under vacuum demonstrating typical quality factors of 100,000, in photoacoustics they are used at atmospheric pressure in the gas to be detected, reducing their quality factors by one order of magnitude to reach approximately 10,000. Enhancement of the quality factor allows for increasing the sensitivity (see Chapter 2) as well as signal background filtering. Nonetheless, using high quality factor detectors, with a lock-in detection scheme, also increases the response time by a multiple of the ratio  $Q$  over  $f_0$ , which can be typically of a few seconds. By using such a configuration a NNEA of  $8.8 \cdot 10^{-7} \text{ W.cm}^{-1}.\text{Hz}^{-1/2}$  was achieved. By using another configuration in which the laser beam is parallel to the prongs, called in-plane configuration (Figure 1.10(c)), the sensitivity was increased by 4 compared to the bare QTF, reaching  $2.2 \cdot 10^{-7} \text{ W.cm}^{-1}.\text{Hz}^{-1/2}$ .

The performance of watch QTFs was improved by other groups reporting NNEAs around  $1 \cdot 10^{-7} \text{ W.cm}^{-1}.\text{Hz}^{-1/2}$  when using watch QTFs in on-beam configuration [80].

Later on, analytical models were created in order to optimise quartz tuning forks for photoacoustics. The sound propagation in free space was modelled as well as acoustic recovery by the QTF and piezoelectric transduction, demonstrating a good agreement with experiment [79].

The advantages of these QTFs are their high quality factor and quadrupolar nature, providing enhanced isolation from signal backgrounds, and enhanced compactness as well as cost scalability as we will discuss in Section 4.3. However, compared to MPAS and CEPAS, the sensitivity of QEPAS using watch QTFs is two or three orders of magnitude lower. In addition, the high resonance frequency makes the measurement of slowly relaxing molecules less sensitive, for example inducing a signal loss of 60% for  $\text{CO}_2$  at  $2 \mu\text{m}$  (see Section 2.1.2). Ultimately, the pass of the laser beam through the prongs, which gap is typically  $300 \mu\text{m}$ , without generating signal background is difficult, especially in the mid-infrared where molecules present strong absorption lines.

### 1.3.2 Custom tuning forks

To mitigate these drawbacks, custom QTFs were designed, presenting lower frequencies, down to 3 kHz [81], higher quality factors at atmospheric pressure, up to 38,000 [81], or increased gap between the prongs, up to 1.5 mm [82]. A few teams have designed custom QTFs and some of them are presented in Figure 1.11, also their parameters are described in Table 1.3. ONERA's work on QTFs will be presented in Section 1.6.

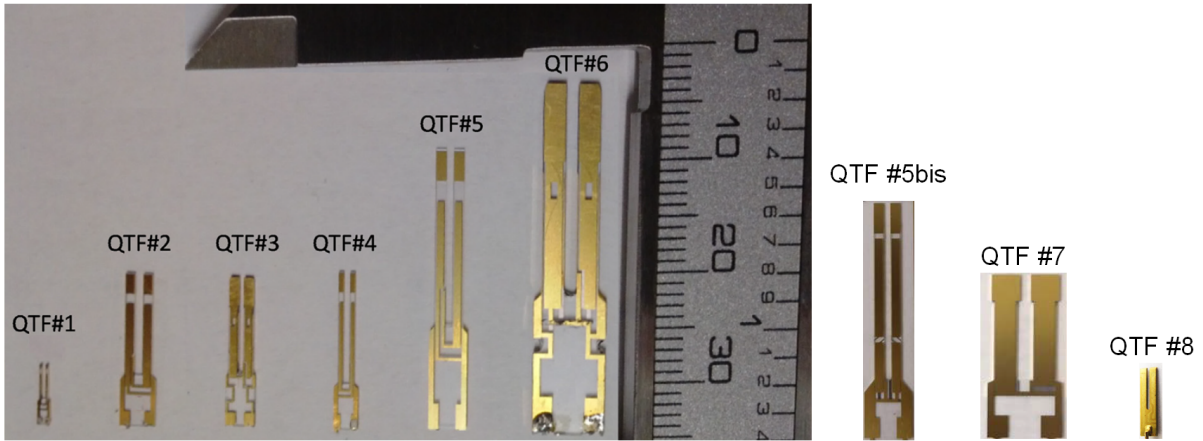


Figure 1.11: Scaled photography of custom quartz tuning forks reported in literature. QTFs 1-6 [81], QTF 5 bis [83, 84], QTF 7 [82], QTF 8 [85].

QTF	$l$	$e$	$L$	$g$	$Q$	$f_0$
1	0.25	0.2	3.5	0.4	7,323	14,049
2	0.25	0.9	10	0.8	8,536	7,230
3	0.5	1	10	0.5	25,485	8,440
4	0.25	0.5	11	0.6	8,388	3,457
5	0.25	1	17	0.7	11,902	2,869
5bis	0.25	1	17	0.7	31,374	17,789
6	0.8	1.4	19	1	37,713	4,250
7	0.25	2	9.4	1	15,540	12,460
8	0.35	0.4	3.3	0.2	7,463	27,987

Table 1.3: Parameters of different custom QTFs found in the literature. The dimensions are given in mm, frequency in Hz. The quality factor is measured at atmospheric pressure.

In [81] a batch of QTFs was produced with different parameters (gap, frequency, etc.) and their quality factor was optimised. The sensitivity of QTF#5 was reported to be  $3.75 \cdot 10^{-11} \text{ W.cm}^{-1}.\text{Hz}^{-1/2}$  while using a terahertz optical source [86]. This sensitivity is three or four orders of magnitude better than any other reported value and is explained by the authors as the enhancement of the photoacoustic signal in the terahertz region. However, since the NNEA is normalised by the gas absorption and laser power, this explanation has to be invalidated. Furthermore, by using the same tuning fork another publication reports a different NNEA of  $4.4 \cdot 10^{-10} \text{ W.cm}^{-1}.\text{Hz}^{-1/2}$  [87]. In addition, another team tried to reproduce these results and reported a NNEA of only  $1.05 \cdot 10^{-6} \text{ W.cm}^{-1}.\text{Hz}^{-1/2}$  [88]. While no team could reproduce this result, there should be a mistake in the evaluation of the NNEA (one could also notice that the authors of [86] changed their computation method afterwards), making this record value questionable. We will also prove in the following chapters through analytical and numerical simulations that these results are not consistent (see Section 3.2.1.1). We thus choose to discard them for benchmark.

QTF#8 was designed with a similar geometry as a watch QTF but the gap between the prongs was reduced to  $200 \mu\text{m}$ , resulting in a signal enhancement and sensitivity of  $1.7 \cdot 10^{-8} \text{ W.cm}^{-1}.\text{Hz}^{-1/2}$  [85]. On the other hand this heavily complicates laser alignment and increases optical background in on-beam configuration.

Other QTFs were designed, as for example a 75 kHz QTF [89] presenting a sensitivity of  $1.9 \cdot 10^{-8} \text{ W.cm}^{-1}.\text{Hz}^{-1/2}$



or even a micro QTF machined in fused silica together with an integrated light interferometer for displacement reading [90].

Later on, the use of overtone was reported. QTF#5 presented in Figure 1.11 was used at its overtone flexural frequency in order to enhance its quality factor [83]. The mode shape presents a displacement node near the middle of the prong (Figure 1.12). The electrode pattern was adapted to the QTF mode, resulting in an octupole pattern seen on QTF#5bis on Figure 1.12. The quality factor was increased from 11,902 to 31,374 while the fundamental frequency was increased from 2,869 Hz to 17,789 Hz. The sensitivity can be derived from [88, 84] to be  $8.38 \cdot 10^{-7} \text{ W.cm}^{-1}.\text{Hz}^{-1/2}$  for the QTF in its fundamental mode and  $1.11 \cdot 10^{-7} \text{ W.cm}^{-1}.\text{Hz}^{-1/2}$  for the overtone. The enhancement should mainly come from the increase of the pressure at higher frequency (expected to be near 6). Ultimately, the use of overtone enables targeting simultaneously 2 gases by employing two lasers focused near the top of the prongs and below the displacement node, respectively modulated at fundamental and overtone frequencies [84].

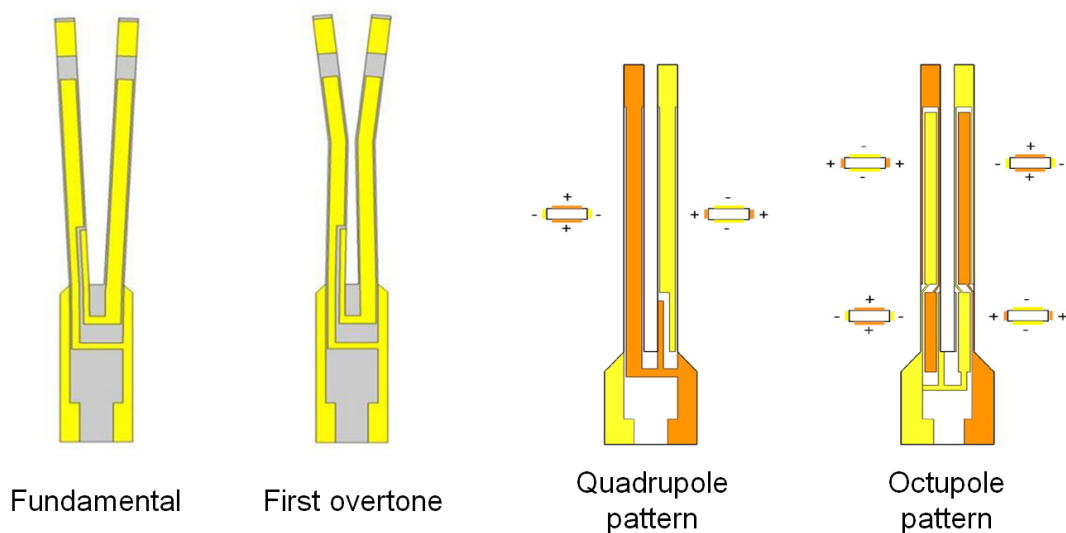


Figure 1.12: Comparison of the beam displacement in fundamental and overtone mode (left) [83]. Schematic of the quadrupole electrode pattern adapted to fundamental mode and octupole pattern for the overtone [91](right).

Eventually, two others techniques can be exploited so as to reduce the resonance frequency and increase the signal. The first is the use of T-shaped QTFs, as for example QTF#7 (Figure 1.11). The center of inertia of the prongs is closer to the top and as a consequence the frequency is reduced, facilitating the detection of slowly relaxing molecules. Also, the gap between the prongs can be wider (up to 1.5 mm [82]) promoting the use of mid or far-infrared sources. Sensitivity of the best T-shaped QTF can be computed to be  $1.8 \cdot 10^{-7} \text{ W.cm}^{-1}.\text{Hz}^{-1/2}$  (for the QTF#7 named S08-T in [92]).

The second technique consists in reducing the prongs mass by carving grooves into it [93]. Doing so allows for reducing the resistance to motion and slightly increases the piezoelectric signal of a factor still needing to be quantified [82].

To conclude, the best custom QTFs present a NNEA around  $1 \cdot 10^{-8} \text{ W.cm}^{-1}.\text{Hz}^{-1/2}$  and optimised parameters such as low frequency or larger gap between the prongs. Their parameters are presented in Table 1.4. This sensitivity is sufficient for many applications for the detection of ppmv level of concentration down to tens of ppbv. However, when targeting the ppbv range (meaning a limit of detection lower, typically 200 pptv) for air quality analysis, for example, it is necessary to improve the sensitivity.

QTF	Gas	Wavenumber (cm <sup>-1</sup> )	Laser power (mW)	Integration time (s)	LOD (1σ)	α <sub>min</sub> (cm <sup>-1</sup> )	NNEA (W.cm <sup>-1</sup> .Hz <sup>-1/2</sup> )	Ref.
Watch QTF	CH <sub>4</sub>	5,999.49	2	1	470 ppmv 1,880 ppmv	1.1 10 <sup>-4</sup> 4.4 10 <sup>-4</sup>	2.2 10 <sup>-7</sup> 8.8 10 <sup>-7</sup>	[28]
	C <sub>2</sub> H <sub>2</sub>	6,529.17	37.2	1	4 ppmv	4.6 10 <sup>-6</sup>	1 10 <sup>-7</sup>	[80]
	C <sub>2</sub> H <sub>6</sub>	2,990.1	300	20	13 ppbv	5.7 10 <sup>-7</sup>	4.4 10 <sup>-7</sup>	[94]
Custom QTF	H <sub>2</sub> O	7,303.23	23	1	560 ppmv 74 ppmv	3.5 10 <sup>-5</sup> 4.7 10 <sup>-6</sup>	8.38 10 <sup>-7</sup> 1.11 10 <sup>-7</sup>	[88]
	CO <sub>2</sub>	6,361.25	38	1	2.3%	4.1 10 <sup>-5</sup>	1.59 10 <sup>-6</sup>	[95]
	H <sub>2</sub> O	7,194.8	5	84	6.3 ppmv	1.5 10 <sup>-6</sup>	1.7 10 <sup>-8</sup>	[85]
			5.8	1	125 ppmv	3 10 <sup>-5</sup>	1.74 10 <sup>-7</sup>	[96]
	C <sub>2</sub> H <sub>4</sub>	966.38	61.6	30	7 ppbv	2.2 10 <sup>-8</sup>	5.47 10 <sup>-7</sup>	[92]
	CHClF <sub>2</sub>	1,320	2	1	2 ppmv	3 10 <sup>-5</sup>	1.9 10 <sup>-8</sup>	[89]
H <sub>2</sub> S	6,320.6	1,520	1,000	2 ppbv	2.8 10 <sup>-11</sup>	5.16 10 <sup>-7</sup>	[97]	

Table 1.4: Sensitivities and detection limits reported for bare QTFs.

### 1.3.3 Coupling of acoustic resonators with QTFs

In a similar way to what was done in MPAS and CEPAS, acoustic resonators can be used to enhance the sensitivity. When presenting the first QTFs in photoacoustics, Kosterev et al. also introduced the use of acoustic resonators in on-beam configuration (Figure 1.13). These took the form of two cylinders positioned around the watch tuning fork and in which the laser beam passed, enhancing the sensitivity of a factor 7 to reach a NNEA of  $1.2 \cdot 10^{-7} \text{ W.cm}^{-1}.\text{Hz}^{-1/2}$  [28].

Acoustic resonators usually take the form of two stainless steel cylinders aligned around the QTF, in on-beam configuration, and longitudinally resonant. The method to enhance acoustic pressure is identical to the one of the resonators presented in MPAS and CEPAS, the pressure is the highest for small radii and long lengths. However, when using such resonators with QTFs a few precautions should be taken. Firstly, the radius should be carefully adapted in order for the laser beam not to touch the acoustic resonator walls nor the QTF branches, otherwise provoking signal loss as well as acoustical and photothermal background. Secondly, the gap between the two cylinders should be chosen to be as small as possible so as to limit acoustic losses while keeping a good excitation of the tuning fork. Thirdly, the space between the prongs and the cylinders should be closely adapted to avoid squeeze or viscous damping of the QTF. Finally, the acoustic resonators resonance frequency should be tuned near the QTF one to benefit from the coupling of the two resonances, this can be accomplished by modifying the length and radius of the cylinders. By carefully designing the system, a good coupling between the mechanic and acoustic resonators shall be obtained, resulting in a maximum of the sensitivity and a minimum of the system quality factor [98, 99].

Dong et al. optimised such resonators for a watch QTF and found an optimal for 4.4 mm long (each) and 300 μm radius cylinders. They demonstrated a sensitivity of  $3.3 \cdot 10^{-9} \text{ W.cm}^{-1}.\text{Hz}^{-1/2}$  [80] (Figure 1.14), representing an enhancement of 30 compared to the bare QTF. A similar enhancement, from 10 to 50, was reported by numerous publications [100, 101, 26], while the system quality factor was decreased from 10,000 down to 3,000 (decrease of 70%) demonstrating the strong coupling between the two resonators.

When using custom tuning forks, higher sensitivity amplification factors were obtained, as for example 60 by using the QTF#7 [82, 92]. This better enhancement might result from a better acoustic coupling between the QTF and the acoustic resonator due to the QTF specific geometry. Others reported a gain of 40 when

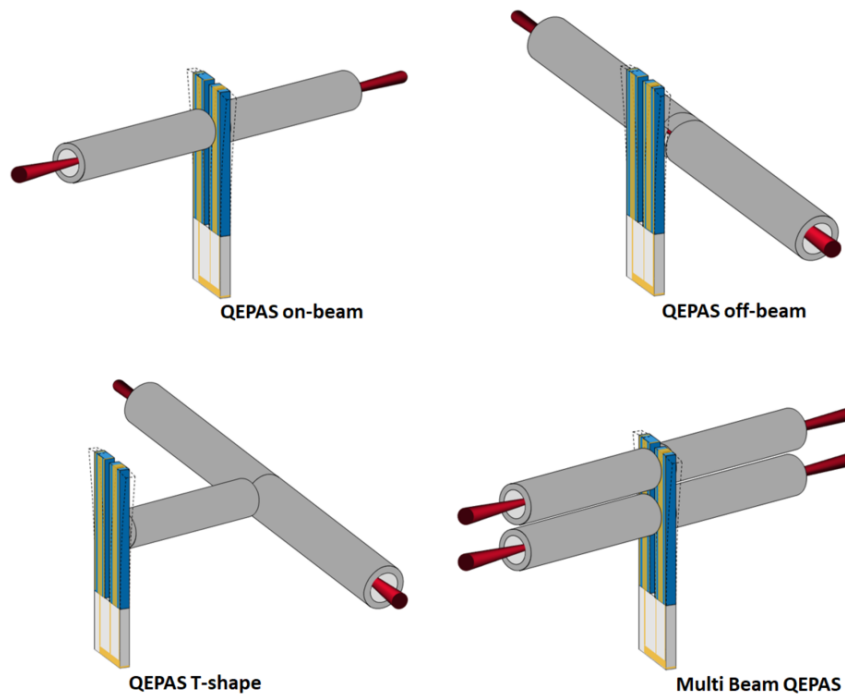


Figure 1.13: Schematic of the different configurations used in resonant QEPAS. Acoustic microresonators are added in order to amplify the pressure generated by the photoacoustic effect.

employing QTF#2 [97] and QTF#6 [102] leading to a computed NNEA of respectively  $4.3 \cdot 10^{-9} \text{ W.cm}^{-1}.\text{Hz}^{-1/2}$  and  $3 \cdot 10^{-9} \text{ W.cm}^{-1}.\text{Hz}^{-1/2}$ .

Yet another publication reported an enhancement of 128 when using QTF#2, reaching a NNEA of  $1.21 \cdot 10^{-8} \text{ W.cm}^{-1}.\text{Hz}^{-1/2}$  [95] which is explained by the authors by the better acoustic coupling. However, the quality factor of the system only decreased by 25%, which is in contradiction with the given explanation. Another possible explanation is the underestimation of the bare QTF sensitivity, indeed in [97] the NNEA of the bare QTF is 3 times better, which would result in a more likely amplification factor of 42.

Apart from enhancing the sensitivity, the use of such resonators also generates drawbacks. The main one is the difficulty to focus the laser beam inside the resonators without touching the walls. It is even more difficult with longer tubes and at longer wavelengths. Also, as it was the case with bare QTFs, the modulated laser can generate a photothermal signal background by touching the QTF itself. For that reason, different configurations were reported, such as off-beam or T-shape, represented in Figure 1.13, in order to remove the laser beam from the QTF prongs.

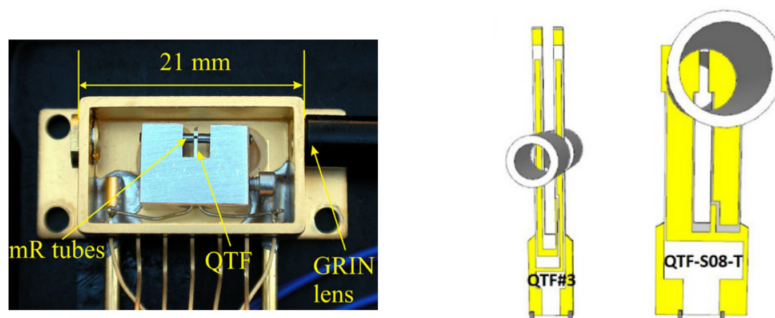


Figure 1.14: Examples of QEPAS with acoustic resonators. Watch QTF with dual tube resonators in a HHL mount [80] (Left). Custom QTFs with single tube resonators [92] (Right).

Off-beam QEPAS consists in placing a longitudinal resonator besides the QTF. The acoustic pressure wave is sent directly inside of the QTF gap through a small carved slit in the resonator. NNEAs of  $4.8 \cdot 10^{-8} \text{ W.cm}^{-1}.\text{Hz}^{-1/2}$  [103] or  $3.05 \cdot 10^{-9} \text{ W.cm}^{-1}.\text{Hz}^{-1/2}$  [104] were reported by using off-beam QEPAS.

T-shape QEPAS is very similar to off-beam configuration except that the slit is replaced by another tube guiding the acoustic wave towards the tuning fork. Geometry of this neck must be closely studied in order to limit the acoustic losses in the main resonator while efficiently exciting the QTF. Sensitivities of  $1.1 \cdot 10^{-8} \text{ W.cm}^{-1}.\text{Hz}^{-1/2}$  [101] or  $3.9 \cdot 10^{-9} \text{ W.cm}^{-1}.\text{Hz}^{-1/2}$  [105] were demonstrated.

Finally, in order to enhance the signal or to detect another gas, it is possible to use an additional pair of resonators, we talk of multi-beam configuration. A sensitivity of  $4.5 \cdot 10^{-9} \text{ W.cm}^{-1}.\text{Hz}^{-1/2}$  was obtained by measuring both  $\text{CO}_2$  and  $\text{H}_2\text{O}$  [106] and a sensitivity of  $1.73 \cdot 10^{-9} \text{ W.cm}^{-1}.\text{Hz}^{-1/2}$  when measuring  $\text{H}_2\text{O}$  [107]. This configuration is particularly interesting when a gas has to be measured to correct the measurement of another, such as  $\text{CO}_2$  which relaxation can be promoted by  $\text{H}_2\text{O}$ .

Despite the many efforts on the matter, the NNEA of systems employing a QTF coupled with acoustic resonators seems to cap around  $1 \cdot 10^{-9} \text{ W.cm}^{-1}.\text{Hz}^{-1/2}$ , which is one order of magnitude lower than state-of-the-art NNEAs reported for MPAS and CEPAS.

One last possibility for enhancing QEPAS detection limits is to increase the laser power. This was accomplished by placing the QTF inside a laser cavity, drastically enhancing the number of laser passes seen by the QTF. Such cavities were presented, enhancing the laser power of a factor 250 [108] and 1,276 [109] (Table 1.5). By using such intracavity setups the LOD is generally improved by a factor close to the number of passes in the cavity. Such a system can reach a LOD of 1 ppbv for  $\text{CO}_2$  at  $2,311.1 \text{ cm}^{-1}$  in a 5 s integration time [108]<sup>2</sup>.

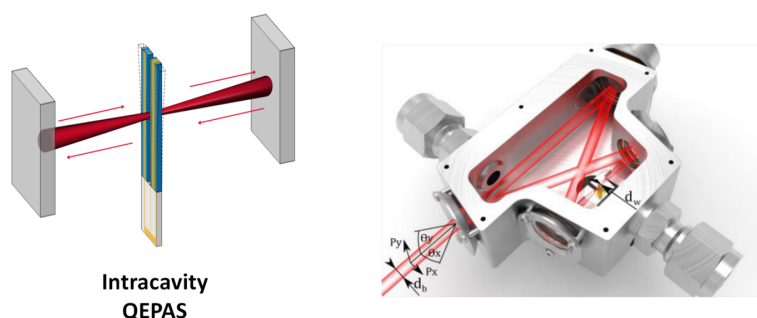


Figure 1.15: (Left) Schematic of intracavity QEPAS configuration. The QTF is placed inside a cavity, enhancing the laser power and thus sensitivity. (Right) Example of a bow-tie cavity for QEPAS enhancing the laser power by a factor 1,276 [109].

Gas	Wavenumber ( $\text{cm}^{-1}$ )	Injected laser power (mW)	Power enhancement factor	Integration time (s)	LOD ( $1\sigma$ )	Ref.
NO	1,900.08	133.2	1,276	0.03	4.8 ppbv	[109]
$\text{CO}_2$	2,311.1	3	250	20	0.3 ppbv	[108]

Table 1.5: Sensitivities and limits of detection reported for intracavity QEPAS systems.

To conclude the presentation of QEPAS techniques, Table 1.6 gives examples of reached limits of detection for different QEPAS setups.

<sup>2</sup>The NEA can be computed to be  $4.3 \cdot 10^{-10} \text{ cm}^{-1}.\text{Hz}^{-1/2}$  in [108].

Configuration	Gas	Wavenumber ( $\text{cm}^{-1}$ )	Laser power (mW)	Integration time (s)	LOD ( $1\sigma$ )	$\alpha_{\min}$ ( $\text{cm}^{-1}$ )	NNEA ( $\text{W} \cdot \text{cm}^{-1} \cdot \text{Hz}^{-1/2}$ )	Ref.
On-beam	CH <sub>4</sub>	5,999.49	2	1	256 ppmv	$6 \cdot 10^{-5}$	$1.2 \cdot 10^{-7}$	[28]
	C <sub>2</sub> H <sub>2</sub>	6,529.17	37.2	1	77 ppbv	$8.8 \cdot 10^{-8}$	$3.3 \cdot 10^{-9}$	[80]
	H <sub>2</sub> S	6,320.6	1,520	1,000	1 ppbv	$1.4 \cdot 10^{-11}$	$1.29 \cdot 10^{-8}$	[97]
	C <sub>2</sub> H <sub>4</sub>	966.38	61.6	10	10 ppbv 34 ppbv	$2.2 \cdot 10^{-8}$ $1 \cdot 10^{-7}$	$9.12 \cdot 10^{-9}$ $3.1 \cdot 10^{-8}$	[92]
Off-beam	C <sub>2</sub> H <sub>2</sub>	915	3	60	60 ppbv	$4.8 \cdot 10^{-7}$	$4.8 \cdot 10^{-8}$	[103]
	H <sub>2</sub> S NH <sub>3</sub>	6,328.88 6,322.45	1,402	132	17 ppbv 52 ppbv	$3.2 \cdot 10^{-10}$ $1.8 \cdot 10^{-10}$	$9.8 \cdot 10^{-9}$	[110]
T-shape	H <sub>2</sub> O	7,161.41	8	1	500 ppbv	$4.8 \cdot 10^{-7}$	$3.9 \cdot 10^{-9}$	[101]
	CH <sub>4</sub>	2,958.02	0.5	10	400 ppbv	$6.6 \cdot 10^{-6}$	$1.1 \cdot 10^{-8}$	[105]
Intracavity	NO	1,900.08	170 W	0.03	4.8 ppbv	$8.2 \cdot 10^{-8}$	-	[109]
	CO <sub>2</sub>	2,311.1	188	5	1 ppbv	$5.8 \cdot 10^{-8}$	$3.2 \cdot 10^{-10}$	[108]

Table 1.6: Sensitivities and detection limits reported for resonant QEPAS systems.

## 1.4 Different signal processing methods

The photoacoustic signal usually has a small amplitude which has to be detected in a wide-band background. The most used signal processing therefore consists in modulating the signal at a given frequency and to extract it from the noise thanks to a lock-in detection scheme. As explained before, the frequency generally matches the resonance frequency of an acoustic resonator or of a mechanical resonator. With the introduction of QTFs in photoacoustics, new challenges appeared. A few original techniques were presented to answer these and are described thereafter.

### 1.4.1 Background compensation: MOCAM

Contrarily to MPAS and CEPAS, in QEPAS the acoustic detector (the QTF) is positioned very close to the laser beam. This is particularly the case in on-beam configuration employing small gap QTFs with strongly diverging lasers (see section 1.3). Usually a portion of the laser beam will hit the tuning fork resulting in a thermal excitation and generation of optical signal background. This background can in some cases become significant compared to the system limiting noise or can also limit the lock-in detection dynamic, both resulting in a limitation of the sensitivity.

A solution has been proposed so as to suppress this optical background and is called modulation cancellation method (MOCAM) [111]. The principle is to compensate the background by exciting the QTF with a second laser beam [112] (Figure 1.16). This second laser should be tuned away from the gas absorption but close to the first laser wavelength in order to keep approximately the same absorption from the QTF material. The second laser is modulated at the same frequency as the other but with a phase shift of  $\pi$ . Hence, the combination of the two forces generates a destructive interference seen by the QTF. The power of the second laser is then adapted in order to completely suppress the background.

However, this technique involves one supplementary laser and therefore increases the complexity and reduces the possibility of multi-gas sensing. In addition, this optical background may be suppressed manually during the signal processing.

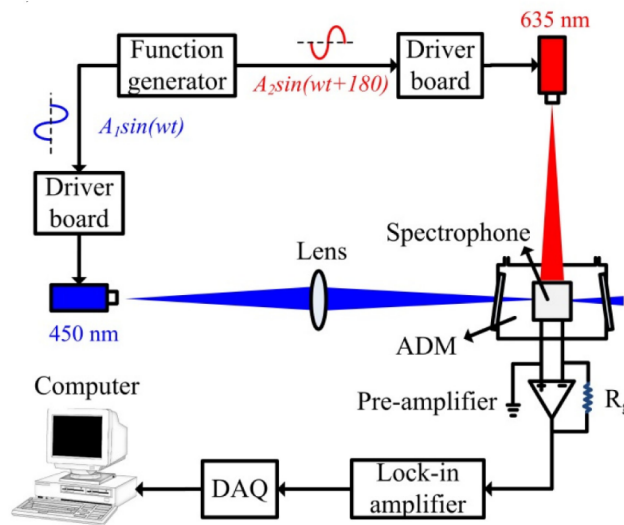


Figure 1.16: Schematic of the MOCAM technique balancing the optical background by employing an anti-phase modulated second laser [112].

To mitigate these drawbacks it was proposed to operate the same principle by replacing the second laser by an electrical excitation resulting in a simplification of the apparatus [113]. A more than 18 fold suppression of the background was obtained allowing to reach the QTF thermal noise. To conclude, this technique allows for suppressing the background generated by the laser beam touching the detector. Yet, other backgrounds exist in QEPAS and are often limiting, particularly in industrial environment, such as acoustic, vibratory or electromagnetic backgrounds. These last sources can rapidly vary in time, making the use of MOCAM impossible.

### 1.4.2 Electrical excitation for calibration and gas relaxation measurement

The measurement of fast fluctuating gas matrix conditions is a difficult task. While photoacoustic signal treatment is capable of measuring concentrations in a wide dynamic range from ppbv to 100%, corrections have to be made in order to precisely follow gas matrix changes. Indeed, the fluctuation of the gas concentrations can change the system state parameters, the quality factor of acoustic and mechanic resonators [114]. Moreover, the QTF frequency will vary due to viscosity and temperature changes, inducing signal fluctuations (as well as noise fluctuations for mechanical resonators). Eventually, environmental backgrounds will also vary.

A solution consists in exciting the QTF electrically at its resonance frequency [90]. The QTF resonance frequency is monitored and fed-back as a trigger to the laser modulation and lock-in detection. Doing so also allows to avoid signal dropouts due to frequency shifts between excitation and demodulation in classic open-loop detection. So as to monitor the QTF quality factor an alternate excitation is set and the QTF signal is demodulated thanks to a lock-in detection. The QTF is first electrically driven, then it is turned off, provoking an exponential decay of the signal which can be fitted to obtain the quality factor and correct measurements. It is also possible to measure the gas concentration. The photoacoustic excitation is turned on right after switching off the electrical driving. By modifying the phase shift of the photoacoustic modulation compared to electrical modulation one can modify the decay time of the exponential. When the two excitation sources are in phase opposition, a destructive interference occurs, modifying the decay time of the signal. This decay time will also depend on the amplitude of the photoacoustic signal compared to electrical signal. Finally, it is possible to demonstrate that the decay times depend on the gas concentration [115, 116]. By using such a method the sensitivity was shown to be comparable to classic open-loop detection, moreover providing for regular calibration of the sensor.

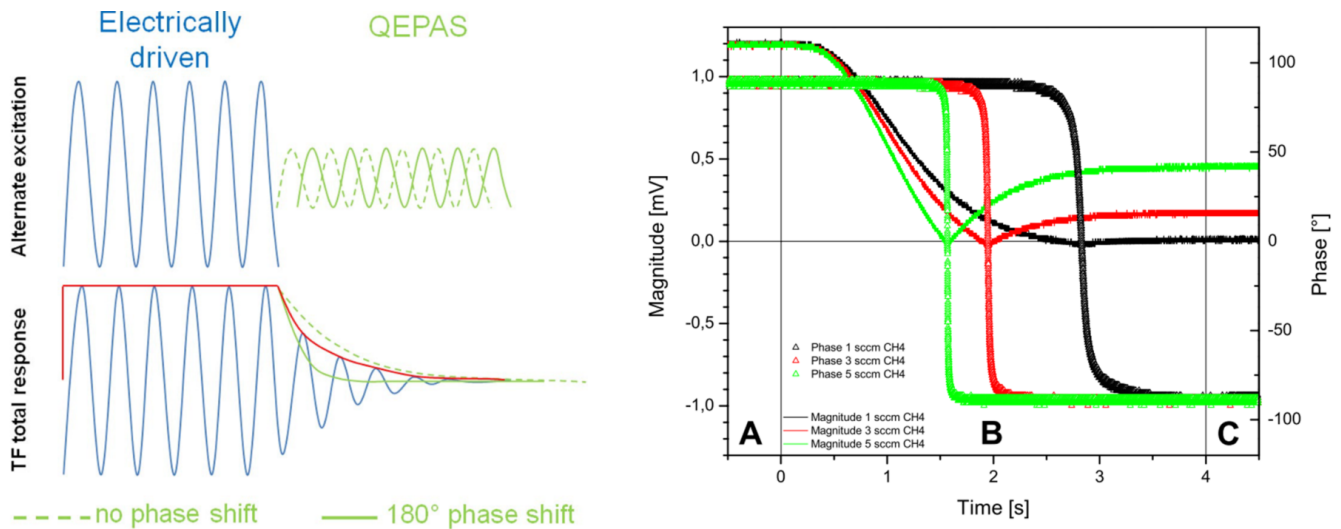


Figure 1.17: Schematic of the alternate electrical excitation [115]. Changing the photoacoustic modulation phase modifies the decay time of the tuning fork response, allowing for measurement of the gas concentration, gas relaxation time, QTF quality factor and frequency (left). Example of amplitude and phase measurement depending on gas concentration [116] (right). The decay time depends on gas concentration.

Still, another correction has to be made when measuring fluctuating gas concentrations with additional modifications of the gas relaxation time, due to changes of colliding partners. Indeed, when the gas relaxation time is shorter than the detection frequency, the signal is attenuated by a corresponding factor (see Section 2.1.2), creating signal fluctuations when the gas relaxation time varies.

As shown before, the phase shift between electric and photoacoustic excitation can be set in order to maximise or minimise the signal. This phase shift depends on the circuit phases, laser propagation as well as gas relaxation time as we will show in Chapter 5. Through measuring a photothermal signal, by directly hitting the QTF with the laser beam, it is possible to obtain the circuit and the laser propagation induced phase shifts, allowing to determine the gas relaxation time. Ultimately, a modulation of this phase shift in time allows for maximising the photoacoustic signal [117].

### 1.4.3 Beat-frequency QEPAS

Another technique for fast calibration of a QEPAS sensor was reported using a beat frequency for rapid scan of the gas absorption [118].

In this technique, called beat-frequency QEPAS, the laser modulation frequency  $f$  is tuned slightly away from the QTF resonance  $f_0$ . The difference of the two frequencies  $\Delta f = |f - f_0|$  has to be kept in the range of the QTF frequency spectrum in order to keep a good excitation. The gas absorption line is then rapidly scanned through generation of a ramp on the laser current. This scan time should be inferior to the decay time of the QTF signal in order to generate acoustic pulses. The QTF is excited by the acoustic pulses and its signal is demodulated by means of a lock-in detection at its resonance  $f_0$ , giving rise to a demodulated beat signal at  $\Delta f$ . The QTF frequency can be determined by measuring the period of the beat signal and the quality factor can be obtained by fitting the decay time of the beat signal. In addition, the gas concentration can be obtained by measuring the maximum amplitude of the beat signal. This technique thus allows for fast in-measurement calibration, reducing the acquisition time down to 30 ms compared to a few seconds in classic detection.

By using this technique, a sensitivity of  $1.3 \cdot 10^{-8} \text{ W.cm}^{-1}.\text{Hz}^{-1/2}$  was reported which is similar to the classic detection one of  $1.81 \cdot 10^{-8} \text{ W.cm}^{-1}.\text{Hz}^{-1/2}$  for  $\text{CH}_4$ . However, a sensitivity of  $2.45 \cdot 10^{-9} \text{ W.cm}^{-1}.\text{Hz}^{-1/2}$  for  $\text{H}_2\text{O}$

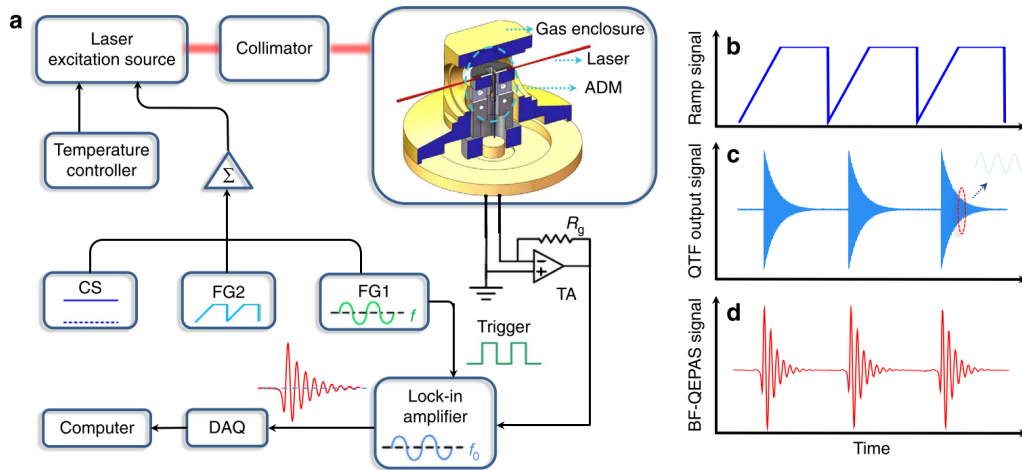


Figure 1.18: Schematic of beat frequency QEPAS (a). The laser current is modulated using a ramp (b) and a sine wave resulting in a beat signal (c) after lock-in demodulation (d) giving the QTF frequency, quality factor and the gas concentration [118].

detection was reported, which is somewhat not coherent with the other reported results obtained both with this new method and with a classic detection [118]. In addition, while we expect a faster response with this method, we do not expect a sensitivity enhancement since the noise will scale with the integration time and be limited by the QTF Brownian noise. Besides, the calibration can only be accomplished with the presence of the target gas with sufficient concentration to precisely fit the beat signal. Another proposed solution is to replace the photoacoustic excitation by an electrical excitation to proceed the calibration [114]. By employing such a system, the authors could demonstrate a satisfying correction of the sensor signal when humidity impacts the QTF quality factor and resonance frequency. Furthermore, by using a resonance tracking they improved the stability of their signal demonstrating a relative error of their signal drift of less than 1% compared to 44% in classic QEPAS detection.

## 1.5 In the industry

While laser absorption techniques such as TDLAS are widely spread across the gas detection market, photoacoustic technologies are less represented. Indeed, only MPAS systems were mature enough to be used in the industry. Such MPAS systems are commercialised by companies such as Pranalytica [119], Mirsense [120], LSE Monitor or Blue Industry and Science, for applications such as process monitoring or emission control. The instruments are generally capable to detect sub-ppbv to ppmv concentration levels in a time varying from a few seconds to a few minutes. The number of gases that can be simultaneously measured usually depends on the employed laser sources and sensor geometry. Currently, developments are at play in order to develop miniature MPAS and CEPAS sensors while keeping a good sensitivity, reducing consumption and increasing robustness. A presentation of a sample of commercial instruments is presented in Table 1.7.

To our best knowledge CEPAS sensors are commercialised by only one company, Gasera [121], exploiting their patent on this technology. Their product is based on the state-of-the-art CEPAS technology presented in Section 1.2 [74]. The sensitivity of such a system is similar to MPAS. The number of target gases is usually larger because of the type of implemented sources (OPO, supercontinuum, etc.). In the years to come we can expect the development of miniaturised CEPAS sensors similar to the ones we presented in Section 1.2.

Concerning QEPAS, no complete sensor is currently on the market to our best knowledge, probably due to the complexity of its development and to the small number of actors in the domain. Another reason for this




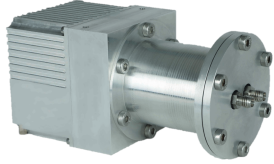

Technique	MPAS	MPAS	CEPAS
Instrument	Nitrolux NH <sub>3</sub> [119]	Multisense V2 [120]	Gasera One [121]
Photography			
Company	Pranalytica	Mirsense	Gasera
LOD	100 pptv/ppb	ppbv/ppmv	sub-ppbv/sub-ppmv
Dynamic range	0-300 ppbv	>4 decades	5 decades
Response time	<min	few s - few min	5 s - few min
Simultaneous gas number	1	2-4	>7
Size (cm)	61x48x25	17x11x10	50x14x44
Power consumption (W)	<150	10	<100
Application examples	<ul style="list-style-type: none"> <li>▪ Process monitoring</li> <li>▪ Pollution control</li> <li>▪ Human breath</li> </ul>	<ul style="list-style-type: none"> <li>▪ Exhaust analysis</li> <li>▪ Leak detection</li> <li>▪ Air quality</li> </ul>	<ul style="list-style-type: none"> <li>▪ Indoor air quality</li> <li>▪ Ship emissions</li> <li>▪ Drugs, explosives</li> </ul>

Table 1.7: Photoacoustic instruments from industry and performances extracted from datasheet.

is the lack of a clear positioning for this technology which does not explicitly demonstrate intrinsic advantages compared to the other technologies as we will discuss in Section 4.3. Yet, recently, one QEPAS module has been released by Thorlabs [122] and its design is based on the work of the University of Bari (Italy). However, this module does not contain a laser nor electrical processing and so it is not destined to the industry but to laboratory experiments. We tested this product ourselves and obtained a NNEA of  $3 \cdot 10^{-9} \text{ W.cm}^{-1}.\text{Hz}^{-1/2}$  which is similar to what was found in [123] and 3 times worse than state-of-the-art of QEPAS. Future work on QEPAS will undoubtedly help maturing this technique.

## 1.6 State of the art at ONERA

ONERA has been working for nearly 10 years in the field of photoacoustics, from the conception of OPO sources to the design of new quartz tuning forks. Particularly, a previous PhD thesis [26] has laid the foundation of photoacoustic modelling paving the way towards a better understanding of QEPAS.

### 1.6.1 Modelling

A complete analytical model of a QEPAS sensor has been developed and experimentally validated by ONERA [26]. This analytical model describes the entire sensor, from the laser to the generation of charges and signal processing. We will further detail this model in Chapter 2.

In addition, an analytical solution for the coupling of tuning forks with acoustic resonators has been given for the first time, describing the system behaviour in terms of quality factor, frequency and sensitivity [98].

Finally, a remarkable work has been achieved concerning the analytical quantification of the quality factor of quartz flexural resonators. Particularly, the quality factor has been optimised at atmospheric pressure, taking into account the viscous losses, squeeze damping and acoustic losses of the QTFs [124, 125].

These analytical models were validated both by finite element simulation and through experiment, demonstrating a very good agreement with both [126, 98].

### 1.6.2 Custom QTFs

The previous analytical models were implemented in a Python library (called PYRATS and described in Chapter 2) and enabled for optimisation of quartz tuning forks for photoacoustics. These were made at ONERA as detailed in Appendix C.

In particular, QTFs were designed with an unprecedented 2 mm gap between their prongs, facilitating laser alignment for lasers presenting a strong divergence. By choosing this gap and a wafer thickness of 2 mm, the quality factor of two QTFs were maximised for the fundamental mode, resulting in the best quality factor QTFs in ambient air, of 75,000 and 28,900, ever used in photoacoustics [124, 125]. Furthermore, the resonance frequency of these QTFs were decreased to reach 5 and 21 kHz, allowing better measurements for slowly relaxing gases while keeping a good immunity to noise background. These two QTFs called U1y and C2 are presented in Figure 1.19 and their parameters as well as the computed NNEA are presented in Table 1.8.

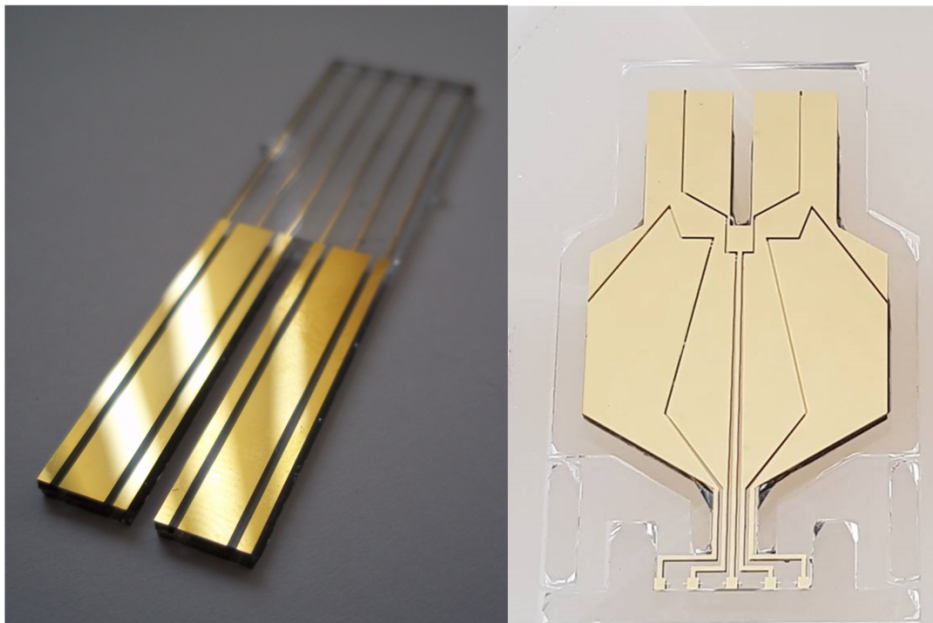


Figure 1.19: Photography of ONERA's custom QTFs, U1y (left) and C2 (right).

QTF	$l$	$e$	$L$	$g$	$Q$	$f_0$ (Hz)	NNEA ( $W.cm^{-1}.Hz^{-1/2}$ )
U1y	2	7	36	2	40,800	5,480	$4.59 \cdot 10^{-8}$
C2	2	8	13.6	2	8,000	21,123	$3.31 \cdot 10^{-8}$
U2	2	3.7	16	2	37,000*	12,700*	$2.13 \cdot 10^{-8}$ *

Table 1.8: Parameters of different custom QTFs designed and fabricated at ONERA. The dimensions are given in mm. The quality factor is measured at atmospheric pressure. \* Analytical results.

By increasing the QTFs quality factor, the NNEA has been improved, however in photoacoustics the NNEA does not only depend on the QTF but also on acoustic generation and efficient recovery. For that reason, a last QTF named U2 was designed with a prong spacing and thickness of 2 mm, and its NNEA was minimised by analytical modelling, resulting in the parameters presented in the previous Table 1.8. Nevertheless, as the

sensitivity gain was not consequent this QTF was not actually fabricated.

### 1.6.3 Acoustic resonators

Ultimately, as can be seen in the previous table, the quality factor of C2 was experimentally measured to 8,000 instead of 75,000. It was demonstrated that this particular resonator geometry induced significant acoustic losses. While every QTF presents acoustic losses, these are generally not limiting, except in the case of C2. As such, an acoustic recovery cavity was created (Figure 1.20(left)) in order to recover the acoustic waves emitted by the QTF. The result of the addition of this new kind of cavity was the enhancement of the quality factor to 75,000 [125], which is, to our best knowledge, the best quality factor ever reported for quartz tuning forks at atmospheric pressure.

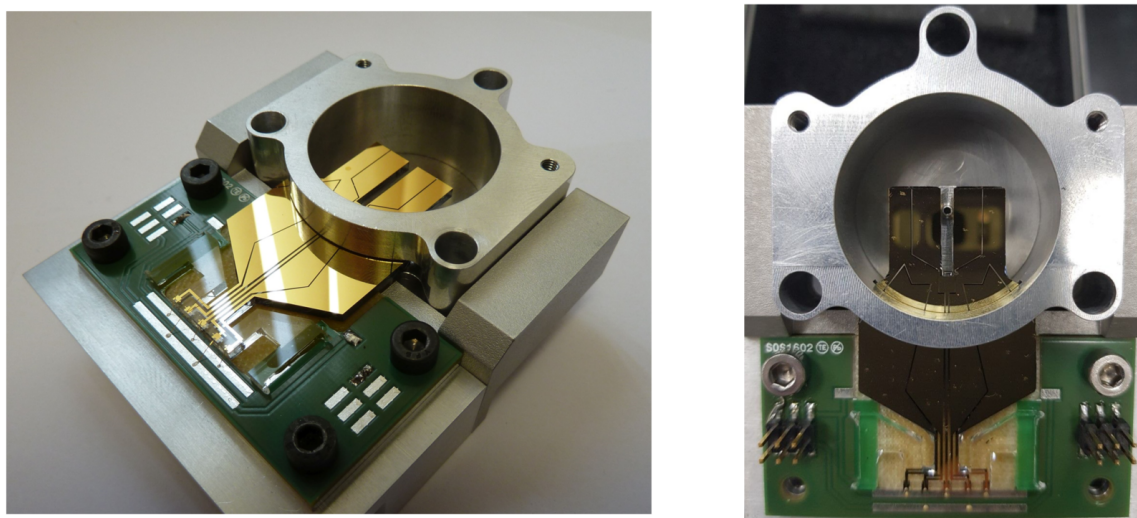


Figure 1.20: Photography of ONERA's custom acoustic resonators. Acoustic recovery cavity allowing to reach a quality factor of 75,000 (left). Acoustic recovery cavity with additional acoustic micro resonators presenting a NNEA of  $1.8 \cdot 10^{-9} \text{ cm}^{-1} \cdot \text{Hz}^{-1/2}$  (right).

Ultimately, acoustic microresonators such as the ones presented before were added to enhance the sensitivity of the sensor (Figure 1.20(right)), leading to a NNEA of  $1.8 \cdot 10^{-9} \text{ cm}^{-1} \cdot \text{Hz}^{-1/2}$  comparable to the state-of-the-art values.

While the previous work presented unprecedented results, the sensitivity of the optimised QTF and of the optimised acoustic resonators reached the same level as watch QTFs coupled with optimised acoustic resonators. Thus a great work still has to be led in order to understand which parameters do influence the sensitivity of a QEPAS sensor. Particularly, the coupling between the QTF and the acoustic resonator is a complex problem that still needs to be understood so as to design new acoustic resonators with best performances (sensitivity, robustness, ease of alignment). We will address these problems in this manuscript. Moreover a new signal processing method was patented but still had to be tested and understood, what we aim to accomplish in Chapter 5.





## Chapter 2

# Photoacoustic analytical and finite element modelling

### Objectives:

In this chapter we report on the models used in this manuscript for the analysis of photoacoustic experiments. First, an analytical model and its hypotheses are detailed for the quantification of the parameters of interest used in photoacoustic spectroscopy, from the laser source to the signal processing. In a second time, in order to confirm or refine this model results, we describe the construction of finite element simulations of photoacoustic sensors with their related hypotheses. Eventually, a new unified modelling is introduced. This model enables to describe the different photoacoustic techniques through the quantification of the physical parameters leading to their sensitivity. We will fully exploit this model in Chapter 4 to compare the different photoacoustic techniques.

## 2.1 Analytical model description

In this section we present the modelling of the different physical phenomena occurring in a photoacoustic sensor. The analytical model presented in this chapter mainly comes from the work of Guillaume Aoust [26]. For the sake of self-consistency, this model is presented first and is then extended to consider the use of acoustic resonators, cantilevers and microphones. Photoacoustics is a complex multiphysical problem that will be treated in different blocks, as presented in Figure 2.1.

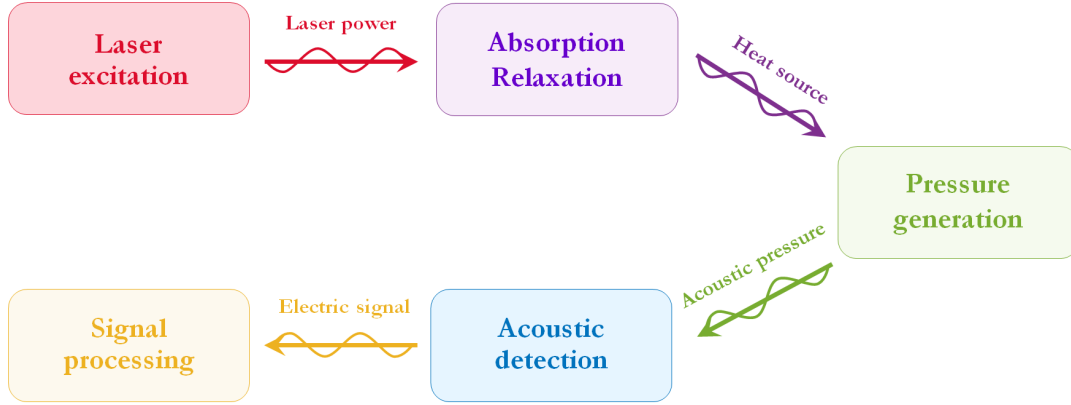


Figure 2.1: Block diagram of the different physical phenomena involved in photoacoustics.

### 2.1.1 Laser excitation

The first block to model is the light source used for gas excitation. In photoacoustics, any kind of modulated light source can be used, e.g., sun light [23], solid-state laser [127], LED [112], QCL [128], OPO [129], etc. For simplicity's sake, we consider a coherent light source, namely a laser. If required, the description of polychromatic light sources could be achieved with further adaptation of the model.

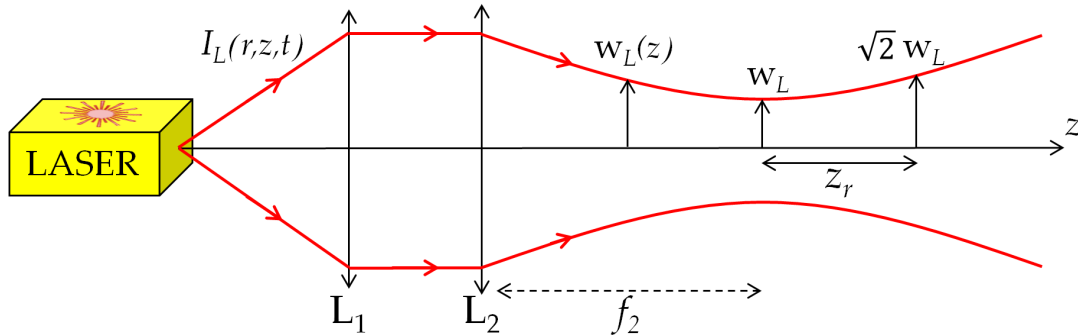


Figure 2.2: Laser beam shaping using collimating and focusing lenses. The intensity profile is represented with parameters of interest such as the laser waist  $w_L$ .

We consider a laser emission at a wavelength  $\lambda_L(t)$  and of mean power  $P_L(t)$ . The laser beam spatial distribution is described by its intensity profile  $I_L(r, z, t)$ , with  $r$  the radial distance from the laser beam axis. For a Gaussian beam profile the intensity can be computed as follows:

$$I_L(r, z, t) = P_L(t) \frac{2}{\pi w_L(z)^2} \exp\left(-2 \frac{r^2}{w_L(z)^2}\right). \quad (2.1)$$

In a photoacoustic setup, the laser beam is usually collimated by a lens  $L_1$  and focused by a second lens  $L_2$  (of focal length  $f_2$ ) where the photoacoustic detector is located.

The beam Gaussian transverse profile is described by the distance  $w_L(z)$  from the propagation axis for which the intensity is divided by  $1/e^2$ . The laser beam shape along the propagation can then be characterised by its waist radius  $w_L$  and Rayleigh parameter  $z_r = M^2 \pi w_L^2 / \lambda_L(t)$ , where  $M^2$  is the beam propagation factor, according to the following equation:

$$w_L(z) = w_L \sqrt{1 + \left(\frac{z}{z_T}\right)^2}. \quad (2.2)$$

As we will see in the next chapters, the laser spatial distribution should be known accurately in order to focus the beam close to the photoacoustic detector without generating signal background. Knowing the laser output divergence  $w_L(0)$  and the lenses focal length, the waist  $w_L$  near the detector can be computed.

## 2.1.2 Absorption by the gas and heat generation

### 2.1.2.1 Gas absorption

As discussed in the introduction, a single molecule can be described by levels of energy quantified over an energy scale, corresponding to its movement degrees of freedom (vibrations, rotations, translations). Absorption spectroscopy techniques such as photoacoustics rely on the absorption of light by the molecules at these energy levels.

The absorption lines corresponding to the energy levels are broadened by the effect of pressure (collisions) and temperature (vibration, translation, rotation or movement in general). In almost all practical cases, the resulting spectral profile can be described by a Voigt profile which is a combination of Lorentzian and Gaussian functions. In general, a Lorentzian fit is sufficient for a very good description of absorption lines at atmospheric pressure and temperature. We call  $\alpha_G$  the maximal linear absorption of the broadened line and FWHM its full width at half maximum. An example of a broadened absorption line for  $C_2H_2$  is given in Figure 2.3 around  $6490.02 \text{ cm}^{-1}$  which is a line we will use in the next chapters<sup>1</sup>. This absorption line is well approximated by a Lorentzian function with the parameters  $\alpha_G = 1.8 \times 10^{-4} \text{ cm}^{-1}$  and  $\text{FWHM} = 0.12 \text{ cm}^{-1}$ .

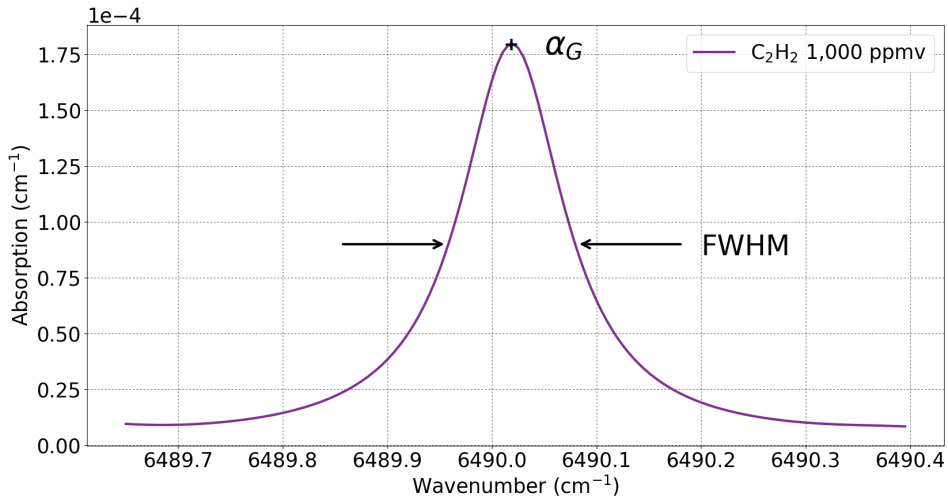


Figure 2.3: Gas absorption profile of  $C_2H_2$  1,000 ppmv at atmospheric conditions ( $25^\circ\text{C}$  and  $101,325 \text{ Pa}$ ) around  $6490.02 \text{ cm}^{-1}$ .

By targeting the molecules absorption lines, a portion of the laser power is absorbed. The probability of laser absorption in a gas sample of length  $|z_2 - z_1|$  is quantified by Beer-Lambert-Bouguer's law:

$$I_L(r, z_2, t) \Big|_{\lambda_L} = I_L(r, z_1, t) e^{-\alpha_G(\lambda_L)|z_2 - z_1|}. \quad (2.3)$$

<sup>1</sup>Every absorption spectrum presented in this manuscript was computed from HITRAN 2012 database [130] at atmospheric conditions, using a Voigt profile.



For small interaction lengths, as commonly encountered in photoacoustics, the transmitted intensity can be considered linear with the absorption coefficient  $\alpha_G$ . That can be obtained by taking the first order derivative of Equation 2.3. This approximation is important when computing figures of merit such as the cell constant or NNEA presented in the next sections.

### 2.1.2.2 Molecular relaxation

As laser radiation is absorbed, molecules are promoted to an excited state of energy. In infrared spectroscopy this state can correspond to increased rotational or vibrational energies. The infrared laser energy is not sufficient to induce electronic state transitions which take place in the ultraviolet and visible domains [25].

At normal pressure and temperature, relaxation of gas molecules will mainly occur through collisions with other molecules or cell walls. Relaxation processes are therefore mainly non-radiative and the absorbed energy is returned into the medium under the form of molecular agitation. This agitation is mainly made of translations causing the formation of a heat wave. For gases, the characteristic time  $\tau_{V-T}$  of a particular vibration-translation transition depends on the collision partners (the target gas itself, a buffer gas, and other gases acting as catalysts) as well as the experimental conditions (pressure, temperature). For example, around 2  $\mu\text{m}$  the relaxation time of pure  $\text{CO}_2$  is 11  $\mu\text{s}$  but can be reduced to 0.1  $\mu\text{s}$  with  $\text{H}_2\text{O}$  acting as a collision partner [131].

### 2.1.2.3 Heat source modulation

In order to generate an acoustic signal the heat source has to be modulated in time. This modulation is usually at the detector resonance frequency  $\omega_0/2\pi$ . Two main modulation schemes are used. The first is amplitude modulation (AM), which consists in tuning the laser wavelength at  $\lambda_L$  to excite the gas, then lighting on and off the laser in order to modulate its power. This is usually done with a square modulation, which is the optimal modulation regarding the generated heat amplitude, or a sine modulation. The second is wavelength modulation (WM) and consists in keeping the same laser power  $P_L$  while scanning the gas absorption line around  $\lambda_L$ , with a wavelength amplitude noted  $\delta$ .

These modulation schemes can be described through laser power and wavelength evolution in time as in Equation 2.4.

$$\begin{array}{cc}
 \text{Amplitude modulation} & \text{Wavelength modulation} \\
 \left\{ \begin{array}{l} P_L(t) = \frac{P_L}{2} \sin(\omega t) \\ \lambda_L(t) = \lambda_L \end{array} \right. & \left\{ \begin{array}{l} P_L(t) = P_L \\ \lambda_L(t) = \lambda_L [1 + \delta \cos(\omega t/2)] \end{array} \right. \quad (2.4)
 \end{array}$$

A few remarks have to be made concerning wavelength modulation.

One can note that the wavelength is modulated at half the fundamental frequency in order to generate an acoustic signal at  $\omega/\pi$ . In addition, for simplicity we consider a sinusoidal modulation, however it was demonstrated that the best shape is a quasi-square corresponding to the inverse Fourier transform of the gas absorption line shape. Using a quasi-square modulation led to a signal enhancement of about 1.3 or 1.57 respectively compared to a sinusoidal modulation [26, 132]. Also, it can be noted that the wavelength tuning is considered immediate, which is sometimes not the case when thermal effects are important in the laser. Furthermore, with wavelength tuning comes a residual amplitude modulation depending on the laser characteristics and operating conditions. For small modulation amplitudes this effect can be neglected [133], it is therefore not taken into account here.

By considering that induced heating of the medium  $\hat{H}(r, \omega)$  is produced at the frequency  $\omega/2\pi$  and at a distance  $r$  from the laser beam axis, one can derive [26]:

$$\begin{cases} \widehat{H}(r, \omega) = \widehat{H}(\omega) |u(r)|^2 \\ \widehat{H}(\omega) = \frac{2e^{-j \tan^{-1}(\omega \tau_{V-T})}}{\sqrt{1 + (\omega \tau_{V-T})^2}} \widehat{c}(\omega) \\ \widehat{c}(\omega) = \frac{\omega}{2\pi} \int_{-\pi/\omega}^{+\pi/\omega} \alpha_G(t) P_L(t) e^{-j\omega t} dt \end{cases} \quad (2.5)$$

Knowing that laser power and gas absorption are real functions, heat phase can be derived as  $\varphi_{PA} = -\arctan(\omega \tau_{V-T})$  which we will use in Chapter 5.

One can observe that the generated heat depends on the gas relaxation time in such way that its amplitude is reduced for higher frequencies and longer relaxation times. For example, if one uses a watch QTF at 32,768 Hz for detection of dry CO<sub>2</sub> around 2 μm, the heat amplitude will be reduced by about 60% compared to a detection around 2,000 Hz. By promoting CO<sub>2</sub> relaxation with H<sub>2</sub>O this signal dropout can be avoided [131]. Finally, the heat amplitude can be compared in both AM and WM modulation schemes. We call  $H$  the maximal amplitude of the heat. In AM modulation,  $H$  can be derived to be equal to  $\alpha_G P_L/2$  for a square modulation with a 50% duty cycle. In WM modulation the result is not trivial. The overlap of laser emission with gas absorption has to be computed, what we will carry out in the following.

We evaluated  $H$  over laser emission wavenumber for C<sub>2</sub>H<sub>2</sub> around 6,490.02 cm<sup>-1</sup> and for a laser mean power  $P_L = 17$  mW, the result is shown in Figure 2.4. We considered gas relaxation to be immediate which is a good approximation at low frequencies and at atmospheric pressure. One can use the value  $\tau_{V-T} = 0.1$  μs at atmospheric pressure [26].

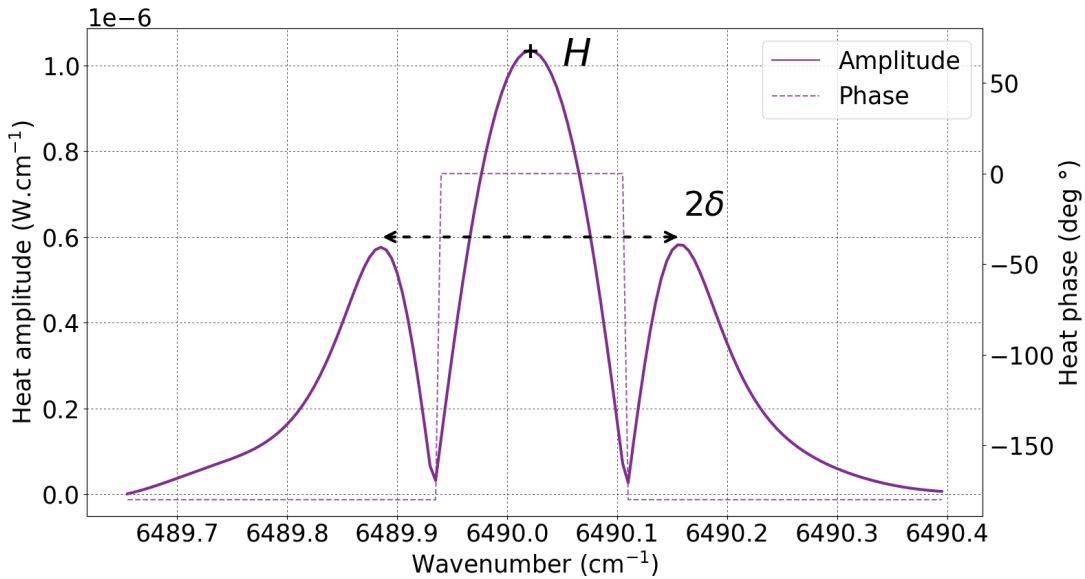


Figure 2.4: Analytical heat source in pure wavelength modulation for C<sub>2</sub>H<sub>2</sub> 1,000 ppmv around 6,490.02 cm<sup>-1</sup> and laser mean power  $P_L$  of 17 mW.

Heat spectrum in WM modulation is constituted of one main lobe centered on the gas absorption line and two side lobes at a distance  $\delta$  from the main one. Modulation amplitude should be carefully adapted to the absorption line in order to maximise the generated heat amplitude. This is demonstrated in Figure 2.5 for different values of the WM modulation amplitude  $\delta$ . An optimum of  $\delta = 0.132$  cm<sup>-1</sup> is found, yielding a heat amplitude  $H$  of approximately  $1.034 \times 10^{-6}$  W.cm<sup>-1</sup>. This optimal amplitude can be derived from the absorption profile and the WM modulation shape, typically  $2\delta = 2.2 \times \text{FWHM}$  for sinusoidal modulation throughout a Lorentzian

absorption profile [132, 134]. However, when the absorption shape gets modified from a Lorentz function, through the effect of temperature, for example, or when laser emission is not a pure sine function, this coefficient changes. In any case, the modulation should be experimentally adapted through maximisation of the signal.

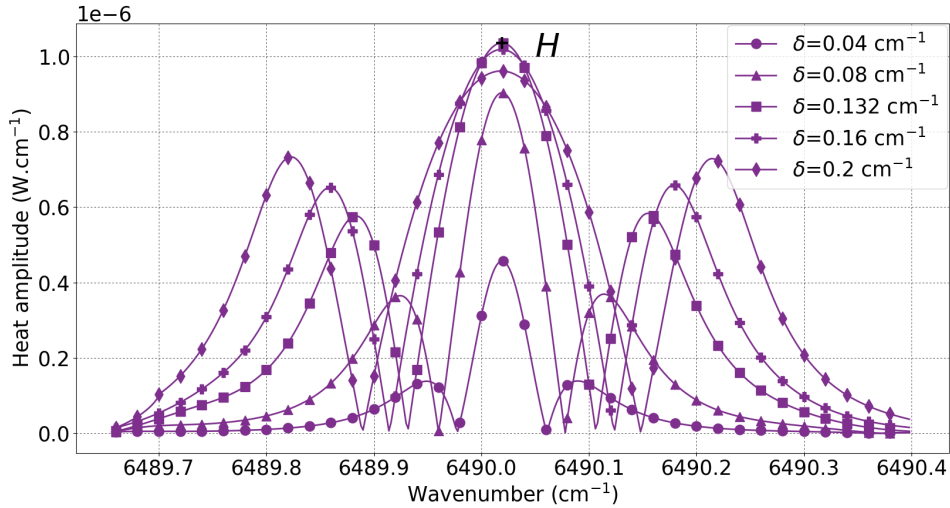


Figure 2.5: Heat source in wavelength modulation depending on modulation depth  $\delta$ .

Concerning the heat amplitude, it is analytically derived to be approximately equal to  $\alpha_G P_L/3$ . This factor 3 is generally a good approximation for any Lorentzian shaped absorption profile and sinusoidal modulation. This means that the sinusoidal WM technique generates 3/2 times less heat than the AM technique. This factor can be observed experimentally in [26] for example and we will evaluate it in Section 3.2.1.3. However, as discussed before, using a quasi-square modulation should allow for reaching the same heat amplitude in both modulation schemes.

Finally, under the previously stated hypotheses, we can give a simplified expression of  $H$  for both modulation schemes:

$$\begin{array}{cc}
 \text{Amplitude modulation} & \text{Wavelength sine modulation} \\
 H = \frac{\alpha_G P_L}{2} , & H \approx \frac{\alpha_G P_L}{3} .
 \end{array} \tag{2.6}$$

### 2.1.3 Acoustic pressure generation

Modulation of the heat source generates cycles of pressure due to molecular collisions, i.e. acoustic waves. In this section we will express the pressure generated after introduction of a heat source amplitude  $H$ . Two main cases are studied, the first is the generation of pressure in free space, which corresponds to the cases where the detectors are used without acoustic resonator (mainly for QEPAS using bare QTFs). The second case consists in the study of pressure generation inside acoustic resonators, for MPAS, CEPAS and QEPAS.

Analytically we consider that the mechanical resonator (microphone, cantilever, tuning fork) does not modify the acoustic wave distribution due to its presence and vibration as in [79]. This approximation enables to simplify the problem and is generally good when the resonator is small compared to the acoustic wavelength. However, we will study in detail the limits of this approximation with finite element simulations in Section 4.1.2.1.

### 2.1.3.1 In free space

By solving the Navier-Stokes equation one can express the pressure distribution  $\widehat{P}$  at a distance  $r$  from the laser axis (Equation 2.7). It consists in the overlap of the heat source distribution with the solution of the Green function for a propagation to infinity. For numerical implementation the infinity will be taken as 100 times the laser waist. This waist  $w_L$  is considered constant and equal to 100  $\mu\text{m}$  along the laser axis, which is a good approximation when the detector is small compared to the Rayleigh parameter  $z_R$ . The pressure writes:

$$\widehat{P}(r, \omega) = \frac{\omega(\gamma - 1)}{4v^2} \widehat{H}(\omega) \left[ \frac{4}{w_L^2} \int_0^{+\infty} r' H_0^{(2)}(k_{ac} r') \exp\left(-2\frac{(r - r')^2}{w_L^2}\right) dr' \right], \quad (2.7)$$

where  $v$  is the sound speed in the gas, which is taken to be equal to 333  $\text{m}\cdot\text{s}^{-1}$  in air and  $\text{N}_2$  matrix.  $k_{ac}$  is the sound wavevector, it can be computed as  $k_{ac} = 1/\lambda_{ac} = \omega/v$  and expressed in  $\text{m}^{-1}$ , with  $\lambda_{ac}$  the acoustic wavelength. Finally,  $H_0^{(2)}$  is the zero order Hankel function of the second kind, without unit. Equation 2.7 can be difficult to integrate, although beyond a distance equal to the laser waist  $w_L$  an approximate expression of the pressure is found that is quite accurate, as seen in Figure 2.6.

$$\widehat{P}(r, \omega) = \frac{\omega(\gamma - 1)}{4v^2} \widehat{H}(\omega) H_0^{(2)}(k_{ac} r) \quad (2.8)$$

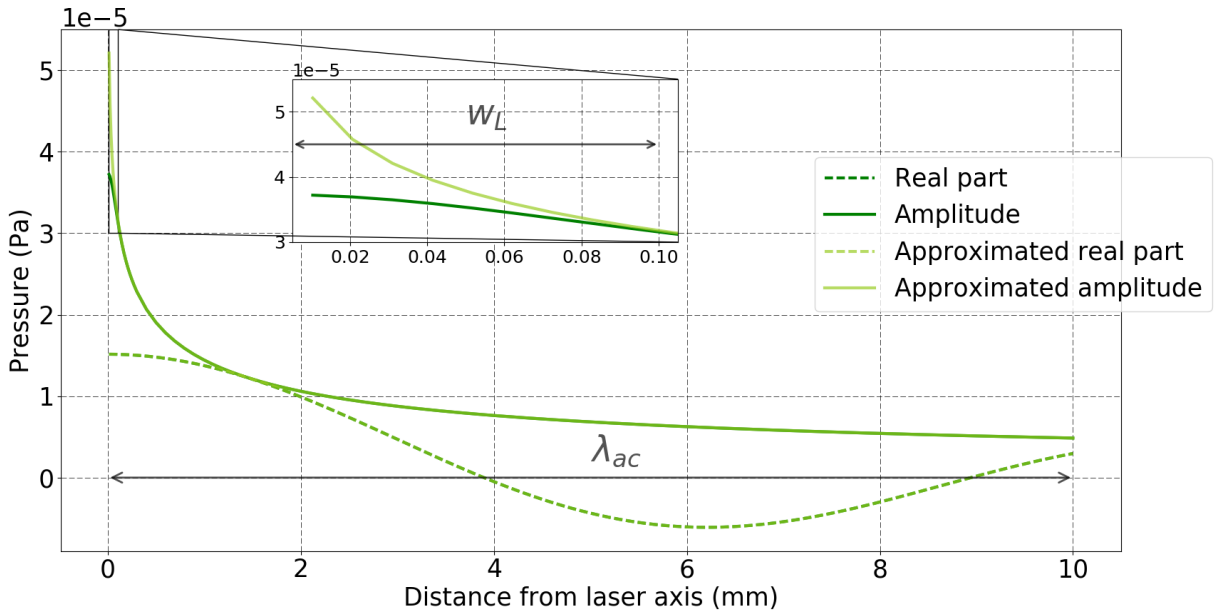


Figure 2.6: Pressure distribution over laser axis computed using Equation 2.7. Approximated pressure computed from Equation 2.8 is presented for comparison. One can see that the curve obtained from the approximated expression is not discernible from the exact one for distances above the laser waist.

For a heat amplitude  $H$  of  $1.034 \times 10^{-6} \text{ W}\cdot\text{cm}^{-1}$  the maximal pressure amplitude generated at a frequency of 32,768 Hz is 37.3  $\mu\text{Pa}$ . At a distance of  $\lambda_{ac} = 10.1 \text{ mm}$ , the pressure amplitude decreases by nearly 8 times to reach 4.8  $\mu\text{Pa}$ . We will name laser constant  $C_L$ , the maximal pressure amplitude generated for a deposited heat  $H$ , in this case  $C_L = 36 \text{ Pa}\cdot\text{W}^{-1}\cdot\text{cm}$ .

For comparison, Petra and al. [79] also modelled the pressure generation in free space and obtained a pressure maximum of 170  $\mu\text{Pa}$ , at 32,800 Hz, for a computed heat amplitude of  $4.04 \times 10^{-6} \text{ W}\cdot\text{cm}^{-1}$ . Our model predicts a pressure of 148  $\mu\text{Pa}$  in their conditions which is close to their value.

Eventually, one can observe that the pressure is directly proportional to the frequency, meaning that in free space higher frequencies are favorable to enhance the sensitivity. This can easily be understood as the pressure duty cycle increases with frequency while pressure is dissipated in the infinite medium. However, this frequency increase is generally limited to a few tens of kHz in order to avoid signal losses for slow relaxing molecules as discussed in the previous section. This frequency dependency is also totally different in the case of a confined medium, as we will see in the next section.

### 2.1.3.2 In acoustic resonators

Using a detector in free space is usually not sufficient in terms of sensitivity for gas detection applications. To tackle this issue, acoustic resonators are used. They generally consist in simple cylindrical resonators or Helmholtz type differential resonators as presented in Figure 2.7.

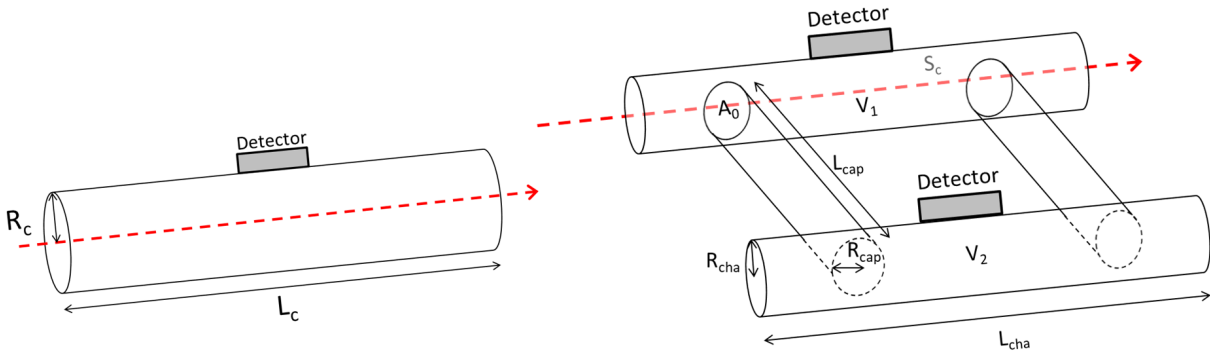


Figure 2.7: Typical acoustic resonators used in PAS. Simple cylinder (left) and Helmholtz type differential resonator (right) and their parameters. The detectors can be microphones, cantilevers or tuning forks.

### Pressure distribution

In order to determine the pressure generated inside the cell, the overlap of laser intensity and acoustic mode spatial distribution  $\hat{P}_n(r)$  must be computed. Let  $\hat{A}_n(\omega)$  be the acoustic mode amplitude, then one can decompose the pressure distribution as the weighted sum of its different spatial modes:

$$\hat{P}(r, \omega) = \sum_n \hat{A}_n(\omega) \hat{P}_n(r). \quad (2.9)$$

Furthermore, the mode amplitude can be derived by solving the wave equation [135, 21]. By considering the sound hard wall condition (the pressure derivative is zero perpendicularly to the walls), the acoustic resonator can be considered as a second order resonator, and one can express  $A_n(\omega)$  as [135]:

$$\hat{A}_n(\omega) = \frac{(\gamma - 1)}{V_c} \frac{j\omega}{\omega^2 - \omega_n^2 + \frac{j\omega\omega_n}{Q_{ac,n}}} \int_{V_c} \hat{H}(r, \omega) \hat{P}_n(r) dV, \quad (2.10)$$

with  $V_c$  the cell volume and  $Q_{ac,n}$  the nth-mode quality factor. We will express the quality factor and resonance frequency in the next paragraphs.

### Resonance frequency

The resonance frequency of simple cylinders acoustic modes can be computed as follows [21, 136]:

$$\omega_{l,m,n} = \pi v \sqrt{\left(\frac{l}{L_{\text{eff}}}\right)^2 + \left(\frac{\alpha_{m,n}}{R_c}\right)^2}, \quad (2.11)$$

with  $l$ ,  $m$ , and  $n$  the longitudinal, azimuthal and radial mode numbers respectively. The values of  $\alpha_{m,n}$  can be computed from the Bessel functions derivative zeros and can be found in tables [136].  $R_c$  is the cylinder cell radius (Figure 2.7).  $L_{\text{eff}}$  is the effective cylinder length. When the cylinder extremities are closed, this effective parameter is equal to the cylinder length, i.e.  $L_{\text{eff}} = L_c$ . If we consider a closed cylinder cell resonating at its first longitudinal mode, its frequency is expressed as  $f_{1,0,0} = v/2 L_c$ . For open ended cylinders, correction factors should be applied [49, 21].

For Helmholtz type resonators, the frequency is obtained differently. Let us consider a differential resonator composed of four cylinders (Figure 2.7). Two of them are called the chambers, of length and radius  $L_{\text{cha}}$ ,  $R_{\text{cha}}$  and volume  $V_1$ ,  $V_2$ . The laser beam passes in one or two of the chambers in order to generate the pressure later detected by the resonator. The two other cylinders are called the capillaries of dimensions  $L_{\text{cap}}$ ,  $R_{\text{cap}}$  and are used for connecting the gas inlet and outlet.

Such a system can be seen as a mass-spring oscillator, in which the gas contained in the capillaries plays the role of the spring. The pressure inside the resonator oscillates in time between the two chambers as previously presented in Figure 1.6. This equivalence enables to derive the resonance frequency of the first differential mode as [46, 21]:

$$\omega_0 = v \sqrt{\frac{A_{\text{eff}}}{V_{\text{eff}} L_{\text{cap}}}}, \quad (2.12)$$

with  $A_{\text{eff}}$  the effective capillary area  $A_{\text{eff}} = 2A_0$ ,  $A_0$  the capillary area and  $V_{\text{eff}} = \left[\frac{1}{V_1} + \frac{1}{V_2}\right]^{-1}$ .

## Acoustic quality factors

The acoustic quality factor accounts for several loss mechanisms. In this paragraph we will use the formalism developed in [135] to express the different loss sources for simple cylinder shaped resonators. The first loss type  $Q_{\text{ac, radiation}, n}$  comes from radiation due to acoustic pressure leakage through openings in the resonator. We will not compute this loss analytically but through finite element method as we will see in Section 2.2.2.3.

The second type of loss  $Q_{\text{ac, volume}, n}$  is volumic and accounts for the heat conduction and viscosity inside the gas matrix. This loss is generally limiting for cells of large volume. It can be computed as follows:

$$Q_{\text{ac, volume}, n}^{-1} = \frac{\omega_n}{v} \left[ l_\mu + (\gamma - 1) l_\kappa \right], \quad (2.13)$$

with  $l_\mu$  and  $l_\kappa$  characteristic lengths defined as:

$$l_\mu = \frac{4}{3} \frac{\mu}{\rho_f v}, \quad l_\kappa = \frac{\kappa}{\rho_f C_p v}, \quad (2.14)$$

where  $\gamma$  is the Laplace coefficient, equal to 1.4 for diatomic gases,  $\rho_f$  the gas density in  $\text{kg.m}^{-3}$ ,  $C_p$  the specific heat capacity in  $\text{J.m}^{-3}.\text{K}^{-1}$ ,  $\kappa$  the thermal conductivity in  $\text{W.m}^{-1}.\text{K}^{-1}$  and  $\mu$  the dynamic viscosity in Pa.s. These parameters values can be found in Appendix A.

The two last loss sources account for viscosity and heat conduction near the cell walls, specifically within boundary layers of thicknesses  $d_\mu$  and  $d_\kappa$ , respectively:

$$d_\mu(\omega) = \sqrt{\frac{2\mu}{\rho_f \omega}}, \quad d_\kappa(\omega) = \sqrt{\frac{2\kappa}{C_p \rho_f \omega}}. \quad (2.15)$$

For example, if we consider a cell filled with air at atmospheric conditions and resonating at 5 kHz, one can compute  $d_\mu = 30 \mu\text{m}$  and  $d_\kappa = 36 \mu\text{m}$ . These losses are usually dominant for small cells with large surfaces  $S_c$ . The associated quality factors are:

$$Q_{\text{ac,viscous},n}^{-1} = \frac{1}{2} (\gamma - 1) \frac{d_\kappa}{V_c} \int_{S_c} |\widehat{P}_n(r)|^2 dS, \quad (2.16)$$

$$Q_{\text{ac,thermal},n}^{-1} = \frac{1}{2} \left( \frac{v}{\omega_n} \right)^2 \frac{d_\mu}{V_c} \int_{S_c} |\nabla \widehat{P}_n(r)|^2 dS. \quad (2.17)$$

If the acoustic resonator mode of resonance is longitudinal, a simplified expression can be obtained [49, 137]:

$$\left[ Q_{\text{ac,viscous},n}^{-1} + Q_{\text{ac,thermal},n}^{-1} \right]^{-1} = \frac{R_c}{d_\mu + (\gamma - 1)d_\kappa(1 + 2R_c/L_c)}. \quad (2.18)$$

Finally, the cell total quality factor can be obtained by summing all of the previous contributions:

$$Q_{\text{ac},n} = \left[ Q_{\text{ac,radiation},n}^{-1} + Q_{\text{ac,volume},n}^{-1} + Q_{\text{ac,thermal},n}^{-1} + Q_{\text{ac,viscous},n}^{-1} \right]^{-1}. \quad (2.19)$$

As an example, the overall acoustic quality factor is evaluated for a closed cylinder cell resonating at its first longitudinal mode, as shown in Figure 2.8. Globally,  $Q_{\text{ac},n}$  is limited by surface losses, thereby increasing with the radius whereas decreasing with the length. A maximum is reached for cells of large radius and small length, nonetheless further decreasing the length (below 5 mm) reduces the quality factor. This can be attributed to the fact that the volume quality factor becomes limiting for cells presenting a small length and big radius.

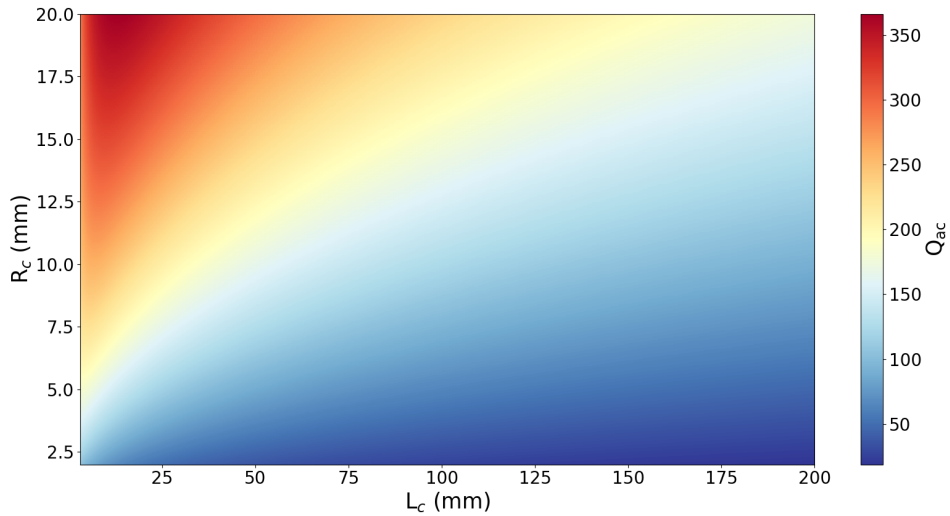


Figure 2.8: Quality factor of a cylinder cell versus its radius and length.

## Cell constant

In this last paragraph we strive to give a simple analytical solution to the pressure amplitude at resonance in a cylinder cell. For that purpose a few approximations are taken.

Firstly, we consider that the generated heat is homogeneous inside the cylinder [21, 61], leading to simplify the integral of Equation 2.10 into  $L_c H$ . This should be a good approximation when the cell radius is of the same order of magnitude as the laser waist, which is generally the case. Secondly, we postulate that acoustic modes do not interfere with each other, which is a good approximation for high  $Q_{ac,n}$  values, typically superior to 10 [21]. Finally, by assuming that the detector is positioned at the maximal pressure location (at  $r = r_{max}$ ) and does not affect the pressure mode (an assumption we will discuss later in Section 3.1), one can approximate:

$$\widehat{P}(r_{max}, \omega_n) = \frac{j(\gamma - 1)H L_c Q_{ac,n}}{\omega_n V_c}. \quad (2.20)$$

From this expression we derive one important parameter named the cell constant  $C$  in  $\text{Pa.W}^{-1}.\text{cm}$ . This parameter represents the cell capacity to amplify pressure independently from the deposited heat amplitude  $H$ .

$$C_n = \frac{(\gamma - 1) L_c Q_{ac,n}}{\omega_n V_c} \quad (2.21)$$

For a Helmholtz type resonator, the volume  $V_c$  should be replaced by  $V_{eff}$  as defined in Equation 2.12. One can remark that contrarily to free space, pressure generation inside an acoustic resonator is inversely proportional to frequency and increased  $Q_{ac,n}$  times. The pressure amplitude is maximised for long lengths and small cell volumes, leading to the use of cylindrical cells (Figure 2.9). This could be misleading because the quality factor however decreases when increasing the cell surface, as explained in the previous section. In fact, decreasing the cell radius is much more efficient for pressure amplification than increasing the cell quality factor, explaining why the cell constant maximum occurs for low quality factor values. However, the cell length cannot be raised infinitely for the same reason that its radius cannot be decreased infinitely. Indeed, the laser beam should not touch the cell walls in order to avoid the creation of an important signal background which could potentially limit the sensor sensitivity.

Again, the cell constant is evaluated in Figure 2.9 for a closed cylinder cell resonating at its first longitudinal mode. For example, let us consider a cell of length 10 cm and of radius 5 mm. We compute its frequency to be 265 Hz while its quality factor is approximately 25. Its cell constant is of about 7,740  $\text{Pa.W}^{-1}.\text{cm}$ , leading to a pressure amplitude of 8 mPa for a deposited heat  $H = 1.034 \times 10^{-6} \text{ W.cm}^{-1}$ . At the same frequency, the maximal pressure amplitude one could obtain in free space would be 0.3  $\mu\text{Pa}$ , i.e. 26,700 times less than the pressure inside the cell, showing the importance of the cell amplification.



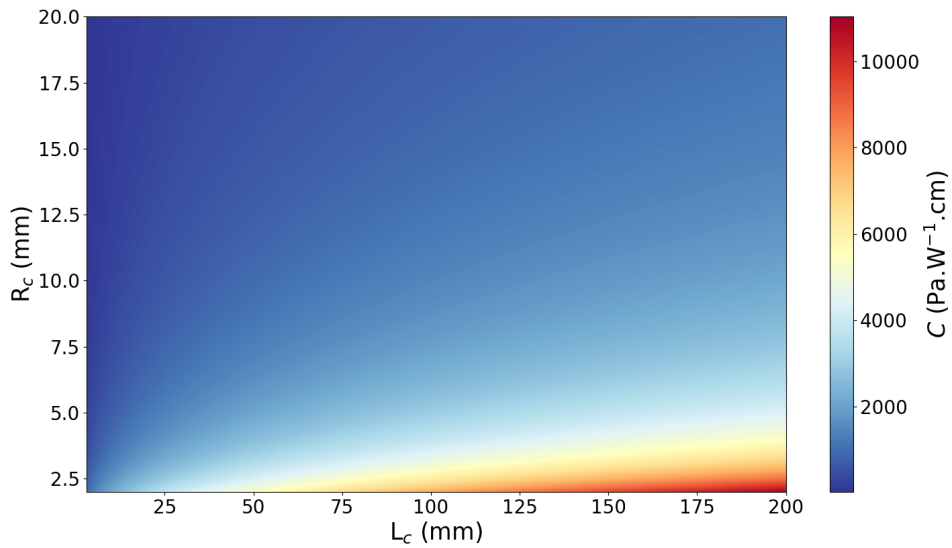


Figure 2.9: Cylinder cell constant versus radius and length.

### 2.1.4 Acoustic pressure detection with mechanical resonators

In order to detect acoustic waves, transducers are used. A transducer converts a force (pressure by surface) into a displacement, usually at a mechanical resonance, which is further read. In photoacoustic gas detection, these resonators are microphones, cantilevers or tuning forks.

In this section, we will not study the case of microphones *ab initio*, but we will base our analysis on data sheets, for two reasons. Firstly, these detectors are mature and widespread in many applications and their fundamental limits in terms of losses and SNR have been reached. Secondly, the SNR of low-noise microphones is often limited by their proximity electronics noise and so by a proprietary design.

We will, in turn, focus our study on the use of cantilever beams and tuning forks. These are schematised in Figure 2.10 with their dimensions. One should note that  $e$  and  $l$  values are reversed depending on the mode of vibration (in or out of the main plane).

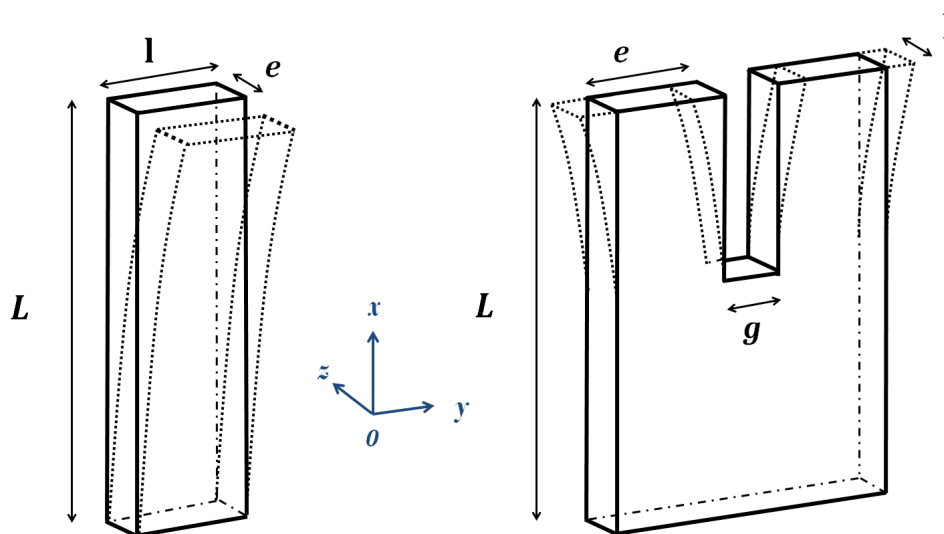


Figure 2.10: Geometrical parameters of cantilevers and QTFs.

### 2.1.4.1 Resonance frequency

Let us consider a clamped-free beam of length  $L$ , vibrating width  $e$  and thickness  $l$  or a tuning fork of gap between the prongs  $g$  (Figure 2.10).

In order to study the beam deformation, a few approximations have to be taken. Firstly, the beam side dimensions are assumed to be small before its length  $L \gg e, l$ . Secondly, the beam sections are supposed to remain planar and parallel to each other under deformation and finally this deformation is considered to be small compared to the beam dimensions. Under these assumptions one can solve Euler-Bernoulli's equation to derive the resonance frequency of a beam (Equation 2.22). We consider a beam of rectangular section, of Young modulus  $E$  ( $E = 78$  GPa for stress charged Quartz and 160 GPa for Silicon) and density  $\rho_q$  ( $2,648 \text{ kg.m}^{-3}$  for Quartz and  $2,330 \text{ kg.m}^{-3}$  for Silicon) (Appendix A). Its resonance frequency is proportional to the ratio  $e/L^2$  and to a constant  $\alpha_n$  defined by the boundary conditions ( $\alpha_0 \approx 1.875$  for a clamped-free beam [138]).

$$\omega_n = \frac{\alpha_n^2 e}{\sqrt{12} L^2} \sqrt{\frac{E}{\rho_q}} \quad (2.22)$$

Bernoulli's hypotheses are verified for most QTFs and a good agreement is found with experimental frequencies (see Section 3.2.1.1). However, we will see that it is not the case for some QTFs designed at ONERA, presenting a large vibrating width and thickness. In those cases, the frequency can be determined by FEM simulations.

The resonance frequency is generally chosen inferior to a few tens of kilohertz in order to limit signal loss due to slowly relaxing gases as discussed in Section 2.1.2. Moreover, values inferior to 1 kHz are generally avoided in order to discard external backgrounds which amplitude is more important at low frequencies.

In photoacoustics, these resonators are immersed in the gas to analyse, also this frequency can be modified by the gas influence on the beam which was not taken into account here. In addition, the gas induces supplementary losses on the resonator as we will explain in the next section.

### 2.1.4.2 Quality factors

Resonator losses are either intrinsic to the resonator itself or come from the interaction with a fluid medium which is necessary for photoacoustics.

Intrinsic losses can be classified into three main types: thermoelastic, structural and electrode damping.

Thermoelastic damping  $Q_{\text{thermo}}$  is the consequence of thermal transfers due to beam motion. When the beam vibrates, heat is generated because of the material thermoelastic properties leading to thermal unbalance and thus losses. This damping value can be computed from Equation 2.23 [139, 140]. It is generally not limiting in our case.

$$Q_{\text{thermo}} = \frac{C_p \rho_q}{E \alpha^2 T} \left( \frac{6}{\xi^2} - \frac{6}{\xi^3} \frac{\sinh \xi + \sin \xi}{\cosh \xi + \cos \xi} \right)^{-1}, \quad (2.23)$$

with  $\alpha$  the material thermal expansion and  $\xi = e \sqrt{\omega \rho_q C_p / (2\kappa)}$ .

Structural damping  $Q_{\text{struct}}$  is defined as the ratio of energy in the resonator with the energy dissipated through its anchoring structure. Independently from the beam geometry, structure damping can be reduced by optimising the resonator anchor structure for the vibrating mode of interest. In the case of clamped-free cantilevers, an expression depending on the beam length and width can be found [141] (Equation 2.24). Nonetheless, we will rather rely on simulations or measurements for accurate computation of this loss source. Typical values

of  $Q_{\text{struct}}$  are of the order of  $10^5 - 10^6$  for tuning forks and usually below  $10^5$  for cantilevers [142, 143].

$$Q_{\text{struct},n} = A_n \frac{L^3}{e^3}, \quad (2.24)$$

with  $A_0 \approx 2$  for the fundamental mode [141].

Finally, for piezoelectric resonators, the deposition of electrodes on the beam constitutes yet another source of damping  $Q_{\text{electrode},n}$ . Indeed, these electrodes represent an additional mass on the resonator. Also the electrode internal viscosity can affect the resonator in complex ways. This loss is usually not limiting for QTFs, however for thin cantilevers it should be carefully studied. For a in-plane vibrating tuning fork it can be approximated as follows considering that the energy is confined in the prongs [144]:

$$Q_{\text{electrode},n} = Q_{\text{Au},n} \frac{E_{\text{Quartz}}}{E_{\text{Au}}} \frac{l}{2l_{\text{Au}}}, \quad (2.25)$$

with  $Q_{\text{Au},n} = E_{\text{Au}}/(\mu_{\text{Au}} \omega_n)$ ,  $\mu_{\text{Au}} \approx 1,462$  Pa.s the gold electrode viscosity and  $l_{\text{Au}}$  the electrode thickness, which is 200 nm for ONERA's QTFs.

In many cases the structural damping will be limiting compared to thermoelastic or electrode damping. In any case, a measurement of intrinsic losses total contribution is often preferable. This is accomplished by measuring the resonator quality factor under vacuum  $Q_{\text{vac}}$ . By considering that the different losses do not overlap one can write:

$$Q_{\text{vac},n} = \left[ Q_{\text{thermo},n}^{-1} + Q_{\text{struct},n}^{-1} + Q_{\text{electrode},n}^{-1} \right]^{-1}. \quad (2.26)$$

In addition to intrinsic damping, losses due to fluid interaction with the mechanical resonator occur. The quality factors we introduce in the following paragraphs are approximated expressions extracted from the overall hydrodynamic force acting on the QTF. The computation of this force was detailed in [26].

The vibroacoustic interaction induces energy exchanges, particularly due to viscous damping  $Q_{\text{viscous},n}$ , for which one can further distinguish the frontal and lateral effects. An approximated expression can be given at atmospheric pressure for high quality factor flexural resonators, depending on beam geometry, fluid density and dynamic viscosity (Equation 2.27). This model has demonstrated a very good agreement with experimental results for beams and tuning forks [138].

$$Q_{\text{viscous},n_{\text{frontal}}} = \frac{\rho_q e}{\pi} \sqrt{\frac{\omega_n}{2\rho_f \mu}} \quad Q_{\text{viscous},n_{\text{lateral}}} = \rho_q l \sqrt{\frac{\omega_n}{2\rho_f \mu}} \quad (2.27)$$

In addition, when the beam is vibrating at a distance  $d$  from a surface, acoustic waves confinement between structures occurs. Depending on the beam direction compared to the facing structure, squeeze or Couette damping [145] can happen. While squeeze damping occurs when a structure moves towards another, Couette damping describes air layer shearing when a structure moves perpendicularly to another structure plane. Again, an approximated expression is given depending on beam geometry and stiffness  $K_n$  (defined later in Equation 2.32) and gas dynamic viscosity  $\mu$  (Equation 2.28). The closest the surface is, the most important the squeeze and Couette damping will be. These losses are worsen when increasing the beam surface  $S$  facing the wall. One can note that squeeze damping can occur between the prongs of a tuning fork.

$$Q_{\text{squeeze},n} = \rho_q \frac{ed^3 \omega_n}{l^2 \mu} \quad Q_{\text{Couette},n} = \frac{d K_n}{\omega_n \mu S} \quad (2.28)$$

Eventually, cantilevers and tuning forks can emit acoustic waves through vibration, constituting the last source of losses. This phenomena is well known, especially for musical tuning forks. In photoacoustics it is rarely limiting, however in very specific cases it can become major. It is for example the case of QTF C2 for which the prong vibrating width is of the same order as the acoustic wavelength [146]. For cantilever beams, the expression of this loss is complex [138], yet for QTFs an approximated expression can be found:

$$Q_{\text{acoustic},n} = \frac{64}{3} \frac{\rho_q}{\rho_f} \frac{1}{k_{\text{ac}}^4 e l (e + g)^2}. \quad (2.29)$$

The resonator total losses can finally be expressed through the definition of a quality factor  $Q_n$  that we will use in the next section to quantify beam displacement. In the other sections of the manuscript, we simplify the notation to  $Q$  to describe the quality factor of the mode of interest. Again, considering that the losses are independent, one can write:

$$Q_n = \left[ Q_{\text{vac},n}^{-1} + Q_{\text{viscous},n}^{-1} + Q_{\text{squeeze},n}^{-1} + Q_{\text{Couette},n}^{-1} + Q_{\text{acoustic},n}^{-1} \right]^{-1}. \quad (2.30)$$

During the previous PhD thesis at ONERA [26], the optimisation of this quality factor was conducted, leading to the design of two QTFs named U1 and C2 presented in Chapter 1 and further studied in the next chapters.

### 2.1.4.3 Beam displacement

The mechanical resonator displacement  $W(x, \omega)$  caused by a photoacoustic force  $F_{\text{PA},n}$  can be expressed by means of Euler-Bernoulli's equation, considering that the beam length is superior to its width and thickness. One can write the resonator displacement for flexural modes of vibration as:

$$\widehat{W}_n(x, \omega) = \frac{|\widehat{F}_{\text{PA},n}|}{K_n + j\eta_n\omega - M_n\omega^2} \Phi_n(x). \quad (2.31)$$

One can observe that the displacement is expressed as a second order harmonic oscillator of stiffness  $K_n$ , damping  $\eta_n$  and equivalent mass  $M_n$  whose expressions are given in Equation 2.32. In addition, beam losses are modelled by introducing the previously derived quality factor  $Q$  in the system.

$$\begin{cases} K_n = \omega_n^2 M_n \\ \eta_n = \frac{\omega_n M_n}{Q_n} \\ M_n = \rho_q e l \int_0^L \Phi_n^2(x) dx \end{cases} \quad (2.32)$$

The expression of the displacement and generalised mass depends on  $\Phi_n(x)$  which is the beam deformation. Its expression can be found in [26]. For normalisation, the integral of the squared deformation was taken to be the beam length (Equation 2.33). Also particular values are given in the following equations [26].

$$\Phi_0(L) \approx 2 ; \quad \int_0^L \Phi_0(x) dx \approx 0.783 \times L ; \quad \int_0^L \Phi_n^2(x) dx = L \quad (2.33)$$

Deformation of a beam is logically maximal at its free end, meaning that the maximal displacement will be obtained by applying a point/singular force at this location. However, for QTFs used in free space, the optimal height along  $z$  where the laser beam is positioned has to be adapted. Indeed, as the laser beam induces a

cylindrical acoustic source, the optimal laser beam height should be slightly beneath the top, usually near 85% of the prong length [28, 79]. This result can be obtained through computation of the photoacoustic force over height.

#### 2.1.4.4 Photoacoustic force

The photoacoustic force acting on the resonator is computed by integrating the acoustic pressure on the resonator faces. Acoustic pressure is projected on the resonator faces as shown in Figure 2.11 for a QTF. We suppose that the beam does not modify the pressure field, i.e. that neither acoustic diffraction or vibroacoustic interaction due to beam vibration are taken into account. This hypothesis validity will be assessed in Section 4.1.2.1. Let us take for example a watch QTF of dimensions  $L = 3.75\text{mm}$ ,  $e = 0.6\text{mm}$ ,  $l = 0.34\text{mm}$  and gap between the prongs  $0.31\text{mm}$ , resonating around  $32,768\text{ Hz}$ . Pressure distribution on the QTF faces for a heat amplitude of  $1.034 \times 10^{-6}\text{ W.cm}^{-1}$  is represented on Figure 2.11 for on-beam or in-plane configuration.

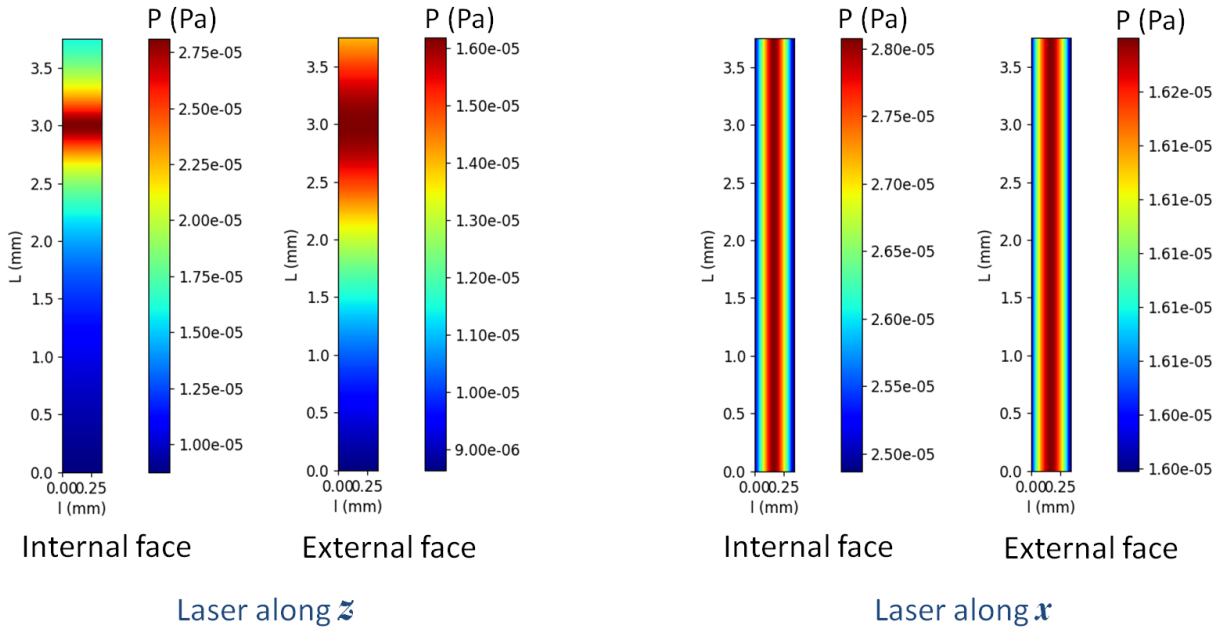


Figure 2.11: Pressure amplitude projection on a watch QTF faces, obtained with the analytical model. (Left) Laser height was optimised at 80% of the total prong length for on-beam configuration. (Right) In-plane configuration in which the laser is parallel to the QTF prongs.

Furthermore, the pressure integral is weighted by the resonator deformation. Assuming that the resonator first face is placed at a position  $d$  one can write:

$$\widehat{F}_{\text{PA},n} = \int_0^L \left[ \int_{-l/2}^{l/2} \left[ P(x, d, z, \omega_n) - P(x, d + e, z, \omega_n) \right] \Phi_n(x) dz \right] dx. \quad (2.34)$$

This formula will be used in the case of resonators in free space such as QTFs. One should note that this force has to be computed for each prong for QTFs. Also, for on-beam configuration, it can be taken as twice the force applied on one prong. As such, the photoacoustic force for on-beam configuration with a watch QTF shown in Figure 2.11 is computed to be  $|\widehat{F}_{\text{PA},0}| = 1.4 \times 10^{-11}\text{N}$ . When using acoustic resonators with QTFs, analytical determination of the pressure can be extremely complex and one should rather rely on finite element simulations. However, for the use of microphones and cantilevers in acoustic resonators, an analytical value can be derived under two approximations. Firstly, the pressure on the second face of the resonator is zero,

which is a good approximation when the resonator acoustic impedance, i.e. the resonator resistance to acoustic propagation, is high. This is the case for microphones and also for cantilevers depending on the design on the frame surrounding them [66]. Secondly, the resonator can be considered to be punctual, which is usually the case given the small resonator dimensions before the acoustic wavelength. These assumptions lead to approximate the pressure to be homogeneous on one of the resonator face, yielding:

$$\widehat{F}_{PA,0} \approx 0.783 L l P(d, \omega_0). \quad (2.35)$$

#### 2.1.4.5 Vibroacoustic coupling of acoustical and mechanical resonators

In many cases an acoustic resonator is used to enhance the mechanical sensor sensitivity. When using mechanical detectors with a high quality factor, this leads to a complex coupling of the acoustic and mechanical modes. It is particularly the case for tuning forks [80, 146] and sometimes the case for cantilevers [147].

An analytical solution can be derived for the coupling of these resonators [98] taking into account the overlap of the pressure with the resonator and a coupling coefficient. By doing so, Aoust et al. demonstrated a good match between the analytical model, the finite element method and experiments [26, 98].

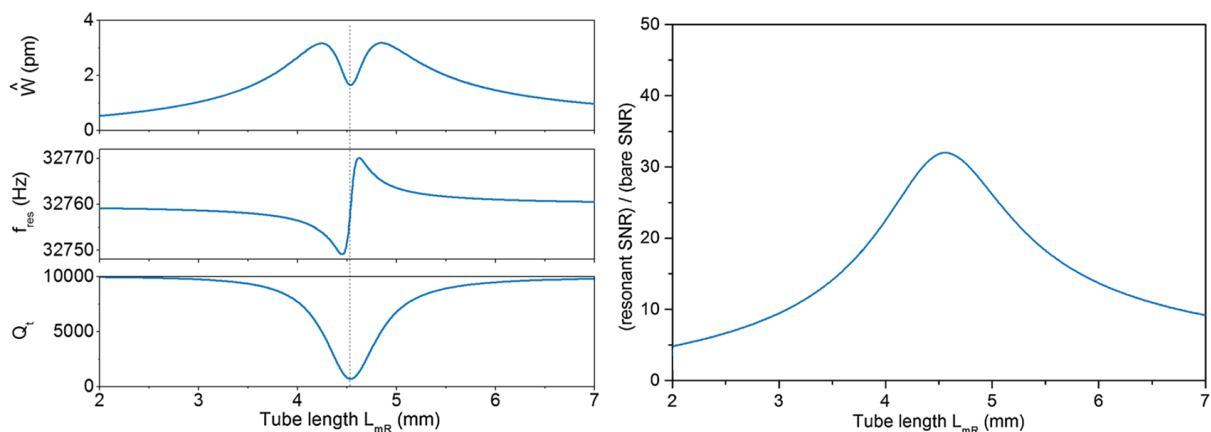


Figure 2.12: Analytical results for the coupling of acoustic microresonators with a watch tuning fork [98]. QTF displacement, frequency and quality factor with resonator length (Left). QTF normalised SNR with resonator length (Right).

As seen in Figure 2.12 coupling between the QTF and the acoustic resonator can be obtained by tuning the acoustic resonator length. When the coupling is maximised, a local minimum of the QTF displacement is obtained which corresponds to a minimum of its quality factor  $Q^*$  and a maximum of the signal-to-noise ratio. A good match between analytical or FEM simulations and experiments can be reached through the fit of a coupling coefficient between the resonators. However, an analytical expression for the coupling coefficient seems difficult to generalise to many different configurations because it depends on the system geometry and parameters. As a result we will only rely on finite element simulation to model the vibroacoustic coupling between resonators.

Eventually, we note that the coupling between resonators is complex. It is not straightforward that the quality factor we defined until now correctly describes the coupled system losses. As a consequence, we will distinguish the quality factor  $Q$  from the coupled system quality factor that we will name  $Q^*$ . Further studies should be made so as to determine if  $Q = Q^*$ .

### 2.1.4.6 Brownian motion and SNR

In order to determine the sensor limit of detection one must express the system limiting noise. We will consider that this noise is always the Brownian noise for cantilevers and QTFs, as it has been reported to be so in several publications [148, 74]. However, in some cases the sensor can be limited by external varying backgrounds or even electronics as it can be the case for microphones [54].

Brownian noise describes the fluctuation of the material molecules due to temperature. This noise induces motion of the resonator that can be modelled by an equivalent noise force  $F_B$ :

$$F_B = \sqrt{\frac{4k_B T \omega_0 M_0 \Delta f}{Q}}, \quad (2.36)$$

where  $k_B$  is the Boltzmann constant,  $T$  the temperature in K, and  $\Delta f$  the equivalent bandwidth in Hz in which the noise is integrated. This notation implies that the noise is considered as a white noise over the overall spectrum. However, for sharply resonant detectors, special care should be taken when computing the sensor noise as we will detail in Section 2.1.6.

Finally, the sensor signal-to-noise ratio can be derived as the ratio of the equivalent photoacoustic force with the noise force:

$$\text{SNR} = \frac{|\widehat{F}_{\text{PA},n}|}{F_B}. \quad (2.37)$$

This SNR is also called SNR at  $1\sigma$ ,  $\text{SNR}_{1\sigma}$ , and its value can be used to derive the sensor minimum detection limit. However, in the industry a stricter SNR criterion is often required to define the sensor detection range and a SNR value at  $3\sigma$  is sometimes preferred  $\text{SNR}_{3\sigma} = 3 \times \text{SNR}_{1\sigma}$ .

## 2.1.5 The particular case of microphones

As we have explained before, we analyse the case of microphones separately from cantilevers and QTFs. These resonators are mature and we report ourselves towards commercial data sheets. However, working with those data may not be straightforward, also we propose in this paragraph to demonstrate how we derive the microphone useful variables from data sheets.

### 2.1.5.1 Microphone sensitivity

For microphones, an useful variable in photoacoustics is the signal output level depending on acoustic pressure. This parameter is called the sensitivity by the manufacturers (not to be confused with NNEA) and can be used to determine the cell constant of acoustic resonators.

Usually the microphone sensitivity, that we name  $R_M$ , is directly given in the data sheet in  $\text{mV.Pa}^{-1}$ . This value can also be given in dBV relative to 1 Pa, and the conversion can easily be made. For example -42 dBV re 1Pa corresponds to  $10^{-42/20} = 7.94 \text{ mV.Pa}^{-1}$ . This value is often given at 1 kHz, however its dependency with frequency is also generally provided as shown in Figure 2.13. It is generally flat in the microphone working frequency range and increases around the microphone resonance frequency, which can be seen around 20 kHz in Figure 2.13.

When using digital microphones the sensitivity is provided in dBFS, meaning decibels of the microphone full scale. In that case, a more complex signal processing has to be used in order to compute the pressure. Finally, one can note that sensitivity depends on the atmospheric pressure, temperature, humidity and gas. As

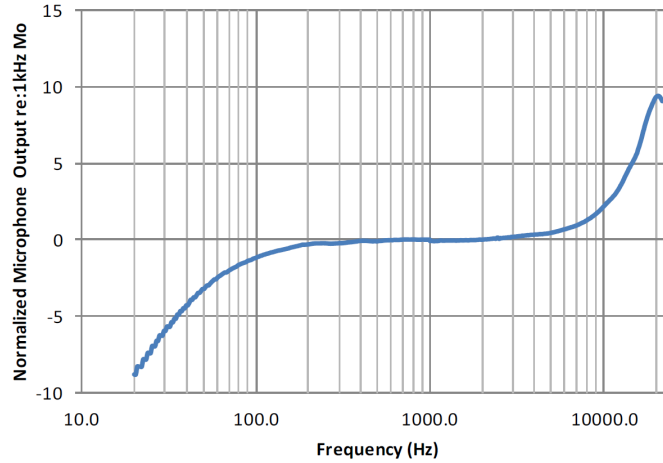


Figure 2.13: Normalised sensitivity in dB over frequency for a typical MEMs condenser microphone (AKU143 [149]). 0 corresponds to -42 dBV re 1 Pa.

a consequence, the best way to perform quantitative measurements is to characterise the microphone response in the experimental conditions with a calibrated source of 1 Pa.

### 2.1.5.2 Microphone noise and SNR

When it is given, the microphone noise can be expressed in  $\text{Pa}\cdot\text{Hz}^{-1/2}$ ,  $\text{dBFS}\cdot\text{Hz}^{-1/2}$  or  $\text{dB(A)}$ . This noise depends on the frequency and is the sum of different contributions such as membrane material loss, ventilation hole, or electronics noise [37]. A noise spectral density example is presented in Figure 2.14 for a digital microphone [150].

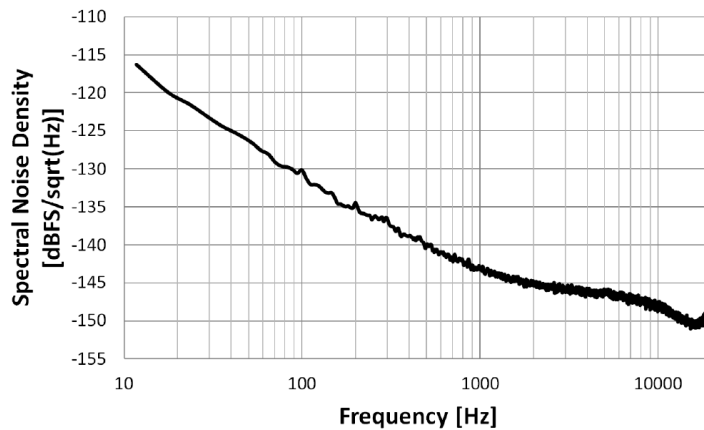


Figure 2.14: Microphone spectral noise density example for a digital microphone IM69D130 [150].

Most commonly, the SNR is given for a pressure of 1 Pa over the entire microphone frequency range. This range usually goes from a tens of Hz to 10 or 20 kHz, corresponding to the Human hearing range. In addition, the SNR is weighted with the A-weighting which enables to correct the microphone sound level to match Human hearing sensitivity to frequency [151]. We considered that  $\text{dB(A)}$  were similar to  $\text{dB}$  in order to simplify computations, which is a good approximation when the frequency is close to 1 kHz. Also, in the many cases in which the noise spectral density is not provided, we considered the SNR to be constant over the microphone frequency range. This last approximation necessary leads to discrepancies as the noise varies with frequency as



we showed on Figure 2.14. On this example we estimated the SNR to 65 dB (from 100 Hz to 10 kHz) whereas the data sheet reports 69 dB(A).

Finally, note that in some cases the SNR is limited by the electronic amplification circuit. Indeed, for low noise microphones the preamplifier noise can be dominating and limit the sensor SNR (as for example in [152]). In this manuscript we will consider the use of commercial microphones, taking into account this effect.

## 2.1.6 Signal processing

The mechanical resonator displacement can be detected optically by laser interferometry, or using capacitive or piezoelectric methods. In this section, we will present the implementation of a classic signal processing scheme we used for piezoelectric detection using quartz tuning forks. This model could easily be adapted to other detection schemes.

### 2.1.6.1 Equivalent electric model

First of all, to facilitate electrical description, we introduce the resonator electrical equivalent model (using Butterworth-Van Dyke model). By analogy with Equation 2.31, a resonator can be described by a RLC circuit (Figure 2.15). In addition a parasitic capacitance  $C_0$  is introduced in parallel to represent the capacitance existing between the resonator electrodes, it is usually of the order of 1 pF.

This analogy is convenient for computation of the resonator generated current as well as simulation and design of the electronic signal processing.

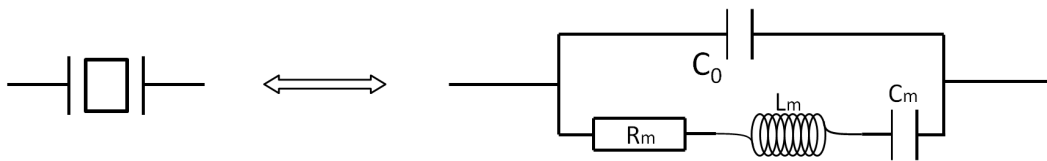


Figure 2.15: Resonator electrical equivalent model.

This model equivalent parameters are called motional resistance, inductance, and capacitance and can be expressed depending on the previously defined mechanical parameters as described in Equation 2.38. In addition a transduction coefficient  $c_X$ , in  $N \cdot V^{-1}$ , is introduced to link the resonator voltage output  $V_n$  to the applied force. This coefficient depends on the piezoelectric efficiency and resonator parameters as well as electrode pattern, it can be computed analytically in simple cases [26] or through simulation. Finally, the resonator generates a current that can be expressed as the ratio of voltage and circuit equivalent impedance.

$$\begin{cases} R_{m,n} = \eta_n / c_X^2 \\ L_{m,n} = M_n / c_X^2 \\ C_{m,n} = c_X^2 / M_n \\ V_n = |\widehat{F}_{PA,n}| / c_X \end{cases} \quad (2.38)$$

### 2.1.6.2 Signal amplification

The resonator generated signal is weak and has to be amplified before further processing. For that purpose, proximity electronics is attached to the resonator and is composed of a preamplifier and followed sometimes by an additional amplifier. Positive and negative charges collected through the electrodes are amplified through

a circuit such as the one presented on Figure 2.16 and a differential is usually set between them. In our case we chose to put one set of electrodes to the ground in order to shield the QTF from electromagnetic backgrounds.

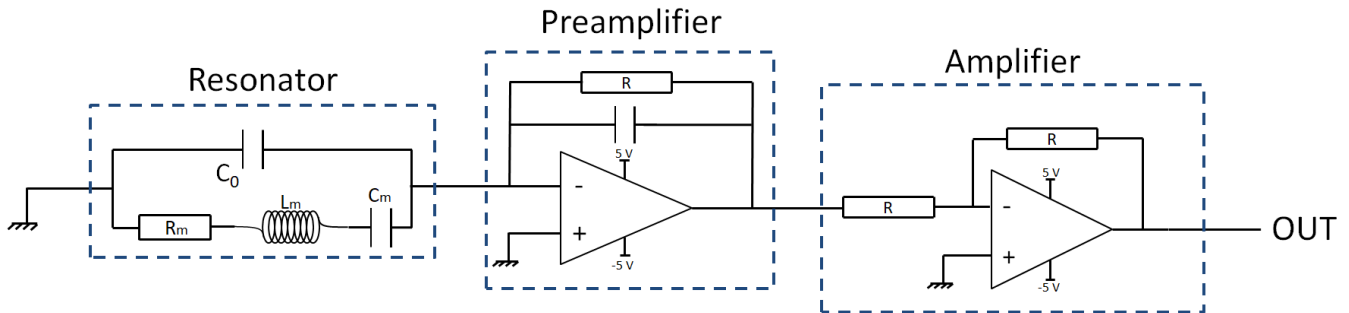


Figure 2.16: Open-loop amplifier circuit constituted of a preamplifier and amplifier.

As seen in the figure above, the preamplifier is a transimpedance operational amplifier allowing for current to voltage conversion. Then, an amplifier circuit increases the voltage to facilitate signal reading and processing. This amplifier can be composed of a simple gain inverting circuit. In our case, we implemented two band-pass Rauch filters at the detector frequency enabling to filter lower and higher frequencies that could disturb the circuit operation. Typical gain of proximity electronic circuit is superior to one million. It is fundamental to note that in most cases, if the circuit is correctly designed, the limiting noise of the sensor should still be the resonator Brownian noise and so the electronics design should have no influence on the sensor SNR. However, for low noise sensors it is possible for the electrical noise to be superior to Brownian noise, for example when using microphones (such as BK4179 [152]), or when detectors are not used at resonance (because the Brownian noise is lower than at resonance).

### 2.1.6.3 Lock-in detection

The second step of signal processing is to determine the amplitude of the signal generated by the proximity electronics. This could be accomplished by simply measuring the signal amplitude with an oscilloscope for example. However, as the signal is weak and subject to potential backgrounds or noises at different frequencies, one generally uses lock-in detection.

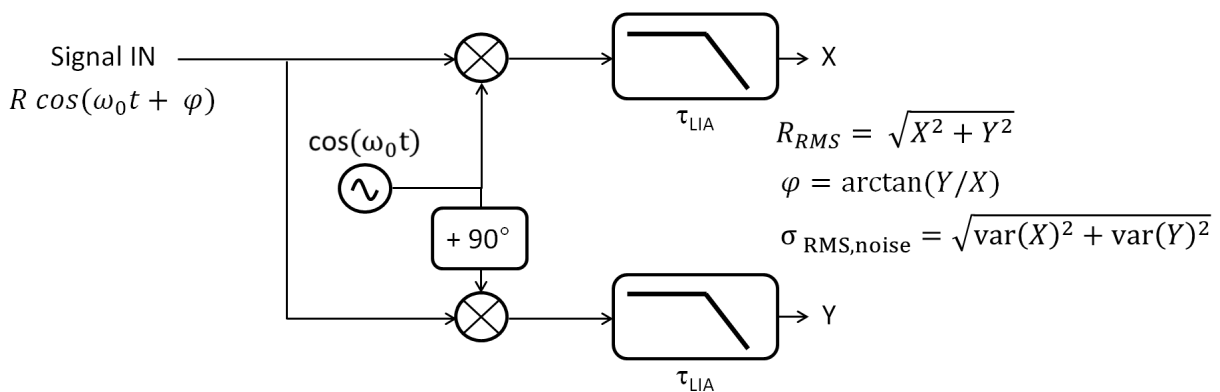


Figure 2.17: Scheme of a lock-in amplifier principle. The input signal is multiplied with a reference locked at the same frequency. The result is filtered and gives the input signal magnitude  $R$  and phase  $\varphi$ .

Lock-in detection consists in modulating the signal at a given frequency and deriving the response at an harmonic of this particular frequency [153]. Practically, the detector signal is multiplied by a reference locked at the same frequency. This results in a signal yielding the information in its continuous component, which is obtained through low-pass filtering of the multiplication result. By increasing the lock-in amplifier (LIA) filter time constant  $\tau_{LIA}$  one can reduce the measurement bandwidth  $\Delta f$  and so increase the SNR. However this in turn increases the measurement integration time. To be effective, the time constant must be greater than the resonator time constant  $\tau_{LIA} > \tau_{resonator}$ . Also, it is important to wait for the LIA output signal to stabilise, also we usually took an integration time of  $10 \times \tau_{LIA}$ .

In order to determine the variation of the sensor signal with integration time one can use the Allan standard deviation. This tool is a two sample variance of the signal over time. It allows for deriving the sensor minimum detection limit and its stability [154, 155].

One should note that special care should be given when measuring the noise of sharply resonant detectors. Often, the LIA computes automatically the noise  $\sigma_{RMS,noise}$  over an equivalent bandwidth of 1 Hz. However, when the resonator presents a high quality factor, the resonance curve bandwidth can be inferior to the LIA bandwidth. In that case, the noise cannot be considered as a white noise and one should verify that the lock-in noise is not underestimated (with a spectrum analyser for example or through Allan deviation analysis). Also, one should note that in those cases, the use of lock-in detection can be questioned. Indeed, as the QTF constitutes a good filter, a simple read of its signal could be made.

For every computation presented in this manuscript we considered a bandwidth of 1/16 Hz corresponding to the value we used experimentally with our LIA. This bandwidth was chosen inferior to the smallest bandwidth of our studied QTFs to consider the noise to be white over the QTFs bandwidth.

### 2.1.7 NNEA

Comparison of different photoacoustic sensors sensitivities is difficult because of the diversity of setups, gas, absorption, optical power, integration time, etc. To tackle this issue, a figure of merit called normalised noise equivalent absorption (NNEA) was introduced in a similar way to what has been done for light detectors with noise equivalent power (NEP) or direct absorption spectroscopy with the noise equivalent absorption (NEA). This NNEA should always be the same for a given sensor, independently from the setup.

Even though, sensors sensitivities are still difficult to compare. Indeed, many computation differences are found through the literature, for example concerning the laser power or detector bandwidth, leading to discrepancies, even for identical sensors used in different setups. In this paragraph, we will define the NNEA we use in order to facilitate photoacoustic sensors comparison.

The difference between our computation and the one generally used in the literature [28] is the introduction of the heat amplitude  $H$  instead of gas absorption  $\alpha_G$  and laser power  $P_L$ . Taking  $H$  into account allows the NNEA to be independent from the laser modulation scheme and the overlapping with the gas absorption line. As such it is also possible to analyse the modulation efficiency by computing the ratio  $H/\alpha_G P_L$ . The closer to 1 this factor is, the better the modulation overlap is.

Moreover, the heat amplitude takes into account the gas relaxation rate, as can be seen in Equation 2.5.

With this modification, the NNEA can be computed as follows:

$$NNEA = \frac{H}{SNR \sqrt{\Delta f}}, \quad (2.39)$$

with  $H$  the heat amplitude, and  $\Delta f$  the equivalent noise bandwidth.

When computing the SNR, the signal value is taken to be its amplitude value and not its root mean square value. In addition, the signal and noise values were scaled in the same bandwidth (assuming a white noise) to compute the SNR.

The heat amplitude may be hard to compute in some cases, for example when using pulsed lasers or when the modulation is not perfectly sinusoidal and the absorption not a perfect Lorentz function. A work around is to compute the minimal detectable absorption, which will allow to find consistent results in any case without computing  $H$ .

With the definition given in Equation 2.39, the NNEA is independent from laser power, modulation, gas absorption and relaxation rate, leading to quantitative comparisons between sensors. Nonetheless, some phenomena could still lead to small discrepancies over the values of NNEA for a same detector. Indeed, we expect gas parameters (pressure, viscosity, temperature, etc.) as well as laser wavelength (laser beam waist, etc.) to slightly modify the sensor sensitivity.

## 2.2 Modelling photoacoustics by FEM

In order to refine the results of the analytical model or to analyse complex cases we used finite element modelling (FEM). The objects to model are the mechanical resonator, the acoustic resonator and source and of course the vibroacoustic interactions between them. In this section we present the simulations assumptions and model construction. We mainly used a solver called OOFELIE::Multiphysics [156] which was historically developed in a partnership with ONERA for quartz resonators modelling. This solver was validated during the previous PhD thesis for the modelling of photoacoustic sensors with a good agreement between analytical model and experiments [26].

### 2.2.1 Mechanical resonator modelling

The first model element is a mechanical resonator which is usually a QTF or a cantilever. This resonator is modelled as a solid, the materials and piezoelectric parameters of Quartz are given in Appendix A. The resonator was meshed with parabolic tetrahedron elements to give an accurate description of the physics. We used both modal and harmonic analysis to compute different parameters that we explicit in the following.

#### 2.2.1.1 Modal analysis

Using modal analysis, the simulations can predict several parameters. The main ones are the resonator eigen frequencies and modes of resonance.

It is also possible to compute the electric potential generated by the piezoelectric effect as shown in Figure 2.18. Doing so enables to design the electrode scheme so as to collect a maximum of the generated charges. It also allows to compute the resonator motional resistance that we will use in Chapter 5 for example.

Furthermore, the model can be used to compute the mechanical constraints as shown in Figure 2.18. The constraints analysis allows to design an adapted anchor structure in order to minimise anchor losses. The structural quality factor is, by definition, the ratio of the constraints energy in the resonator  $E_{\text{resonator}}$  with the constraints energy in the anchor  $E_{\text{anchor}}$  (Equation 2.40). For flexural resonators such as QTFs, it can be computed from the strain constraints.

$$Q_{\text{struct}} = 2\pi \frac{E_{\text{resonator}}}{E_{\text{anchor}}} \quad (2.40)$$

These constraints can also enable to determine the zones that are the most sensitive to thermal excitation. Directing the laser beam towards these zones should be avoided to limit the presence of signal background. On the contrary, it can be used in photothermal spectroscopy to excite the QTF with the laser radiation [157, 158].

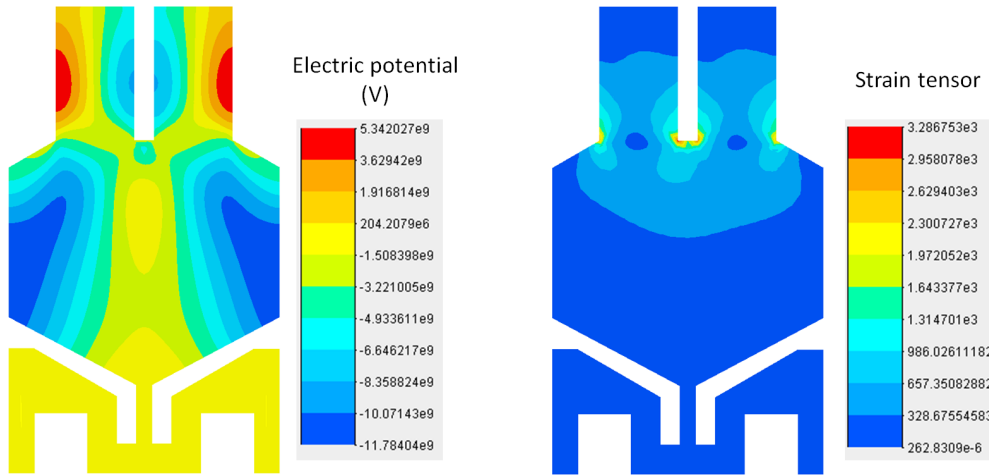


Figure 2.18: Modal analysis of the QTF C2, electric potential (left) and strain tensor (right).

### 2.2.1.2 Harmonic analysis

Harmonic analysis was mainly used to compute the effect of the resonator vibration on the surrounding gas medium as we will detail in next sections. In these models, the resonator anchor structure is clamped by locking rotations and translations. In addition, its losses are imposed through the definition of its structural quality factor  $Q_{\text{struct}}$ . This quality factor can be determined from the resonator measured quality factor under vacuum  $Q_{\text{vac}}$  or derived from the analytical model, or from other modal FEM simulations as we previously saw.

## 2.2.2 Acoustic modelling

The second model element is the fluid inside acoustic resonators or surrounding the mechanical resonator. The fluid was not considered viscous to simplify the computations. Generally, we worked with air at atmospheric conditions by imposing a density of  $1.225 \text{ kg}\cdot\text{m}^{-3}$  and a sound speed of  $340 \text{ m}\cdot\text{s}^{-1}$ . Air elements were also meshed with parabolic tetrahedron elements. The element size was kept inferior to the acoustic wavelength and was adapted depending on the precision required (fine near the QTF and large away). Through FEM we modelled the complex phenomena linked to the acoustic domain: acoustic diffraction, vibroacoustic interaction, radiation quality factors, etc. The construction of the different acoustic elements is developed in the next sections.

### 2.2.2.1 Acoustic source

Rather than modelling the laser beam and light absorption by the gas molecules, which cannot be modelled by the solver, an acoustic source is defined. It is a cylinder of same radius as the laser waist, i.e.  $100 \mu\text{m}$ , through which an acoustic flow rate is defined. The pressure profile can be defined as Gaussian along the laser direction, however we considered an homogeneous pressure inside the cylinder which we found to be a good approximation in free space. Furthermore, the volume flow rate was normalised to be equal to  $1 \text{ m}^3\cdot\text{s}^{-1}$  to simplify comparisons between simulations.

The length of this acoustic source has been studied for correct modelling in free space. As we have seen in Section 2.1.3, the pressure generated in free space has a cylindrical profile because of the source points contribution along the source direction. In FEM, the acoustic source is not an infinite line but a cylinder of length  $L_{\text{source}}$ , as shown in Figure 2.19. The impact of the length value on the pressure profile near the resonator was studied in order to reduce the model memory size. For a good description of the source, the mesh size was set to  $\lambda_{\text{ac}}/10$ . We then varied the source length and analysed the acoustic profile along the  $y$  axis. We found a significant deviation from a cylindrical profile if  $L_{\text{source}} < \lambda_{\text{ac}}/4$ , so we usually took  $L_{\text{source}} = \lambda_{\text{ac}}/2$  or more in

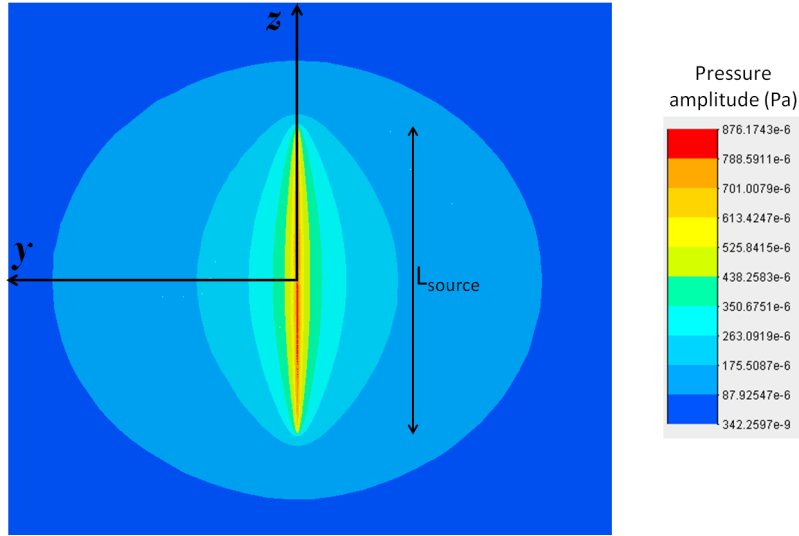


Figure 2.19: Pressure amplitude simulation of a cylindrical acoustic source of length  $L_{\text{source}} = \lambda_{\text{ac}}/2$  at 4,765 Hz in free space. The red cylinder is the acoustic source.

simulations to correctly describe the cylindrical shape of the acoustic source.

### 2.2.2.2 Acoustic boundaries

The definition of acoustic boundaries is also an important element of simulations in order to simulate infinite extension media.

In free space, a perfectly matched layer (PML) was defined around the resonator surrounding air. This layer absorbs the acoustic waves coming from every direction in order to avoid parasitic back reflections that could modify the simulated acoustic modes. To reduce model size this layer thickness is taken to be at least  $\lambda_{\text{ac}}/4$ .

In resonators it could be more appropriate to use absorbant panels instead of PMLs to model the acoustic losses through open ends. It can simply be done by imposing an impedance condition at the resonator open end face. In this case the acoustic impedance must be equal to the product of fluid mass density and sound speed  $\rho_f \times v$ . Nonetheless, this condition is not perfect as waves which are not perpendicular to the face normal direction can still cause minor back reflections.

### 2.2.2.3 Acoustic resonator quality factor

Modelling of acoustic resonators was made through the definition of solids with a sound hard wall condition. This condition means that the acoustic waves are reflected by walls without any loss. By doing so we were able to model acoustic resonators quality factor due to loss at openings:  $Q_{\text{ac,radiation}}$ . Nonetheless we saw in Section 2.1.3 that at atmospheric pressure the limiting quality factor of small resonators is the thermoviscous one  $\left[Q_{\text{ac,thermal}}^{-1} + Q_{\text{ac,viscous}}^{-1}\right]^{-1}$ . At the time of our FEMs simulations we could not model these losses with our solver because they were not implemented yet. Instead we were able to use the software Comsol [159, 60] which enables simulation of thermoviscous losses.

In order to model acoustic resonator thermoviscous quality factor two ways are possible with Comsol. The first one consists in deriving the cell quality factor through computation of the acoustic mode amplitude  $\hat{A}_n(\omega)$  in modal analysis. This method is straightforward and the computation in modal analysis is fast. A very good agreement between analytical and FEM quality factor as well as cell constant was demonstrated [135].

The second method consists in meshing the thermoviscous boundary layers  $d_\kappa$  and  $d_\mu$  in harmonic analysis [160]. By using the thermoviscous domain in Comsol it is possible to define the fluid viscosity, thermal capacity, etc. The cell constant can be derived from the harmonic analysis as well as the cell quality factor. Nonetheless, due to the use of boundary layers, this method requires an enormous memory size and thus the simulation of detailed acoustic resonators can be impossible, enforcing experimental approaches. Thanks to this model we could estimate the quality factor of a new resonator we will present in Section 4.2.2. We also attempted to model Mirsense's cell we will present in Section 3.1.4.3 but could not obtain results due to the memory size limitation.

### 2.2.3 Vibroacoustic interaction modelling

Finally, the simulations model the interaction of the mechanical resonator with surrounding air. This is accomplished by defining a vibroacoustic interaction between the mechanical elements and acoustical ones. The mesh nodes are then interpolated to provide a good match between the two physical domains. After computation, the solver displays the portion of the surfaces that were taken into account depending on the mesh quality. For the different models we realised, we meshed the interacting elements so as to obtain a very good portion taken into account, superior to 99.9%.

The vibroacoustic interaction enables the exchange of energy between the mechanical and acoustical elements. This allows to take into account the mechanical resonator acoustic losses  $Q_{\text{acoustic}}$ . To determine this quality factor we forced the resonator structural quality factor  $Q_{\text{struct}}$  to a very high value, to make sure it was not limiting. We then computed the resonator quality factor  $Q_{\text{acoustic}}$  in harmonic analysis.

### 2.2.4 Conclusion

The model we have presented enables the computation of the sensors main parameters: frequencies, quality factors, pressure amplitude, photoacoustic force, etc. This model was refined by the use of finite element simulations to take into account complex phenomena such as the acoustic diffraction and resonances as well as coupling between the acoustic and mechanic resonators. The model will be applied in Chapter 3 to describe different systems found in MPAS, CEPAS and QEPAS.

However, the numerical results obtained for different systems do not tell if there is still any margin for improvement in the sensitivity of photoacoustic sensors. Particularly, even if we can optimise the sensitivity of our QTF, the reasons behind this optimisation is not clear. It is even more difficult when studying coupled systems such as QTFs with acoustic resonators. To gain some physical insight into the limitations of photoacoustic systems, we are going to present a new modelling in the next section.

## 2.3 Definition of a new unified modelling

Herein, we describe a new unified modelling, capable of describing the different factors leading to the sensitivity of a photoacoustic sensor, whatever its nature (MPAS, CEPAS, or QEPAS). Through this model we propose to improve our understanding of the physics behind those photoacoustic sensors.

The different factors occurring in photoacoustics are presented in Figure 2.20. To define this model we considered that each factor was independent from the others.

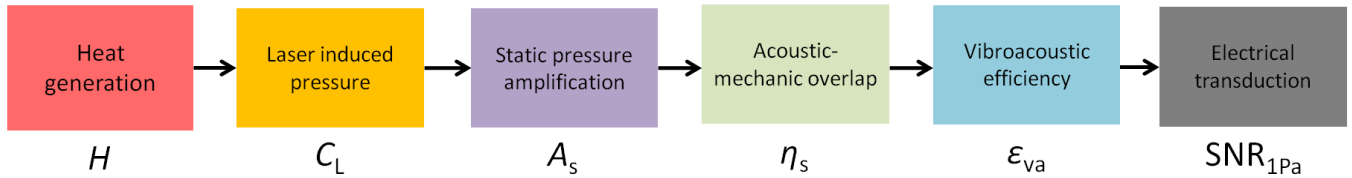


Figure 2.20: Sum up of the different physical phenomena occurring in a photoacoustic sensor.

### 2.3.1 Heat source $H$

The first factor involved in our model is the maximal heat amplitude generated in the medium. We already introduced this factor and discussed its value depending on the modulation scheme (see Section 2.1.2). When the laser wavelength is tuned to a gas absorption line, the gas absorbs the laser energy and relaxes under the form of heat through collisions mainly. The heat maximal amplitude  $H$  in  $\text{W}\cdot\text{cm}^{-1}$  depends on the laser mean power  $P_L$  and gas absorption  $\alpha_G$  that we compute analytically.

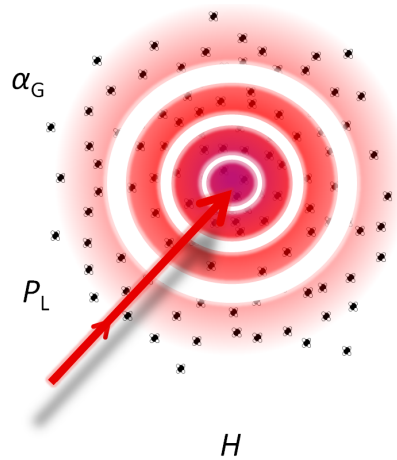


Figure 2.21: Illustration of the heat density. Modulated heat is produced when the laser targets the gas absorption line. The heat front has a cylindrical shape (circular symmetry around the laser beam).

### 2.3.2 Pressure generation: laser constant $C_L$

The second factor quantifies the pressure generated from the deposited heat amplitude  $H$ . We name  $C_L$  the laser constant in  $\text{Pa}\cdot\text{W}^{-1}\cdot\text{cm}$  which is the maximal pressure amplitude generated in free space. Its value allows to determine the pressure we would obtain when removing an acoustic resonator for example. We compute its value analytically based on the deposited heat and use the non-approximated value of Equation 2.7. Its maximum is located on the laser axis and is represented in Figure 2.6. Its value depends on the modulation frequency and is linear with it.



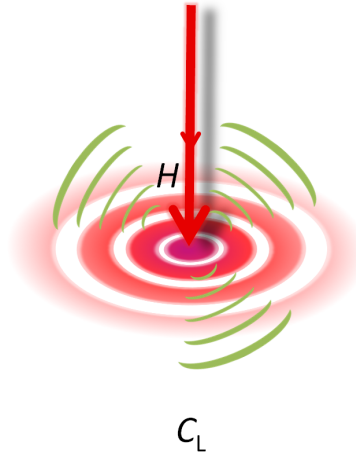


Figure 2.22: Illustration of the generated pressure amplitude  $C_L$  after a heat deposition  $H$ .

### 2.3.3 Pressure amplification and cell constant: amplification factor $A_s$

The third factor is the static amplification factor  $A_s$ . It is the unit-less ratio of the maximal pressure in space (amplified thanks to an acoustic resonance) to the maximal pressure created by the laser beam  $C_L$ . Static pressure amplification is realised by acoustic resonators in MPAS and CEPAS, and by the QTF prongs alone or by acoustic resonators in QEPAS, as shown in Figure 2.23. For the acoustic resonators used in MPAS and CEPAS we determine  $A_s$  analytically, while we use FEM simulations for QEPAS. The maximum value is taken by considering the pressure all over space, and is not necessarily the one experienced by the sensor.  $A_s$  accounts only for static, geometrical amplification of sound pressure. As a consequence when using FEM we immobilised the detector to avoid the modification of pressure while vibrating.

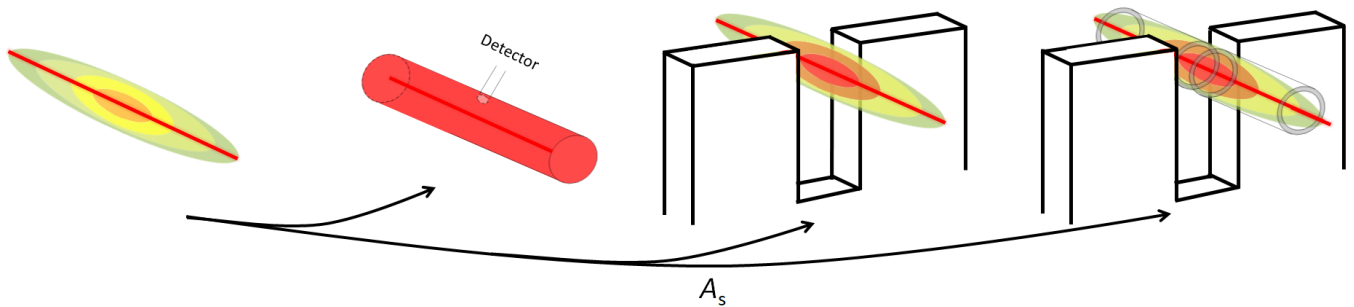


Figure 2.23: Illustration of the pressure amplification factor  $A_s$ . Pressure can be amplified by acoustic cells (left), by the resonance between a QTF prongs (middle) or by acoustic resonators (right).

In addition, we extend the definition of the cell constant presented before for MPAS (Section 2.1.3). The generalised acoustic cell constant in  $\text{Pa}\cdot\text{W}^{-1}\cdot\text{cm}$ , which can be applied to any photoacoustic technique, is defined as the product of the free space pressure and the static amplification factor:

$$C = C_L \times A_s. \quad (2.41)$$

A slight difference is that we take the maximum over space while in the previous definition the pressure was approximated to be homogeneous on the detector.

### 2.3.4 Acoustic-mechanic overlap $\eta_s$

The fourth factor is the static acoustic-mechanic overlap  $\eta_s$ , without unit. It represents the overlap of the acoustic mode on the detector as illustrated in Figure 2.24. We chose to normalise it compared to a homogeneous pressure of 1 Pa on one face of the detector. It can be computed by dividing the photoacoustic force by the photoacoustic force generated by 1 Pa on one face and by the maximal pressure as described in Equation 2.42.

$$\eta_s = \frac{F_{PA}}{F_{1Pa}} \times \frac{1}{HC_L A_s} \quad (2.42)$$

For example, if a pressure of 1 Pa is applied on one face of a traditional microphone (a circular membrane fixed to a support by its rim, one face oriented towards the environment while the other faces the back volume), we have  $\eta_s = 1$ . The maximal value of  $\eta_s$  is equal to the number of faces of the detector, considering that they are identical and face the same pressure source. For a microphone or a cantilever the maximum is 2, for a QTF the maximum is 4. Its value enables to derive the efficiency of the pressure overlap on the resonator and should depend on resonator geometry, frequency, etc. Also, we can analytically attribute the force contribution on the different faces.  $\eta_s$  can be computed analytically or by FEM to take into account pressure diffraction by the detector edges and resonances. To derive it from FEM, the photoacoustic force is extracted when the QTF is immobilised, to avoid the modification of the pressure field by the vibration.

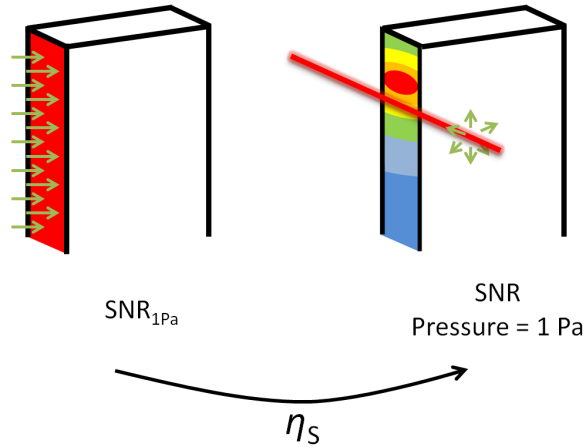


Figure 2.24: Illustration of the static acoustic-mechanic overlap  $\eta_s$ .

### 2.3.5 Vibroacoustic efficiency $\varepsilon_{va}$

The fifth factor is the vibroacoustic efficiency  $\varepsilon_{va}$ . Until now we considered analytically that applying a homogeneous pressure of 1 Pa on one face generates an equivalent force of amplitude  $F_{PA} = 1 \times S$  with  $S$  the face area. Nonetheless, we found that the detector modifies the acoustic field when vibrating. We determined by FEM that the equivalent force generated by a homogeneous pressure of 1 Pa on one face in vibroacoustics differs from what we derived analytically in static regime. This new factor enables to quantify the ratio of the modified force with the analytical one of  $F_{PA,static} = 1 \times S$  as given by Equation 2.43. We expect this factor to depend on the detector frequency, quality factor and geometry and will determine it by FEM.

$$\varepsilon_{va} = \frac{F_{PA,vibroacoustic}}{F_{PA,static}} \quad (2.43)$$

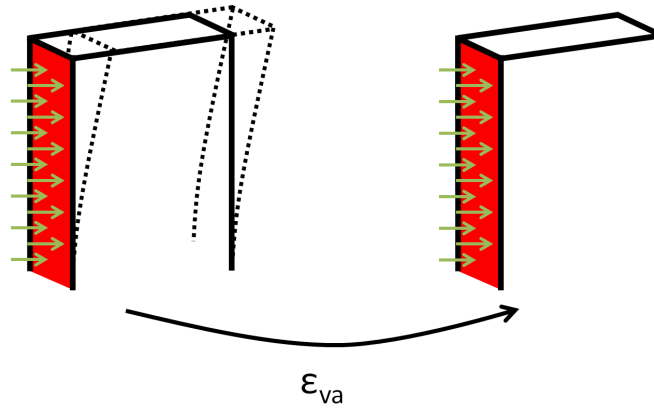


Figure 2.25: Illustration of the vibroacoustic efficiency  $\epsilon_{va}$ .

### 2.3.6 Normalised signal to noise ratio $\text{SNR}_{1\text{Pa}}$

The last factor of the model is the SNR per unit of pressure, i.e. the SNR normalised to 1 Pa on one detector face  $\text{SNR}_{1\text{Pa}}$  in  $\text{dB}\cdot\text{Pa}^{-1}$ , in the same way as what is done for commercial microphones. It is computed analytically by taking the ratio of the force equivalent to the 1 Pa pressure ( $F_{\text{PA}} = 1 \times S$ ) with the noise equivalent force. It depends on the frequency, quality factor, surface and mass by definition (see Section 2.1.4). This factor allows to compare the detectors with the best excitation possible. In this manuscript, we computed it over a bandwidth of 1/16 Hz as explained in Section 2.1.6.3.

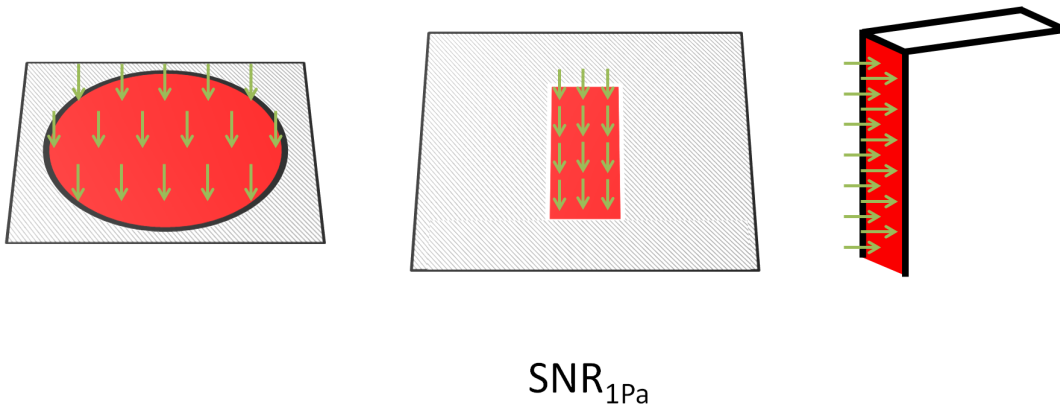


Figure 2.26: Illustration of the signal-to-noise ratio normalised for 1 Pa applied homogeneously on 1 face of the detector.

### 2.3.7 SNR

Ultimately, the sensor SNR (without unit) can be derived using the model factors. The SNR is the product of every factor we introduced, as written in Equation 2.44. The NNEA can be derived from this SNR identically to Equation 2.39.

$$\text{SNR} = H \times C_L \times A_s \times \eta_s \times \epsilon_{va} \times \text{SNR}_{1\text{Pa}} \quad (2.44)$$

## 2.4 Conclusion

In this chapter we presented the analytical and FEM description of a photoacoustic sensor using acoustic resonators, microphones, cantilevers or QTFs. The analytical model enables to describe and quantify the different physical phenomena occurring in a photoacoustic sensor: heat deposition, acoustic generation and detection, sensitivity, etc. The equations presented in this chapter were further implemented in a Python library so as to study the influence of parameters on the different systems.

In order to refine the analytical results we also presented the construction of finite element method simulations to describe photoacoustic sensors. Particularly, these simulations will be used to describe the effects of vibroacoustic interaction between the resonator and surrounding fluid as well as coupling between resonators.

These models will be used in the next chapters. In Chapter 3 their validity will be evaluated by experimental comparisons for different sensors we studied or from literature. In Chapter 4, our new unified modelling will be used for comparison between the different photoacoustic techniques.







## Chapter 3

# Comparison through experiments for representative cases

### Objectives:

This chapter aims at validating the analytical model described in Chapter 2, using representative photoacoustic experiments: MPAS, CEPAS and QEPAS reported in the literature, as well as Mirsense's MPAS sensor and ONERA's QEPAS sensors. This validation also enables to confirm and compare the sensitivities of the different photoacoustic techniques. We will also highlight the specific problem of coupling a tuning fork with an acoustic resonator and present our original approach to address this topic.

## 3.1 Study of typical MPAS and CEPAS setups

In this section we propose to study the case of microphone (MPAS) and cantilever (CEPAS) based photoacoustic sensors. These detectors are similar in many ways: they both are thin membranes generally used well below their resonance frequency, and they are often employed in pipe-like acoustic resonators with dimensions far superior to the detector itself.

We will first derive the SNR of these detectors alone and then estimate the sensitivity using different types of acoustic resonators.

### 3.1.1 Microphones and cantilevers analytical signal-to-noise ratio

#### 3.1.1.1 Determination of the SNR at 1 Pa of commercial microphones

We studied microphones used in the literature or in our experiments that are representative of the ones generally used in photoacoustics. These microphones can be divided into two categories: classical and MEMs microphones which are smaller as detailed in Table 3.1.

In order to compare these microphones, we determined  $SNR_{1Pa}$ , their signal-to-noise ratio for a uniform excitation of 1 Pa. This value can be found or derived from the datasheet, and is equal to the 94 dB standard pressure level (SPL), corresponding to 1Pa, minus the equivalent noise level also expressed in dB. To be able to use these values and compare them to experiments an additional computation must be made. Indeed, the microphone SNR and noise level are usually given over its entire frequency working range, i.e. several kHz, while in photoacoustics, the signal is detected with a lock-in amplifier selecting only a small frequency band. As a consequence, we derived the  $SNR_{1Pa}$  value in a reduced bandwidth. We chose a bandwidth of 1/16 Hz identical to the one we used for QTFs in order to directly compare those in Chapter 4. The detail of the computation is



given in Appendix B with the different microphones datasheets.

Among classical microphones, the BK4179 presents one of the highest  $SNR_{1Pa}$  of  $151 \text{ dB.Pa}^{-1}$ . We considered in the following that this microphone represents the state-of-the-art sensitivity for MPAS [54, 46]. However, this microphone is bulky and not compatible with the miniaturisation of photoacoustic sensors. In addition, the cost of such a microphone is high, reaching several thousand dollars. That is why MEMs microphones are used, presenting sizes down to a few millimeters and low costs, but much poorer  $SNR_{1Pa}$  reaching  $120 \text{ dB.Pa}^{-1}$  at best.

Type	Classical			MEMs		
Photograph						
Microphone Reference	UC-57 [161]	BK4179 [152]	Sennheiser KE4 [162]	SPU0409HD5H [163]	AKU143 [164]	EK 23024 [165]
Working range (Hz)	10 – 16k	20 – 20k	20 – 20k	100 – 10k	50 – 11.5k	100 – 10k
Membrane diameter (mm)	13	25	4	<1	<1	<1
Maximal size (mm)	100	100	15	4	4	5
Approximated price (\$)	>1k	>1k	100	1	1	20
$SNR_{1Pa}$ ( $\text{dB.Pa}^{-1}$ ) in 1/16 Hz	135	151	122	111	117	120

Table 3.1: Presentation of different microphones and their parameters. Microphones BK4179 and UC-57 are presented with their adapted electronic preamplifier.

The microphones we presented here are representative of the commercial offer for general acoustic applications. We do not expect to find microphones exhibiting significantly better  $SNR_{1Pa}$ . Generally, to increase this value one should increase the membrane size, explaining why the biggest microphones exhibit the best SNR. Nonetheless, at some point extending the membrane will inevitably cause the increase of other losses such as support losses. A compromise can usually be found between the different losses to increase the SNR [38, 166]. Microphones such as the BK4179 already use the largest membranes, of one inch diameter, partly explaining their performance.

It may be possible to design better microphones for photoacoustics by carefully choosing its resonance frequency and adapting its use to detection within a small bandwidth. This is essentially what was accomplished with the introduction of cantilevers in photoacoustic spectroscopy [64].

### 3.1.1.2 Determination of the SNR at 1 Pa of cantilevers

Concerning cantilevers we will refer to different cases from literature. In every case the displacement was detected optically. Cantilevers are made of stainless steel or Silicon with a gold coating facilitating detection of its movement and preventing a background signal due to laser absorption.

The first study case is the use of custom cantilevers (named A and B) that are presented in the CEPAS state-of-the-art literature [74, 167]. These cantilevers are rectangular Silicon beams a few millimeters long and large and a few  $\mu\text{m}$  thin. The second study case concerns a custom cantilever we name C, made of stainless steel. These cantilevers are presented in Table 3.2 with their geometrical parameters. The dimensions of cantilever A were not given in the article [74] so we took similar dimensions to the ones given in publications of the same research team [66, 167].

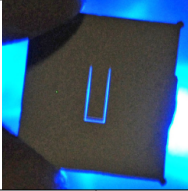

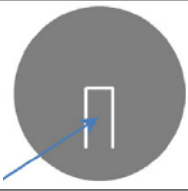
Cantilevers			
Photograph			
Cantilever Reference	A [74]	B [167]	C [76]
Working range (Hz)	10-550	10-715	1,408
Length (mm)	4	5	2.51
Width (mm)	2	1.2	1
Thickness ( $\mu\text{m}$ )	5	10	10
Material	Gold coated Silicon		Stainless steel

Table 3.2: Presentation of different cantilevers found across literature and their geometry.

In order to derive the cantilevers  $\text{SNR}_{1\text{Pa}}$  we will first determine their resonance frequency and quality factors at atmospheric pressure and ambient temperature. This is presented in Table 3.3 along with values reported in published experimental results.

Cantilever	A	B	C
Analytical $f_0$ (Hz)	381	518	1,253
Experimental $f_0$ (Hz)	550	715	1,408
$Q_{\text{thermo}}$	$7.7 \cdot 10^7$	$1.5 \cdot 10^7$	$2.3 \cdot 10^4$
$Q_{\text{viscous}}$	31	65	340
$Q_{\text{acoustic}}$	$3.2 \cdot 10^{10}$	$1.4 \cdot 10^{10}$	$1.2 \cdot 10^{10}$
Total analytical $Q$	31	65	340
Experimental $Q$	20*	30*	46.3
$\text{SNR}_{1\text{Pa}}$ ( $\text{dB} \cdot \text{Pa}^{-1}$ ) in 1/16 Hz	153	150	140

Table 3.3: Cantilevers analytical frequency and quality factor contributions at atmospheric conditions and comparison to experiment.\* Cantilever A quality factor is taken to be 20 as explained in this paragraph. \* Cantilever B experimental results were obtained at 350 mbar and 50° C.

There is a difference between analytical and experimental frequencies, representing a relative error of about 40% for cantilevers A and B, while it is lower for cantilever C, around 12%. This discrepancy may be due to silicon parameters that differ between model and experiment. Concerning the quality factors, we analytically derived the thermoelastic losses, as well as viscous and acoustic damping. We could not model support losses due to the lack of information, neither the gold layer thermoviscous effect on the cantilever. However, these losses should be negligible before the effect of viscous damping on the cantilever [66]. In any case, viscous damping is indeed limiting as a cantilever exhibits a large surface and a small mass.

For cantilever A the comparison to experiments is difficult as we do not know the exact dimensions of the cantilever. For cantilever B, we also observe major discrepancies. We derived a total quality factor of 30 from publication [167] at 350 mbar and 50° C, while our model predicts a value of 65. The difference is difficult to explain, as we did not have this object at disposal. It might be due to a poor description we made of the

used Silicon (doping, constraints, etching, ...). Concerning cantilever C, a large difference is observed which is difficult to understand.

To calculate the  $SNR_{1Pa}$ , we forced the quality factor and frequency values to the experimental ones in our analytical model. For cantilever A, as its total quality factor is not given we took a value of 20 which is representative of the value cantilever B would reach at atmospheric conditions.

Finally, based on these values we determined the cantilevers  $SNR_{1Pa}$  through analytical computation of their damping ratio and applied photoacoustic force (see Section 2.1.4). This value reaches around  $150 \text{ dB.Pa}^{-1}$  for A and B and  $140 \text{ dB.Pa}^{-1}$  for cantilever C. These values are similar to the one of the best commercial microphone.

### 3.1.2 Analytical cell constant and sensitivity using simple cylinder shaped resonators

After determining the detector  $SNR_{1Pa}$ , we will evaluate the second parameter, that is the amplification of the pressure applied onto the detector owing to an acoustic resonator. To this end, we will compute the cell constant of simple cylindrical resonators found in the literature and compare them to the reported values. The geometrical parameters of these cells are presented in Table 3.4 as well as the derived resonance frequency and quality factor under normal temperature and pressure conditions.

System Reference	Cell 1 [49]	Cell 2 [49]	Cell 3 [54]	Cell 4 [54]	Cell 5 [168]	Cell 6 [74]	Cell 7 [167]	Cell 8 [76]
Cell geometry								
Length $L_c$ (mm)	170	170	100	100	150	100	95	120
Radius $R_c$ (mm)	6	3	3	2	7.5	1.5	2	4
Detector	-	-	EK23024	BK4179		cant. A	cant. B	cant. C
Resonance characteristics								
$f_0$ (Hz)	1,000	1,000	1,700	1,700	1,133	1,700	1,790	1,417
Quality factor $Q_{ac}$	60	30	39	26	78	20	27	47
Photoacoustic response								
Cell constant $C$ ( $\text{Pa.W}^{-1}.\text{cm}$ )	3,351	6,777	5,157	7,785	2,495	10,413	7,583	4,228
NNEA ( $\text{W.cm}^{-1}.\text{Hz}^{-1/2}$ )	-	-	$7.8 \cdot 10^{-10}$	$1.4 \cdot 10^{-11}$	$4.5 \cdot 10^{-11}$	$8.6 \cdot 10^{-12}$	$1.7 \cdot 10^{-11}$	$9.5 \cdot 10^{-11}$

Table 3.4: Analytical study of different cylindrical acoustic resonators taken from the literature.

As presented in Chapter 2 the cell pressure amplification can be approximated from their dimensions, frequency and quality factor. We evaluated the cell constant  $C$  using Equation 3.1 and presented the results in the previous table.

$$C = \frac{(\gamma - 1)L_c Q}{\omega_0 V_c}, \quad (3.1)$$

The cells found in the literature present cell constants of a few thousands  $\text{Pa.W}^{-1}.\text{cm}$ , enabling huge amplification of the photoacoustic pressure. Pressure amplification is higher for cells presenting a long length and a small diameter as discussed before (Section 2.1.3). Nonetheless, these cells are usually not longer than 10 cm and their radius not smaller than 2 mm in order for the laser to pass without touching the cell walls.

The NNEA can be computed from the cell constant and the detector  $\text{SNR}_{1\text{Pa}}$ . For that purpose we consider two assumptions, being the fact that the detector presence (cantilever or microphone) does not modify the cell resonance mode and that the pressure field is homogeneous on the surface used for detection. These assumptions are supported by the fact that microphones and cantilevers are usually used below their resonance frequency, reducing their displacement, and by the fact that their dimensions are small before the acoustic cell ones, making the pressure homogeneous on the detector. Finally, we can derive the NNEA as follows, taking the microphone  $\text{SNR}_{1\text{Pa}}$  in linear scale:

$$\text{NNEA} = \frac{1}{\text{SNR}_{1\text{Pa}} C \sqrt{\Delta f}}. \quad (3.2)$$

Results are presented in Table 3.4. The computed NNEA range from  $10^{-10}$  to  $10^{-12} \text{W.cm}^{-1}.\text{Hz}^{-1/2}$  and we can see the importance of having a large cell constant and a high detector  $\text{SNR}_{1\text{Pa}}$  to reach the ultimate sensitivity.

### 3.1.3 Comparison to experimental results

To validate that we can model the pressure amplification by resonators and the detector  $\text{SNR}_{1\text{Pa}}$  we chose several examples from the literature enabling its computation. In this section we will give the parameters of interest reported through the literature and the parameters we derived. We will compare both the cell constants and evaluate the NNEA of the given sensors with their detectors. As there are slight differences between MPAS and CEPAS sensors we will treat these cases separately.

#### 3.1.3.1 MPAS sensors from the literature

Concerning MPAS, we chose a few publications from Besson [49] and Bijnen et al. [54]. Unfortunately, we did not find other publications with enough details enabling us to derive the cell constant and the NNEA. In many cases, crucial data are not given such as the microphone model, signal amplification, lock-in bandwidth, noise, etc. leading to major discrepancies or impossibility to derive the parameters of interest. Nonetheless, the following examples presented enough details and are representative of other setups found in the literature.

From these publications we extracted or derived the different values of interest concerning the laser and gas parameters, resonance characteristics and photoacoustic response, presented in Table 3.5. When it was not given we computed the cell constant as follows:

$$C = \frac{S}{R_M H}, \quad (3.3)$$

with  $S$  the photoacoustic signal in mV and  $R_M$  the microphone sensitivity in  $\text{mV.Pa}^{-1}$ .

We also derived the microphone  $\text{SNR}_{1\text{Pa}}$  based on its sensitivity, reported noise values and computed the resulting NNEA.

System Reference	Cell 1 [49]	Cell 2 [169]	Cell 3 [54]	Cell 4 [54]	Cell 5 [168]
Setup					
Gas	CH <sub>4</sub>		C <sub>2</sub> H <sub>4</sub>		CH <sub>4</sub>
Concentration	5,000 ppmv		1.2 ppmv		1 ppbv
Absorption (cm <sup>-1</sup> )	2.22 10 <sup>-3</sup>		5 10 <sup>-5</sup>		3 10 <sup>-9</sup>
Laser power (mW)	20		2,000		2,000
Heat amplitude $H$ (W.cm <sup>-1</sup> )	2.22 10 <sup>-5</sup>		5 10 <sup>-5</sup>		3 10 <sup>-9</sup>
Resonator geometry					
$L_c$ (mm)	170	170	100	100	150
$R_c$ (mm)	6	3	3	2	7.5
Resonance characteristics					
$f_0$ (Hz)	964	974	1,650	950	1,030
Quality factor $Q$	54	28	30	12	40
Experimental photoacoustic response					
Signal (mV)	-		6.6	150	6 10 <sup>-3</sup>
Noise density ( $\mu\text{Vrms.Hz}^{-1/2}$ )	-		0.04	0.2	2
Noise equivalent bandwidth (Hz)	-		1/16		
SNR	-		6.6 10 <sup>5</sup>	3 10 <sup>6</sup>	12
Cell constant $C$ (Pa.W <sup>-1</sup> .cm)	6,552	13,232	6,000	3,000	2,000
Microphone	-		EK23024	BK4179	
Microphone sensitivity (mV.Pa <sup>-1</sup> )	10		22	1,000	1,000
Microphone SNR <sub>1Pa</sub> (dB.Pa <sup>-1</sup> )	-		127	146	126
NNEA (W.cm <sup>-1</sup> .Hz <sup>-1/2</sup> )	-		3 10 <sup>-10</sup>	6.7 10 <sup>-11</sup>	1 10 <sup>-9</sup>
Analytical values for comparison					
Cell constant $C$ (Pa.W <sup>-1</sup> .cm)	3,351	6,777	5,157	7,785	2,495
Microphone SNR <sub>1Pa</sub> (dB.Pa <sup>-1</sup> )	-		120	151	151
Analytical NNEA (W.cm <sup>-1</sup> .Hz <sup>-1/2</sup> )	-		7.8 10 <sup>-10</sup>	1.4 10 <sup>-11</sup>	4.5 10 <sup>-11</sup>

Table 3.5: Experimental results on the use of cylindrical acoustic resonators with microphones and analytical comparison.

A good agreement is found between experimental and analytical results for the resonance frequency and the quality factor. The remaining discrepancies come from environmental differences. Indeed, for analytical calculations, we used normal atmospheric conditions whereas the experimental results were obtained for different gases, pressures and temperatures. Another significant discrepancy comes from the detector presence. Indeed, the microphone is connected to the main cylinder by another smaller one constituting an additional volume, modifying the frequency and quality factor. In addition, the microphone itself constitutes a volume which is not negligible (400 mm<sup>3</sup> for BK4179 at 250 Hz for example) and that should be modelled in FEM simulations. The influence of additional volumes has been studied in [54], explaining why the resonance frequency of Cell 4 is lower than for Cell 3 despite similar geometries.

A good agreement is also generally obtained concerning the cell constants with a relative error around 20% for cells 3 and 5. The cell constant of Cells 1,2 are somewhat twice better than the analytical ones, however we cannot explain the discrepancy as there are not enough details in the publication. For Cell 4, the cell constant is twice smaller than the analytical one which might come from the additional volume introduced by the microphone which also may have modified the mode of resonance.

Concerning the microphones  $SNR_{1Pa}$ , discrepancies between theory and experiments are also observed. Microphone EK23024 exhibits a  $SNR_{1Pa}$  7 dB increased while BK4179 presents a 5 dB decreased one. While we approximated the noise to be white over the entire microphone working range, it is not the case in reality, which may explain the difference. Another possible explanation is the modification of the microphone response when used in a gas. Indeed, the microphone signal for 1 Pa is given in the datasheets for given conditions such as atmospheric pressure and temperature and 50% relative humidity. Using the microphone in other conditions can modify its response [170, 171]. To tackle this issue the microphone response should be characterised in the experimental conditions by exciting it with a 1 Pa acoustic pressure (using a pistonphone for example). Another major discrepancy is found: for BK4179 two different values were computed, 126 and 146  $dB.Pa^{-1}$  compared to the 151  $dB.Pa^{-1}$  we derived from datasheets. The publications from Bijnen et al. [54, 168] demonstrated that the microphone intrinsic noise floor was not reached for Cell 5 because an important acoustic background from the laboratory was present, degrading its sensitivity of a factor 10 compared to Cell 4. This demonstrates that working with low noise microphones increases the impact of fluctuating acoustic backgrounds, and that the most of the sensitivity is not always taken.

The addition of these discrepancies on both parameters lead to the ones observed on the NNEA, with a factor 3 for Cell 3 and 5 for Cell 4.

These differences partly come from the fact that we exploited systems from the literature. In order to refine our analytical model we would need more details on the photoacoustic setups, such as the microphone noise spectrum (which is usually given for more recent microphones) and know which noise is limiting. Moreover, if we knew the exact setups geometries, we would be able to use finite element simulations and may find a better agreement with experimental cell constants.

### 3.1.3.2 CEPAS sensors from the literature

For CEPAS sensors we first studied two similar setups presenting state-of-the-art sensitivities (Table 3.6) [74, 167]. The cantilevers are positioned in the middle of an acoustic cell and both the cantilever and the cell are used below their resonance frequency. We studied yet another setup [76] for which both the cantilever and the cell are resonant and coupled at the same frequency.

The fact that the cantilever is not used at its resonance in Cell 6 and 7 does not affect its SNR. Indeed, both the signal and the noise are amplified by the cantilever transfer function. If we consider that the limiting noise is the cantilever Brownian noise, the SNR thus remains constant. Nonetheless, outside of the cantilever resonance the dominating noise can come from other sources such as the electronic noise. For example, Adamson et al. [172] observed a SNR twice lower when working below the AFM cantilever resonance frequency.

On the contrary, the fact that cells 6 and 7 are not used at their resonance frequency does reduce acoustic amplification. We computed their resonance around 1,700 Hz but they were used at 10 Hz and 140 Hz respectively. This is what is usually called "non resonant mode". In such a mode of operation, the pressure amplitude inside the resonator oscillates at the modulation frequency [21] and we can estimate the pressure by considering the quality factor to be equal to unity [21, 171]. The analytical cell constants we computed previously (Table 3.4) then have to be divided by the analytical quality factor passing from 10,413 and 7,583 to 521 and 281  $Pa.W^{-1}.cm$ . Despite presenting a reduction of the pressure of about 20, this configuration allows for performing FTIR analysis in parallel according to the authors [74, 167]. The resulting NNEA reach

$1.7 \cdot 10^{-10} \text{ W.cm}^{-1}.\text{Hz}^{-1/2}$  and  $4.5 \cdot 10^{-10} \text{ W.cm}^{-1}.\text{Hz}^{-1/2}$  which is in good agreement with the reported values.

System Reference	Cell 6 [74]	Cell 7 [167]	Cell 8 [76]
Setup			
Gas	CO <sub>2</sub>	CH <sub>2</sub> O	C <sub>2</sub> H <sub>2</sub>
Concentration	1.9 ppmv	1.3 ppbv	169 pptv
Absorption (cm <sup>-1</sup> )	3.6 · 10 <sup>-9</sup>	1.32 · 10 <sup>-8</sup>	9.5 · 10 <sup>-11</sup>
Laser power (mW)	30	47	1,000
Heat amplitude $H$ (W.cm <sup>-1</sup> )	1.1 · 10 <sup>-10</sup>	6.2 · 10 <sup>-10</sup>	9.5 · 10 <sup>-11</sup>
Resonator geometry			
$L_c$ (mm)	100	95	120
$R_c$ (mm)	1.5	2	4
Resonance characteristics			
$f_0$ (Hz)	-	-	1,408
Quality factor $Q$	-	-	46.3
Experimental photoacoustic response			
Noise equivalent bandwidth (Hz)	0.38	1	0.05
SNR	1	3	1
Cell constant $C$ (Pa.W <sup>-1</sup> .cm)	-	-	2,684
Cantilever	A	B	C
Cantilever sensitivity (nm.Pa <sup>-1</sup> )	-		2,224
Cantilever SNR <sub>1Pa</sub> (dB.Pa <sup>-1</sup> )	-		131
NNEA (W.cm <sup>-1</sup> .Hz <sup>-1/2</sup> )	1.7 · 10 <sup>-10</sup>	2.1 · 10 <sup>-10</sup>	4.2 · 10 <sup>-10</sup>
Analytical values for comparison			
Cell constant $C$ (Pa.W <sup>-1</sup> .cm)	521	281	4,228
Cantilever SNR <sub>1Pa</sub> (dB.Pa <sup>-1</sup> )	153	150	140
NNEA (W.cm <sup>-1</sup> .Hz <sup>-1/2</sup> )	1.7 · 10 <sup>-10</sup>	4.5 · 10 <sup>-10</sup>	9.5 · 10 <sup>-11</sup>

Table 3.6: Experimental results on the use of cylindrical acoustic resonators with cantilevers.

Another possibility is to use both the cantilever and the cell at their resonance. This is what was reported in [76] by coupling a stainless steel cantilever with a cylindrical acoustic resonator. From this publication we derived a cell constant of 2,684 Pa.W<sup>-1</sup>.cm which is twice smaller than the analytical value we computed. Also, the cantilever SNR<sub>1Pa</sub> is 9 dB lower. Whereas no clear evidence is shown in the article, the two resonators must be coupled, affecting both the cantilever quality factor, hence its SNR, and the acoustic pressure inside the acoustic resonator, possibly explaining the observed discrepancies. The reported NNEA reaches  $4.2 \cdot 10^{-10} \text{ W.cm}^{-1}.\text{Hz}^{-1/2}$ , which is only two times the state-of-the-art value, showing the interest in the use of resonant systems.

### 3.1.4 Study of differential MPAS setups

#### 3.1.4.1 Study cases parameters

After validating that we could correctly evaluate the performance of simple cylindrical resonators, we performed the same study with differential acoustic resonators. Differential resonators provide significant cancellation of background noise, a known limit to the sensitivity of single resonators, using an anti-symmetrical resonance mode of the cell.

We selected a few representative examples from the literature. Among them, the Cell<sub>diff</sub> 1 setup demonstrated the state-of-the-art NNEA for MPAS sensors. The Cell<sub>diff</sub> 2 setup is similar in all respects except for the geometry and the microphone. Finally, we present the cell used in the first version of Mirsense products, which we characterised experimentally. The geometrical parameters of these cells are given in Table 3.7.

System Reference	Cell <sub>diff</sub> 1 [46]	Cell <sub>diff</sub> 2 [173]	Mirsense cell This work
Cell geometry			
Chamber length $L_{cha}$ (mm)	100	50	20
Chamber radius $R_{cha}$ (mm)	5	15x10	0.375
Capillary length $L_{cap}$ (mm)	100	50	20
Capillary radius $R_{cap}$ (mm)	2	2	0.375
Effective volume $V_{eff}$ (m <sup>3</sup> )	$3.9 \cdot 10^{-6}$	$3.7 \cdot 10^{-6}$	$4.4 \cdot 10^{-9}$

Table 3.7: Differential acoustic resonators cases to study. Cell<sub>diff</sub> 2 chamber is not cylindrical but has a rectangular section which we indicated.

#### 3.1.4.2 Analytical cell constant and sensitivity

Constants of differential cells can be estimated analytically in the same way as those of simple cylinder shaped resonators. The main differences lie in the computation of the cell resonance frequency and effective volume as explained in the analytical model description (cf. Section 2.1.3). To avoid discrepancies we used the experimental frequency and quality factor in our model which we indicated in the table.

The determined cell constant is higher for cells presenting a smaller volume such as Mirsense's cell. The one of Cell 2 is approximately twice smaller than for Cell 1 which mainly comes from a twice smaller length. These constants are in the order of a few thousands Pa.W<sup>-1</sup>.cm which is typical of the photoacoustic cells presented in the literature as seen in the previous section. The value calculated for Mirsense's cell is much higher, reaching 45,690, which seems too high compared to equivalent cells [174]. For such small cells, the analytical model is not sufficient anymore and one should rely on FEM as we will show later through experiments in Section 3.1.4.3.



System Reference	Cell <sub>diff</sub> 1 [46]	Cell <sub>diff</sub> 2 [173]	Mirsense cell This work
Cell resonance experimental characteristics			
$f_0$ (Hz)	320	589	3,800
Quality factor $Q_{ac}$	6.5	9.5	6
Pressure amplification			
Cell constant $C$ (Pa.W <sup>-1</sup> .cm)	3,293	1,388	45,690 *
Detector			
Microphone	BK4179	UC-57	AKU143
SNR <sub>1Pa</sub> (dB.Pa <sup>-1</sup> )	151	135	117
Sensitivity			
NNEA (W.cm <sup>-1</sup> .Hz <sup>-1/2</sup> )	2.4 10 <sup>-11</sup>	3.6 10 <sup>-10</sup>	8.74 10 <sup>-11</sup>

Table 3.8: Analytical determination of differential resonators cell constants and sensitivities. The frequency and quality factor are taken from experiments to obtain a better sensitivity agreement. \* We will see later that for small cells such as Mirsense's, our analytical model is not valid anymore.

Finally, based on these analytical cell constants and on the microphones SNR<sub>1Pa</sub>, we compute the sensor NNEA using Equation 3.4. The factor  $\sqrt{2}$  in the denominator is an approximation to take into account the differential measurement. It was demonstrated in [175] that the SNR is increased with the squared root of the microphone number.

$$NNEA = \frac{1}{\sqrt{2} SNR_{1Pa} C \sqrt{\Delta f}} \quad (3.4)$$

For the three cells we obtained a NNEA in the range from 10<sup>-10</sup> to 10<sup>-11</sup> W.cm<sup>-1</sup>.Hz<sup>-1/2</sup> which is similar to what we obtained previously for simple cylindrical cells.

### 3.1.4.3 Comparison to experimental results

In order to validate the analytical results we will compare them to experiments.

#### In the literature

For the first two cells we summed up the parameters found in the literature or that we derived in Table 3.9.

Compared to the cylindrical resonators studied before, these differential cells present similar geometries and are also used at resonance, however they present smaller quality factors around 10. This smaller quality factor could be attributed to the bigger surface of the resonator (two chambers and capillaries) as suggested by Equation 2.16.

It should be noted that we computed the cell constants differently from what is generally done in the literature [46]. Indeed, the sensitivity is generally taken as the one of a single microphone which is equivalent to say that one microphone sees the differential pressure (and the other one nothing) which is not representative of the system. In these resonators, the pressure amplitude oscillates between the two chambers in time and is measured by two microphones. To describe this system physics, we introduced a factor 2 at the denominator, leading to compute the cell constant as:

$$C = \frac{S_{\text{diff}}}{2R_M H}, \quad (3.5)$$

with  $S_{\text{diff}}$  the differential signal in mV and  $R_M$  the sensitivity of one microphone in  $\text{mV.Pa}^{-1}$ . The introduced factor 2 is a good approximation, considering that the pressure is equivalent in both chambers (generally true when the quality factor is high) and that both microphones have the same sensitivity. In practice, the sensitivity of both microphones should be measured (using a pistonphone for example), as well as the ratio of the differential signal compared to the signal of one microphone.

System Reference	Cell <sub>diff</sub> 1 [46]	Cell <sub>diff</sub> 2 [173]
Setup		
Gas	CH <sub>4</sub>	CH <sub>4</sub>
Concentration	0.3 ppmv	0.37 ppmv
Absorption ( $\text{cm}^{-1}$ )	$1.2 \cdot 10^{-7}$	$1.76 \cdot 10^{-6}$
Relaxation time ( $\mu\text{s}$ )	-	-
Laser power (mW)	4	5
Heat amplitude H ( $\text{W.cm}^{-1}$ )	$2.4 \cdot 10^{-10}$	$4.4 \cdot 10^{-9}$
Resonance characteristics		
$f_0$ (Hz)	320	589
Quality factor Q	6.5	9.5
Photoacoustic response		
Signal ( $\mu\text{V}$ )	0.17	0.46
Noise density ( $\mu\text{Vrms.Hz}^{-1/2}$ )	0.17	0.46
Noise equivalent bandwidth (Hz)	1	1
SNR	1	1
Cell constant $C$ ( $\text{Pa.W}^{-1}.\text{cm}$ )	3,542	620
Microphone sensitivity ( $\text{mV.Pa}^{-1}$ )	100	84
Exp. Microphone $\text{SNR}_{1\text{Pa}}$ ( $\text{dB.Pa}^{-1}$ )	127	117
Exp. NNEA ( $\text{W.cm}^{-1}.\text{Hz}^{-1/2}$ )	$2.4 \cdot 10^{-10}$	$4.4 \cdot 10^{-9}$
Analytical values for comparison		
Cell constant $C$ ( $\text{Pa.W}^{-1}.\text{cm}$ )	3,293	1,388
Microphone $\text{SNR}_{1\text{Pa}}$ ( $\text{dB.Pa}^{-1}$ )	151	135
NNEA ( $\text{W.cm}^{-1}.\text{Hz}^{-1/2}$ )	$2.4 \cdot 10^{-11}$	$3.6 \cdot 10^{-10}$

Table 3.9: Experimental results on the use of differential acoustic resonators from literature.

We derived cell constants of  $3,542 \text{ Pa.W}^{-1}.\text{cm}$  for Cell<sub>diff</sub> 1 and  $620 \text{ Pa.W}^{-1}.\text{cm}$  Cell<sub>diff</sub> 2. We thus obtain a good agreement with our analytical model for Cell<sub>diff</sub> 1 while a discrepancy of a factor two is found for Cell<sub>diff</sub> 2.

Both microphone  $\text{SNR}_{1\text{Pa}}$  do not correspond to analytical values with a missing factor 16 for the first cell and 8 for the second. This is very probably due to acoustic background noise coming from the laboratory

[168]. This high external noise therefore impacts the overall NNEA, reaching  $2.4 \cdot 10^{-10} \text{ W.cm}^{-1}.\text{Hz}^{-1/2}$  and  $4.4 \cdot 10^{-9} \text{ W.cm}^{-1}.\text{Hz}^{-1/2}$ . As these papers aim was to perform gas measurements, the microphones ultimate  $\text{SNR}_{1\text{Pa}}$  were not reached. We thus expect the NNEA to reach  $2.4 \cdot 10^{-11} \text{ W.cm}^{-1}.\text{Hz}^{-1/2}$  in [46] with careful isolation to background noise.

## Study of Mirsense’s differential cell

### Setup

To measure the cell performance we used parts of a Mirsense commercial photoacoustic sensor. Laser control and signal processing are entirely handled by Mirsense electronics and further controlled by us on a computer interface.

We used a Mirsense DFB QCL emitting around  $1,745 \text{ cm}^{-1}$  at  $30 \text{ }^\circ\text{C}$ . It was operated in CW rather than pulsed mode in order to facilitate result interpretation (avoiding wavelength chirp due to transient heating). As a consequence this laser produced significant heat and so the chip was placed on a Copper baseplate and contacted with thermal grease. The baseplate temperature was monitored with a thermistor and cooling was done with a Peltier element controlled by Mirsense electronics. The laser beam was focused using two lenses of focal lengths  $0.7 \text{ mm}$  and  $100 \text{ mm}$  as shown in Figure 3.1. The laser chip output divergence was simulated by Mirsense engineers enabling us to compute the laser waist  $w_L$  of  $775 \text{ }\mu\text{m}$  horizontally and  $175 \text{ }\mu\text{m}$  vertically. The laser divergence is very important and is more so in one direction compared to the other, due to the small size of the laser output and its rectangular section (this is classical when using semiconductor lasers such as laser diodes).

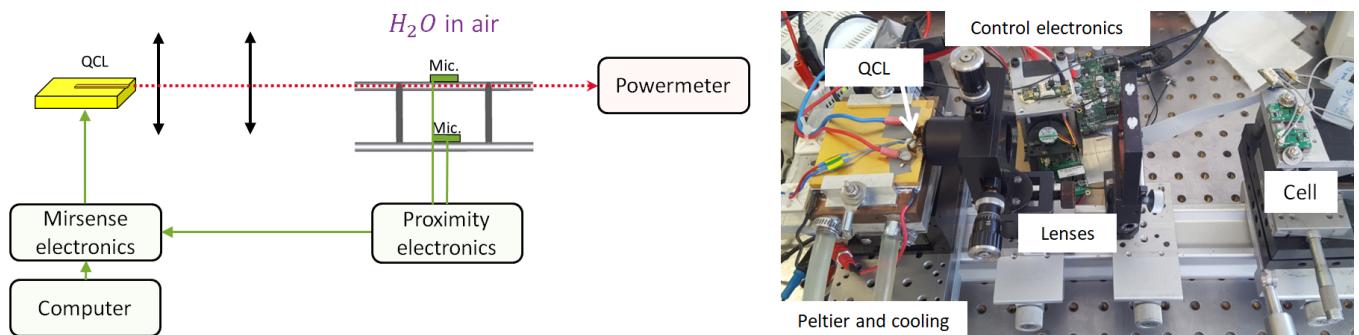


Figure 3.1: Photoacoustic measurement setup for Mirsense cell characterisation.

The laser beam was focused in the middle of the photoacoustic differential cell chamber. The power entering the cell was measured to be  $26 \text{ mW}$ , while the cell output power was  $3.8 \text{ mW}$  for a laser temperature of  $32 \text{ }^\circ\text{C}$ . Part of this power does not enter the cell as the laser beam diameter is larger than the cell window. Another part of this power is absorbed by the cell walls, but this effect is very hard to quantify. Yet another part is directly absorbed by the target gas along the laser beam pathway.

### Target gas

We targeted water vapor in ambient air in the range of the QCL emission (around  $1,745 \text{ cm}^{-1}$ ) by modifying the Peltier temperature. The ambient air concentration was determined using a hygrometer (Testo-608-H-1) giving us the relative humidity and temperature at atmospheric pressure. We measured a relative humidity of

36% at a room temperature of 23 °C, from which we derived a concentration of 10,120 ppmv of water vapor, which is a typical value. For this concentration we computed the absorption spectrum, using HITRAN database [130], as shown in Figure 3.2 and found an absorption of  $6.64 \cdot 10^{-3} \text{ cm}^{-1}$  for the peak at  $1,744.6 \text{ cm}^{-1}$ .

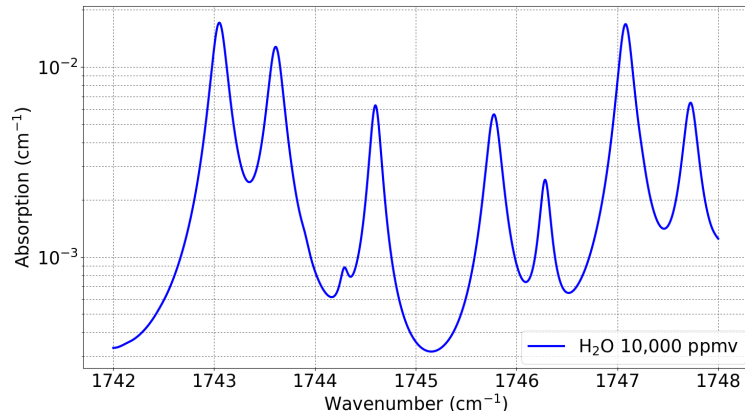


Figure 3.2: Absorption spectrum of the targeted gases over the QCL emission range.

### Photoacoustic measurement

To generate the photoacoustic signal we modulated the laser current to modulate its wavelength following a sine law. The modulation depth was adapted to the absorption linewidth by maximising the photoacoustic signal amplitude. The photoacoustic signal was measured with two MEMs microphones AKU143 [164], presenting a sensitivity  $R_M$  of  $7.94 \text{ mV.Pa}^{-1}$ . This signal was amplified a hundredfold and was processed by Mirsense electronics in which lock-in amplifiers are implemented.

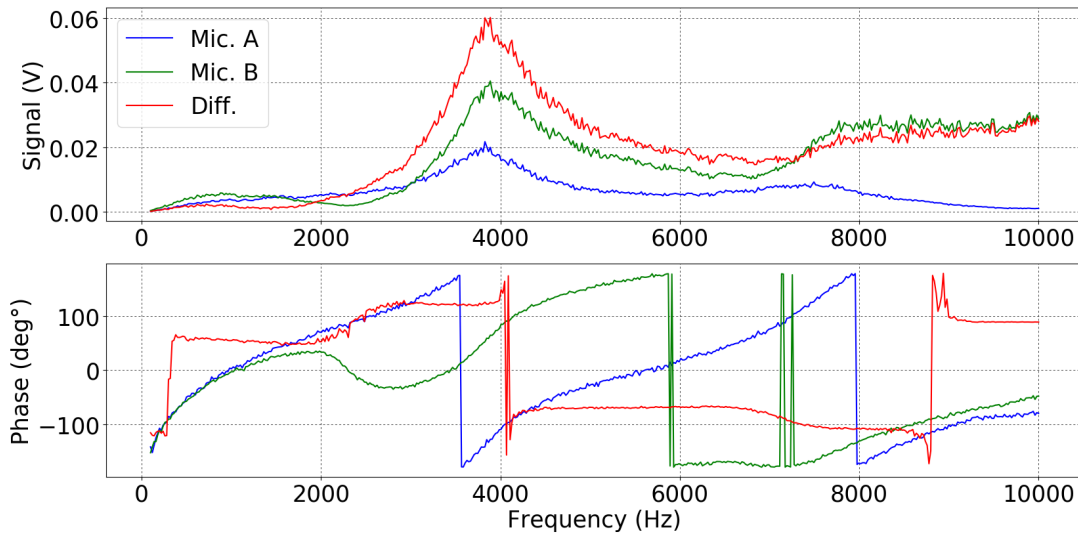


Figure 3.3: Experimental Mirsense's cell resonance obtained in WM. The signal amplitude was not optimised.

We first characterised the differential acoustic resonator response by varying the modulation frequency. Several resonance modes can be observed as shown in Figure 3.3. There is a weak mode below 2 kHz which is common to the two microphones and due to the gas circuit. The fundamental resonance occurs at 3,800 Hz with a quality factor of 5.7 and is attributed to the anti-symmetrical mode of interest. Another mode is present around 8,000 which can be attributed to a harmonic of the fundamental mode.

Concerning the mode of interest, the signals from the two microphones are not equal. Afterwards we found the cause to be the plugging of one of the capillaries due to the cell machining. Also, we observed that the resonance from each microphone does not occur at the same frequency which could be attributed to the low quality factor of the cell. Finally, the differential signal is maximal at 3,800 Hz, along with a shift of the phase. The phase values are somewhat shifted compared to the amplitude maxima which may be attributed to cell plugging.

Wavelength modulation (WM) was set to 3,800 Hz and the photoacoustic signal was optimised. We then scanned the water vapor absorption spectrum by tuning the laser temperature, and obtained the differential signal presented in red in Figure 3.4.

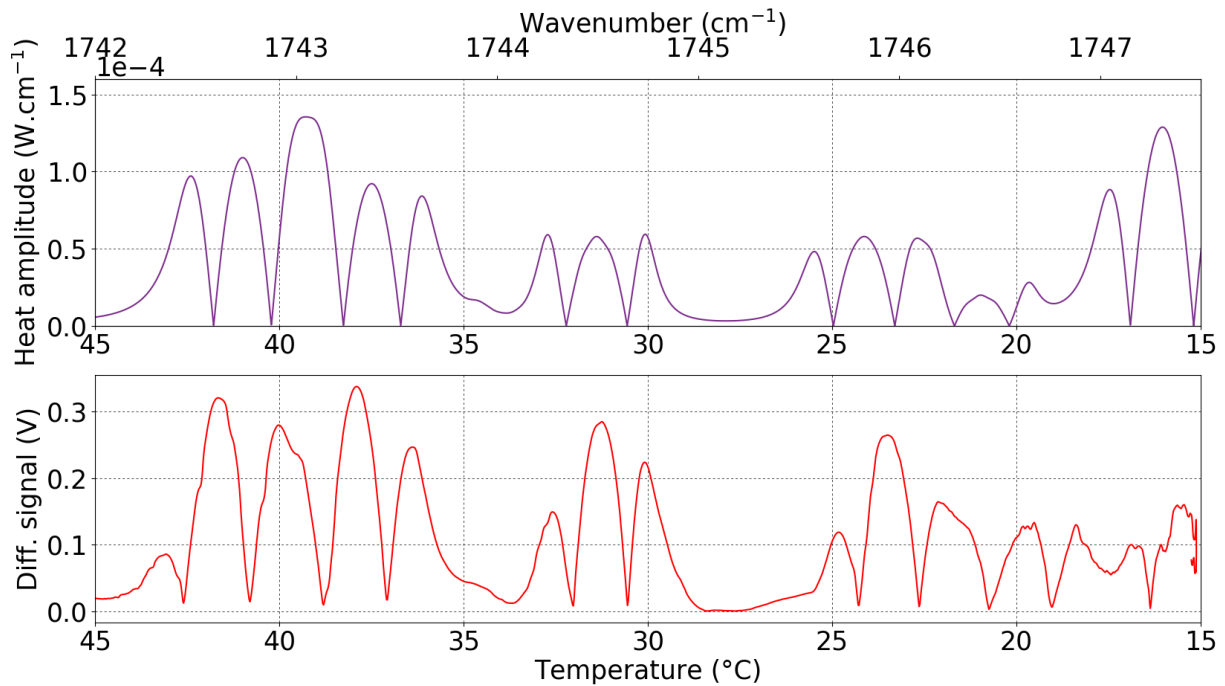


Figure 3.4: Analytical heat amplitude in the QCL emission range in WM modulation (top). Experimental water vapor spectrum using Mirsense's cell (bottom).

We observed several absorption peaks of water vapor, making the analysis more complicated in WM. To facilitate the analysis, we computed the analytical generated heat amplitude (shown in purple) based on the gas absorption spectrum (Figure 3.2). To better compare these spectra we corrected the heat amplitude by the laser power which is modified with temperature. Thanks to this computation we could easily determine the laser emission wavelength, corresponding to  $1744.6 \text{ cm}^{-1}$  at  $32 \text{ }^\circ\text{C}$  for example.

However, several discrepancies can be observed. Firstly, the signal below  $20 \text{ }^\circ\text{C}$  seems to be noisy and the peak does not appear. This was caused by direct absorption due to the elevated water concentration and elevated laser power at low temperature. Secondly, the peaks are not centered exactly at the same temperature as what we computed. This effect is caused by the temperature measurement, the thermistor was placed at a few millimeters from the laser and the cooling element was bulk, provoking a thermal latency during the scan. Thirdly, the amplitude of the peaks beyond  $35 \text{ }^\circ\text{C}$  should be higher than the others, which is not the case. We might have overestimated the laser power because of the poor precision of our laser power characterisation with temperature. Another very likely explanation is the non adaptation of the modulation depth during the scan, causing signal dropouts. The last discrepancy is the uneven amplitude of the side lobes compared to computations. We expect this effect to come from the laser power asymmetry with the temperature or from thermal effects.

Despite the slight discrepancies we observed when scanning the temperature, we could determine the cell performances using the absorption line at  $1,746.44 \text{ cm}^{-1}$ . For this point we summed up the experimental results in Table 3.10. We considered that gas relaxation rate did not impact the measurement which is a good approximation given the cell low resonance frequency.

System	Mirsense cell
Setup	
Gas	H <sub>2</sub> O
Concentration	10,120 ppmv
Absorption ( $\text{cm}^{-1}$ )	$6.64 \cdot 10^{-3}$
Laser power (mW)	26
Heat amplitude $H$ ( $\text{W}\cdot\text{cm}^{-1}$ )	$5.8 \cdot 10^{-5}$
Resonance characteristics	
$f_0$ (Hz)	3,800
Quality factor $Q$	5.7
Photoacoustic response	
Signal (V)	0.28
Noise density ( $\mu\text{Vrms}\cdot\text{Hz}^{-1/2}$ )	8
Noise equivalent bandwidth (Hz)	0.39
SNR	56,164
Cell constant $C$ ( $\text{Pa}\cdot\text{W}^{-1}\cdot\text{cm}$ )	3,040
Microphone sensitivity ( $\text{mV}\cdot\text{Pa}^{-1}$ )	794
Exp. Microphone $\text{SNR}_{1\text{Pa}}$ ( $\text{dB}\cdot\text{Pa}^{-1}$ )	116
Exp. NNEA ( $\text{W}\cdot\text{cm}^{-1}\cdot\text{Hz}^{-1/2}$ )	$1.6 \cdot 10^{-9}$

Table 3.10: Experimental results obtained with Mirsense's cell and a Mirsense QCL for measurements of water vapor in ambient air.

We derived a cell constant  $C$  of  $3,040 \text{ Pa}\cdot\text{W}^{-1}\cdot\text{cm}$  which is similar to the values for bigger cells from literature [46]. Nonetheless, there is a huge difference with the value we derived analytically of  $45,690 \text{ Pa}\cdot\text{W}^{-1}$ . Indeed, for such small cells the analytical model is not valid anymore (low quality factor, need for more precision for cell description). In addition, microphones equivalent volume should be considered as it is significant compared to the cell total volume, modifying the cell frequency, quality factor and cell constant. When analysing such cells one should rely on FEM models, nonetheless necessitating a high level of precision when describing the cell and microphone geometries, causing very important simulation time instead. We tried to simulate Mirsense's cell constant with Comsol thermoviscous module [160], but the high precision mesh caused a memory limitation that prevented the model computation.

Furthermore, we measured the noise level from the signal standard deviation and derived the microphone  $\text{SNR}_{1\text{Pa}}$  to  $116 \text{ dB}\cdot\text{Pa}^{-1}$  which is very close to the one we derived from its datasheet ( $117 \text{ dB}\cdot\text{Pa}^{-1}$ ). Finally, we derived the NNEA to  $1.6 \cdot 10^{-9} \text{ W}\cdot\text{cm}^{-1}\cdot\text{Hz}^{-1/2}$  which is also very different from the analytical one due to the poor estimation of the cell constant. The experimentally-derived NNEA is one order of magnitude larger than the state-of-the-art one, which can mainly be explained by the use of microphones presenting a

smaller  $\text{SNR}_{1\text{Pa}}$ . Nonetheless, as the best microphones are big and expensive they are not compatible with these miniaturised and cost effective cells.

To confirm Mirensé's cell sensitivity we later built a bench using a laser diode operating at  $1.392\ \mu\text{m}$  (Eblana photonics). The laser diode beam presents a small divergence and we could much more precisely measure the power passing through the cell. Also, it allowed to avoid the important thermal effects occurring when using our non packaged QCL. We found a NNEA of  $1.4 \cdot 10^{-9}\ \text{W}\cdot\text{cm}^{-1}\cdot\text{Hz}^{-1/2}$ , confirming our previous measurement.

### 3.1.5 Conclusion on MPAS and CEPAS

To conclude this section, we demonstrated that we could model the  $\text{SNR}_{1\text{Pa}}$  of some microphones and cantilevers, with a good experimental agreement. Nonetheless, it is important to emphasize that low noise detectors (such as the microphone BK4179) did not reach their theoretical limitation since they are very sensitive to ambient acoustic background, which, while varying, is difficult to suppress. This induces a discrepancy compared to the analytical sensitivities we derived. Also, in most cases we could not verify the values of the  $\text{SNR}_{1\text{Pa}}$  experimentally for cantilevers due to the lack of details in publications.

Furthermore, we determined the cell constants for simple cylindrical cells and differential cells. While the agreement with theory is good in a few cases, values up to twice the theoretical ones are generally found. Unfortunately, as we referred to the literature we could not verify the reported results.

For the MPAS case we studied, i.e. Mirensé's cell, the analytical model predicted unrepresentative values of the cell constant due to the small size of the cell. In this case we tried to rely on FEM simulations, but the need for a fine mesh of the boundary layers led to memory size limitations. For the study of such small cells, we then privileged the experimental approach.

Based on detectors  $\text{SNR}_{1\text{Pa}}$  and cells constants, we derived the different setups NNEA. We generally obtained a good agreement with the experimental NNEA, with a factor two at most, except in the cases where the detector was limited by the acoustic background.

## 3.2 Study of QEPAS setups

In this section we will study the performance of QEPAS sensors using either bare QTFs or QTFs coupled with acoustic resonators, coming from ONERA or from scientific publications.

### 3.2.1 The case of bare QTFs

#### 3.2.1.1 QTFs characteristics

In order to validate our model we will analyse the performances of six different QTFs:







QTFs						
Photograph						
QTF name	Euroquartz	QTF#5 [81]	U1	U2	C1	C2
$f_0$ (Hz)	32,768	2,871	4,927	12,663	42,700	21,220
$e$ (mm)	0.6	1	7	3.7	4	8
$l$ (mm)	0.34	0.25	2	2	1	2
$L$ (mm)	3.75	17	36	13	6.8	13.6
$g$ (mm)	0.31	0.7	2	2	1	2

Table 3.11: Bare QTF cases to study. The picture for U2 is taken from a FEM simulation since it was not fabricated.

- Euroquartz MH32768 [176]: This QTF is a typical watch QTF from the industry which we characterised and studied at ONERA. Watch QTFs are designed to be used in the clock industry as a time reference (usually resonating at 32,768 Hz) and are used under vacuum. They are not optimised for photoacoustics but are widespread in the literature owing to their availability [28, 80]. This case is important to study as a reference and also because watch QTF based QEPAS sensors present high sensitivities in the literature.
- QTF#5 : It is a custom QTF reported by Spagnolo's group [81, 86, 88] and presented in Section 1.3. This QTF is representative of the other custom QTFs from the same research group. Also, it is interesting because this QTF is small compared to the acoustic wavelength and we will be using this aspect for comparisons in Chapter 4.
- U1: It is one of the custom QTFs designed and fabricated at ONERA (see Appendix C) during the previous PhD thesis [26, 124]. Its geometry is similar to the one of a watch QTF but at a larger scale. By taking a wafer thickness and gap between the prongs of 2 mm as inputs, this QTF quality factor at atmospheric pressure was optimised using the analytical model presented in Section 2.1.4. Compared to the literature, it is the bare QTF presenting the highest quality factor at atmospheric pressure using the fundamental resonance mode.
- U2: This QTF was also designed at ONERA in a similar way as U1 [26]. However, its SNR was optimised instead of its quality factor. This QTF was not fabricated because the sensitivity gain predicted by the model was not significant compared to the others.
- C1 and C2: These are two other custom QTFs produced at ONERA. C1 is the half-scale version of C2. These resonators were designed to present a prong width equal to half the acoustic wavelength. By doing so, these QTFs can theoretically present a better coupling with acoustic waves and resonators. Their quality factor was optimised with the use of an additional acoustic resonator, particularly C2 with its acoustic cavity presents the highest quality factor from the literature at atmospheric pressure [125, 146].

### 3.2.1.2 Analytical and FEM results

#### Analytical determination of the frequency and quality factor



Two important parameters of the QTF must be quantified before the sensitivity: the resonance frequency and the quality factor. These parameters are computed analytically and are hereafter compared to FEM modelling and experiments (Table 3.12).

QTF	Analytical $f_0$	FEM $f_0$	Experimental $f_0$
Euroquartz	37,505	32,761	32,768
QTF#5 [81]	3,033	2,783	2,871
U1	5,993	4,765	4,927
U2	19,193	12,663	-
C1	75,837	42,880	42,700
C2	37,918	21,162	21,220

Table 3.12: Comparison of tuning forks fundamental frequencies in Hz, determined through analytical or FEM modelling and experiments. Experimental results are obtained by characterising the QTF resonance in ambient air using an impedancemeter (4294A, Keysight).

While the frequency determined through FEM is close to the experimental one, the analytical model prediction is inaccurate in most cases with relative errors up to 77%. The error on the analytical frequency is relatively small for QTFs that are closer to Bernoulli's hypotheses (Euroquartz, QTF#5, U1, U2), meaning a long length and a small section in comparison. For QTFs presenting a large section such as C1 and C2, the frequency predicted by the analytical model is far from the right one, so we should rather rely on FEM simulations. The discrepancies between FEM and experiments are of a few percents and can mainly be explained by the manufacturing of the objects. Indeed, the processed tuning forks are not exact replicates of the ideal object, due, for example, to the presence of wedges on the prongs sides coming from the chemical etching of Quartz. Depending on etching time for example, we can observe a maximal difference of 500 Hz between two different QTFs. In addition, our tuning forks are laboratory objects and are not standard compared to watch QTFs for which the frequency is fixed using laser cutting. Considering the frequency measurement using photoacoustics as will be presented in the next paragraphs, a last source of discrepancy is the effect of the surrounding gas, through its sound speed particularly or viscosity, temperature, etc. This can typically shift the resonance frequency of a few Hertz, nonetheless this bias is not an error as it can be precisely described analytically and through simulations.

The discrepancy between the analytical frequency and the experimental one can lead to substantial differences in the other parameters we derive analytically such as the quality factor or the sensitivity. For accurate analysis of a QTF we will now use the FEM or experimental frequency as input in all our models (analytical or FEM).

The second parameter to model is the quality factor. In order to derive the QTF total quality factor we express the different contributions which we presented in Section 2.1.4.

The first step is to introduce the QTF structural quality factor  $Q_{\text{struct}}$ . When modelling QTFs that were not made nor modelled by FEM, this quality factor is taken to be 1,000,000. This implies that a very good reduction of structural losses has been made by carefully adapting the anchor structure to the QTF mode of resonance [177]. For a case study it can be derived from FEM analysis of the QTF, this result is the one used in Table 3.13. The other effects limiting the quality factor in vacuum are mainly electrode viscosity and thermoelastic damping which can be computed analytically.

As can be seen, the resulting vacuum quality factor  $Q_{\text{vac}}$  is comparable to the measured one particularly for QTF#5 and U1. The discrepancies for other QTFs might come from the fact that they are more complex than what is modelled. The QTF Euroquartz is not a simple rectangular fork, the geometry is more complex, so is the electrode pattern. The QTFs C1 and C2 do not respect Bernoulli's hypotheses and the electrode pattern

is also more complex. Indeed, the model used for electrode damping is an approximation and a further study of the energy confinement in the QTF should be carried out. Regarding the limiting loss in vacuum, no general conclusion can be made as it strongly depends on the QTF. From now on, we will use the experimental value of  $Q_{vac}$  when available.

QTF	Euroquartz	QTF#5	U1	U2	C1	C2
Experimental $f_0$ (Hz)	32,768	2,871	4,927	12,663	42,700	21,220
FEM $Q_{struct}$	$2.8 \cdot 10^7$	$1.1 \cdot 10^5$	$2.9 \cdot 10^5$	$1 \cdot 10^5$	$7.9 \cdot 10^6$	$1.3 \cdot 10^6$
Analytical $Q_{electrode}$	$2.2 \cdot 10^5$	$1.8 \cdot 10^6$	$8.6 \cdot 10^6$	$3.3 \cdot 10^6$	$5 \cdot 10^5$	$2 \cdot 10^6$
Analytical $Q_{thermo}$	$4.7 \cdot 10^5$	$1.2 \cdot 10^5$	$9.6 \cdot 10^6$	$6.9 \cdot 10^6$	$2.7 \cdot 10^7$	$5.3 \cdot 10^7$
Analytical $Q_{vac}$	$1.5 \cdot 10^5$	55,617	$1.4 \cdot 10^5$	95,712	$4.6 \cdot 10^5$	$7.8 \cdot 10^5$
Experimental $Q_{vac}$	77,000	34,800	$1.5 \cdot 10^5$	-	$7.8 \cdot 10^5$	$1.5 \cdot 10^5$
Analytical $Q_{viscous}$	20,413	7,314	68,537	73,328	$1 \cdot 10^5$	$1.5 \cdot 10^5$
Analytical $Q_{squeeze}$	$5.8 \cdot 10^5$	$1.8 \cdot 10^6$	$7.9 \cdot 10^6$	$1 \cdot 10^7$	$2 \cdot 10^7$	$3.9 \cdot 10^7$
Analytical $Q_{acoustic}$	$1.2 \cdot 10^6$	$7.6 \cdot 10^9$	$6 \cdot 10^5$	72,737	7,720	7,724
FEM $Q_{acoustic}$	$1.12 \cdot 10^7$	$\gg 2 \cdot 10^7$	$1.3 \cdot 10^6$	79,142	9,339	8,701
Total analytical $Q$	15,677	6,023	45,140	26,362	8,445	7,795
Experimental $Q$	12,300	4,750	39,430	-	8,724	7,568

Table 3.13: Analytical and FEM study of the different loss sources contributions for studied QTFs and experimental comparison.

Concerning QTF losses due to their use in a gas, we modelled viscous, squeeze and acoustic damping analytically. In addition, we used FEM simulation to predict  $Q_{acoustic}$  more accurately. The value for QTF#5 could not be determined more precisely due to frequency precision of our FEM model. The acoustic damping values are in good agreement for U2, C1 and C2. Nonetheless, they are more distant for the others, which might be explained by the fact that their prong length is small compared to the acoustic wavelength as suggested in [26].

Concerning the dominating losses, one can distinguish different groups of QTFs. The first group, composed of Euroquartz and QTF#5, is limited by the effect of viscous damping on their prongs, while the other losses are not significant. This loss worsens for small dimensions of the prongs and for low resonance frequencies, which is in agreement with these results. Indeed, these QTFs are the smallest of our study, in addition, QTF#5 has the lowest resonance frequency. Other QTFs, C1 and C2, are limited by their acoustic losses. These two tuning forks present a special design with a prong size comparable to the acoustic wavelength, promoting acoustic waves emission. The last QTFs, U1 and U2, present a compromise between viscous and acoustic losses. Generally, squeeze damping is negligible due to the important gap between the prongs. Let's note that the influence of structural losses should not be neglected as it represents a few percents of the total quality factor.

Eventually, one can conclude that the experimental quality factor is well approximated analytically despite the differences between the ideal objects and the real ones. Being able to model the fork quality factor is crucial in order to derive its sensitivity, particularly for objects that were not fabricated and is also interesting to make quick comparisons when varying model parameters. For actual forks, we will in turn introduce the experimental quality factor in our models for more accurate comparisons to experiments.

## Determination of the sensitivity

Having determined the resonator frequency and quality factor, it is now possible to derive its photoacoustic sensitivity. We here provide analytical results for the different QTFs. Particularly, we detail the different parameters leading to the system NNEA in Table 3.14.

We consider a typical experiment of on-beam QEPAS, the laser beam is positioned at optimal height and focused between the prongs. We target a  $C_2H_2$  absorption line with a wavelength modulated laser, yielding a heat deposition of  $H = 1.04 \times 10^{-6} \text{ W.cm}^{-1}$ . The maximal generated pressure is also given in the table, as well as the equivalent photoacoustic force seen by the QTF. The noise is integrated over a bandwidth of 1/16 Hz which is a typical value for photoacoustic experiments and enables to consider a white spectral density for our QTFs presenting small bandwidths (see Section 2.1.6.3). Finally, the NNEA is computed and corrected by FEM modelling in order to take into account the phenomena not described analytically, such as acoustic diffraction by the tuning fork. The corrections made through FEM will be further detailed in Chapter 4.

QTF	Euroquartz	QTF#5	U1	U2	C1	C2
Heat amplitude ( $\text{W.cm}^{-1}$ )	$1.04 \cdot 10^{-6}$					
Maximal pressure amplitude ( $\mu\text{Pa}$ )	37.3	5.2	8	17.8	45.5	27
Photoacoustic force amplitude (N)	$1.43 \cdot 10^{-11}$	$1.69 \cdot 10^{-12}$	$1.4 \cdot 10^{-10}$	$1.76 \cdot 10^{-10}$	$2.34 \cdot 10^{-10}$	$4.71 \cdot 10^{-10}$
Equivalent bandwidth (Hz)	1/16					
Brownian noise equivalent force (N)	$1.64 \cdot 10^{-13}$	$1.7 \cdot 10^{-13}$	$9.18 \cdot 10^{-13}$	$8.87 \cdot 10^{-13}$	$1.67 \cdot 10^{-12}$	$3.32 \cdot 10^{-12}$
SNR	87	10	152	198	140	142
Ana. NNEA ( $\text{W.cm}^{-1}.\text{Hz}^{-1/2}$ )	$4.7 \cdot 10^{-8}$	$4.2 \cdot 10^{-7}$	$2.7 \cdot 10^{-8}$	$2.1 \cdot 10^{-8}$	$3 \cdot 10^{-8}$	$2.9 \cdot 10^{-8}$
FEM NNEA ( $\text{W.cm}^{-1}.\text{Hz}^{-1/2}$ )	$3.3 \cdot 10^{-8}$	$3.5 \cdot 10^{-7}$	$2.6 \cdot 10^{-8}$	$1.5 \cdot 10^{-8}$	$2.2 \cdot 10^{-8}$	$4.4 \cdot 10^{-8}$

Table 3.14: Analytical determination of tuning forks sensitivities. The NNEA is corrected by FEM to take into account more complex acoustic phenomena described extensively in Chapter 4.

The sensitivities computed by the analytical model are quite similar for all considered QTFs, of the order of  $10^{-8} \text{ W.cm}^{-1}.\text{Hz}^{-1/2}$ , except for QTF#5 which presents a sensitivity one order of magnitude worse. Despite the difference between the generated pressures, no major difference can be observed between the QTFs NNEA, showing that the QTF design is a compromise of many parameters, such as frequency, quality factor, detection surface, gap between the prongs, etc. Also, the model refinement made by FEM, taking into account acoustic diffraction and vibroacoustic coupling, does not modify the NNEA significantly, demonstrating that the hypotheses we took to model the acoustic pressure field are relevant to describe the problem.

### 3.2.1.3 Experimental comparison

In order to validate the analytical model results we sought to perform quantitative measurements for a few available QTFs at ONERA (Euroquartz, U1 and C2). The analytical results for other watch QTFs and QTF#5 will instead be compared to literature.

### Experimental setup

In order to measure the tuning forks sensitivities, we used a photoacoustic bench with a telecom laser diode emitting around  $1.5 \mu\text{m}$ . The laser diode temperature and current were controlled (using ITC 510, Thorlabs) and its wavelength was monitored with a wavemeter (WS6 785, HighFinesse). The target gas was either  $C_2H_2$

at  $6,490.02 \text{ cm}^{-1}$  presenting a peak absorption of  $1.88 \times 10^{-7} \text{ cm}^{-1}.\text{ppmv}^{-1}$  and a FWHM of  $0.12 \text{ cm}^{-1}$  or  $\text{CO}_2$  at  $6,490.05 \text{ cm}^{-1}$  presenting a peak absorption of  $1.84 \times 10^{-10} \text{ cm}^{-1}.\text{ppmv}^{-1}$  and a FWHM of  $0.16 \text{ cm}^{-1}$ . These absorption coefficients were computed from HITRAN database [130] considering a Voigt absorption profile and atmospheric temperature and pressure. Before each measurement the cell was purged and filled with a certified mixture of either 1,000 ppmv of  $\text{C}_2\text{H}_2$  in nitrogen or 100%  $\text{CO}_2$ . The residual humidity in the cell was monitored with a hygrometer (SHT85, Sensirion), nonetheless there is no cross talk with the targeted species as shown in Figure 3.5.

The laser beam was focused between the QTF prongs, presenting a waist of  $45 \text{ }\mu\text{m}$  and a Rayleigh range of 4 mm. The QTF was placed inside a vacuum chamber and its position was set using a 4 axes mount (horizontal and vertical translations, yaw and pitch). The chamber is made of Dural and coated with black Teflon<sup>®</sup> to avoid molecular adsorption and minimize diffusion of laser light. Two anti-reflection coated windows allowed laser beam pathway through the cell.

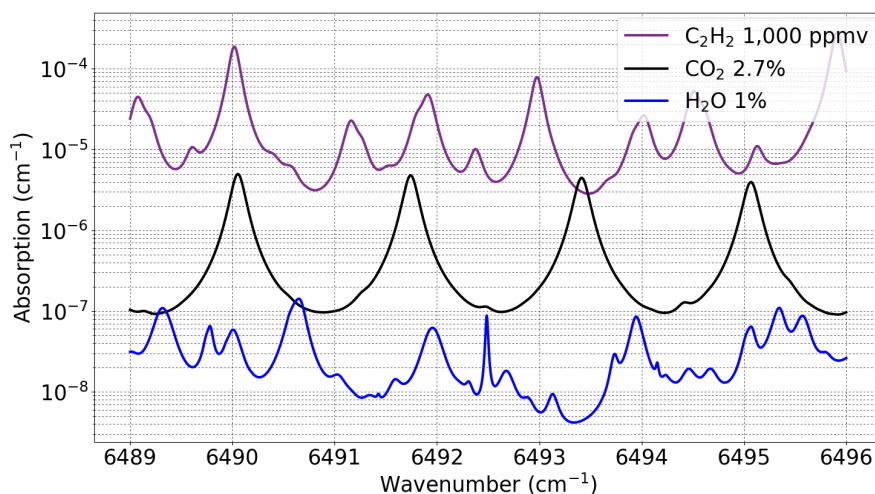


Figure 3.5: Absorption spectrum of the targeted gases over the laser diode emission range. The gases are in  $\text{N}_2$  at atmospheric pressure and temperature which are the conditions we used analytically, considering a Voigt absorption profile and data from HITRAN database [130]. A residual water vapor spectrum is given in order to assure that it does not interfere with our measurements.

In order to generate the photoacoustic signal a modulation was set with a function generator (33000B, Agilent Technologies) either in amplitude by means of a fibered Mach-Zehnder modulator or in wavelength using the external modulation input of the diode controller. Again, the wavelength modulation is not pure and a residual amplitude modulation is observed, nonetheless it is not important as the modulation amplitude is small and is not significant in the computation of the overall sensitivity. Amplitude modulation was obtained through imposing a sinusoidal voltage on the Mach-Zehnder modulator, giving rise to an optical modulation close to a square wave of 50% duty cycle.

The QTF signal was amplified by means of its proximity electronics card (see Section 2.1.6) and was fed to a lock-in amplifier with the function generator trigger signal as a reference. Two different lock-in amplifiers were used, either SR530 (Stanford Research Systems) or Ametek 7230 (Ametek) for automated measurements. Finally, the bench instruments were controlled by means of Python scripts in order to perform automated measurements. The schematic diagram of the bench and a picture of the vacuum cell are given in figures 3.6 and 3.7.

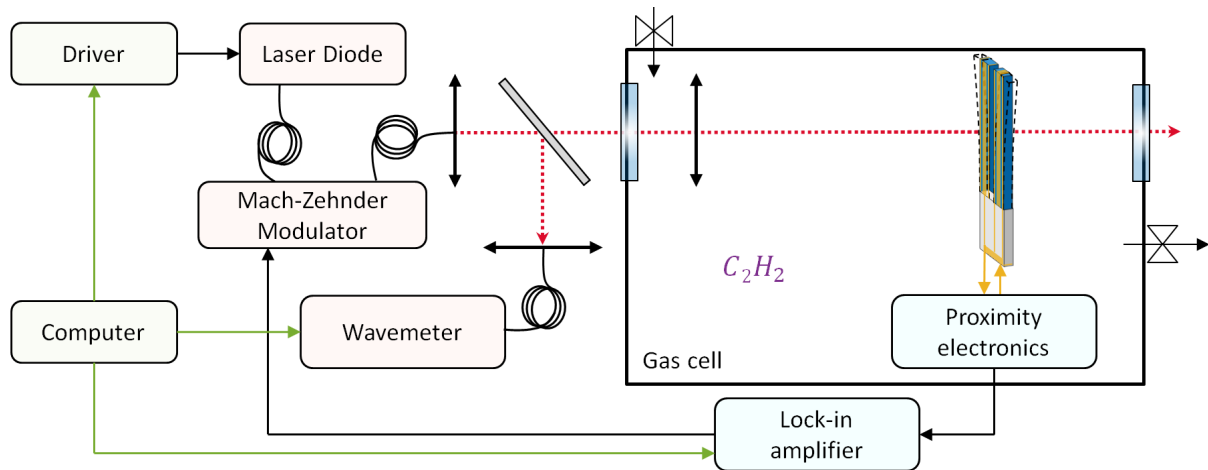


Figure 3.6: Photoacoustic measurement setup.

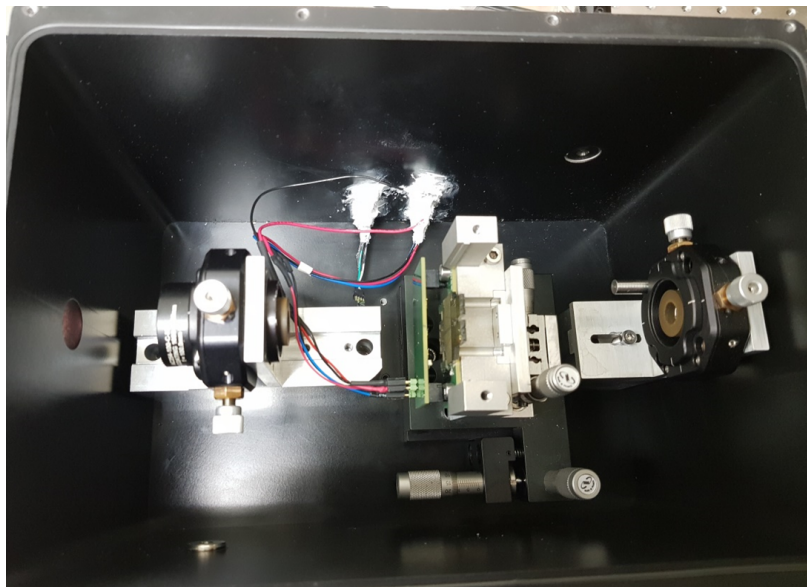


Figure 3.7: Vacuum chamber in which the QTF is placed. From the left to the right, a lens is used for focusing the laser beam, the QTF is placed on a multi-axis mount in the middle with its proximity electronics, a last lens is used to focus the laser beam onto an external photodiode or powermeter.

### Modulation scheme

Even though wavelength modulation (WM) is not the technique leading to maximum signal generation (Section 2.1.2), it is highly convenient to reduce the acoustic background generated by laser absorption. We approximated the heat amplitude for a sine modulation to  $H \approx \alpha_G P_L / 3$ . This approximation is not well known in the photoacoustic domain, hence we will attempt to verify it experimentally. For that purpose we will compare the generated signal for amplitude and wavelength modulation schemes using the QTF U1. The heat amplitude generated using AM is straightforward, indeed, the laser is operated in continuous mode and is tuned on the gas absorption line while its power is divided by two (since the laser power is modulated by a square wave of 50% duty cycle), yielding  $H = \alpha_G P_L / 2$ .

The relevant setup parameters are given in Table 3.15. The gas absorption is computed using HITRAN database and a Voigt profile for line broadening, the laser power is measured, and the expected heat amplitude is computed analytically. The resulting signal in AM is approximately 1.58 bigger than the one in WM which corresponds to the expected factor of 3/2. The slight discrepancy may come from experimental uncertainties or non-perfect sine modulation of the laser wavelength. Nonetheless, this factor is very well approximated and we will use it in order to compute the NNEA values in this manuscript.

Modulation scheme	AM	WM
Setup		
Absorption $\alpha_G$ ( $\text{cm}^{-1}$ )	$4.97 \cdot 10^{-6}$	
Laser power $P_L$ (mW)	8.5	17
Heat amplitude $H$ ( $\text{W}\cdot\text{cm}^{-1}$ )	$4.22 \cdot 10^{-8}$	$2.82 \cdot 10^{-8}$
Photoacoustic response		
Signal (mV)	11.6	7.3

Table 3.15: Experimental comparison between AM and WM modulation schemes using the QTF U1 for humidified  $\text{CO}_2$  measurement.

One can note that sine wavelength modulation is not the one generating the highest signal for absorption lines with a Voigt or Lorentzian profile. Triangular or quasi-square modulation of the wavelength result in a signal increase of a factor approximately 1.15 [26] compared to a sine one. Nonetheless, sine modulation is usually performed for simplicity.

### Determination of the system limiting noise

Prior to determining the system sensitivity it is primordial to characterise the system limiting noise. For QTFs, this noise should be the Brownian noise arising from thermal agitation of the charge carriers [148]. Its spectral density is the result of the multiplication of a white noise by the QTF transfer function, it is therefore peaked at the QTF resonance frequency and exhibits the same quality factor. For example, we present the noise spectral density measured for a QTF C2 in Figure 3.8. We used a spectrum analyser (Agilent 35670A) for studying the QTF and its proximity electronics noise, in ambient air at atmospheric pressure and temperature. Other results concerning Euroquartz can be found in [26].

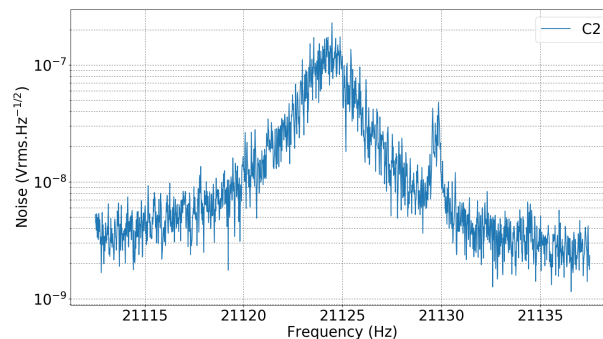


Figure 3.8: Noise measurement for bare QTF C2 in air at atmospheric conditions.

We found a noise peak at the QTF resonance frequency and a similar quality factor around 10,000. The presence of this peak indicates that the system noise is limited by its fundamental limit, i.e. the QTF Brownian

noise. We can nonetheless observe a secondary peak at 21,130 Hz that may come from an electrical resonance inside the preamplifier circuit. It does not influence the photoacoustic measurement since we integrated the noise in a 1 Hz bandwidth.

### Experimental results for the on-beam configuration

In this paragraph we study the on-beam configuration which is the most used in QEPAS. In order to perform more reliable measurements, we used wavelength modulation to prevent the possible influence of signal backgrounds. In any case, we verified that no significant signal background influenced the measurements by tuning the laser off the gas absorption line or by switching the laser off.

Before switching to WM, the background was first reduced in AM and the optimal position of the laser beam along the prong height was found by maximising the signal. Then, the tuning fork signal was maximised by tuning the modulation frequency to match the QTF fundamental mode and by adjusting the wavelength modulation amplitude. The quality factor was measured photoacoustically by measuring the signal versus the QTF frequency. The modulated laser power was measured close to the QTF, while laser absorption between the entrance window and the QTF was negligible.

The results are presented for different representative QTFs in Table 3.16. The results for QTF#5 come from the literature [88].

QTF	Euroquartz [26]	QTF#5 [88]	U1	C2
Setup				
Gas	CO <sub>2</sub>	H <sub>2</sub> O	C <sub>2</sub> H <sub>2</sub>	C <sub>2</sub> H <sub>2</sub>
Concentration	100%	1%	1,000 ppmv	1,000 ppmv
Absorption (cm <sup>-1</sup> )	1.84 10 <sup>-4</sup>	6.24 10 <sup>-4</sup>	1.88 10 <sup>-4</sup>	1.88 10 <sup>-4</sup>
Relaxation time (μs)	0.1	-	0.1	0.1
Laser power (mW)	23	23	17	17
Heat amplitude (W.cm <sup>-1</sup> )	1.41 10 <sup>-6</sup>	4.78 10 <sup>-6</sup>	1.07 10 <sup>-6</sup>	1.07 10 <sup>-6</sup>
Resonance characteristics				
<i>f</i> <sub>0</sub> (Hz)	32,738.1	2,868	4,926.8	21,537.14
Quality factor <i>Q</i>	9,100	5,800	28,000	9,614
Photoacoustic response				
Optimal laser height <i>h/L</i> (%)	85	88	84	75
Signal (mV)	10.6	12.1 10 <sup>-3</sup>	17.1	16.8
Noise density (μVrms.Hz <sup>-1/2</sup> )	300	3.2	636	283
Noise equivalent bandwidth (Hz)	1/8	0.25	1/8	1/8
SNR	100	7.6	76	168
Exp. NNEA (W.cm <sup>-1</sup> .Hz <sup>-1/2</sup> )	4 10 <sup>-8</sup>	1.25 10 <sup>-6</sup>	4 10 <sup>-8</sup>	1.8 10 <sup>-8</sup>
FEM NNEA (W.cm <sup>-1</sup> .Hz <sup>-1/2</sup> )	3.3 10 <sup>-8</sup>	3.5 10 <sup>-7</sup>	2.6 10 <sup>-8</sup>	4.4 10 <sup>-8</sup>

Table 3.16: Experimental results in WM modulation for bare QTFs

Compared to the analytical result one can observe a few discrepancies that we will comment in the following. Concerning the quality factors the results are similar to the ones measured with the impedancemeter in air except for U1. This might come from the measurement uncertainty, the bandwidth of the QTF is indeed very small, of

the order of 100 mHz. The quality factor determined electrically is the more reliable due to the better frequency precision and fit of the equivalent electrical parameters.

Concerning the NNEA, for Euroquartz we found  $4 \cdot 10^{-8} \text{ W.cm}^{-1}.\text{Hz}^{-1/2}$  which is close to what we can find in other publications. For example, in [80] we can derive the NNEA to be  $3 \cdot 10^{-8} \text{ W.cm}^{-1}.\text{Hz}^{-1/2}$ . The relative error to the NNEA computed by FEM is of 21%.

The experimental NNEA for QTF#5 is approximately 3 times higher than the one we computed. As this result comes from the literature we cannot explain this discrepancy. It was not possible to confirm it through other publications involving the same QTF since they report inconsistent NNEA values of  $3.75 \cdot 10^{-11} \text{ W.cm}^{-1}.\text{Hz}^{-1/2}$  [86] or  $4.4 \cdot 10^{-10} \text{ W.cm}^{-1}.\text{Hz}^{-1/2}$  [87].

The sensitivity for U1 is 54% away from the FEM one. This discrepancy could not be studied to date. The cause might be the degraded quality factor or a problem we had concerning laser power measurement, with no mean to verify it afterwards. We should verify this measurement in the future.

The sensitivity error for C2 is about 59%. It is the only QTF for which the experimental NNEA is better than the analytical one. The reason could not be determined and further measurements should be performed to understand it.

To conclude, we generally found a good agreement between our modelling and the experimental results for the main parameters. The largest discrepancies are observed between calculated and measured NNEA values, which is due to the fact that the NNEA is a multi-parameter figure of merit in which all the uncertainties add up. We can nevertheless emphasise that most calculated and measured NNEAs remain within a factor of two from the experimental values. This shows that our model and its hypotheses are consistent with the description of photoacoustic experiments and that we have a sufficient knowledge of our experimental setup to derive quantitative values to compare to the model.

### 3.2.2 The case of QTFs coupled with acoustic resonators

In the previous section, we demonstrated that QTFs alone could reach sensitivities of the order of  $10^{-7}$  to  $10^{-8} \text{ W.cm}^{-1}.\text{Hz}^{-1/2}$  with a good match with the analytical model. Such sensitivities can be sufficient for many applications such as the control of industrial emissions, however it is not sufficient for air quality analysis for example. In this section, we will study the coupling of QTFs with acoustic resonators. As in MPAS and CEPAS, the acoustic resonator amplifies the acoustic pressure which is later detected by the QTF. Between these two resonators a complex coupling exists, which we strive to understand through the analysis of different QTF/acoustic resonator systems. The description of such systems being complex, we will rely on FEM simulations rather than on analytical modelling.

#### 3.2.2.1 Watch QTF with longitudinal dual-tube microresonators

The first case we will describe is the most widespread in the literature. It was introduced first by Kosterev et al. at the same time as the use of watch QTFs in photoacoustics [28]. Two longitudinal acoustic resonators were placed on each side of a watch QTF and a sensitivity enhancement by a factor 7 was reported compared to the bare QTF in on-beam configuration. Later on, the use of such longitudinal resonators has been studied as well as its coupling with the QTF. Several variations can be found, such as the off-beam [103] and T-shape [101] configurations (see Figure 1.13) or the use of a single tube when possible [99, 95]. We propose to study this case as a reference in order to validate our FEM models. Parts of the following results were presented in [26].

#### Problem definition

We consider the same watch QTF we used before: Euroquartz. Two tubes are placed from each side of the QTF at a distance  $e_{\text{mr}}$  from the QTF surface. We will call this distance the penetration depth, which is equal



to 0 mm at the prong surface and can be negative if the tube enters the fork gap as defined in Figure 3.9. The tubes have a length  $L_{mr}$  each, an inner radius  $R_I$  and outer radius  $R_O$ . Their centers are placed at a height  $h_{mr}$  corresponding to the optimal height for excitation of the QTF. These parameters values are given in Table 3.17 and are representative of the experimental case we will study.

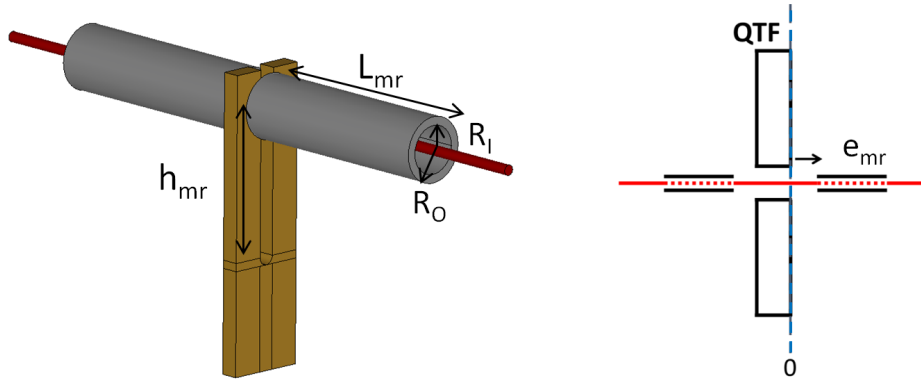


Figure 3.9: Euroquartz QTF with a dual-tube resonator: geometrical description (left). Top view of the QTF (right).

Tube geometry			
$L_{mr}$	4.3	$h_{mr}$	3.2
$e_{mr}$		0.02	
$R_I$	0.46	$R_O$	0.64

Table 3.17: Tubes geometrical parameters in mm.

According to Chapter 2, these tubes are modelled as perfectly reflecting hard walls and so, only their radiative quality factor  $Q_{ac,radiation}$  is taken into account in the FEM model, quantifying the acoustic losses through openings. We simulated by FEM such tubes and found a radiative quality factor equal to 30. For comparison, we can compute these resonators thermoviscous quality factor as we did previously in this chapter (Section 3.1.2). To simplify this study, we consider that the tubes are equivalent to one single tube of length 8.6 mm. By matching its frequency to the one of the QTF we obtain a thermoviscous quality factor of about 26. The total tube quality factor, taking into account the thermoviscous losses determined analytically and the radiative losses determined by FEM is then derived to  $Q_{ac} = 14$  and its cell constant  $C$  to  $4,092 \text{ Pa}\cdot\text{W}^{-1}\cdot\text{cm}$ . These parameters correspond well with the ones observed experimentally for similar geometries studied before. The small radius of the tubes enables a significant amplification of the sound pressure.

### Theoretical study of the resonators coupling

To increase the pressure seen by the QTF, the resonating tubes have to be tuned at the QTF frequency. This is carried out by modifying the tubes length. The influence of tube length over system frequency, quality factor and SNR is depicted in Figure 3.10.

As for every of our FEM models, we considered non-viscous air, of density  $\rho_f = 1.225 \text{ kg}\cdot\text{m}^{-3}$  and sound speed  $v = 340 \text{ m}\cdot\text{s}^{-1}$ . The laser is a cylinder of radius  $w_L = 50 \mu\text{m}$ . Eventually, we forced the bare QTF quality factor to 10,000 which is similar to the experimental one.

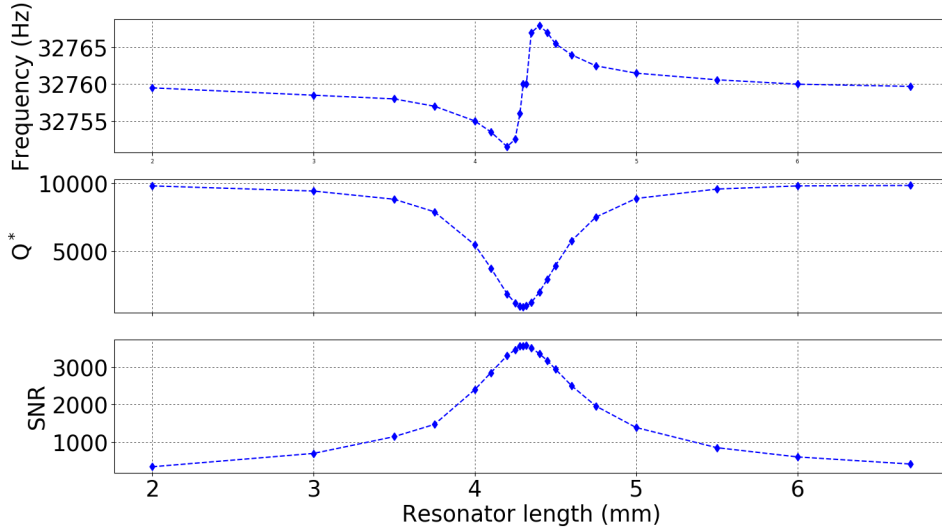


Figure 3.10: FEM study of the resonators coupling when varying the tubes length. The other tube parameters were not modified.

As can be seen in Figure 3.10, the coupling of the two resonators gives rise to a frequency antiresonance as well as a minimum of the quality factor and a maximum of the SNR for  $L_{\text{mr}} = 4.3$  mm. This phenomenon is well known when coupling resonators in QEPAS [98, 80, 99].

The presence of a longitudinal mode of resonance driving the QTF can be evidenced by observing the simulated pressure amplitude in the tubes (Figure 3.11).

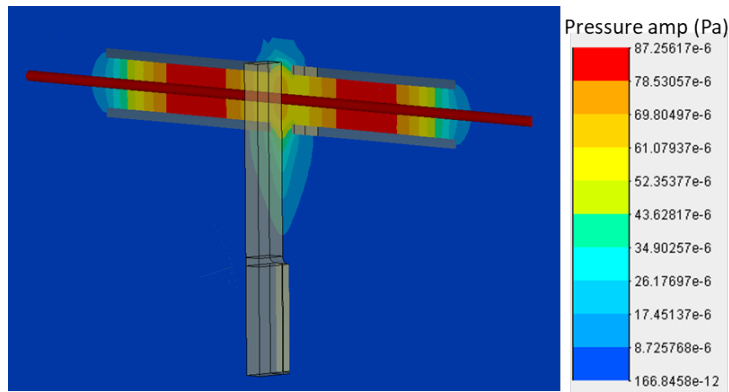


Figure 3.11: Pressure amplitude modelling with FEM of Euroquartz with dual-tube resonators of length  $L_{\text{mr}} = 4.3$  mm. The QTF is coloured in brown, the tubes in grey and the laser in red. One can observe a longitudinal mode of resonance in the tubes. The pressure amplitude scale is normalised, its values do not correspond to the present study.

This important coupling induces a drop of the quality factor, reaching  $Q^* = 874$ . While the tuning fork alone exhibits a quality factor of 10,000, we estimate the tubes quality factor to be  $Q_{\text{ac,radiation}} = 30$  by immobilising the fork in another FEM simulation. The coupling with an acoustic resonator of small quality factor necessarily reduces the total quality factor, related to a destructive acoustic interference between the acoustic waves emitted by the QTF and the ones emitted by the tubes. In contrast to what could be expected for ideally coupled systems, the system quality factor is not equal to 30 but to 874. Indeed, in a simple case in which two resonators exchange energy without losses, one could expect that the coupled quality factor is equal to the sum of the two quality factors, i.e.  $1/Q_{\text{total}} = 1/Q_{\text{QTF}} + 1/Q_{\text{ac}}$ . This means that the coupling is not

perfect between the resonators, only a portion of the resonators energy interferes destructively at the interface between the QTF and the tubes.

While the quality factor drops, the SNR is instead maximised. The pressure generated by the tubes increases, which increases the tuning fork displacement. Moreover, as the quality factor decreases, so does the noise equivalent displacement as described by Equations 2.31 and 2.36. Consequently, the sensor SNR reaches its maximum when the quality factor is minimum, making the quality factor measurements primordial in experiments when coupling resonators. It is interesting to note that it is possible to work away from this optimal coupling. For applications in which a high quality factor is required, particularly to filter external backgrounds, one could operate the sensor at a degraded coupling. Indeed, a small shift in tube length from optimal coupling does not degrade significantly the SNR while it significantly increases the overall quality factor. For example, for a tube length of 4.5 mm, the system exhibits a quality factor of 3,900 (4.5 times more than the lowest quality factor) and a SNR of 2,950 (1.2 times less than the best SNR).

Finally, the sensitivity can be derived. The simulation enables the computation of the QTF maximal displacement and acoustic pressure which are coupled with our analytical model to derive the sensitivity. The determined NNEA is equal to  $1.2 \cdot 10^{-9} \text{ W.cm}^{-1}.\text{Hz}^{-1/2}$  which is about 30 times the one of the bare QTF as observed in literature [80]. Nonetheless, the acoustic quality factor of the tubes is overestimated by the simulations. Indeed, in FEM we find  $Q_{ac} = 30$  when our analytical model predicts  $Q_{ac} = 14$ . This leads to correct the cell constant of the tubes and then the NNEA to  $2.6 \cdot 10^{-9} \text{ W.cm}^{-1}.\text{Hz}^{-1/2}$  as we detailed in Table 3.18.

A more detailed study of the physical phenomena leading to this sensitivity will be given in Chapter 4.

QTF parameters	
$f_0$ (Hz)	32,761
Coupled quality factor $Q^*$	874
Dual tubes parameters	
$L_{mr}$	4.3
FEM $Q_{ac,radiation}$	30
Corrected $Q_{ac}$	14
Photoacoustic response	
Heat amplitude ( $\text{W.cm}^{-1}$ )	$1.07 \cdot 10^{-6}$
Maximal pressure amplitude ( $\mu\text{Pa}$ )	608
Maximal displacement (m)	$5.1 \cdot 10^{-11}$
Noise equivalent bandwidth (Hz)	1/16
Noise equivalent displacement (m)	$1.4 \cdot 10^{-14}$
SNR	3,572
FEM NNEA ( $\text{W.cm}^{-1}.\text{Hz}^{-1/2}$ )	$1.2 \cdot 10^{-9}$
Corrected FEM NNEA ( $\text{W.cm}^{-1}.\text{Hz}^{-1/2}$ )	$2.6 \cdot 10^{-9}$

Table 3.18: FEM results for Euroquartz with dual tube resonators when the coupling is maximal.

## Experimental validation

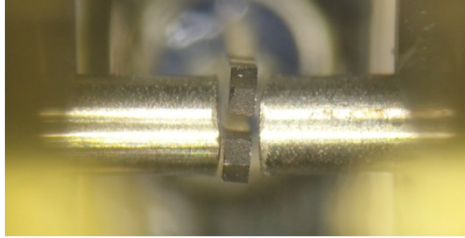


Figure 3.12: Microscope photograph of the experimental setup. The QTF is placed in the center and tubes are aligned around it.

With the same setup described before for validation of bare QTF performances, this QEPAS sensor was studied [26]. The tubes were cut from stainless steel surgical needles ([178], BD) of internal and external radii  $R_I = 460 \mu\text{m}$  and  $R_O = 640 \mu\text{m}$  which is similar to the simulated ones. The resonators are aligned close to the QTF gap at the same height as for the bare QTF, with an approximate penetration depth  $e_{\text{mr}}$  of  $20 \mu\text{m}$ . The laser is focused in the tubes and the background in AM is minimised, while the signal in WM is maximised. By varying the tubes length, one can obtain similar results as the ones presented before (Figure 3.13).

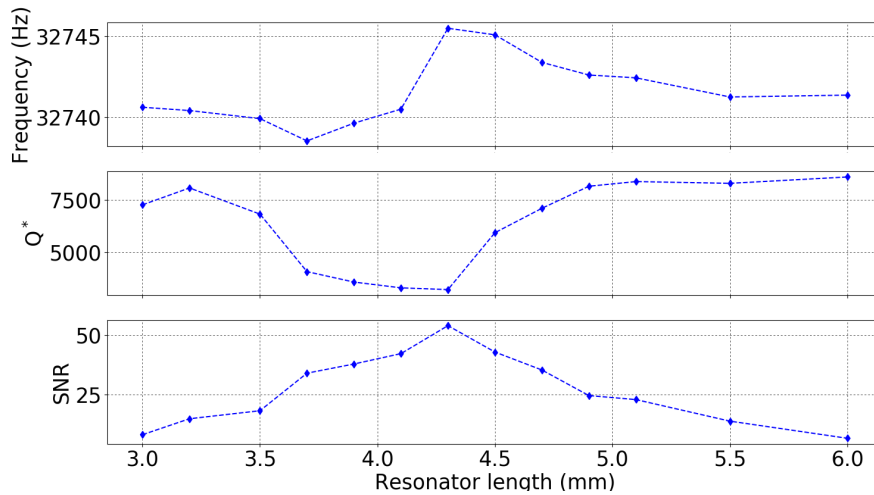


Figure 3.13: Experimental study of the resonators coupling when varying the tubes length.

Despite the experimental difficulty to properly cut the tubes and align them, we obtain the same type of curve we obtained through FEM (Figure 3.10). A frequency antiresonance is observed, as well as a minimum of the quality factor, reaching 3,200 for  $L_{\text{mr}} = 4.3 \text{ mm}$ , demonstrating an optimal coupling between the resonators. The quality factor derived through FEM was three times smaller, reaching 874. This difference may be explained by the fact that the experimental coupling was lower due to imperfect positioning, tuning of the tubes, etc. Finally, the SNR reaches an optimum of 54 for the same tube length.

System	Euroquartz + dual-tubes
Setup	
Gas	CO <sub>2</sub>
Concentration	2.7%
Absorption (cm <sup>-1</sup> )	5 10 <sup>-6</sup>
Relaxation time (μs)	0.1
Laser power (mW)	23
Heat amplitude (W.cm <sup>-1</sup> )	3.83 10 <sup>-8</sup>
Resonance characteristics	
$f_0$ (Hz)	32,740
Coupled quality factor $Q^*$	3,200
Dual tubes parameters	
$L_{mr}$ (mm)	4.3
$e_{mr}$ (μm)	20
$R_I$ (μm)	460
$R_O$ (μm)	640
Photoacoustic response	
Optimal laser height $h/L$ (%)	85
Signal (mV)	3.1
Noise density (μVrms.Hz <sup>-1/2</sup> )	230
Noise equivalent bandwidth (Hz)	1/16
SNR	54
Exp. NNEA (W.cm <sup>-1</sup> .Hz <sup>-1/2</sup> )	2.8 10 <sup>-9</sup>
Corrected FEM NNEA (W.cm <sup>-1</sup> .Hz <sup>-1/2</sup> )	2.6 10 <sup>-9</sup>

Table 3.19: Experimental results for Euroquartz with dual tube resonators when the coupling is maximal.

In order to derive the sensor sensitivity we summed up all of these parameters in Table 3.19. A NNEA of  $2.8 \cdot 10^{-9} \text{ W.cm}^{-1}.\text{Hz}^{-1/2}$  is obtained which is close to the one determined through FEM of  $2.6 \cdot 10^{-9} \text{ W.cm}^{-1}.\text{Hz}^{-1/2}$  with a relative error of 8%. This sensitivity is about 13 times the one of the bare QTF, which is typical when using a watch tuning fork with dual tubes. For example, in [80] Kosterev et al. reported a NNEA of  $3.3 \cdot 10^{-9} \text{ W.cm}^{-1}.\text{Hz}^{-1/2}$  which may be corrected to  $1.2 \cdot 10^{-9} \text{ W.cm}^{-1}.\text{Hz}^{-1/2}$  considering our definition of the NNEA (using heat load instead of laser power). Similar values were obtained in many other publications [179, 99, 106]. Compared to our measurement, they obtained a SNR approximately 3 times higher, probably because they used acoustic resonators with a two times smaller diameter, leading to a fourfold increase of the pressure. Concerning the gain compared to the bare QTF, it usually ranges from 15 to 40 [97, 95], demonstrating the efficiency of such resonators.

To conclude, the use of micro resonators enables to improve the sensitivity to reach  $10^{-9} \text{ W.cm}^{-1}.\text{Hz}^{-1/2}$ , allowing to extend the range of applications for photoacoustic sensors. Although they allow to reach high sensitivities while keeping a compact sensor, their implementation, practical use, and reliability are questionable, particularly in terms of alignment, machining and robustness. This is why we will propose new acoustic resonator designs in the following section.

### 3.2.2.2 Custom QTF C2 with an acoustic recovery cavity

The second case we study is the coupling of a QTF to an acoustic recovery cavity. The QTF C2 was designed by optimising its quality factor without taking into account its acoustic losses. As a consequence, this QTF energy losses mainly came from the emission of acoustic waves, reducing its quality factor down to 7,800 [125] and could be improved by recovering the acoustic waves. Usually, the acoustic quality factor is not limiting for tuning forks. In our case, the QTFs C1, C2 and also U2, designed at ONERA, present important acoustic losses due to their geometry as presented in Table 3.13. Such acoustic losses can be observed by FEM as illustrated in Figure 3.14 for C2.

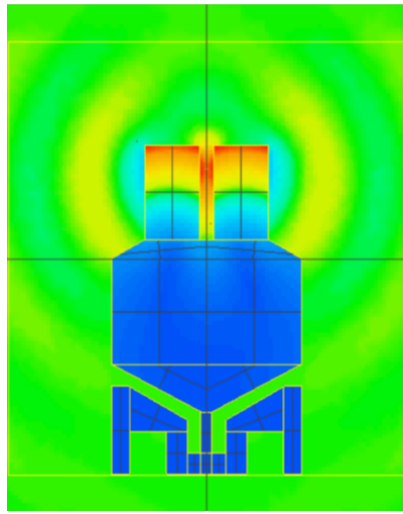


Figure 3.14: FEM simulation of C2 acoustic emission [125]. The QTF color represents its displacement. The color of the air surrounding the QTF represents the pressure waves.

In order to tackle this issue, a cavity was designed to recover the acoustic waves emitted by the QTF. Its cylindrical geometry was chosen to match the spherical shape of the emitted acoustic mode.

#### Problem definition

The cylindrical cavity has a radius  $R_I$ , a length  $L_{mr}$  and its center is positioned at a height  $h_{mr}$ . A 3 mm large slit is cut in its bottom in order to let the QTF prongs inside.

The cylinder radius is adapted in order to recover the emitted waves at the QTF frequency. Acoustic wave recovery happens when the distance between the resonator wall and the QTF prong equals  $\lambda_{ac}/2$  (see Figure 3.15) so that reflected sound waves positively interfere with waves emitted by the prongs. As the QTF prong width also is equal to  $\lambda_{ac}/2$ , this cavity radius was chosen to be equal to  $\lambda_{ac} = 16$  mm. Its vertical position is the same at the optimal laser beam height  $h_{mr} = 10.2$  mm.

It should be noted that while enabling recovery of the acoustic waves, destructive interference may occur with the acoustic source. Indeed, the source is placed in the middle of the QTF gap which is placed at a distance  $\lambda_{ac}$  from the cavity, possibly reducing the pressure inside the cavity.

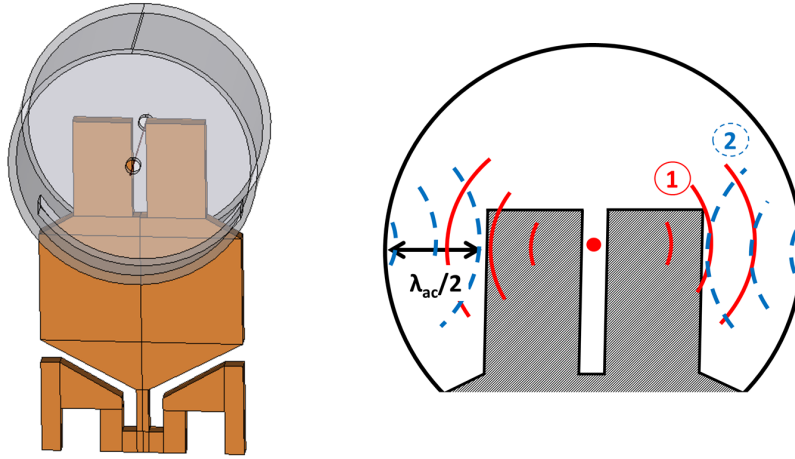


Figure 3.15: C2 with acoustic recovery CAD (left) and schematic (right).

### Recovery of the acoustic waves

We first evaluated the contributions of different physical phenomena to the quality factor by performing FEM studies and electrical measurements. The results are presented in Table 3.20.

QTF	C2	C2 with recovery cavity
Experimental $f_0$ (Hz)	21,220	
$Q_{\text{struct}}$	$1.3 \cdot 10^6$	
$Q_{\text{electrode}}$	$2 \cdot 10^6$	
$Q_{\text{thermo}}$	$5.3 \cdot 10^7$	
$Q_{\text{vac}}$	$7.8 \cdot 10^5$	
Experimental $Q_{\text{vac}}$	$1.5 \cdot 10^5$	
$Q_{\text{viscous}}$	$1.5 \cdot 10^5$	
$Q_{\text{squeeze}}$	$3.9 \cdot 10^7$	
$Q_{\text{acoustic}}$	7,724	-
FEM $Q_{\text{acoustic}}$	8,701	$2.6 \cdot 10^6$
Total analytical $Q$	7,795	72,761
Experimental $Q$	7,568	59,000

Table 3.20: Analytical quality factor of the system C2 + recovery cavity of radius 16 mm and length 16 mm. The acoustic losses are determined through both the analytical and FEM models. The experimental parameters were measured with an impedancemeter, in air at atmospheric conditions.

The FEM simulations predict a very good recovery of the emitted acoustic waves with an acoustic quality factor  $Q_{\text{acoustic}}$  of  $2.6 \cdot 10^6$  compared to 8,701 for the bare QTF. The analytical model then predicts a total quality factor of 72,761, nearly ten times that of a bare QTF. In comparison, we measured a quality factor close to 59,000 in air or in  $\text{N}_2$ , representing a relative error of 38%. During the previous PhD thesis a quality factor of 75,000 was measured [125]. This difference should originate from the manufacturing differences between the tuning forks used in those works (different wafers, etchings, etc), resulting in different resonance frequencies

and then different efficiencies for the coupling of the QTF with the cavity. Nonetheless, in any case a recovery of the acoustic waves is observed, yielding a quality factor ranging from 40,000 to 75,000. The increase of the quality factor should also enable an increase of the sensor sensitivity. Indeed, the sensitivity is proportional to the square root of the quality factor. At first glance, we can estimate an improvement of a factor about 3 on the sensitivity, giving  $6 \cdot 10^{-9} \text{ W.cm}^{-1}.\text{Hz}^{-1/2}$ , which we will aim to verify.

### Determination of the sensitivity with the recovery cavity

The FEM simulation demonstrates the establishment of standing waves inside the cavity enabling acoustic waves recovery (Figure 3.16).

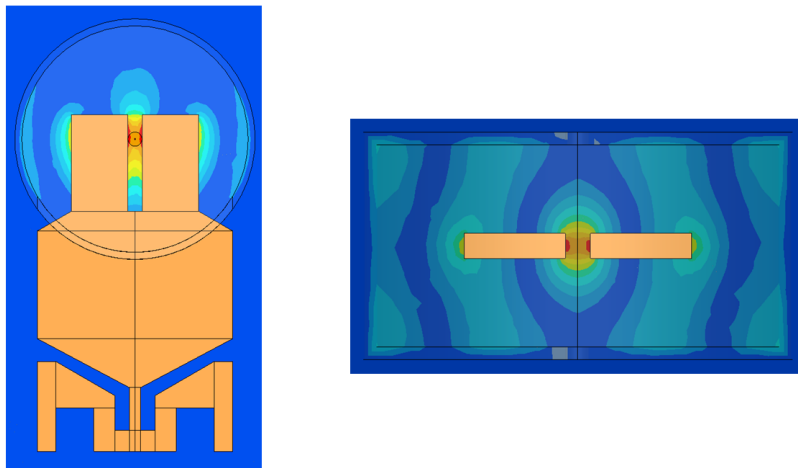


Figure 3.16: Pressure amplitude FEM modelling of C2 with its recovery cavity of radius  $R_1 = 16 \text{ mm}$  and length  $L_{\text{mr}} = 16 \text{ mm}$ . The QTF is coloured in brown and the laser in red. Front view (left), top view (right).

To avoid having to run time expansive simulations we imposed a  $Q_{\text{vac}}$  of 100,000, instead of forcing this quality factor to the experimental value. This results in an overall quality factor of 95,803 for the system that we will have to correct for experimental comparison. The derived sensitivity reaches  $7.6 \cdot 10^{-9} \text{ W.cm}^{-1}.\text{Hz}^{-1/2}$  (Table 3.21), representing an increase of 6 compared to the bare QTF sensitivity determined analytically. This improvement is close to the one we computed by taking into account the quality factor modification alone. The fact that this improvement may be attributed entirely to the quality factor enhancement demonstrates that the pressure inside the cavity is not amplified or not correctly seen by the QTF. This could be attributed to destructive interference with the source or other complex effects which we will study in Chapter 4.



QTF parameters	
$f_0$ (Hz)	21,161.4
Coupled quality factor $Q^*$	95,803
Cavity parameters	
$L_{mr}$ (mm)	16
$R_I$ (mm)	16
Photoacoustic response	
Heat amplitude ( $W.cm^{-1}$ )	$1.07 \cdot 10^{-6}$
Maximal pressure amplitude ( $\mu Pa$ )	252
Maximal displacement (m)	$9.3 \cdot 10^{-12}$
Noise equivalent bandwidth (Hz)	1/16
Noise equivalent displacement (m)	$1.7 \cdot 10^{-14}$
SNR	550
FEM NNEA ( $W.cm^{-1}.Hz^{-1/2}$ )	$7.6 \cdot 10^{-9}$

Table 3.21: C2 with recovery cavity: FEM results.

The acoustic recovery cavity was designed and machined in stainless steel [125] as presented in Figure 3.17. The cavity is closed by two plates to avoid acoustic losses, and a hole is made in the middle at the optimal height for QTF excitation.

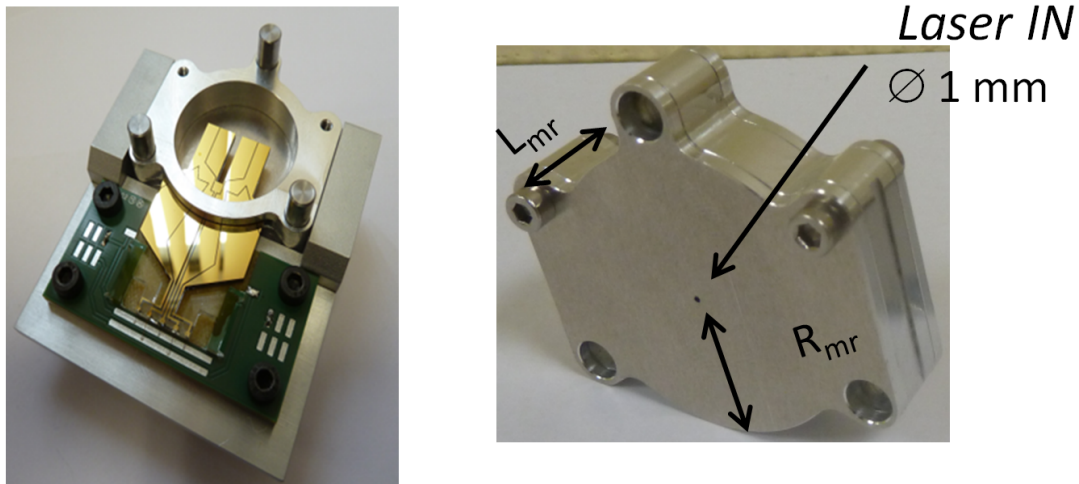


Figure 3.17: Photograph of experimental setup: C2 with acoustic recovery cavity.

The cell is filled with  $C_2H_2$  1,000 ppmv in  $N_2$ . The laser is tuned to target this absorption line in WM modulation and the modulation depth is optimised.

By scanning through the QTF resonance we measured a quality factor of 59,000, compared to 7,800 for the bare QTF, as explained previously.

A sensitivity of  $8.95 \cdot 10^{-9} W.cm^{-1}.Hz^{-1/2}$  is derived which is close to the one we computed with FEM simulations (Table 3.22). The discrepancy is mainly explained by the difference between the experimental and FEM quality factors as discussed before. A rule of three correction of the FEM NNEA using the experimental quality factor gives  $9.9 \cdot 10^{-9} W.cm^{-1}.Hz^{-1/2}$ , which represents a relative error of 10%.

System	C2 + recovery cavity
Setup	
Gas	C <sub>2</sub> H <sub>2</sub>
Concentration	1,000 ppmv
Absorption (cm <sup>-1</sup> )	1.88 10 <sup>-4</sup>
Relaxation time (μs)	0.1
Laser power (mW)	17
Heat amplitude (W.cm <sup>-1</sup> )	1.07 10 <sup>-6</sup>
Resonance characteristics	
$f_0$ (Hz)	21,123.7
Coupled quality factor $Q^*$	59,000
Cavity parameters	
$L_{mr}$ (mm)	16
$R_I$ (mm)	16
Photoacoustic response	
Optimal laser height $h/L$ (%)	75
Signal (mV)	79.5
Noise density (μVrms.Hz <sup>-1/2</sup> )	665
Noise equivalent bandwidth (Hz)	1/8
SNR	338
Exp. NNEA (W.cm <sup>-1</sup> .Hz <sup>-1/2</sup> )	8.95 10 <sup>-9</sup>
Corrected FEM NNEA (W.cm <sup>-1</sup> .Hz <sup>-1/2</sup> )	9.9 10 <sup>-9</sup>

Table 3.22: Experimental results for C2 with its recovery cavity.

To conclude, a good agreement with theory is found, making the use of such cavities interesting to increase QTFs quality factors while increasing the sensitivity. Such a possibility should be kept in mind when the acoustic quality factor is found to be limiting.

Furthermore, using this cavity we also demonstrated an enhanced shielding from external acoustic backgrounds (the sound seen by the QTF was reduced by a factor 8) [146], in addition from a shielding from electromagnetic backgrounds. Such shielding is an advantage that could benefit to the use of the sensor in industrial environment.

### Sensitivity enhancement with dual tube resonators

Despite the higher system quality factor, the sensitivity is still one order of magnitude worse than the state-of-the-art [80] (see Chapter 1). We thus found interesting to verify if the use of dual tube resonators with our custom QTF enables a significant sensitivity enhancement such as the one obtained for watch QTFs.

We kept the QTF C2 and its acoustic recovery cavity and tubes were inserted into the cavity as shown in Figure 3.18.

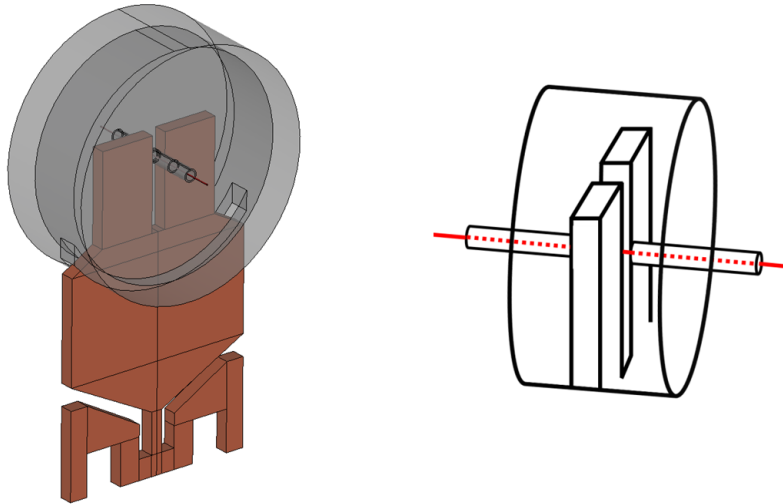


Figure 3.18: C2 with acoustic recovery and dual tube resonators CAD (left) and schematic (right).

The FEM simulations predict an optimum coupling for a tube geometry with corresponding parameters listed in Table 3.23. A longitudinal mode is established inside the tubes which is illustrated in Figure 3.19. At this optimum, a coupled quality factor of 6,266 is reached. The sensitivity is equal to  $1.17 \cdot 10^{-10} \text{ W.cm}^{-1}.\text{Hz}^{-1/2}$  which is one order of magnitude better than state-of-the-art. Nonetheless, as already discussed, this result has to be corrected to take into account the thermoviscous losses. Simulations predict an acoustic quality factor  $Q_{ac,radiation}$  of 343 for these resonators while we determined analytically  $Q_{ac} = 11$ , leading to a NNEA of  $3.65 \cdot 10^{-9} \text{ W.cm}^{-1}.\text{Hz}^{-1/2}$ .

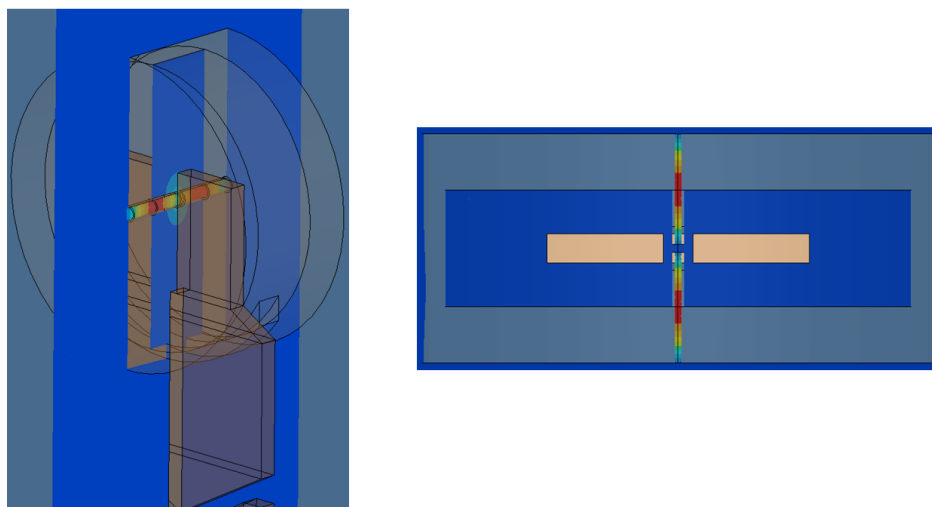


Figure 3.19: Pressure amplitude FEM modelling of C2 with its recovery cavity and dual-tubes. Front view (left), top view (right).

QTF parameters	
$f_0$ (Hz)	21,163.6
Coupled quality factor $Q^*$	6,266
Tube parameters	
$L_{mr}$ (mm)	7.6
$R_I$ (mm)	248
$e_{mr}$ (mm)	-0.8
Photoacoustic response	
Heat amplitude ( $W.cm^{-1}$ )	$1.07 \cdot 10^{-6}$
Maximal pressure amplitude ( $\mu Pa$ )	337
Maximal displacement (m)	$1.55 \cdot 10^{-10}$
Noise equivalent bandwidth (Hz)	1/16
Noise equivalent displacement (m)	$4.36 \cdot 10^{-15}$
SNR	35,521
FEM NNEA ( $W.cm^{-1}.Hz^{-1/2}$ )	$1.17 \cdot 10^{-10}$
Corrected FEM NNEA ( $W.cm^{-1}.Hz^{-1/2}$ )	$3.65 \cdot 10^{-9}$

Table 3.23: C2 with recovery cavity and dual-tubes: FEM results.

In order to verify this result, we first determined the best tube geometry experimentally, by measuring the system quality factor with an impedancemeter for different lengths and radii. The penetration depth was taken equal to -0.8 mm and the height at 10.2 mm. The quality factor measurements are presented in Figure 3.20.

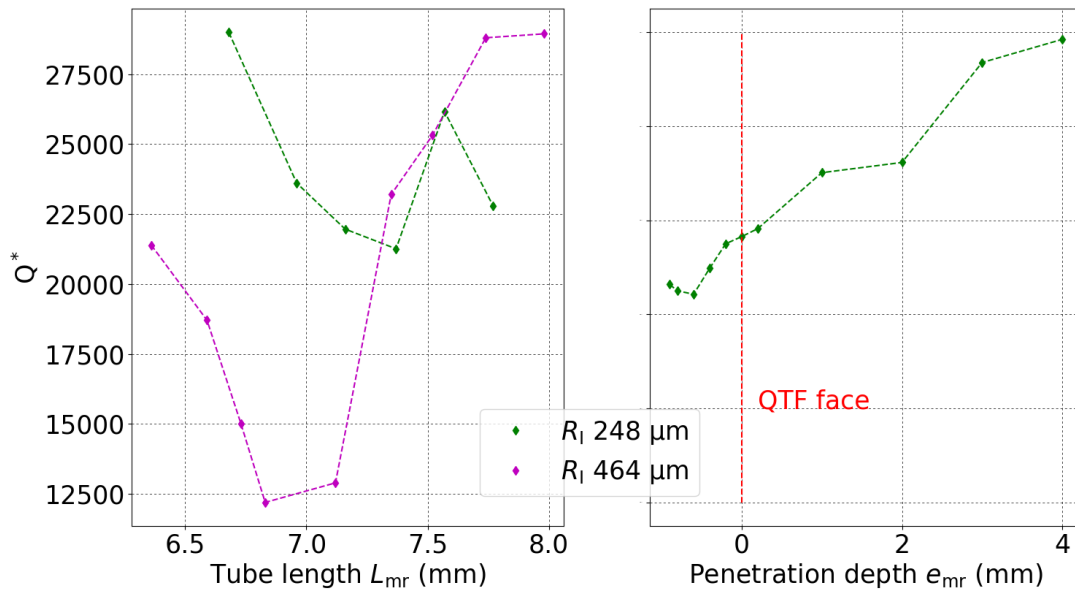


Figure 3.20: Experimental determination of the best coupling for C2 with dual tube resonators for a penetration depth  $e_{mr}$  of -0.8 mm and a height  $h_{mr}$  of 10.2 mm.

As can be seen, an optimum is reached when varying the tube length. Using the tubes of smallest radius (represented in green), a minimal quality factor of 21,259 is found for  $L_{mr} = 7.3$  mm, while using larger tubes

results in a minimum of 12,196 for  $L_{mr} = 6.8$  mm. We then can assume that the coupling between resonators is better using larger tubes, very probably because of the higher acoustic impedance for smaller tubes, limiting the interaction between acoustic waves and the QTF. Furthermore, it can be noted that the optimum does not occur for the same tube length, even if the mode of resonance is longitudinal. This is caused by the small effect of the radius on the longitudinal mode frequencies for finite tube lengths.

Moreover, we studied the influence of tube penetration depth. Unlike with watch QTFs, we were able to place the tubes inside the QTF prongs thanks to the large gap of 2 mm, explaining why the penetration depth can be negative. Again an optimum is found, for a penetration  $e_{mr}$  of  $-0.6$  mm, yielding a quality factor of 21,073. Below this distance (for  $-0.8$  and  $-0.9$  mm) the coupling deteriorates which is explained by the fact that the acoustic mode remains confined inside the tubes and does not make its way to the QTF prongs. On the other hand, when the tubes are placed further away, the coupling also decreases as a result of frequency detuning between the QTF and the tubes and due to the poorer coupling between the two tubes.

In order to validate these electrical measurements, we performed photoacoustic measurements with these different sets of tubes as illustrated in Figure 3.21. The same needles previously used were cut to match the QTF frequency, and others were designed to be directly machined in the cavity walls to facilitate alignment.

We found a sensitivity optimum for tubes of length 7.3 mm, radius 248  $\mu\text{m}$  and penetration depth of  $-0.8$  mm, yielding a quality factor of 22,600 and a state-of-the-art NNEA of  $1.92 \cdot 10^{-9} \text{ W.cm}^{-1}.\text{Hz}^{-1/2}$ . This matches the quality factor measurements we previously presented. This result is presented in Table 3.24. A more complete study presenting the photoacoustic results for various lengths is available in [26] (Page 158).



Figure 3.21: Photograph of experimental setup: C2 with acoustic recovery cavity and dual tube resonators (left). CAD view of a designed cavity wall with integrated tube (right).

When using the largest tubes a sensitivity optimum is reached for a length of 7.3 mm and penetration depth of  $-0.8$  mm, yielding a quality factor of 15,000 and a NNEA of  $1.9 \cdot 10^{-9} \text{ W.cm}^{-1}.\text{Hz}^{-1/2}$ . Unlike what we measured electrically (Figure 3.20), the optimum is found for tubes of length 7.3 mm, this might come from experimental uncertainties when positioning or machining the tubes.

Despite changing the tube radius we obtained similar NNEA values. Presumably, the fact that the pressure amplification is more important when using smallest tubes is compensated by the fact that the coupling is degraded, explaining the similar values. Another possible explanation is that it is harder to pass the laser beam through the smallest tubes, leading to a signal diminution. Yet another explanation is the difficult alignment between the tubes themselves, reason why we later designed tubes that could be machined directly in the cavity walls, benefiting of a better robustness and simpler tube alignment.

System	C2 + recovery cavity + dual tubes
Setup	
Gas	CO <sub>2</sub>
Concentration	2.7%
Absorption (cm <sup>-1</sup> )	5 10 <sup>-6</sup>
Relaxation time (μs)	0.1
Laser power (mW)	23
Heat amplitude (W.cm <sup>-1</sup> )	3.83 10 <sup>-8</sup>
Resonance characteristics	
$f_0$ (Hz)	21,133.1
Coupled quality factor $Q^*$	22,600
Cavity parameters	
$L_{mr}$ (mm)	8
$R_I$ (mm)	16
Tube parameters	
$L_{mr}$ (mm)	7.3
$e_{mr}$ (mm)	-0.8
$h_{mr}$ (mm)	10.2
$R_I$ (μm)	248
$R_O$ (μm)	407
Photoacoustic response	
Optimal laser height $h/L$ (%)	75
Signal (mV)	11.3
Noise density (μVrms.Hz <sup>-1/2</sup> )	566
Noise equivalent bandwidth (Hz)	1/8
SNR	57
Exp. NNEA (W.cm <sup>-1</sup> .Hz <sup>-1/2</sup> )	1.92 10 <sup>-9</sup>
Corrected FEM NNEA (W.cm <sup>-1</sup> .Hz <sup>-1/2</sup> )	1.92 10 <sup>-9</sup>

Table 3.24: Experimental results for C2 with its recovery cavity and optimal dual-tube resonators.

Despite the fact that the simulation predicts an acoustic quality factor higher than the real one (343 instead of 11), the FEM coupled quality factor (6,266) is lower than the measured one (22,600) which is unexpected. This difference might come from experimental uncertainties as the tubes are difficult to machine and align which may lead to a modified coupling with the tuning fork.

Taking into account the quality factor difference (rule of three of the squared root quality factor difference), we may correct the simulated value to  $1.92 \cdot 10^{-9} \text{ W.cm}^{-1}.\text{Hz}^{-1/2}$  which is identical to the experimental value and similar to state-of-the-art sensitivity [80].

Finally, this example warn us about the validity of our models in such cases. Despite the fact that we can explain the discrepancy, we started to have thermoviscous damping implemented in our solver which should correct most of the observed discrepancies.

### 3.3 Conclusion

To conclude this chapter, we presented the analysis of different detectors and setups used in photoacoustics. The comparison between analytical model and experiments is summed up in Tables 3.25 and 3.26. Concerning MPAS and CEPAS, we demonstrated that we could model the detector  $SNR_{1Pa}$  and the acoustic amplification using resonant or "non-resonant" cells. The experimental results are usually of the same order of magnitude as the analytical ones. Nonetheless, large discrepancies are observed when the detector  $SNR_{1Pa}$  was limited due to important acoustic background noise or electronic noise. Other discrepancies originate from the fact that we did not possess sufficient details to precisely model the setups from literature. To find a better agreement we would need to deeper study these systems experimentally which was not possible nor the aim of this PhD thesis. We finally studied the first version of Mirsense differential cell and found that the theoretical description of such small cells is difficult even with FEM simulations. For such cells, the experimental analysis should be privileged.

We also studied in detail the use of watch or custom QTFs and found a good agreement with our analytical model when computing their frequency and quality factor. For these we chose not to use their  $SNR_{1Pa}$  here (but in Chapter 4), as this value cannot be derived from experiments, due to the complex coupling of acoustic waves with QTFs. Instead, we compared the analytical and experimental NNEA values for which we found a good agreement.

Microphones						Cantilevers				
Name		UC-57	BK4179	EK23024	AKU143	Name		A	B	C
$SNR_{1Pa}$ (dB.Pa <sup>-1</sup> )	Ana.	135	151	120	117	$SNR_{1Pa}$ (dB.Pa <sup>-1</sup> )	Ana.	153	150	140
	Exp.	117	146 / 126 / 127	127	116		Exp.	-	-	131

QTFs							
Name		Euroquartz	QTF#5	U1	U2	C1	C2
NNEA (W.cm <sup>-1</sup> .Hz <sup>-1/2</sup> )	Ana.	3.3 10 <sup>-8</sup>	3.5 10 <sup>-7</sup>	2.6 10 <sup>-8</sup>	1.5 10 <sup>-8</sup>	2.5 10 <sup>-8</sup>	4.4 10 <sup>-8</sup>
	Exp.	4 10 <sup>-8</sup>	1.25 10 <sup>-6</sup>	4 10 <sup>-8</sup>	-	-	1.8 10 <sup>-8</sup>

Table 3.25: Comparison of the different detectors  $SNR_{1Pa}$  or NNEA.

MPAS							
System Reference		Cell 3 [54]	Cell 4 [54]	Cell 5 [168]	Cell <sub>diff</sub> 1 [46]	Cell <sub>diff</sub> 2 [173]	Mirsense cell This work
NNEA (W.cm <sup>-1</sup> .Hz <sup>-1/2</sup> )	Ana.	7.8 10 <sup>-10</sup>	1.4 10 <sup>-11</sup>	4.5 10 <sup>-11</sup>	2.4 10 <sup>-11</sup>	3.6 10 <sup>-10</sup>	8.74 10 <sup>-11</sup>
	Exp.	3 10 <sup>-10</sup>	6.7 10 <sup>-11</sup>	1 10 <sup>-9</sup>	2.4 10 <sup>-10</sup>	4.4 10 <sup>-9</sup>	1.6 10 <sup>-9</sup>

CEPAS				
System Reference		Cell 6 [74]	Cell 7 [167]	Cell 8 [76]
NNEA (W.cm <sup>-1</sup> .Hz <sup>-1/2</sup> )	Ana.	1.7 10 <sup>-10</sup>	4.5 10 <sup>-10</sup>	9.5 10 <sup>-11</sup>
	Exp.	1.7 10 <sup>-10</sup>	2.1 10 <sup>-10</sup>	4.2 10 <sup>-10</sup>

QEPAS				
System Reference		Euroquartz + tubes This work	C2 + recovery cavity This work	C2 + recovery cavity + tubes This work
NNEA (W.cm <sup>-1</sup> .Hz <sup>-1/2</sup> )	Ana.	2.6 10 <sup>-9</sup>	9.6 10 <sup>-9</sup>	1.92 10 <sup>-9</sup>
	Exp.	2.8 10 <sup>-9</sup>	8.95 10 <sup>-9</sup>	1.92 10 <sup>-9</sup>

Table 3.26: Sensitivity comparison of the different sensors.

Ultimately, let us conclude on the NNEA of the detectors with acoustic resonators. CEPAS using a cantilever and a cell below their resonance reaches the reported state-of-the-art value of  $1.7 \cdot 10^{-10} \text{ W.cm}^{-1}.\text{Hz}^{-1/2}$  [74], accurately confirmed by our models. MPAS using a simple cell can reach  $6.7 \cdot 10^{-11} \text{ W.cm}^{-1}.\text{Hz}^{-1/2}$  [54] while using differential cells could reach  $2.4 \cdot 10^{-10} \text{ W.cm}^{-1}.\text{Hz}^{-1/2}$ . This difference between state-of-the-art NNEA values of simple or differential cells is unexpected. Nonetheless, the same microphone used in the two setups demonstrated great sensitivity to the environment, which may have been better shielded in [54].

Furthermore, we studied the coupling of QTFs with acoustic resonators, i.e. QEPAS, by means of FEM simulations. We found results similar to the literature and to experiment for the reference case (state-of-the-art watch QTF with dual tubes). We also found a very good agreement for the coupling of C2 with a cavity and tubes.

We observe that the state-of-the-art NNEA for QEPAS is still one order of magnitude inferior to MPAS and CEPAS, as seen in the literature (see Chapter 1). Despite many efforts to optimise QTFs, the sensitivity is hardly improved. We propose to study this limitation in Chapter 4.









## Chapter 4

# Comparison of photoacoustic technologies through an unified modelling

### Objectives:

The goal of this chapter is to explain the physical origins of the limitations of different photoacoustic techniques (MPAS, CEPAS and QEPAS). We will present the different systems studied in the previous chapter and draw their advantages and drawbacks, based on the new unified modelling we introduced in Chapter 2. Perspectives for improvement of QEPAS will be discussed, with the demonstration of new configurations we developed. Finally, this analysis will be extended to the different techniques.

## 4.1 Determination of the model factors for the three photoacoustic techniques

In this section we aim at describing different setups we studied in the previous chapter through quantifying the different model factors (see Section 2.3). We will keep the same heat amplitude in every computation to allow direct comparisons between the values.

### 4.1.1 Determination of the model factors for MPAS and CEPAS

For MPAS and CEPAS sensors we made two major hypotheses. We assumed that the detector did not modify the pressure field, i.e. the vibroacoustic efficiency  $\varepsilon_{va} = 1$  and that the pressure applied on the detector was homogeneous and equal to the maximal pressure amplitude generated, i.e. the acoustic-mechanic overlap  $\eta_s = 1$ . This also implies that the detector is placed where the pressure is maximal within the cell.

To support these hypotheses, the first point is that microphones and cantilevers are generally used well below their resonance frequency. Since they are not used at resonance, their displacement is limited (the displacement is proportional to the quality factor, see Equation 2.31). As a consequence, the vibration amplitude is reduced and then the pressure field near the detector should not be significantly disturbed. The second point is that the detectors are usually small with respect to the acoustic resonator and compared to the acoustic wavelength. As such, the pressure distribution on the detector should be homogeneous. This hypothesis is verified in the case of Helmholtz type differential acoustic resonators, since the pressure mode is homogeneous in the chambers and detector volume. Regarding the pressure seen by the detector, it depends on the sensor design. The detector is usually placed in the cell wall or connected to the cell by a small pipe. In the later case, it is probable that the maximum pressure amplitude inside the cell is not equal to the one experienced by the detector, due to presence

of other modes of resonance for example. To make sure of it we should study these sensors by FEM, but we do not possess enough details to do so.

We can note that these hypotheses would be invalidated if these detectors were used at their resonance frequency. In those unusual cases we should rely on FEM simulations as the detector might alter the pressure field. In addition, a vibroacoustic coupling can occur and the detector  $\text{SNR}_{1\text{Pa}}$  can be modified, as in [147] for example with a cantilever and acoustic microresonators.

Based on these hypotheses we determined the laser constant  $C_L$  and amplification factor  $A_s$  using the cell constants we derived in the previous chapter, as well as the normalised SNR (see Section 3.1).

Cell Reference	MPAS				CEPAS	
	3 [54]	4 [54]	Cell <sub>diff1</sub> [46]	Mirsense This work	6 [74]	7 [167]
$f_0$ (Hz)	1,650	950	320	3,800	10	140
$H$ ( $\text{W.cm}^{-1}$ )	$1.07 \cdot 10^{-6}$				$1.07 \cdot 10^{-6}$	
$C_L$ ( $\text{Pa.W}^{-1}.\text{cm}$ )	2.67	1.54	0.52	6.14	0.02	0.23
$A_s$	1,933	5,069	6,365	495	32,224	1,241
$C$ ( $\text{Pa.W}^{-1}.\text{cm}$ )	5,157	7,785	3,293	3,040	521	281
$\eta_s$	1				1	
$\varepsilon_{\text{va}}$	1				1	
$\text{SNR}_{1\text{Pa}}$ ( $\text{dB.Pa}^{-1}$ )	120	151	151	117	153	150
SNR	5,518	295,558	176,803	4,606	24,901	9,508
NNEA ( $\text{W.cm}^{-1}.\text{Hz}^{-1/2}$ )	$7.8 \cdot 10^{-10}$	$1.4 \cdot 10^{-11}$	$2.4 \cdot 10^{-11}$	$1.6 \cdot 10^{-9}$	$1.7 \cdot 10^{-10}$	$4.5 \cdot 10^{-10}$

Table 4.1: Model factors for microphone-based (MPAS) and cantilever-based (CEPAS) photoacoustic spectroscopy. Both techniques are enhanced by acoustic resonators. The cells were described in Section 3.1.2.

As shown in Table 4.1, the amplification factor  $A_s$  is of the order of a few thousands and is strongly correlated to the laser constant value. We expected this behaviour as the pressure in free space is proportional to the frequency while it is inversely proportional to it in resonators. As the laser constant is linear with the frequency, it is smaller for the CEPAS sensors we studied which are used below resonance at much lower frequencies than MPAS. The laser constant value enables to evaluate the NNEA that would be obtained without acoustic resonator. If the laser was focused near the detector (in a setup close to that of QEPAS) and the pressure was homogeneous on it, the microphone of Cell 4 would reach  $7.3 \cdot 10^{-8} \text{ W.cm}^{-1}.\text{Hz}^{-1/2}$  and the cantilever of Cell 6 would reach  $4.5 \cdot 10^{-6} \text{ W.cm}^{-1}.\text{Hz}^{-1/2}$ . Nonetheless, these values are computed at the same detection frequency as the complete sensors ones and could be improved linearly with the frequency. For example, if the cantilever from Cell 6 was used at its resonance frequency of 550 Hz, the NNEA would reach  $8.1 \cdot 10^{-8} \text{ W.cm}^{-1}.\text{Hz}^{-1/2}$ , provided that our model approximations still hold true.

As we already discussed in Chapter 3, the best microphones reach  $\text{SNR}_{1\text{Pa}}$  values of  $151 \text{ dB.Pa}^{-1}$ , similarly to the best cantilevers, while MEMs microphones present lower values around  $120 \text{ dB.Pa}^{-1}$ .

## 4.1.2 Determination of the model factors for QEPAS

### 4.1.2.1 Bare QTFs

Based on our analytical modelling of QTFs developed in Chapter 2, we determined the different factors of our new model. We considered  $A_s$  equal to 1 since the effect of acoustic resonance between the QTF prongs is negligible as we will see later. In addition, we approximated at first that the QTF did not modify the pressure field when vibrating as we did not model it analytically, inducing  $\varepsilon_{va} = 1$ . Eventually, we determined the value of the acoustic-mechanic overlap  $\eta_s$  by projecting the acoustic mode on the QTF faces. For that purpose we approximated that the QTF did not distort the acoustic field by its presence. This hypothesis is a good approximation when the acoustic wavelength is large with respect to the QTF dimensions, which is generally the case. To understand and validate the behaviour of  $\eta_s$  we studied particular cases, presented in the following.

#### Validation of $\eta_s$ values for limiting cases

In this paragraph we present theoretical cases which are not representative of real systems but enable to study the model behaviour. For the different cases we studied (Table 4.2) we forced the acoustic frequency to 21.5 kHz to avoid adapting the QTF geometry and facilitate our study. The acoustic wavelength is equal to  $\lambda_{ac} = 15.5$  mm at this frequency. We arbitrarily fixed the prong length to this value in every case. In addition, we defined the gap between the prongs to be inferior to the laser waist of 100  $\mu\text{m}$  to consider that the laser pressure is homogeneous on the internal faces.

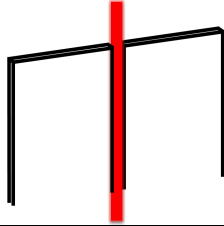
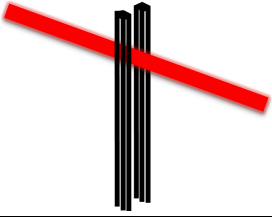
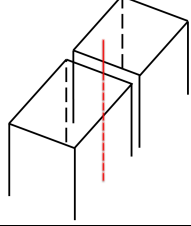
Case	1	2	3
Schematic			
$e$ (mm)	6.35	0.006	15.5
$l$ (mm)	0.001	0.001	15.5
$L$ (mm)	15.5	15.5	15.5
$g$ ( $\mu\text{m}$ )	2	2	2
$f_0$ (kHz)	21.5		
Configuration	In-plane	On-beam	In-plane
$\eta_s$	2.36	$6.5 \cdot 10^{-5}$	0.22

Table 4.2: Limit cases definition for the acoustic-mechanic overlap  $\eta_s$ .

For the first case we wanted to evaluate the maximum value of  $\eta_s$  for a given working frequency. We fixed the prong thickness  $l$  to 1  $\mu\text{m}$  so that the pressure generated is homogeneous on the prong internal face. The individual overlap  $\eta_s$  on the internal faces is then equal to 1. Afterwards we maximised the pressure differential between the external and internal prongs by varying  $e$ . We found a maximum for  $e = 6.35$  mm which is slightly inferior to half the acoustic wavelength. Indeed as we can observe in Figure 2.7, the maximal differential pressure is obtained for a distance from laser axis slightly inferior to  $\lambda_{ac}/2$ . We obtained a maximal value of  $2.36 = 1 + 1 + 0.18 + 0.18$ , meaning the pressure amplitude on one external face is approximately 6 times inferior than on the internal one at this frequency. This also means that at this frequency the overlap  $\eta_s$  of a bare QTF

will never reach the maximal possible value of  $\eta_s = 4$ . Indeed, before reaching the external faces, the pressure is reduced significantly. This is worsen when the gap between the prongs is important compared to the laser waist. This maximum of 4 is thus impossible to reach for any QTF in free space.

For the second case, we wanted to verify that we could minimise the value of  $\eta_s$ . We kept the same prong thickness as for the first case but reduced the prong width to  $e = 6.35 \mu\text{m}$ . This way, the pressure on the external prongs is very close to the one on the internal prongs and the differential is minimised. We also changed the configuration to on-beam so that the pressure is no longer homogeneous on the prongs. As a consequence we verified that the overlap value tends towards zero.

Finally, we studied a last case to make an important remark about our factor  $\eta_s$ . In order to maximise the pressure seen by the QTF faces (thus the photoacoustic force) we studied a QTF whose dimensions are far larger than the laser waist. This resulted in an overlap value of 0.22. Despite maximising the photoacoustic force, the value of the overlap was not increased compared to the previous cases. This is because our factor takes into account not only the photoacoustic force but also the homogeneity of the pressure amplitude on the detector faces. In this case, as the QTF prong thickness is superior to the laser waist, the pressure amplitude is not homogeneous on the QTF faces and the value of the overlap is reduced compared to Case 1.

Through the study of these cases we demonstrated a good understanding of the acoustic-mechanic overlap factor  $\eta_s$ , which will help us interpret the results for real cases.

### Model factors for bare QTFs

In this section, we determined the different factors for the QTFs we studied in Chapter 3 and presented the results in Table 4.3. We here consider the use of on-beam configuration as it is the most widely used in QEPAS. We will comment on the different values and the resulting sensitivity.

QTFs						
Name	Euroquartz	QTF#5	U1	U2	C1	C2
$f_0$ (Hz)	32,768	2,871	4,765	12,700	42,700	21,500
$H$ ( $\text{W.cm}^{-1}$ )	1.07 $10^{-6}$					
$C_L$ ( $\text{Pa.W}^{-1}.\text{cm}$ )	36	5	7.7	17.2	44	26
$A_s$	1					
$C$ ( $\text{Pa.W}^{-1}.\text{cm}$ )	36	5	7.7	17.2	44	26
$\eta_s$	0.38	0.10	0.35	0.49	0.97	0.82
$\varepsilon_{\text{va}}$	1					
$\text{SNR}_{1\text{Pa}}$ ( $\text{dB.Pa}^{-1}$ )	136	146	155	147	130	136
SNR	87	10	152	198	140	142
NNEA ( $\text{W.cm}^{-1}.\text{Hz}^{-1/2}$ )	$4.7 \cdot 10^{-8}$	$4.2 \cdot 10^{-7}$	$2.7 \cdot 10^{-8}$	$2.1 \cdot 10^{-8}$	$3 \cdot 10^{-8}$	$2.9 \cdot 10^{-8}$

Table 4.3: Analytical model factors for QTFs in free space and in on-beam configuration.

Firstly, the laser constant  $C_L$  is linear with the frequency in free space<sup>1</sup>, by definition (Equation 2.7), which is more beneficial for C1 and Euroquartz. However, it should be kept in mind that working at high frequencies

<sup>1</sup>A small discrepancy can be observed due to the difficult convergence of the non-approximated equation for the computation of the pressure amplitude.

with gases presenting slow relaxation times reduces the overall sensitivity (see Section 2.1.2).

Secondly, the acoustic-mechanic overlap  $\eta_s$  values spread out from 0.10 to 0.97. These are well below the maximum of 4, meaning that the different QTFs catch only a small fraction of the maximal pressure amplitude generated by the laser beam. We determined that this factor was linearly correlated with the ratio of the prong length with the acoustic wavelength,  $L/\lambda_{ac}$ , as shown in Figure 4.1. Increasing this ratio allows to catch a more important part of the pressure amplitude. This pressure amplitude decreases with the distance from the laser beam (Figure 2.6) and is more important at distances below the acoustic wavelength. We also observe that the values are distributed from each part of the linear fit. This distance to the fitted line depends on the QTF prong thickness and width. The smallest the QTF thickness is compared to the laser waist, the better the overlap, because the pressure will be homogeneous on the prong. For example, despite similar design, as C1 thickness is halved compared to C2, its overlap value is higher. Concerning the QTF prong width, it modifies the pressure differential between the external and internal faces. Also, QTFs presenting a low frequency such as QTF#5 will present lower overlaps because, their size being limited, their width cannot be adapted to the acoustic wavelength. For the same reason, high frequency QTFs for which the prong width was not adapted to the acoustic wavelength will present average overlaps (e.g. Euroquartz, U1 and U2). Ultimately, QTFs adapted to the acoustic wavelength will present higher overlaps (e.g. C1 and C2). It should be noted that the QTF gap should also be taken into consideration: the smaller the gap, the larger the pressure amplitude applied on the prongs.

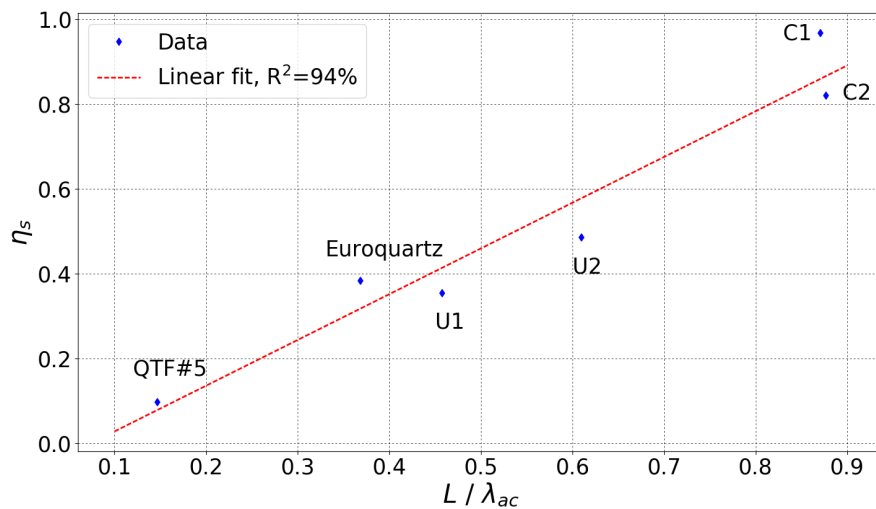


Figure 4.1: Evolution of the static overlap  $\eta_s$  with the ratio of the prong length with the acoustic wavelength.

The third factor,  $SNR_{1Pa}$ , is maximised when the prong surface is large and the damping is small (high quality factor, small mass and low frequency) by definition (Equation 2.37). The smallest values are around  $130 \text{ dB.Pa}^{-1}$  for C1, which is  $10 \text{ dB.Pa}^{-1}$  better than for MEMs microphones. The best value of  $155 \text{ dB.Pa}^{-1}$  was obtained for U1 which is higher than the one of the best microphones and cantilevers (see Table 4.1).

To conclude, despite presenting the best  $SNR_{1Pa}$ , U1 presents a similar sensitivity compared to others QTFs. The same goes for the C1 and Euroquartz for which the pressure amplitude is greater. We conclude that the sensitivity is not the result of a single factor. To obtain good sensitivities a good compromise between the laser constant  $C_L$  (resonance frequency), overlap  $\eta_s$  and  $SNR_{1Pa}$  must be reached. Optimising only one of these factors might not allow to improve the sensitivity of a bare QTF. Nonetheless, we can note that for maximising the acoustic-mechanic overlap of any QTF we may use another configuration. By using the QTF in in-plane configuration, where the laser beam is parallel to the QTF prongs contrarily to on-beam, the overlap should be increased as we will verify in Section 4.2.1.



## FEM modelling in static operation

Analytically, we considered that the QTF does not modify the pressure field by its presence which is a common hypothesis [79]. To determine if this hypothesis is correct, we modelled the different QTFs by FEM. At first, we studied the case in which the QTFs do not vibrate and obtained the results presented in Table 4.4.

QTFs						
Name	Euroquartz	QTF#5	U1	U2	C1	C2
$A_s$	1.16	1.01	1.15	1.15	1.47	1.25
Analytical $\eta_s$	0.38	0.1	0.35	0.49	0.97	0.82
FEM $\eta_s$	0.6	0.12	0.36	0.89	0.91	0.98

Table 4.4: Model results obtained through FEM for QTFs in static operation and comparison with analytical acoustical-mechanical overlap.

The static amplification factor  $A_s$  is close to 1 in each case as we expected. By definition, this factor takes into account the acoustic pressure amplification that should be equal to 1 without resonator. In order to understand the results, we studied the influence of the QTF parameters on it. Particularly we found that this factor increases when the gap between the prongs becomes comparable to the acoustic wavelength, as shown in Figure 4.2. This increase is explained both by a resonance of the acoustic waves inside the gap space and by the diffraction of the acoustic waves by the QTF. It should also depend on the QTF thickness. At most we obtained a value of  $A_s = 1.47$  for C1. In this case, the analytical model thus presents a discrepancy of 47% compared to FEM.

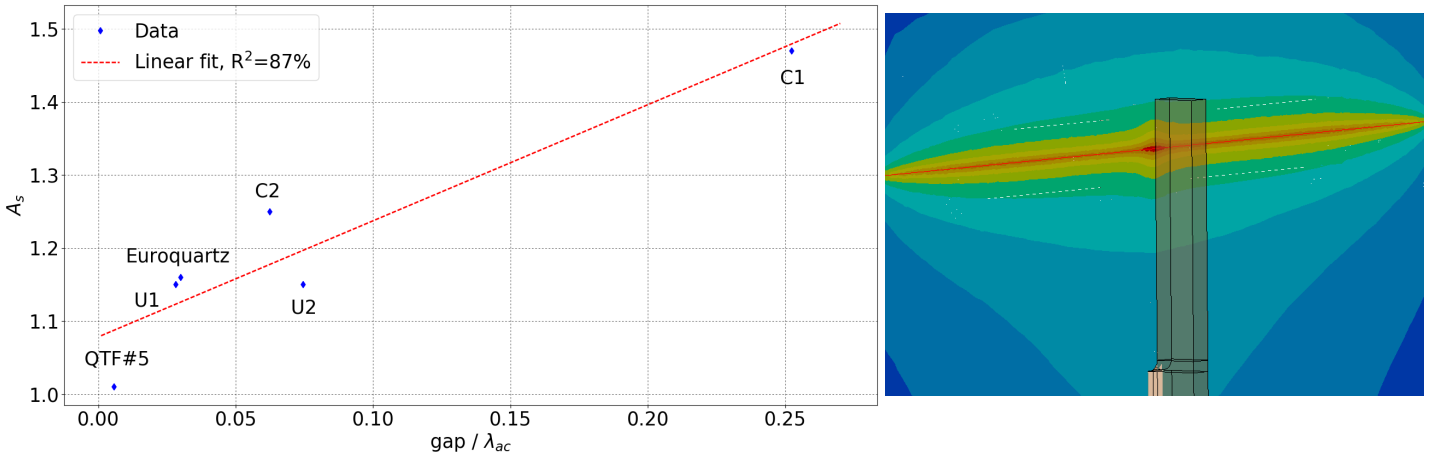


Figure 4.2: (Left) Evolution of the static pressure amplification  $A_s$  with the ratio of the gap with the acoustic wavelength. (Right) FEM simulation of the acoustic pressure amplitude around the QTF Euroquartz immobilised.

We also derived the static overlap from FEM simulations. In most cases a good agreement is reached. Nonetheless, for Euroquartz, for example, we found 0.6 instead of 0.38, representing a relative error of 57 %. For the same reason as presented for  $A_s$ , the acoustic mode shape is modified by the QTF. As can be seen in Figure 4.2 for Euroquartz, the QTF presence induces a distribution of the pressure amplitude inside the prongs. This effect is more important when the gap is of the same order as the laser waist. Another difference compared to the analytical case is the pressure modification on the external face due to the geometrical shielding of the source by the prong. This second effect is limited when the QTF dimensions are smaller than the acoustic wave-

length. Indeed, in these cases, the laser contribution to the overall generated pressure will be greater outside of the prong space compared to the inside, given the small QTF thickness.

To conclude, the hypothesis that the QTF does not modify the acoustic pressure field is generally a good approximation and enables to avoid time consuming simulations. However, when a better precision is required we should rather rely on FEM, particularly in cases where the QTF dimensions are close to the acoustic wavelength or when the gap is small compared to the laser waist.

### FEM modelling of the vibroacoustic interaction and discussion on $\varepsilon_{va}$

We previously showed that the presence of the QTF does not significantly impact the pressure field in static operation. However, the vibroacoustic effect also has to be taken into account. When vibrating, the resonator displacement induces a modification of the acoustic pressure field as shown in Figure 4.3 and interferes with the photoacoustic source. To our best knowledge, this effect has never been taken into account analytically for QTFs in photoacoustic spectroscopy. Herein, we will present new FEM simulations to evaluate its impact.

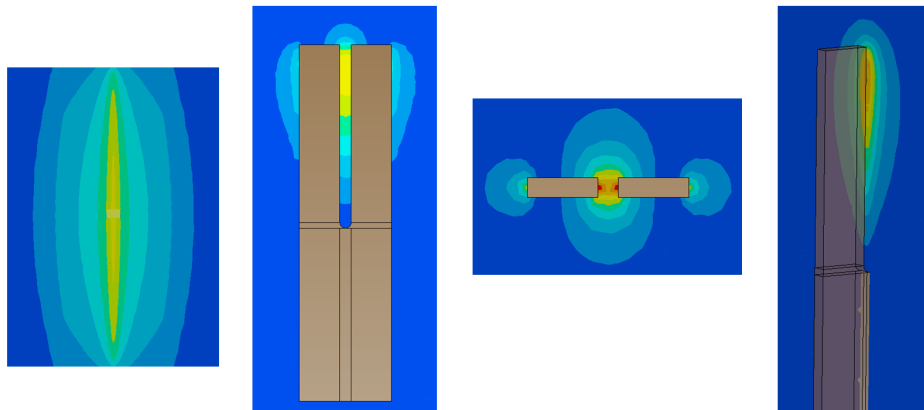


Figure 4.3: Illustration of the quadrupolar emission of a QTF (U1 in this case). Pressure amplitude distribution generated by the laser source (Left). Pressure amplitude generated by the vibration of the QTF excited by a mechanical force: from the left to the right; face, top and three-quarter view.

We can study the pressure amplitude resulting from the interference of the QTF vibroacoustic emission with the acoustic source, as shown in Figure 4.4. We first observe that some QTFs modify the surrounding pressure field more than others. For example, QTF#5 is very small compared to the acoustic source and to the acoustic wavelength and no major impact on the pressure field is observed by FEM. The Euroquartz and U1 motions do slightly affect the acoustic source while U2, C1 and C2 motions significantly alter the pressure distribution. We expect these modifications to depend on many parameters such as the QTF geometry, frequency and quality factor. To determine their origin, these effects were quantified by means of our model and we present the results in Table 4.5.

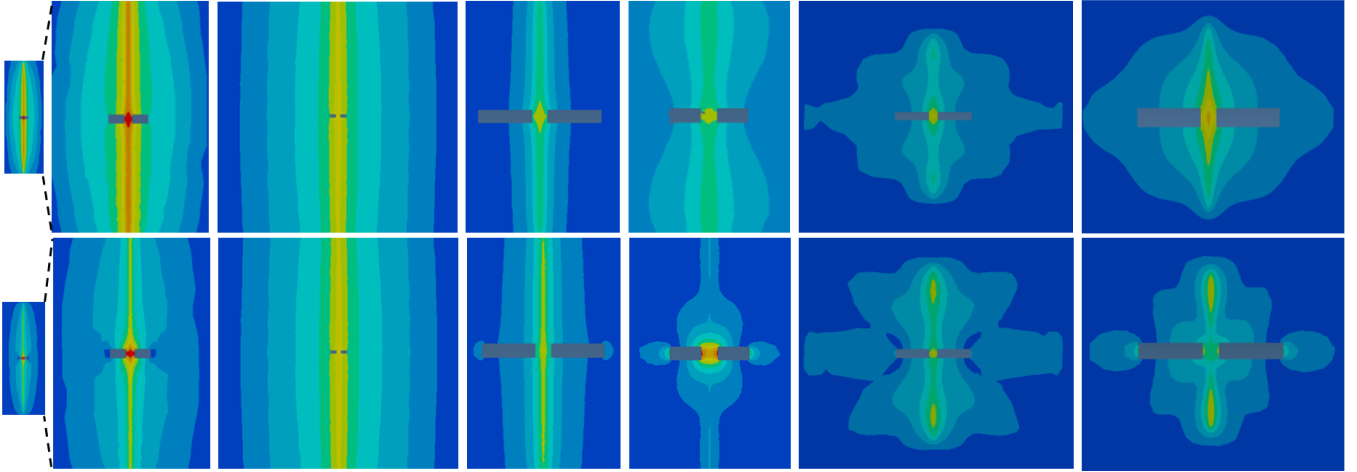


Figure 4.4: Top view FEM simulated pressure amplitude for the studied QTFs immobilised (top) and resonating (bottom). The QTFs are scaled geometrically, the pressure amplitude colors were not scaled and are different for each case. From the left to the right: Euroquartz, zoomed Euroquartz, QTF#5, U1, U2, C1, C2.

QTFs						
Name	Euroquartz	QTF#5	U1	U2	C1	C2
$H$ ( $\text{W.cm}^{-1}$ )	$1.07 \cdot 10^{-6}$					
$C_L$ ( $\text{Pa.W}^{-1}.\text{cm}$ )	36	5	7.7	17.2	44	26
$A_s$	1.16	1.01	1.15	1.15	1.47	1.25
$C$ ( $\text{Pa.W}^{-1}.\text{cm}$ )	41.8	5	8.9	19.8	64.7	32.5
$\eta_s$	0.6	0.12	0.36	0.89	0.91	0.98
$\varepsilon_{va}$	0.79	0.96	0.77	0.54	0.86	0.44
$\text{SNR}_{1\text{Pa}}$ ( $\text{dB.Pa}^{-1}$ )	136	146	155	147	131	136
SNR	126	12	159	281	186	94
NNEA ( $\text{W.cm}^{-1}.\text{Hz}^{-1/2}$ )	$3.3 \cdot 10^{-8}$	$3.5 \cdot 10^{-7}$	$2.6 \cdot 10^{-8}$	$1.5 \cdot 10^{-8}$	$2.2 \cdot 10^{-8}$	$4.4 \cdot 10^{-8}$

Table 4.5: FEM model factors for QTFs vibrating in free space.

As seen in Figure 4.4, Euroquartz vibration amplifies the pressure between the prongs, U2 amplifies it near its prongs, in turn, C1 and C2 deplete the acoustic source pressure amplitude. We expect this modification to come from the prong displacement, squeezing the fluid volume inside the gap.

We derived the vibroacoustic efficiency  $\varepsilon_{va}$  (defined in Section 2.3) and found values ranging from 0.44 to 0.96. This means that if we apply a force on a vibrating C2, the resulting force that would be obtained in static is more than halved. Based on these values we can say that the QTFs QTF#5, C1, Euroquartz, and U1 catch the most efficiently the applied photoacoustic force, while C2 and U2 perform poorly.

The origin of this factor is complex. We expect that while the QTF vibrates it pushes away the fluid surrounding it. By doing so, a part of the acoustic force is lost because it no longer applies on the prongs. To understand this factor we studied its evolution depending on the system parameters. We found that the inverse of the vibroacoustic efficiency depends on the ratio of the gap with the acoustic wavelength, in the same way as the static overlap  $\eta_s$ . We plotted it in Figure 4.5 and found a satisfying fit of 99%. Nonetheless, we had to discard C1 whose value is surprisingly far from the one of C2 despite their similitude. We could not find an explanation for this difference but it is possible that the relation we found is not exact and that other parameters should be taken into account.

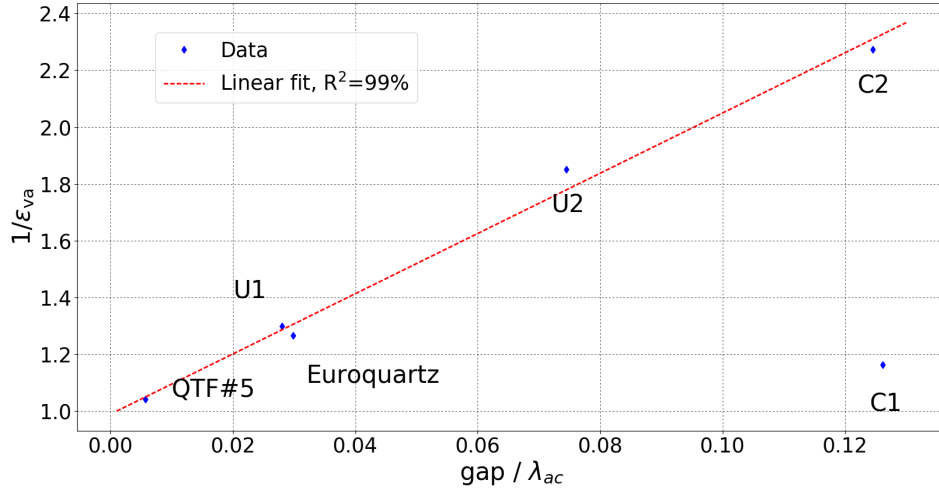


Figure 4.5: Evolution of the vibroacoustic coupling efficiency  $\varepsilon_{va}$ .

Finally, these factors induce a modification of the overall sensitivity. In Table 4.6 we presented the NNEA values we derived analytically and by FEM. In most cases we obtained a relative error of a few tens of percents. This relatively small difference is surprising giving the different effects we pointed out, occurring due to vibroacoustics or acoustic resonances that were not modelled analytically. Looking at these results may suggest that the analytical model is sufficient in most cases, however we cannot exclude that in particular cases, bigger discrepancies may occur. In any case, the use of FEM simulations is preferable for quantitative analysis of the system sensitivity.

QTF	Euroquartz	QTF#5	U1	U2	C1	C2
Analytical NNEA ( $\text{W.cm}^{-1}.\text{Hz}^{-1/2}$ )	$4.7 \cdot 10^{-8}$	$4.2 \cdot 10^{-7}$	$2.7 \cdot 10^{-8}$	$2.1 \cdot 10^{-8}$	$3 \cdot 10^{-8}$	$2.9 \cdot 10^{-8}$
FEM NNEA ( $\text{W.cm}^{-1}.\text{Hz}^{-1/2}$ )	$3.3 \cdot 10^{-8}$	$3.5 \cdot 10^{-7}$	$2.6 \cdot 10^{-8}$	$1.5 \cdot 10^{-8}$	$2.2 \cdot 10^{-8}$	$4.4 \cdot 10^{-8}$
Relative error (%)	42	20	4	40	36	34

Table 4.6: Comparison of the analytical and FEM NNEA.

To conclude this section, we evaluated the different model factors for tuning forks in free space. We demonstrated that the hypothesis stating that the QTF does not modify the acoustic pressure field is a good approximation in most cases. However, for large resonators compared to the acoustic wavelength, especially in the case of C2, more important discrepancies can be observed. This is also the case when an acoustic resonance occurs inside the QTFs prongs, as for the watch QTF for example. In the process, we highlighted the different phenomena occurring in a resonant photoacoustic sensor and demonstrated their dependency on the system parameters. The analysis we performed should enable us to better understand complex cases as the ones we will see in the next section.

#### 4.1.2.2 QTF coupling with acoustic resonators

After analysing the different QTFs in free space we propose to study their coupling to acoustic resonators. In the scientific literature of QEPAS, acoustic microresonators, similar to small tubes, are used and very small variations between publications are observed. As a consequence we can ask ourselves if these microresonators are already adapted and optimal, particularly in terms of overall NNEA. The coupling of QTFs with acoustic resonators is complex, reason why we will investigate the occurring effects through our unified model.

## Computation of the normalised SNR at 1 Pa

The computation of the model factors is similar to what we achieved with QTFs in free space except for one. When coupling resonators, aside from the pressure amplification another effect rises which is the modification of the total quality factor. We previously saw for example that coupling a watch tuning fork with dual tube resonators presenting quality factors of 9,100 and 14 respectively, results in a system overall quality factor of 3,200 (see Section 3.2.2). To take into account this effect we chose to take the quality factor modification effect inside the factor  $\text{SNR}_{1\text{Pa}}$  (defined in Section 2.3). This means that in the cases where the overall quality factor decreases, the  $\text{SNR}_{1\text{Pa}}$  will also decrease.

## Watch QTF with dual tubes microresonators

In this section we will study the coupling of the QTF Euroquartz with dual tube resonators that we already presented in Section 3.2.2. To better understand the evolution of the different factors in this first case we computed them for different tube lengths from each part of the optimal coupling. We remind that we obtained an optimal coupling, i.e. lowest system quality factor, for tubes measuring 4.3 mm each and presenting a radius of 0.46 mm. The factors obtained for the best coupling are summed up in Table 4.7.

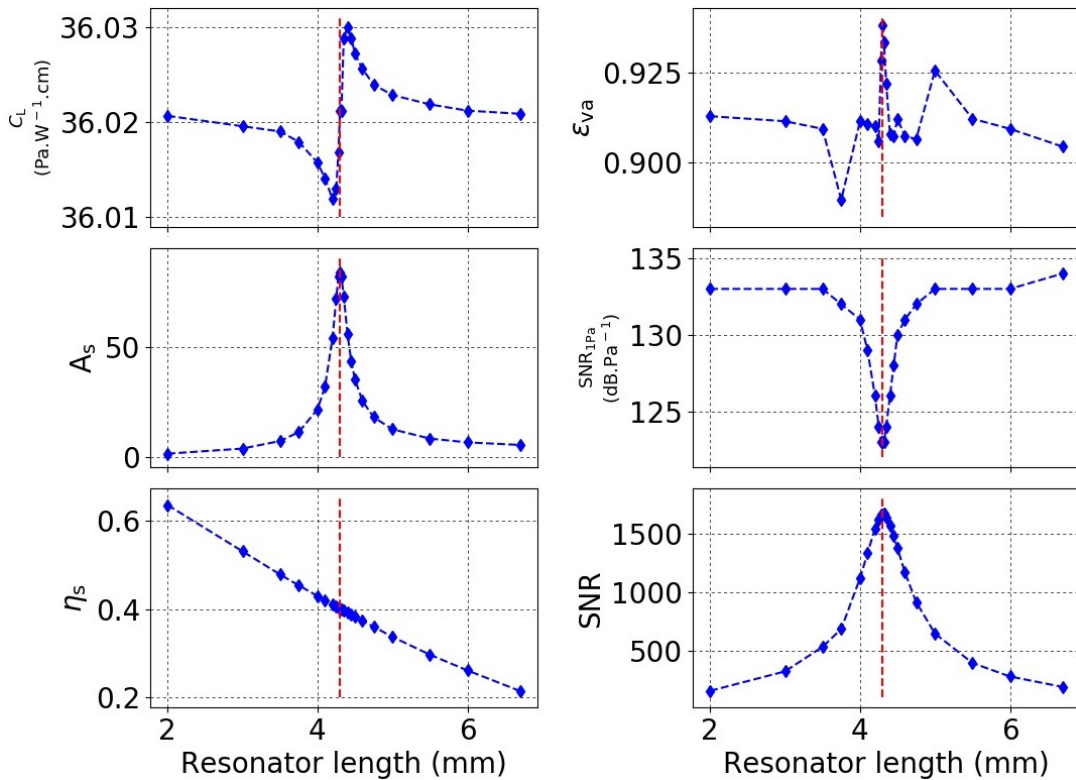


Figure 4.6: Evolution of the model factors for the coupling of Euroquartz with dual tubes

When changing the resonator length, a frequency anti-resonance is observed. By definition, the laser constant  $C_L$  is proportional to the frequency and hence presents the same shape as shown in Figure 4.6. The frequency varies of 10 Hz, inducing a very little variation of the laser constant around 36.02 Pa.W<sup>-1</sup>.cm.

The second factor is the static pressure amplitude amplification  $A_s$  that was approximately equal to 1 in

free space. Here we see that by tuning the resonator length we increase the pressure amplitude up to a factor 82. This amplification is due to the tuning of the dual tube resonator to its longitudinal resonance frequency. It should be noted that the maximal pressure amplitude is located in the middle of each tube. Taking into account these first two factors, the cell constant then reaches  $2,945 \text{ Pa.W}^{-1}.\text{cm}$ .

We also derived the static acoustical mechanical overlap  $\eta_s$  and found values from 0.2 to 0.6. These are similar to the one obtained for the QTF in free space for which we found 0.6. The presence of the tube thus does not significantly change the resulting overlap. The mean value is far from the theoretical maximum of 4 we defined for QTFs meaning that the pressure is not homogeneous on the prongs and that its value is far from the maximum pressure generated by the tubes. We can also remark that its value decreases with the resonator length. This effect is surely due to the fact that the pressure maximum inside the tube is more and more distant from the QTF (since the maximum is located in the middle of a tube and that the tube length increases) and then that the pressure arriving onto the QTF is reduced compared to the maximum.

The vibroacoustic efficiency  $\varepsilon_{va}$  is almost constant with a small peak reaching 0.94 for the optimal coupling. This value can be compared to 0.8 in free space, showing that the effect of the QTF vibration is almost constant for this QTF, despite the addition of the resonators.

The  $\text{SNR}_{1\text{Pa}}$  value decreases when the best coupling is obtained that is induced by the system quality factor drop when coupling low quality factor acoustic resonators to high quality factor QTF. It passes from  $136 \text{ dB.Pa}^{-1}$  in free space to  $123 \text{ dB.Pa}^{-1}$ , hence a decrease of a factor 4.

Finally, the SNR increases by a factor 13 compared to free space and its maximal value is obtained at the best coupling. Despite the many effects we saw previously, the SNR curve shape is remarkably similar to the static pressure amplitude amplification.

System	Euroquartz	Euroquartz + dual-tubes
$H \text{ (W.cm}^{-1}\text{)}$	$1.07 \cdot 10^{-6}$	
$C_L \text{ (Pa.W}^{-1}\text{.cm)}$	36	
$A_s$	1.16	81.8
$C \text{ (Pa.W}^{-1}\text{.cm)}$	41.8	2,945
$\eta_s$	0.6	0.4
$\varepsilon_{va}$	0.79	0.94
$\text{SNR}_{1\text{Pa}} \text{ (dB.Pa}^{-1}\text{)}$	136	123
SNR	126	1,671
$\text{NNEA (W.cm}^{-1}\text{.Hz}^{-1/2}\text{)}$	$3.3 \cdot 10^{-8}$	$2.6 \cdot 10^{-9}$

Table 4.7: FEM model factors for Euroquartz with dual tubes at the optimal coupling ( $L_{mr} = 4.3 \text{ mm}$ ).

To conclude, the use of dual tube resonators enables a huge increase of the cell constant  $C$  by a factor 82. Nonetheless, this pressure maximum is located in the middle of the tubes and is not efficiently distributed on the QTF prongs as the overlap suggests. Furthermore, the sensor  $\text{SNR}_{1\text{Pa}}$  is reduced due to the coupling of the two resonators. Despite these non-optimal factors, the overall sensitivity still is increased by a factor 13, reaching the state-of-the art. From these results we conclude that there may be a way to increase QEPAS sensitivity, through the optimisation of the resonator coupling to the QTF. Particularly, by increasing the overlap of the acoustic pressure on the QTF and by increasing the system quality factor it should be possible to design acoustic resonators better adapted to QEPAS.

## C2 with acoustic resonators

After analysing the different results for a reference case, we herein present the study of the different acoustic resonators we have coupled with QTF C2. In Section 3.2.2, we presented two different systems. Firstly, the use of an acoustic recovery cavity that enables the recovery of the acoustic waves emitted by the QTF. Secondly, the addition of dual tubes resonators in a same way as what is done for watch QTFs. For these systems, we derived the model factors for the optimal coupling and presented the results in Table 4.8.

System	C2	C2 + recovery cavity	C2 + recovery cavity + tubes
$H$ (W.cm <sup>-1</sup> )	1.07 10 <sup>-6</sup>		
$C_L$ (Pa.W <sup>-1</sup> .cm)	26		
$A_s$	1.25	1.32	300
$C$ (Pa.W <sup>-1</sup> .cm)	32.5	34.3	7,800
$\eta_s$	0.98	0.83	0.027
$\varepsilon_{va}$	0.44	0.8	0.86
SNR <sub>1Pa</sub> (dB.Pa <sup>-1</sup> )	136	145	141
SNR	94	431	2,163
NNEA (W.cm <sup>-1</sup> .Hz <sup>-1/2</sup> )	4.4 10 <sup>-8</sup>	9.9 10 <sup>-9</sup>	1.92 10 <sup>-9</sup>

Table 4.8: FEM model factors for C2 with acoustic resonators derived for the optimal coupling.

About the use of the acoustic recovery cavity, the static pressure amplification is similar to the one in free space because this cavity is not resonant with the acoustic source. The same goes for the static overlap  $\eta_s$  passing from 0.98 to 0.83. When the QTF vibrates, the force seen by the QTF is increased by a factor 2, as can be inferred from the value of  $\varepsilon_{va}$ , which may be explained by the recovery of the acoustic waves. Finally, the enhancement of the system quality factor, due to recovery of the acoustic waves, induces an increase of the SNR<sub>1Pa</sub> passing from 136 to 145 dB.Pa<sup>-1</sup>. Despite the fact that this cavity does not amplify the pressure, the SNR is improved by a factor 4 that is mainly the result of the quality factor enhancement.

When adding dual tube resonators to the previous cavity, the pressure is importantly amplified by a factor 300 due to the small radius of these tubes. Nonetheless, the static overlap value is importantly reduced, even more than for the watch QTF. The difference here is that the tubes radius is smaller and the QTF way bigger, causing an important acoustic impedance between the tubes and then a reduced pressure caught by the QTF as well as its non-homogeneity. The vibroacoustic efficiency is equal to 0.86, similar to the cavity alone. Finally, the SNR<sub>1Pa</sub> is slightly decreased compared to the case of the cavity, passing from 145 to 141 dB.Pa<sup>-1</sup>. Thanks to the huge pressure amplification, the system overall sensitivity is improved by a factor 5 compared to the cavity alone, and by 23 compared to the bare QTF.

As a conclusion, we demonstrated that the two different systems represent two different paradigms. In the first, the use of a cavity to recover the acoustic waves emitted by the QTF enables an increase of the quality factor and so of the SNR<sub>1Pa</sub>, but in turn does not increase the pressure amplitude. In the second, the use of small tubes enables a huge pressure amplification. Nonetheless, their coupling to the QTF is far from optimal, as the pressure seen by the QTF is importantly reduced compared to the one generated inside the tubes. In addition, the coupling of small quality factor resonators to QTFs decreases the system quality factor.

These systems show that the acoustic resonators used in QEPAS are not optimal. To increase the sensitivity of QEPAS, a compromise might be found between the acoustic resonator quality factor and its pressure amplification. Furthermore, particular attention should be given to the optimisation of the overlap of the pressure mode on the QTF.

## 4.2 New developments for QEPAS sensors

Based on the conclusions of the previous section we searched for improvements of the QEPAS technique. In this section we will present two different answers which are the in-plane configuration and a radial resonator used for the first time to our knowledge in QEPAS.

### 4.2.1 In-plane configuration

In order to increase the acoustic-mechanic overlap  $\eta_s$  we evaluated the use of the technique called "in-plane" in order to quantify the achievable gain compared to on-beam configuration. Contrarily to on-beam where the laser beam is perpendicular to the prongs, the beam is now parallel to them. It has been shown in some publications that a gain, ranging from 2 to 40, could be obtained using this configuration [28, 180]. Nonetheless, this gain is hard to determine in advance for any QTF, as the prongs deformation has to be taken into account. Using our analytical model, we calculated the expected improvement of the NNEA when applying this configuration to the QTFs presented before (Section 3.2.1.1).

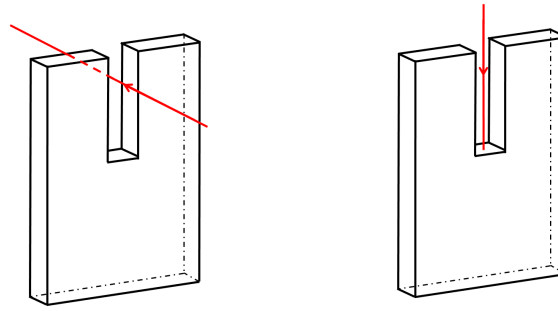


Figure 4.7: Scheme of on-beam (left) and in-plane (right) configurations.

#### 4.2.1.1 Analytical study

We implemented the use of in-plane configuration in our analytical model. The same hypothesis is made concerning the photoacoustic force computation: the QTF does not modify the pressure field (see Section 2.1.4). The results obtained for the different QTFs are presented in Table 4.9.

QTF	Euroquartz	QTF#5	U1	U2	C1	C2
$\eta_s$ on-beam	0.38	0.1	0.35	0.49	0.97	0.82
$\eta_s$ in-plane	0.79	0.43	0.75	0.72	1.29	1.1
Enhancement factor compared to on-beam	2.1	4.4	2.1	1.5	1.3	1.3
NNEA ( $\text{W}\cdot\text{cm}^{-1}\cdot\text{Hz}^{-1/2}$ )	$2.3 \cdot 10^{-8}$	$9.4 \cdot 10^{-8}$	$1.3 \cdot 10^{-8}$	$1.4 \cdot 10^{-8}$	$2.2 \cdot 10^{-8}$	$2.2 \cdot 10^{-8}$

Table 4.9: Analytical determination of tuning forks sensitivities for in-plane single pass configuration.

For most QTFs the sensitivity enhancement compared to on-beam configuration is of the order of 1 to 2, while it is expected to be larger for QTF#5. This enhancement is the result of a better overlap of the acoustic pressure on the QTF prongs and also depends on the frequency. The increase in sensitivity is thus higher for QTFs presenting a small prong length compared to the acoustic wavelength such as QTF#5, as we demonstrated previously (Section 4.1.2.1).



#### 4.2.1.2 In-plane double pass inside a custom QTF prong space

In order to validate the analytical results we studied this configuration experimentally with the setup presented in Section 3.2.1.3. We used the QTF U1 presenting a gap between the prongs of 2 mm, enabling easy laser beam alignment. The QTF was oriented horizontally and the laser beam was focused between the prongs (see Figure 4.8). To avoid the huge signal background provoked by laser heating of the QTF where the constraints are maximal, we placed a gold-coated mirror between the prongs. This mirror was cut from an available piece of gold-coated semiconductor wafer, its dimensions were 1 cm long and 1 mm large to fit between the prongs. This mirror was either oriented in order to evacuate the laser beam perpendicularly to the incident beam or oriented in autocollimation setup. Its position was set by means of a 3-axis stage (height, depth and yaw). Its reflectivity was measured to be 94% while it transmitted 100  $\mu\text{W}$  ( $<1\%$  of incident power). Also, a slight portion of the beam was diffracted and illuminated the prongs with no significant impact on the signal background in WM. To our best knowledge, this is the first time that such a multipass configuration with a bare QTF has been reported.

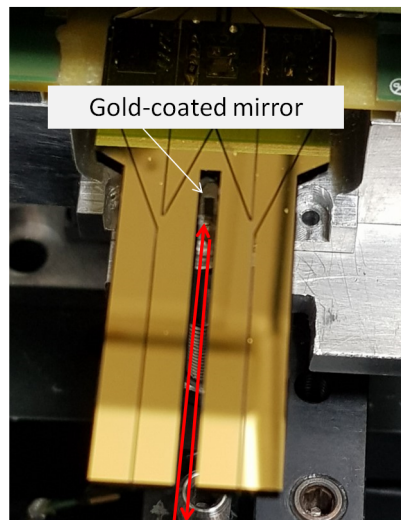


Figure 4.8: Experimental study of in-plane configuration with U1. The laser beam is focused between the prongs on the gold-coated mirror. Here the mirror was placed in autocollimation enabling a double pass between the branches.

The results are presented in Table 4.10. We compared the signal and noise in different configurations. The noise was similar in every configuration, meaning that the portion of laser beam hitting the prongs had no impact on the noise.

In-plane double pass configuration provided approximately 1.5 more signal than in single pass and 5 times more than on-beam configuration, yielding an equivalent NNEA of  $7.7 \cdot 10^{-9} \text{ W.cm}^{-1}.\text{Hz}^{-1/2}$ . A major remark can be done concerning the single and double pass configurations. The signal is not proportional to the number of laser passes as one would expect. A plausible explanation is that the laser beam single pass is not equivalent to an acoustical single pass or possibly due to acoustic interferences in double pass. Indeed, the laser beam evacuated from the prongs space must have induced a signal that contributed to the overall photoacoustic force seen by the QTF. This explanation is supported by the fact that the acoustic wavelength is large, about 7 cm, meaning that any acoustic wave generated under a multiple of this range will contribute to the signal. The signal produced by a "true" single pass configuration would be 42.5 mV, which is 2.5 times better than for on-beam. This enhancement is close to the analytical one of 2.1. The remaining difference between these values could

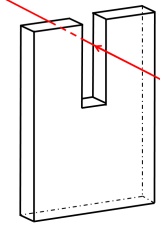
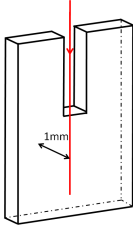
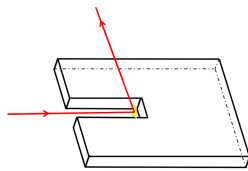
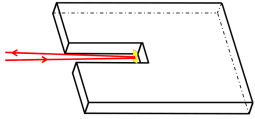
Configuration	On-beam	Vertical off-beam	In-plane single pass	In-plane double pass
Schematic				
Photoacoustic response				
Signal (mV)	17	23	57	85
Noise ( $\mu\text{V}_{\text{rms}}$ )	566			
SNR	30	40	100	155
NNEA ( $\text{W}\cdot\text{cm}^{-1}\cdot\text{Hz}^{-1/2}$ )	$4 \cdot 10^{-8}$	$3 \cdot 10^{-8}$	$1.2 \cdot 10^{-8}$	$7.7 \cdot 10^{-9}$

Table 4.10: Experimental study of in-plane configuration using a QTF U1 and wavelength modulation when measuring acetylene 1,000 ppmv. Results for on-beam configuration with the same QTF are presented for comparison.

come from more complex phenomena occurring in the QTF prong space such as acoustic diffraction which was not modelled.

We also studied another configuration where the laser beam grazes the QTF surface, we called "vertical off-beam". We placed the QTF at 1 mm from the beam (2 mm from the QTF center), this resulted in a slightly better signal than for on-beam. Such a setup facilitates laser alignment and reduces the problems due to signal background, representing an interesting option in the design of QEPAS sensors with bare QTFs.

For comparison, in [28] a NNEA enhancement of a factor 4 was reported with a watch QTF such as Euroquartz. Nonetheless, there is no indication of the experimental setup leading to this increase (single pass, double pass, laser orientation compared to the QTF,...), it is then difficult to explain the difference. More recently, a factor 40 was reported in [180], which is one order of magnitude bigger than what we computed for most QTFs. We are surprised by this enhancement based on our computations for most QTFs. A potential explanation is that the used QTF presents a different geometry from classical ones (similar to QTF#7 presented in Figure 1.11). The T-shape prongs induce a more important mass at the top of the prongs. As a consequence, the beam deformation should be more important close to the top than it is for classical QTFs, meaning a better efficiency when exalting a given surface of the prongs. Nonetheless, this difference in design hardly explains the claimed factor of 40. Anyway, this better enhancement using in-plane configuration does not necessarily mean that a QTF with such a T-shape will enable better sensitivity than a classical QTF.

To conclude, when designing a QTF the use of in-plane configuration should be kept in mind. This configuration possibly provides a significant sensitivity gain that can easily be modelled as an enhancement of the acoustic-mechanic overlap. Apart from QTFs with large gaps, the use of a laser beam passing between the prongs is hard to consider. Nonetheless, we also demonstrated that it is possible to benefit from a sensitivity gain compared to on-beam by positioning the laser beam right next to the QTF in vertical off-beam configuration.

## 4.2.2 A new radial resonator for QEPAS with C2

We have demonstrated earlier that the so-called microresonators were not the optimal resonators for efficient acoustic coupling with a QTF. Indeed, even if a large cell constant can be reached, the pressure experienced by the QTF is reduced due to the non-adaptation of the acoustic resonators, evidenced by the poor acoustic-mechanic overlap  $\eta_s$ . Moreover, the acoustic quality factors are very low (usually below 10), inducing a drop of the overall quality factor and so of the effective  $\text{SNR}_{\text{IPa}}$  of the QEPAS setup.

To tackle these issues we aimed at designing an acoustic resonator whose mode of resonance is more adapted to the QTF and of higher quality factor. We will present this new resonator in the following.

### 4.2.2.1 Design and analytical results

#### Problem definition

The new resonator looks similar to the recovery cavity presented before but relies on a different paradigm. While the recovery cavity enhances the system quality factor by cancelling the QTF acoustic emissions, it does not amplify the pressure and may also partially induce destructive interferences with the acoustic source. We here propose to study the use of a radial mode of resonance of this cavity.

Instead of recovering the acoustic waves, the cavity is made resonant with the acoustic source. This means that the resonator wall should be placed at a distance  $\lambda_{ac}/2$  from the laser beam as shown in Figure 4.9, which should theoretically increase the pressure inside the cavity and the sensor sensitivity. This new resonant cavity could thus allow to get rid of the tube resonators and offer a more convenient implementation.

The geometry of this resonator is a cylinder of length  $L_{\text{mr}} = 16$  mm, radius  $R_1$  and height  $h_{\text{mr}} = 10.2$  mm (see Figure 3.9 for geometrical parameters definition).

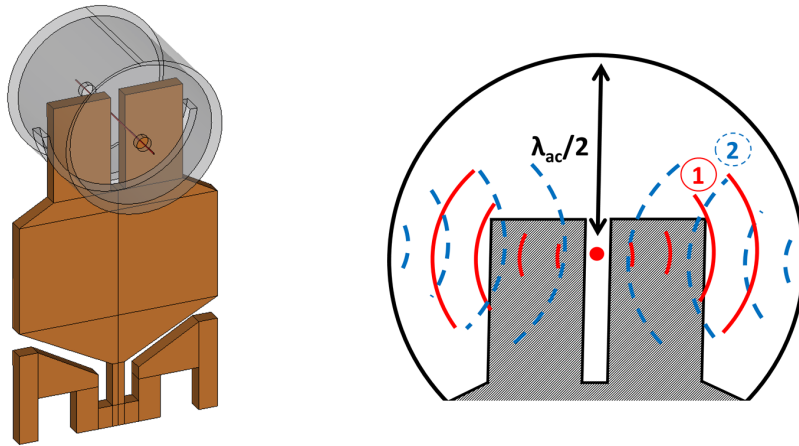


Figure 4.9: C2 with radial resonator CAD (left) and scheme presenting the condition to achieve for enabling a radial resonance of the resonator (right).

#### Theoretical study of the resonators coupling

To optimise the resonator, the first step is to adapt its frequency to match the tuning fork one. Since the acoustic mode of resonance is radial, this is accomplished by modifying the cylinder inner radius  $R_1$ . The results obtained by FEM simulations are presented in Figure 4.15.

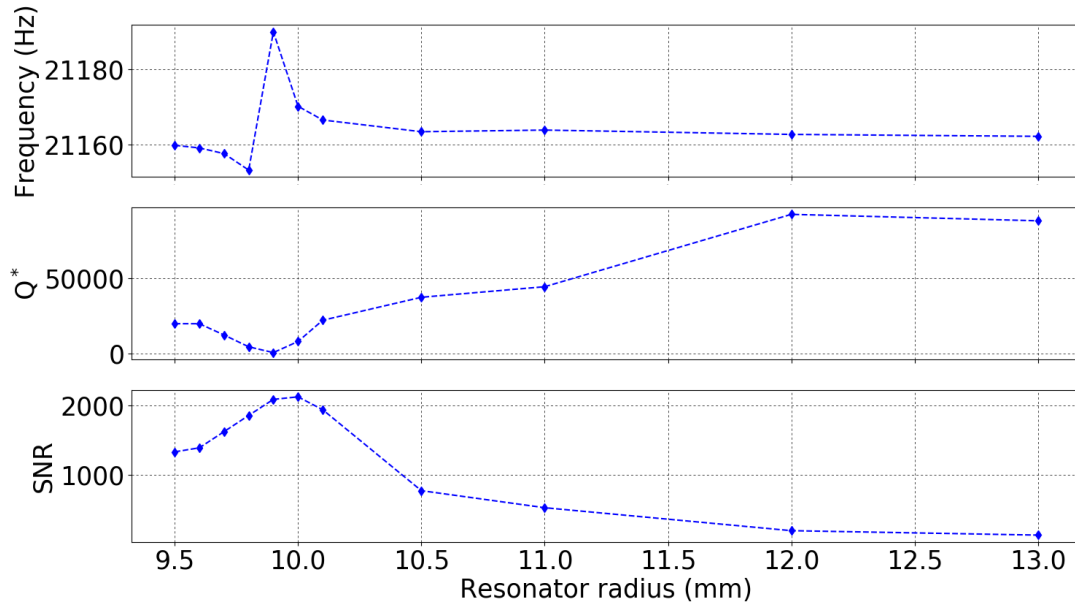


Figure 4.10: FEM results for frequency, quality factor and SNR for C2 when varying the radial resonator radius.

Radii smaller than 9.5 mm cannot be studied since the acoustic resonator would be too small for the QTF to fit in, meaning that we will not be able to access one part of the graphs. Nonetheless we recognise the typical curves obtained when coupling resonators with a best coupling for  $R_1 = 9.88$  mm. The system quality factor starts from 94,000 when the systems are not coupled for a radius of 12 mm, and decreases down to 602 when the coupling is maximum. We should note that this decrease is more important than for the same QTF with the recovery cavity and tubes. The SNR instead reaches a maximum of 2,129 around  $R_1 = 9.88$  mm. It is approximately 15 times the SNR we derived for the bare QTF, that is similar to the enhancement we obtained using C2 within its cavity and tubes.

For the optimal radius one can observe the establishment of a radial mode of pressure inside the resonator, as can be seen on Figure 4.11. The pressure is amplified between the QTF prongs which is in addition extended along the laser beam axis. We can also remark that a portion of the pressure leaks through the holes made in the resonator for laser beam pass and through the slit made for the fork to fit in.

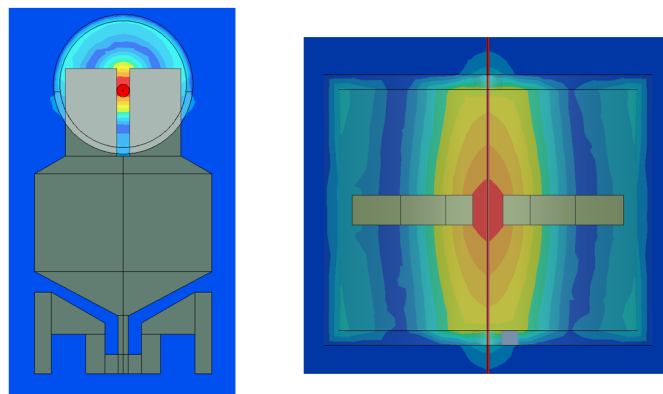


Figure 4.11: Pressure amplitude FEM modelling of C2 with the optimal radial resonator of radius  $R_1 = 9.88$  mm. The QTF is coloured in grey and the laser in red. Front view (left), top view (right).

For such a resonator, we derive the acoustic quality factor to  $Q_{ac,radiation} = 246$  using our FEM solver (without considering thermoviscous losses), when the tuning fork is present but not vibrating. When we remove

the QTF, this quality factor goes up to 2,335, showing that its presence inside the resonator significantly impacts the mode of resonance.

We also estimated the thermoviscous losses analytically. Considering a perfect cylinder, with no openings, of same radius and length, we found analytically a quality factor  $\left[Q_{ac,volume,n}^{-1} + Q_{ac,thermal,n}^{-1} + Q_{ac,viscous,n}^{-1}\right]^{-1} = 500$ , which was confirmed using FEM with Comsol thermoviscous module [160].

The total quality factor  $Q_{ac}$  can then be derived to be 165 when the QTF is present and 412 when it is not.

Finally, the system sensitivity was computed to be equal to  $1.95 \cdot 10^{-9} \text{ W.cm}^{-1}.\text{Hz}^{-1/2}$ , which we corrected by taking into account thermoviscous losses to  $2.9 \cdot 10^{-9} \text{ W.cm}^{-1}.\text{Hz}^{-1/2}$ . This sensitivity is similar to the one obtained experimentally for the watch tuning fork and its tubes.

These results are summed up in Table 4.11.

QTF parameters	
$f_0$ (Hz)	21,140
Coupled quality factor $Q^*$	602
Cavity parameters	
$L_{mr}$ (mm)	16
$R_I$ (mm)	9.88
FEM $Q_{ac,radiation}$	246
Corrected $Q_{ac}$	165
Photoacoustic response	
Heat amplitude ( $\text{W.cm}^{-1}$ )	$1.07 \cdot 10^{-6}$
Maximal pressure amplitude (mPa)	1
Maximal displacement (m)	$2.9 \cdot 10^{-12}$
Noise equivalent bandwidth (Hz)	1/16
Noise equivalent displacement (m)	$1.35 \cdot 10^{-15}$
SNR	2,129
FEM NNEA ( $\text{W.cm}^{-1}.\text{Hz}^{-1/2}$ )	$1.95 \cdot 10^{-9}$
Corrected FEM NNEA ( $\text{W.cm}^{-1}.\text{Hz}^{-1/2}$ )	$2.9 \cdot 10^{-9}$

Table 4.11: FEM results for C2 with its radial resonator for the best SNR.

## Computation of the model factors

Based on the previous results we computed the model factors to better understand the coupling of the two resonators. We presented the results in Table 4.12.

System	C2	C2 + radial resonator
$H$ ( $\text{W.cm}^{-1}$ )	$1.07 \cdot 10^{-6}$	
$C_L$ ( $\text{Pa.W}^{-1}.\text{cm}$ )	26	
$A_s$	1.25	21.2
$C$ ( $\text{Pa.W}^{-1}.\text{cm}$ )	32.5	551
$\eta_s$	0.98	1.93
$\varepsilon_{va}$	0.44	0.7
$\text{SNR}_{1\text{Pa}}$ ( $\text{dB.Pa}^{-1}$ )	136	125
SNR	94	1,428
NNEA ( $\text{W.cm}^{-1}.\text{Hz}^{-1/2}$ )	$4.4 \cdot 10^{-8}$	$2.9 \cdot 10^{-9}$

Table 4.12: FEM model factors for C2 with the new radial resonator derived for the best SNR.

Compared to the bare QTF, a good pressure amplification is obtained. It is nonetheless, 5 times inferior to the pressure generated using tubes. The static overlap  $\eta_s$  reaches the best value amongst the different QEPAS systems we studied, reaching 1.93 when the theoretical maximum is 4. This best overlap is mostly due to the good match between the acoustic mode and the QTF geometry. As a result, the pressure maximum is distributed more homogeneously on the QTF prongs and the pressure difference between the external and internal prongs is optimised. Furthermore, the vibroacoustic efficiency  $\varepsilon_{va}$  is improved passing from 0.44 to 0.7. This is similar to what we obtained with the non-resonant recovery cavity. Concerning the  $\text{SNR}_{1\text{Pa}}$ , its value is importantly decreased passing from 136 to 125  $\text{dB.Pa}^{-1}$ . The resulting NNEA is improved by 23 compared to the bare QTF. While, the pressure amplification is ten times worse than when using tubes, the match between the mechanical and acoustical resonances is better, resulting in a similar sensitivity.

One should note that the good sensitivity enhancement compared to the bare QTF is obtained only thanks to the specific design of C2. Indeed, this QTF was designed to be coupled to an acoustic resonator, with a prong width equal to half the acoustic wavelength. The generated radial mode of resonance can then better overlap with the QTF prongs thanks to the pressure difference between the internal and external faces of the prongs.

To support this claim we also studied the addition of a radial resonator around a watch QTF. In this later case, we found that the optimal radial resonator dimensions were  $L_{mr} = 3 \text{ mm}$  and  $R_I = 6.5 \text{ mm}$ . The resulting coupled quality factor was derived to 9,813, compared to the 10,000 quality factor of the bare QTF, which demonstrates a poorly efficient coupling, while the sensitivity was only enhanced by a factor of 2. This enhancement is small compared to the factor 15 we obtained with C2, and can be explained by the fact that the watch QTF prongs are small before the acoustic wavelength, making the pressure differential between the internal faces and external ones very small.

These results show the importance of the QTF design when coupling acoustic resonators to it, making the QTFs similar to C2 very promising for QEPAS applications.

#### 4.2.2.2 Experimental study of the system

To confirm the promising results found in the previous paragraphs, we designed the radial resonator in duraluminium. The easiest and cost effective solution was to make cylinders of different radii and to place them inside the existing recovery cavity as shown in Figure 4.12. A metallic foil was inserted between the two mechanical parts so as to block the cylinders movement. For the smallest radii, the mechanical positioning was difficult as the space between the QTF top of the prong and the acoustic resonator wall is less than 100  $\mu\text{m}$ . The acoustic resonator was slightly machined to avoid the contact between the resonators. This could be improved in the future by adapting the geometry of the resonator and increasing the tolerances.

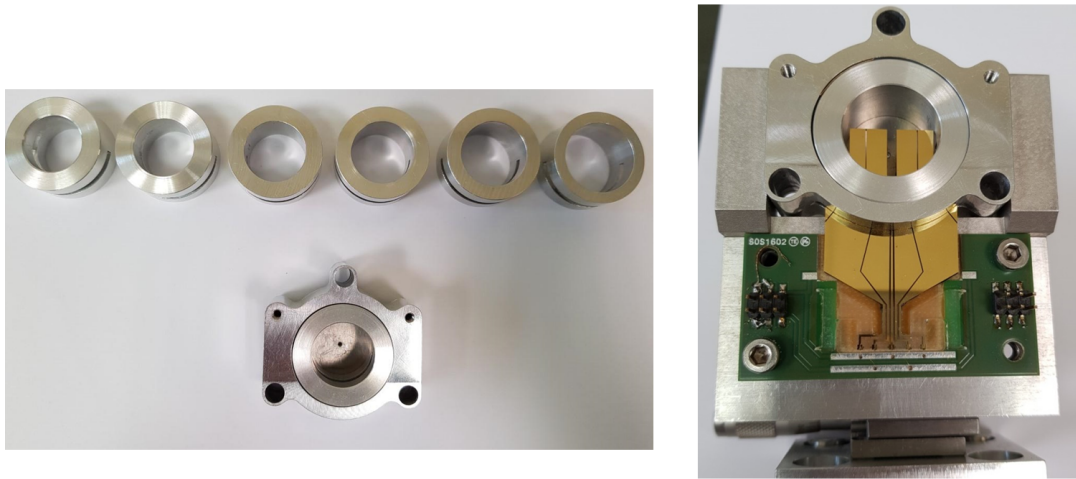


Figure 4.12: Photograph of the radial resonator with different radii (left) and photograph with C2 for a radius of 9.7 mm (right).

#### Measurement of the acoustic resonator quality factor

As this resonator is the first of the type in QEPAS, we performed additional measurements to better understand the phenomena at play.

For that purpose, we measured the photoacoustic signal in WM by use of a microphone (EK 23133, Knowles) inserted inside the resonator without the QTF, as shown in Figure 4.13. We recorded the generated photoacoustic signal depending on the frequency and sampled the resonance of the resonator found around 21,500 Hz. This resonance curve yields a quality factor of about 77 for the cylinder of radius 9.7 mm, and around 100 for other radii. This value is 4 times smaller than the value of 412 we computed when the QTF is not present. We can hardly explain this discrepancy, nonetheless an hypothesis is that the presence of the microphone, even it is small compared to the resonator, alters the mode of resonance. Additional verification should be made in the future to verify this point.

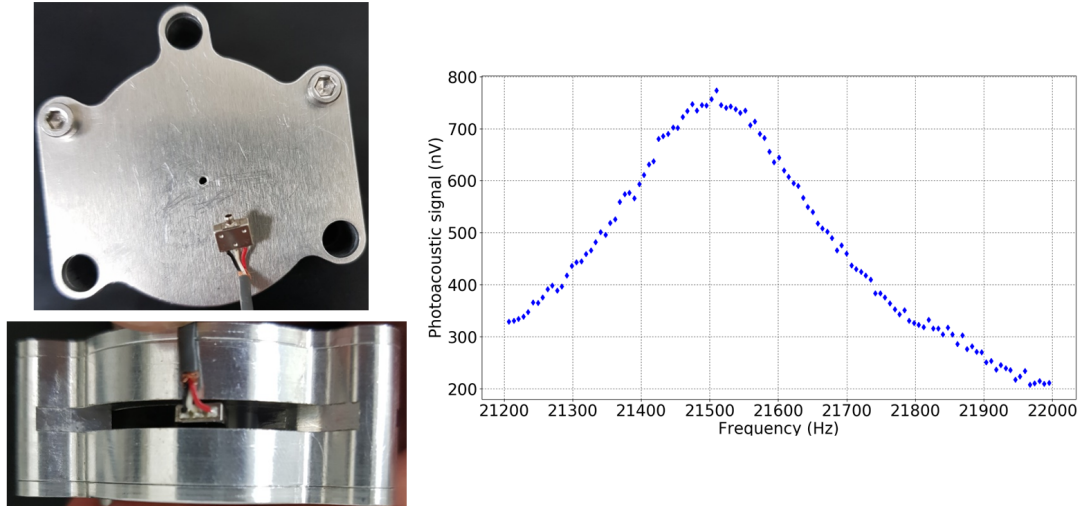


Figure 4.13: Experimental photoacoustic measurement of the radial resonator quality factor with a microphone (EK 23133, Knowles). Photographs of the resonator and microphone (left). Obtained resonance curve of fitted quality factor  $Q_{ac} = 77$  (right).

### Determination of the system limiting noise

Secondly, we verified that the noise in each case is still limited by the QTF Brownian noise. This is important to verify since the addition of the resonator induces a coupling modifying the system quality factor, hence modifying the system noise level. We performed these measurements with an electric spectrum analyser (35670A, Agilent Technologies) in atmospheric conditions and also derived the quality factor with an impedancemeter (4294A, Keysight). The resulting noise spectra are presented in Figure 4.14. We can observe that the limiting noise is the Brownian noise of the QTF in every case, despite the presence of a parasite around 21,130 Hz which most likely originates from electrical noise. Particularly, we found that the best coupling occurs for a radius of 10 mm, yielding a quality factor of 2,106.

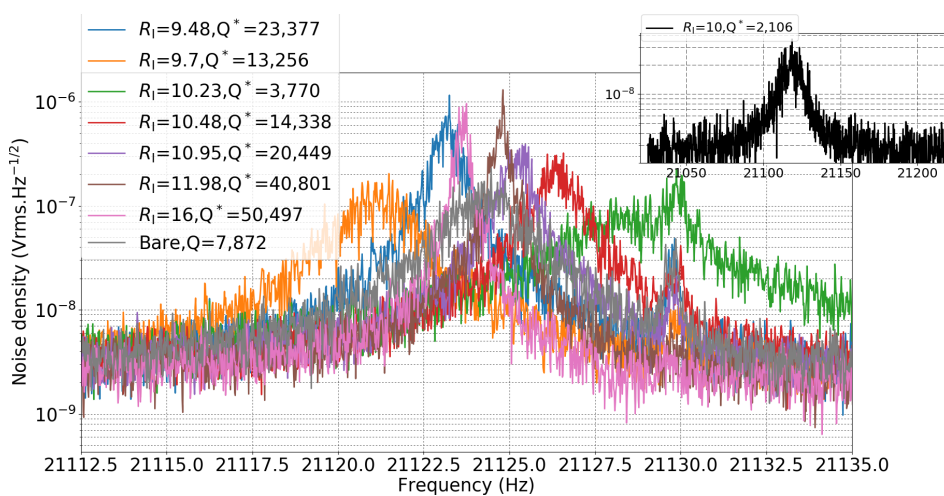


Figure 4.14: Experimental noise spectral density for C2 with radial resonator, recovery cavity and bare QTF. The radii values are given in mm. The spectrum were measured in air at atmospheric conditions with a spectrum analyser (Agilent 35670A).



## Photoacoustic measurement

We finally studied the coupling of the resonators with the QTF by performing photoacoustic measurements with the same setup as before. For each and every radius, we measured the photoacoustic signal, noise, frequency, and quality factor, resulting in the curves presented in Figure 4.15.

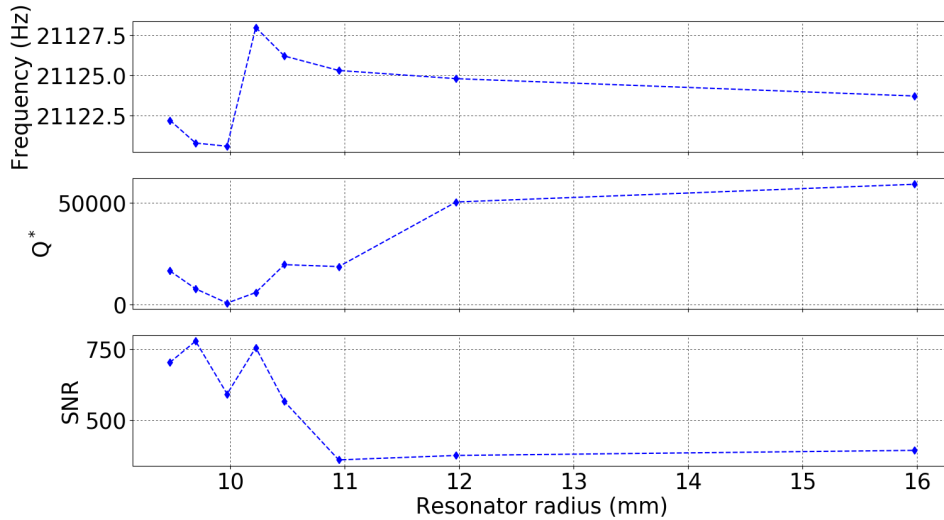


Figure 4.15: Experimental coupling results for C2 when varying the resonator radius. An optimal SNR is obtained for a radius of 9.7 mm but is different to the best coupling obtained for a radius of 9.88 mm.

A first remark is that the system quality factor for the smallest radii does not decrease drastically, which would be the case if the resonators touched each other or if squeeze damping occurred. These effects can therefore be discarded.

An optimal coupling is obtained for a radius  $R_I = 9.98$  mm. This optimal is identical to the one found by electrical measurements of the noise. For this resonator, a minimal quality factor of 704 is obtained photoacoustically which is remarkably similar to the coupled quality factor of 602 determined through FEM. Compared to the case of the watch tuning forks and its tubes, the radial resonator quality factor is mainly limited by acoustic radiation through openings, explaining the good agreement between simulated and experimental values. Nonetheless, the quality factor for other radii does not match simulations. For a radius of 12 mm, we measured 50,300 compared to 94,000 calculated by FEM. This discrepancy is the same as already experienced with the recovery cavity and may be explained by more important losses of the acoustic resonator than the one computed for radiation through the openings.

Concerning the SNR, we can recognise the typical curve when coupling resonators. However, a discrepancy is present for the best coupling. Indeed, the SNR decreases at this particular point, passing from 777 and 754 before and after to 591. Despite repeating this particular measurement and positioning differently the resonator, we always obtained the same result. The reason might be the difficult positioning compared to the QTF which was unfortunately not perfectly glued and presented an angle with the mechanical elements. To verify this particular point we would need to improve mechanical centering and parallelism. As a consequence we distinguish the radius for which the coupling is the best (lowest  $Q^*$  factor,  $R_I = 9.88$  mm) from the one allowing to obtain the best SNR ( $R_I = 9.7$  mm).

For the best SNR we derived a sensitivity of  $3.9 \cdot 10^{-9} \text{ W.cm}^{-1}.\text{Hz}^{-1/2}$  (Table 4.13). This NNEA is slightly worse than the one predicted analytically. The difference might come from the acoustic resonator quality factor lower than predicted or the discrepancy we observed for the best coupling.

System	C2 + radial resonator
Setup	
Gas	C <sub>2</sub> H <sub>2</sub>
Concentration	1,000 ppmv
Absorption (cm <sup>-1</sup> )	1.88 10 <sup>-4</sup>
Relaxation time (μs)	0.1
Laser power (mW)	17
Heat amplitude (W.cm <sup>-1</sup> )	1.07 10 <sup>-6</sup>
Resonance characteristics	
$f_0$ (Hz)	21,120.8
Coupled quality factor $Q^*$	7,708
Resonator parameters	
$L_{mr}$ (mm)	16
$R_I$ (mm)	9.7
Photoacoustic response	
Optimal laser height $h/L$ (%)	75
Signal (mV)	119
Noise density (μVrms.Hz <sup>-1/2</sup> )	431
Noise equivalent bandwidth (Hz)	1/8
SNR	777
Exp. NNEA (W.cm <sup>-1</sup> .Hz <sup>-1/2</sup> )	3.9 10 <sup>-9</sup>
Corrected FEM NNEA (W.cm <sup>-1</sup> .Hz <sup>-1/2</sup> )	2.9 10 <sup>-9</sup>

Table 4.13: C2 with radial resonator : experimental results for the best SNR obtained.

To conclude we demonstrated the first radial resonator used in QEPAS. This new type of resonator offers unique advantages compared to classical longitudinal acoustic resonators. The resonator is easily machined, its positioning around the QTF should be made easier and laser alignment is not a problem anymore. In addition, such a resonator allows to consider innovating configurations for the coupling of QTFs with acoustic resonators. To increase the NNEA further, and possibly overcome the state of the art, one could also consider the addition of longitudinal resonators. However, we advise against this solution because of the alignment problems associated to small tubes, especially in the mid infrared. In turn, we could try to combine the effect of both the acoustic cavity and the radial resonator.

### 4.2.3 Conclusion

In this section we demonstrated two interesting alternatives to the classical configurations found in QEPAS. Firstly, the use of in-plane configuration allows to increase the acoustic-mechanic overlap hence improving the sensitivity. Secondly, we demonstrated the possibility to use acoustic resonators different from the traditional tubes and of similar sensitivity. The radial acoustic resonator was adapted to the QTF design, improving the coupling between the two and balancing for the smaller pressure amplitude generated. The design of acoustic resonators well coupled to the QTF then represents a change of paradigm for QEPAS. This could potentially lead to an increase of QEPAS state-of-the-art sensitivity and/or to the design of acoustic resonators that would present advantages over tubes, such as easier alignment with respect to mid-infrared laser beams, easier

machining, etc.

### 4.3 Comparison of existing photoacoustic techniques

Based on the definition of our unified modelling and on our experience in photoacoustics, we herein aim at comparing the different techniques (MPAS, CEPAS, QEPAS). We will focus on the sensors sensitivities and determine the advantages and drawbacks concerning other parameters such as the sensitivity to environment or the compactness.

#### 4.3.1 Study of the limit of sensitivity

We have seen in the previous paragraphs that calculating the ultimate limit of sensitivity of photoacoustic sensors ab initio can be difficult. The computation itself is challenging and many discrepancies with experiments can be found. This is particularly true for CEPAS and QEPAS sensors which are the most recent techniques in photoacoustics, for which some crucial experimental details can be missing in publications.

By collecting the different NNEA values found in the literature in Figure 4.16, trends and limits can be observed for the existing photoacoustic techniques.

The best reported MPAS sensors present NNEAs between  $6.7 \cdot 10^{-11}$  and  $10^{-10} \text{ W.cm}^{-1}.\text{Hz}^{-1/2}$ . The best reported CEPAS sensors reach  $10^{-10} \text{ W.cm}^{-1}.\text{Hz}^{-1/2}$ . The best bare QTFs reach  $10^{-8} \text{ W.cm}^{-1}.\text{Hz}^{-1/2}$  while the best QEPAS sensors reach  $10^{-9} \text{ W.cm}^{-1}.\text{Hz}^{-1/2}$ .

It appears that the best QEPAS sensors yet do not reach the best sensitivities reported for the other techniques. In order to understand this difference, we propose to study these three different technologies under the light of our unified modelling.

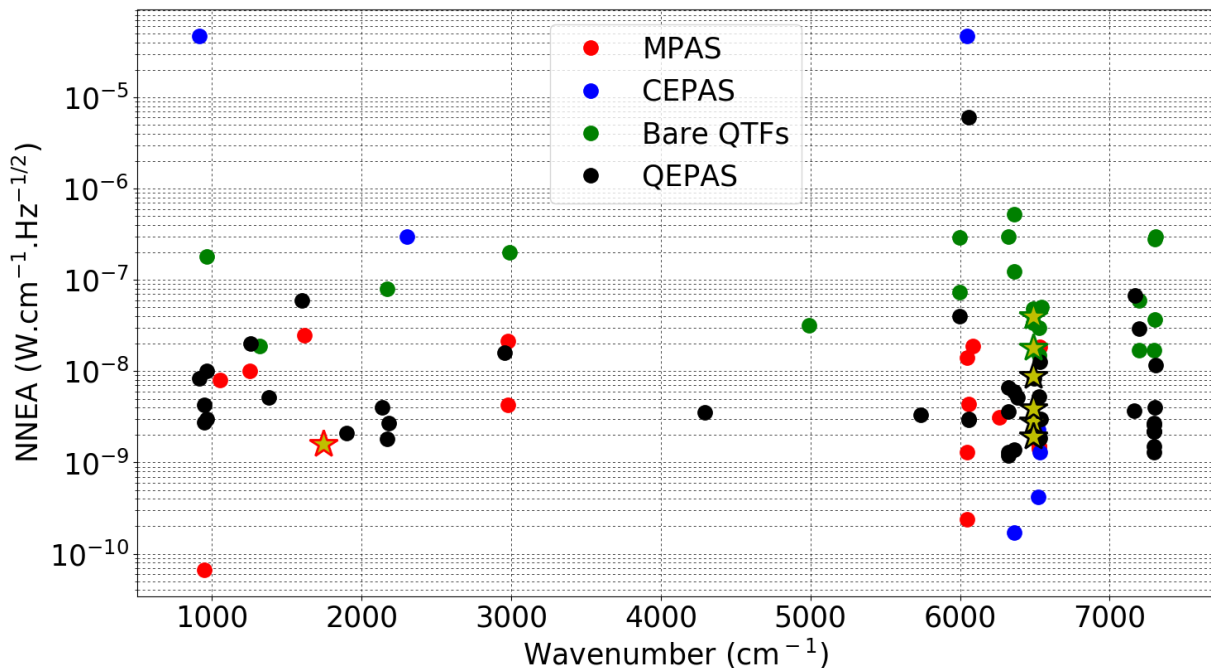


Figure 4.16: Review of the different NNEA values reported in the literature for the different techniques. The stars represent the work presented in this manuscript.

#### 4.3.1.1 Ultimate sensitivity of the mechanical pressure detector

We can first compare the detectors independently from acoustic signal generation. The theoretical ultimate sensitivity of the mechanical detector  $SNR_{ult}$  can be obtained from its  $SNR_{1Pa}$  multiplied by its number of faces (theoretical maximum of the acoustic-mechanic overlap). We then consider that each detector is exalted homogeneously with a pressure of 1 Pa on all its faces. We do the same for commercial microphones even if, in their current implementation, they can only use one of their two faces. The resulting values are presented in Table 4.14.

Microphones					Cantilevers	
Name	EK23024	BK4179	AKU143		A	B
$SNR_{ult}$ (dB.Pa <sup>-1</sup> )	126	157	123		159	156
QTFs						
Euroquartz	QTF#5	U1	U2	C1	C2	
148	158	167	159	142	148	

Table 4.14: Comparison of the mechanical detectors ultimate SNR.

Among all of the systems we studied, the best  $SNR_{1Pa}$  is obtained for QTF U1 and reaches 167 dB.Pa<sup>-1</sup>. The best microphone reaches a similar  $SNR_{1Pa}$  value as the best cantilevers, as well as QTF U2 and QTF#5. Other QTFs perform more poorly, reaching 148 dB.Pa<sup>-1</sup>, followed by MEMs microphones, reaching only 126 and 123 dB.Pa<sup>-1</sup>.

Based on these results, we conclude that the best mechanical detectors of each technique perform equally. Contrarily to what is sometimes suggested in scientific publications, there is no clear superiority of one detector over the others. The differences in sensitivity between photoacoustic techniques must then come from the acoustic domain.

#### 4.3.1.2 Sensitivity enhancement with acoustic resonators

In this section we will determine if there is indeed a difference between photoacoustic techniques regarding the acoustic pressure experienced by the mechanical detector. We first propose to compare the maximal pressure amplitude generated in each case, i.e. the cell constant  $C$ . We will compare the different systems using acoustic resonators that present the best sensitivities and discard the use of the detectors alone. The cell constants we computed for the different systems are summed up in Table 4.15.

MPAS					CEPAS	
Cell	3	4	Cell <sub>diff1</sub>	Mirsense	6	7
Reference	[54]	[54]	[46]	This work	[74]	[167]
$C$ (Pa.W <sup>-1</sup> .cm)	5,157	7,785	3,293	3,040	521	281
QEPAS						
System	Euroquartz + dual-tubes	C2 + recovery cavity	C2 + recovery cavity + tubes	C2 + radial resonator		
$C$ (Pa.W <sup>-1</sup> .cm)	2,945	34.3	7,800	551		

Table 4.15: Comparison of cell constant values between photoacoustic techniques.

The cell constants for MPAS, using acoustic resonators at resonance, reach a few thousands  $\text{Pa}\cdot\text{W}^{-1}\cdot\text{cm}$ . The constant of CEPAS cells reaches lower values of a few hundreds  $\text{Pa}\cdot\text{W}^{-1}\cdot\text{cm}$ . This is a consequence of operating the acoustic cell at frequencies well below its resonance frequency.

The cell constant presented by watch QTFs using tubes in on-beam configuration is equivalent to the cell constant of MPAS cells. In this work, we tried several approaches to increase the sensitivity, using custom QTFs and acoustic cavities. Adding an acoustic recovery to QTF C2 does not improve the pressure, explaining the small cell constant. We demonstrated a better cell constant than the MPAS state-of-the-art one, of  $7,800 \text{ Pa}\cdot\text{W}^{-1}\cdot\text{cm}$ , by adding microtubes to QTF C2. Eventually, the radial resonator enabled a better pressure amplification compared to the recovery cavity, but the cell constant was reduced compared to the use of tubes because of a bigger volume and the presence of the tuning fork inside.

#### 4.3.1.3 Overall sensitivity enhancement

We demonstrated that the best mechanical detectors present similar  $\text{SNR}_{1\text{Pa}}$  values, and that the cells constants used in the different techniques can reach similar values. Yet, QEPAS sensors present reduced sensitivities compared to the two other techniques. In order to understand this difference, let us take a look at the model factors which are the mechanic-acoustic overlap  $\eta_s$ , the vibroacoustic efficiency  $\varepsilon_{\text{va}}$  and the  $\text{SNR}_{1\text{Pa}}$ , which values are summed up in Table 4.16.

	MPAS	CEPAS	QEPAS
System	Cell 4	Cell 6	C2 + recovery cavity + tubes
Reference	[54]	[74]	This work
$H$ ( $\text{W}\cdot\text{cm}^{-1}$ )	$1.07 \cdot 10^{-6}$		
$C_L$ ( $\text{Pa}\cdot\text{W}^{-1}\cdot\text{cm}$ )	1.54	0.02	26
$A_s$	5,069	32,224	300
$C$ ( $\text{Pa}\cdot\text{W}^{-1}\cdot\text{cm}$ )	7,785	521	7,800
$\eta_s$	1	1	0.027
$\varepsilon_{\text{va}}$	1	1	0.86
$\text{SNR}_{1\text{Pa}}$ ( $\text{dB}\cdot\text{Pa}^{-1}$ )	151	153	141
SNR	295,558	24,901	2,163
NNEA ( $\text{W}\cdot\text{cm}^{-1}\cdot\text{Hz}^{-1/2}$ )	$1.4 \cdot 10^{-11}$	$1.7 \cdot 10^{-10}$	$1.92 \cdot 10^{-9}$

Table 4.16: Comparison of analytical model factors for state-of-the-art MPAS, CEPAS and QEPAS sensors.

For MPAS and CEPAS, we estimated that the maximal pressure is seen by the detector, so  $\eta_s$  is close to 1. To support this approximation, we already explained that in MPAS and CEPAS, the detector is small before the acoustic wavelength and small before the acoustic resonator dimensions, leading to a homogeneous pressure on it. In traditional QEPAS, the contrary happens: the QTF is usually bigger than the acoustic resonator. The coupling between the two resonators is then difficult, as evidenced by the much lower value of the acoustic-mechanic overlap  $\eta_s$ , well below the maximal theoretical value of 4. Despite good pressure amplification, the pressure is not well collected by the QTF prongs. We conclude that the acoustic resonators used in QEPAS are not efficient due to their poor coupling with the QTF.

Another factor explaining a decreased sensitivity is the vibroacoustic efficiency  $\varepsilon_{\text{va}}$ . Since the QTF is used at resonance, its vibration reduces the applied force compared to the static case. In most cases this factor however remains close to 1 and does not significantly differ from the others.

The acoustic resonators used in QEPAS present very low quality factors (below 10) while QTFs present high quality factors of a few thousands. Since both are used at resonance, acoustic coupling occurs between the two that decreases the overall quality factor and then the  $\text{SNR}_{1\text{Pa}}$ . This decrease represents a sensitivity loss of a factor 2 for the C2 with tubes, and a factor 5 for the traditional watch QTF with tubes in on-beam configuration.

The combined contributions of  $\eta_s$ ,  $\varepsilon_{\text{va}}$  and  $\text{SNR}_{1\text{Pa}}$  lead to the decrease of QEPAS sensitivity compared to the other techniques.

#### 4.3.1.4 Perspectives

Thanks to our unified model we highlighted the different phenomena occurring in MPAS, CEPAS and QEPAS sensors. We identified what limited the sensitivity of each technique. One main question resides: Are sensitivity improvements still possible? In this paragraph we propose to bring the first answers to this question.

#### MPAS sensors

The MPAS technique is the most mature of the photoacoustic techniques. The used cells generally present high cell constants of a few thousands  $\text{Pa}\cdot\text{W}^{-1}\cdot\text{cm}$ . To increase the pressure amplification it would be necessary to increase the cell length and decrease its radius. However, doing so will inevitably lead to difficulties for laser alignment and also machining of the cell. As a consequence, we expect that cell constants have reached their practical limit. However it may be possible to use multipass, or rather intracavity setups in order to increase the generated pressure.

Nonetheless, future improvements may be achieved for the microphones. We demonstrated that the best microphone we found reached an analytical  $\text{SNR}_{1\text{Pa}}$  of  $151 \text{ dB}\cdot\text{Pa}^{-1}$ . We also found that this value was degraded due to the presence of acoustic background noise [54]. We expect that the studied microphone is importantly subject to this background because its equivalent input noise is extremely low, around  $-2.5 \text{ dB(A)}$  (see Appendix B). With the presence of a background it is then difficult to reach the theoretical  $\text{SNR}_{1\text{Pa}}$  for this microphone. Then, it may be interesting to study the design of microphones presenting a lower resonance frequency so as to increase the noise floor while keeping their good  $\text{SNR}_{1\text{Pa}}$ . In addition, to discard the possible limitations of the noise by the electronics, using an optical detection of the membrane displacement would be interesting and is already demonstrated for MEMs microphones [181].

Generally, microphones used in photoacoustics are not optimised for this application, and specific developments could lead to possible enhancements. In a way, this optimisation has already been done with the invention of cantilevers for photoacoustics, as we are going to explain.

#### CEPAS sensors

As microphones, cantilevers are bipolar mechanical resonators used well below their resonance. Cantilevers used in photoacoustics have been optimised in the sense that they present a lower resonance frequency, which makes Brownian noise the limiting noise. Furthermore, detection of their displacement is made optically to avoid the presence of other noises such as the electronic one.

The best cantilevers we have studied reach a  $\text{SNR}_{1\text{Pa}}$  of  $153 \text{ dB}\cdot\text{Pa}^{-1}$ . This high value originates from an important detection surface and from a reduced damping. To further reduce the damping, a compromise should be found between the cantilever surface, thickness and quality factor. However, further increasing the cantilever surface, and decreasing its thickness will reduce its quality factor and lead to other drawbacks, such as a limited dynamic range due to non-linearities. To make sure that the performance of  $153 \text{ dB}\cdot\text{Pa}^{-1}$  is the

best, a parametric study would be necessary.

Possible improvements of CEPAS sensors concern the pressure amplification. State-of-the-art setups use cells at frequencies below the resonance, yielding cell constants of a few hundreds ( $521 \text{ Pa}\cdot\text{W}^{-1}\cdot\text{cm}$  at most). The given reason to use cells below their resonance is to enable the use of FTIR operation of the cell according to the authors [74], which is unclear to us. If we discard this problematic, we can expect that the cells used in CEPAS reach the same cell constants as in MPAS, because the cells geometries are similar. As a consequence, using a resonating cell would lead to a similar theoretical limit of sensitivity as for MPAS, that we estimate to  $10^{-11} \text{ W}\cdot\text{cm}^{-1}\cdot\text{Hz}^{-1/2}$ .

## QEPAS sensors

Concerning bare QTFs, we already introduced different possible improvements, such as the use of the in-plane configuration to increase the acoustic-mechanic overlap. This configuration should be preferred when designing QTFs so as to maximise the sensitivity. We also showed that in vertical off-beam, a signal more important than in on-beam arises. This last configuration could be considered for intracavity or multipass sensing, facilitating laser alignment.

Concerning the intrinsic QTF sensitivity, multiple QTFs from the literature were studied and all presented a NNEA not better than  $10^{-8} \text{ W}\cdot\text{cm}^{-1}\cdot\text{Hz}^{-1/2}$ . In addition, based on our analytical model, a QTF (U2) was optimised in terms of sensitivity [26]. As a consequence, we do not expect significant NNEA improvements for bare QTFs. Nevertheless, one possibility is often discarded in photoacoustics and may be the source of new developments. The resonators frequency is often limited to a few tens of kHz to avoid limitations due to slowly relaxing gases. In the contrary, as we saw, the pressure amplitude in free space is linear with the frequency, making the use at low frequencies not favourable. The study of high frequency resonators in free space may lead to sensitivity enhancement and other advantages. Of course, these will not be suited to the detection of gases presenting slow relaxation times, but could be adapted to others. To determine if this approach is interesting, an analytical study should be made on the design of QTFs at high frequencies ( $>50 \text{ kHz}$ ), possibly using higher order harmonics, as well as the determination of different gases relaxation time in classic gas matrices.

Concerning QEPAS, studies should be made so as to enhance the acoustic-mechanic overlap  $\eta_s$  between acoustic resonators and the QTF. This is what we did by designing QTF C2, a tuning fork emitting strong acoustic waves, and coupling it with a radial acoustic resonator. A better compromise may be found between the cell constant and the cell quality factor so as to limit the decrease of the QTF quality factor while keeping a good pressure amplification. In a more exploratory way, the use of other modes of resonance, such as the out-of-plane mode should be considered.

To limit the quality factor decrease when coupling resonators, a solution could be to use the QTFs below their resonance frequency. The acoustic resonator could be tuned slightly below the QTF frequency (while avoiding other modes of resonance). In addition, we already showed that the mechanical resonator SNR is constant at, or below its resonance frequency. This would provide an improvement of a factor 5 for example for a watch QTF with tubes. Nonetheless, by doing so, using a piezoelectric material would be useless and one should rather rely on optical detection. However, this last possibility would make the use of QTFs less interesting compared to cantilevers for example.

To conclude on the use of QEPAS, finding new configurations enhancing the acoustic-mechanic overlap  $\eta_s$  while keeping a good cell constant  $C$  will be a difficult task. The resonant use of QTFs and their high quality factors make them hard to couple with low quality factor acoustic resonators. As a consequence, the ultimate sensitivity of QEPAS might not reach the same level as for MPAS and CEPAS but may rather reach  $10^{-10} \text{ W}\cdot\text{cm}^{-1}\cdot\text{Hz}^{-1/2}$ .

Another way of improvement is intracavity or multipass QEPAS. In these setups the laser beam passes several times between the gap of a tuning fork to generate more signal. Generally, focusing the laser beam between the QTF prongs is challenging because of the small gap (usually  $300 \mu\text{m}$  for watch QTFs). The addition of micro-

tubes makes this task even more delicate. The use of QTFs developed at ONERA would be interesting as they present the largest gap reported in the literature (2 mm), facilitating laser beam alignment, while keeping a similar sensitivity as bare watch QTFs. Moreover, the new radial resonator we presented do not require any advanced laser beam alignment and would facilitate the use of multipass or intracavity configurations. If we consider a laser power enhancement of 1,000 as reported in an intracavity setup [109], this would lead to  $10^{-12} \text{ W.cm}^{-1}.\text{Hz}^{-1/2}$ .

To conclude, we found different axes for sensitivity improvements in each technique that will need further studies to confirm. Nonetheless, we know that sensitivity is not the only parameter of interest for photoacoustic sensors, particularly for industrial use. We then propose to study other parameters in the next sections to have a good overall view of the advantages and drawbacks of each technique.

### 4.3.2 Frequency

Apart from the sensitivity, the frequency is also an important parameter in photoacoustics. Indeed, when the target gas presents a slow relaxation time  $\tau_{V-T}$ , the detector should present a slower response. If, in the contrary, the detector is faster, the generated signal is reduced. This effect is taken into account in the generated heat amplitude (Equation 2.5) and is used in our definition of the NNEA (Equation 2.39). As a consequence, the frequency effect on the signal is independent from the NNEA value we discussed previously.

Presenting a low operating frequency is then often a requirement in photoacoustics, so as to enable a good SNR for most applications. This is favourable for CEPAS sensors, which can work at very low frequencies (down to 10 Hz) and also to MPAS sensors, generally working at a few hundreds Hz. However, in QEPAS the QTF rarely presents a resonance frequency below 1 kHz and watch QTFs are designed at 32,768 Hz. Such high frequencies can cause significant signal dropouts. For example, the generated heat is reduced by 60% at 32,768 Hz compared to 2 kHz, when targeting dry  $\text{CO}_2$  at  $2 \mu\text{m}$  (see Section 2.1.2).

### 4.3.3 Sensitivity to the environment

Another important concern is the sensitivity of photoacoustic sensors to their environment. On the one hand, they are sensitive to modifications of the gas pressure, temperature, density, and sometimes to humidity, leading to signal variations which must require frequent calibrations using environmental sensors. On the other hand they are sensitive to external background noises, particularly to sound and vibrations. Generally, these backgrounds cannot be subtracted as they vary in time and can be hard to shield the sensor from. This aspect is an obstacle to the development of sensitive and robust photoacoustic sensors in the industry or in noisy environments.

To reduce the intrinsic sensitivity of the sensor to vibrations, two conditions should be satisfied. The first is a good structural quality factor of the resonator so as to limit energy transmission through the anchor structure. Cantilevers and QTFs present important structural quality factors, however, microphones may present lower values, due to their direct anchorage to the cartridge. The second condition is that the resonator should be shielded against acoustic background generated by the vibration of air in the cell. This effect can be cancelled by design, using a balance cell for example [74].

From a more general point of view, the acoustic background generated by vibrations or from external environment can be reduced in different ways. The first is the decrease of the measurement bandwidth and the use of the detector at its resonance frequency. The second can be the use of acoustic buffers so as to reduce the background generated by the laser absorption or from the gas circuitry [21]. Another possibility is to use differential acoustic resonators, to subtract the background [46].

Eventually, the nature of the detector itself can contribute to the sensor immunity. We expect microphones and cantilevers to be very sensitive to the acoustic background. Because of their mode of resonance, they may be



more easily excited by sounds and vibrations. In the contrary, QTFs are usually used at their anti symmetrical mode of resonance, meaning that an external acoustic wave hitting one prong will hit the second prong similarly, so that no signal is generated. This quadrupolar nature of QTFs should make their excitation harder. Another advantage of QTFs in this respect is their higher working frequency that enables to avoid low frequencies where environmental acoustic noises are the most important.

In order to enhance QEPAS immunity to the environment we worked on several improvements. The first, is the use of the recovery cavity that we presented before (see Section 3.2.2.2). Such a cavity allows not only to increase the QTF quality factor but also to reduce the external acoustic and electromagnetic backgrounds thanks to its presence. To support this claim, we performed an experimental comparison between the two systems (bare QTF and QTF with cavity) submitted to sound generated by a loud speaker [146]. The response of the two systems is given in Figure 4.17 and demonstrates that the cavity enables to reduce the sound by a factor 8.

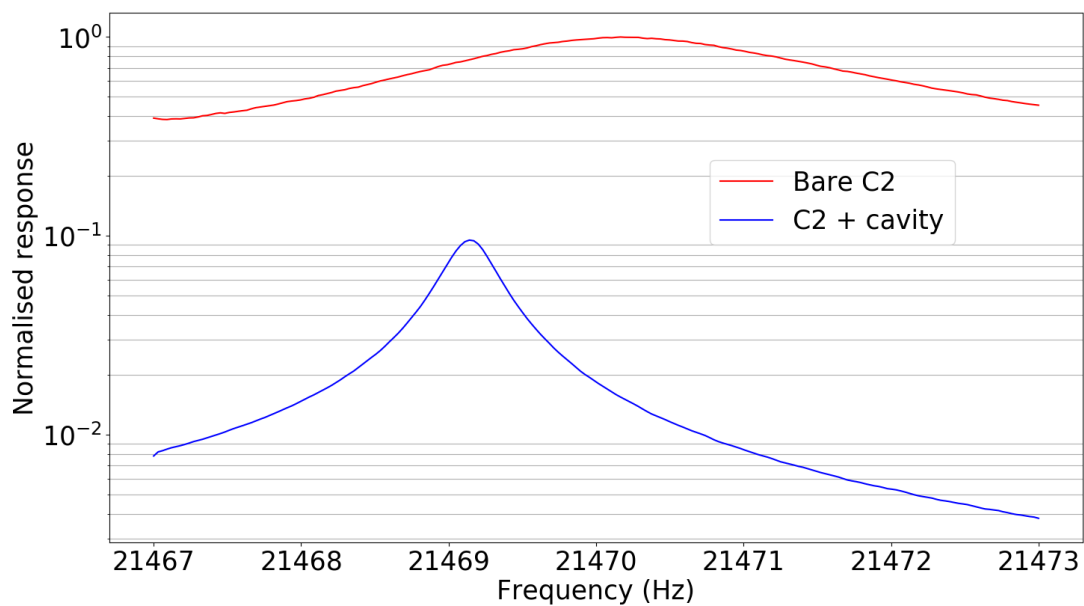


Figure 4.17: Experimental comparison of C2 and C2 with recovery cavity immunity to sound. The two systems were placed inside a chamber with a loudspeaker their response was measured over frequency. The cavity enabled a decrease of the acoustic background by a factor 8.

The second is the use of a new detection method that we will present in Chapter 5. This new method enables a differential measurement with a QTF as well as the increase of the detection bandwidth. By means of an active tracking, the resonator frequency and quality factor can be measured, allowing to correct the signal and to compensate for the effects of temperature for example. The photoacoustic phase can also be monitored which allows to correct the signal variations with the gas matrix composition. Compared to the traditional detection scheme for QTFs, the widened bandwidth allows to reduce the sensor response time and to correct the signal fast variations.

Based on these explanations, we expect QEPAS systems to shield more efficiently external sounds and vibrations. Nonetheless, to our best knowledge, no study has been reported that compares the sensitivity of photoacoustic sensors to the environment. It might be explained by the fact that this experimental comparison can only be made on complete systems and that a generalisation might be difficult. The answer to this question is however primordial to determine the interest of using tuning forks in photoacoustic sensors for real world applications.

### 4.3.4 Compactness

The last aspect we will study is sensor compactness. We saw through the literature that photoacoustic detectors present a great variety of sensitivities and sizes, and one could ask if there is a correlation between the two. To check this point we have plotted the ultimate achievable SNR for the different detectors versus their maximum size (Figure 4.18). Regarding microphones, we see that there is a clear trade-off between sensitivity and size. The improvement of MEMS microphones, which can fit into cellular phones but offer poor performance, is still an active research topic [182], particularly with piezoelectric microphones. We observe that a good compromise can be reached between a small size and high SNR for QTFs. At comparable size, cantilevers present a higher SNR than QTFs and MEMs microphones. However, we should keep in mind that optical detection has to be added to the cantilever to measure its displacement, making the system larger. Watch QTFs present a good trade off between size and SNR, and their detection is piezoelectric, allowing for a miniature electronic detection system.

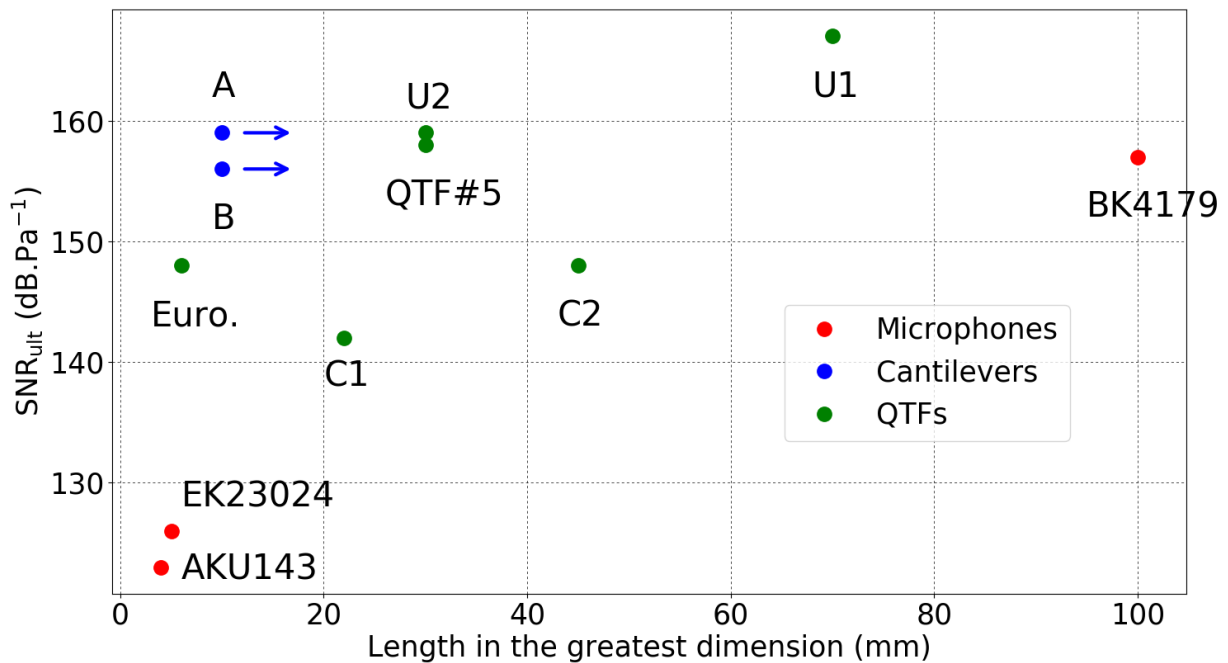


Figure 4.18: Comparison of the SNR and size of mechanical detectors. For cantilevers the optical detection system size should be taken into account, which we represented by the blue arrows.

We have also studied the compromise between the experimental NNEA and the laser interaction length with the gas in Figure 4.19. At first sight we observe that sensors for which the interaction length is small present the worst sensitivities, which is the case for bare QTFs. For slightly increased interaction lengths, QEPAS sensors present better sensitivities, while MPAS and CEPAS present the best sensitivities for much longer optical lengths. As a consequence, QTFs and QEPAS sensors present the best compromise between sensitivity and size. We also note that Mirsense's differential cell enables an even better sensitivity at a reduced size. These observations should be balanced by taking into account the maximal size of the different sensors. For QTFs, their length in the greatest dimensions is superior to the interaction length (gap size). For MPAS and CEPAS sensors, this maximal length is given by the acoustic cell length as the detector is usually smaller, making the displayed values more representative than for QTFs.

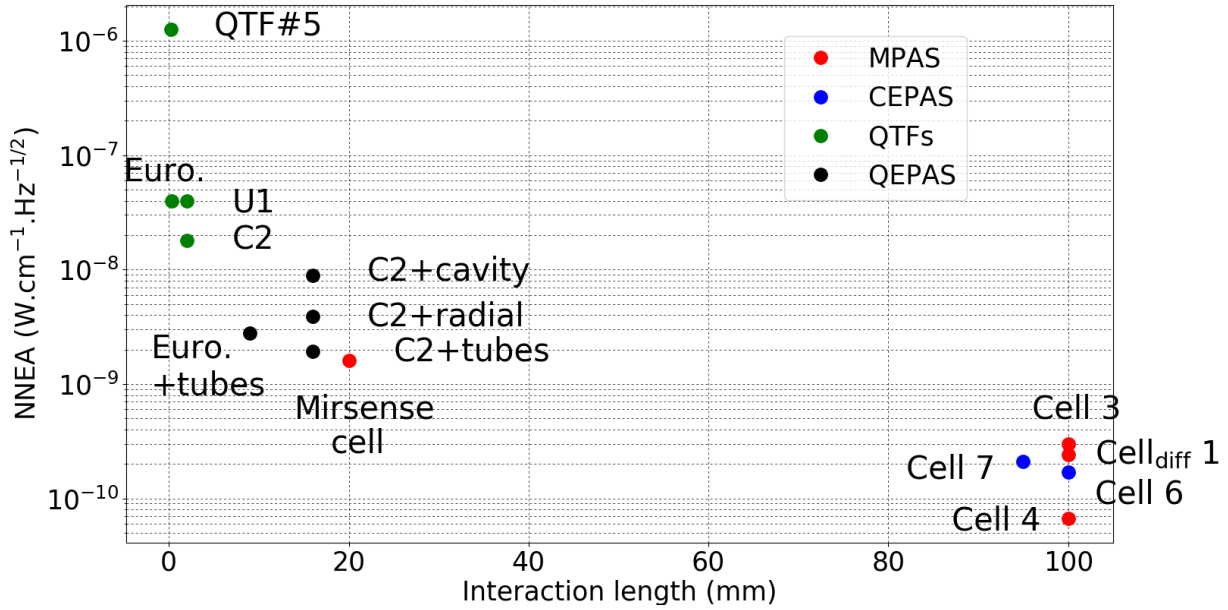


Figure 4.19: Comparison of the detectors NNEA and laser interaction length.

## 4.4 Conclusion

By the means of our unified model we identified and quantified the different physical phenomena occurring in a photoacoustic sensor. Particularly, we found that contrarily to MPAS and CEPAS, the coupling of the acoustic source with the QTF was not optimal, even when pipe-like acoustic resonators are added. Furthermore, we demonstrated that the use of acoustic resonators with QTFs lowered their overall sensitivity and partially explained the limitation of NNEA values for QEPAS sensors in the literature. To tackle these issues, we presented two major improvements. The first is the use of the in-plane configuration that enables a better acoustic-mechanic overlap and increases the sensitivity in the case of a bare QTF. The second is the demonstration of the first radial resonator used in QEPAS. This resonator also enables to increase the acoustic-mechanic overlap and led to a sensitivity close to the state-of-the-art one while presenting other unique advantages, such as a facilitated laser beam alignment, resonator machining and positioning, etc.

Eventually, to determine the interest of using QTFs in photoacoustics and optical sensing techniques in general, we performed a sensitivity comparison with the optical path length, presented in Figure 4.20. We based our analysis on the literature [22] for optical gas sensing methods.

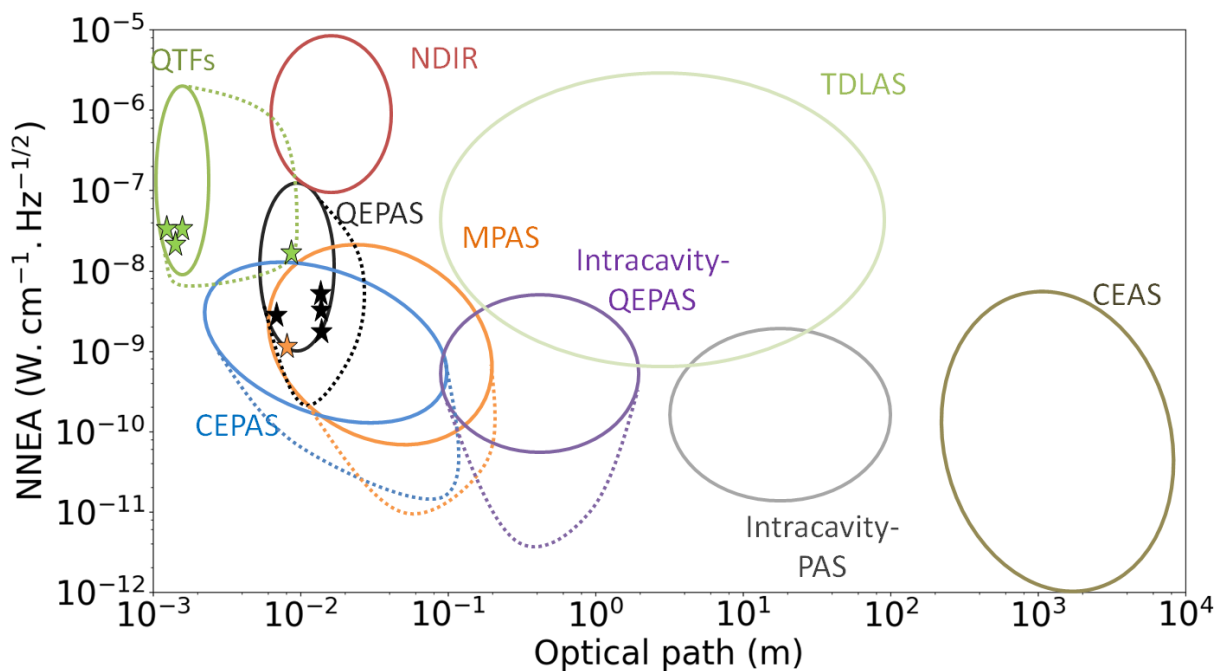


Figure 4.20: Sensitivity comparison of gas sensing methods. Perspectives for photoacoustics sensors are represented with dashed lines. The experimental setups we studied are represented with a star.

Compared to optical sensing methods, photoacoustic techniques can reach similar sensitivities. PAS sensors are usually better than non-dispersive infrared spectroscopy (NDIR) and can be more compact. However, it should be noted that NDIR sensors present very low costs that will be difficult to reach using laser spectroscopy. Photoacoustic techniques reach similar or better sensitivities compared to tunable diode laser spectroscopy (TDLAS), with a reduced optical path. Nonetheless, the best optical sensors remain the cavity enhanced techniques (CEAS) thanks to very long optical paths. For example, while the best CRDS sensors reach a NEA of  $10^{-14} \text{ cm}^{-1} \cdot \text{Hz}^{-1/2}$  [13], intracavity QEPAS or PAS could reach to date NEAs around  $10^{-11} \text{ cm}^{-1} \cdot \text{Hz}^{-1/2}$  with a laser power of 1W.

While most optical gas sensing methods have reached their fundamental limits in terms of sensitivity, photoacoustic techniques could still be improved. We illustrated the perspectives discussed in this chapter with dashed lines.

Among photoacoustic methods, we found that QEPAS may present an interesting compromise between the sensor size and sensitivity. Nonetheless, QEPAS sensors usually work at high frequencies that limit their sensitivity for the measurement of slowly relaxing gases. In turn, this high frequency also participates to QEPAS sensors immunity to the acoustic and vibratory environment that may be better than for MPAS and CEPAS.







## Chapter 5

# Study of a new signal processing method for time stable and background-free photoacoustic measurements

### Objectives:

The aim of this chapter is to study a new electronic processing technique for photoacoustic sensing. This method principle is described and an analytical model is derived, which is further compared to experimental results. Advantages and drawbacks of the technique are also presented and a comparison to the usual QEPAS detection scheme is provided.

## 5.1 Motivation and principle

### 5.1.1 Motivation

The introduction of quartz tuning forks in photoacoustic spectroscopy led to a new paradigm. Whilst high quality factor QTFs present the advantage of background noise isolation, drawbacks such as frequency drift and longer measurement time arise. These QTFs generally present quality factors from 1,000 to 75,000 (see Chapter 1), representing spectral bandwidths from a few Hz down to 100 mHz and a typical measurement time of a few seconds. Drifts of the quality factor and frequency will lead to signal dropouts and sensor instability in fluctuating environments [116], especially when working with high quality factor resonators.



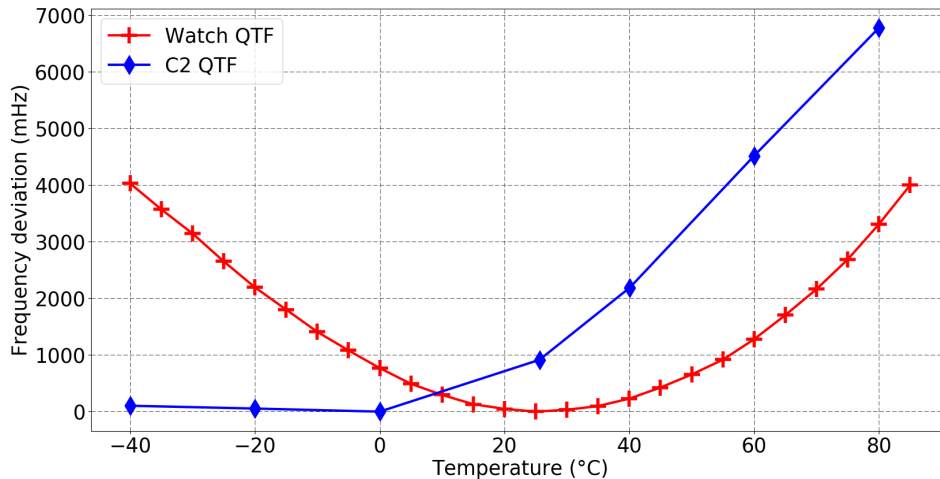


Figure 5.1: Deviation of the resonance frequency of a commercial Z-cut quartz crystal oscillator [183] (red). Deviation measured for C2 QTF which is also Z-cut (blue). The deviation reference is the turnover point of each curve.

In particular, temperature changes will induce, over time, a drift of the resonator eigen frequency. As shown in Figure 5.1, this drift is parabolic with temperature change. For a commercial QTF, a frequency deviation of approximately 800 mHz occurs when passing from 0 to 25 °C and this deviation increases the more the QTF is used far from the turnover point at 25 °C here. This point value depends on the wafer cut and resonance mode and working at this point should be privileged for stable mode of operation. For our C2 QTF a similar deviation of 900 mHz is obtained when passing from 0 to 25 °C. In addition, pressure changes, QTF aging, vibrations, or gas matrix properties (viscosity, dew point, adsorption, etc.) can worsen the frequency drift and so the signal instability.

In order to circumvent these problems, different techniques can be used as we described in Chapter 1. In particular, it is possible to alternatively track the frequency and quality factor of the QTF and measure the gas concentration in a classic detection scheme, however provoking periodic sensor dead time [117, 114]. By doing so, a consequent reduction of the signal drift (mainly due to the addition of water vapor) was reported, passing from 44% in classic detection to less than 1% with QTF resonance tracking [114]. Yet another technique allows to calibrate while measuring the photoacoustic signal by using a beat frequency [184].

As an alternative approach, we have introduced a new detection scheme enabling measurement of the photoacoustic signal by measuring the shift of the oscillator frequency [185]. In addition, a differential measurement is set so as to reduce external backgrounds and compensate for frequency drifts.

### 5.1.2 Principle

The method relies on the actuation of the resonator at resonance by means of an electronic oscillator circuit and monitoring of its frequency. When an additional photoacoustic force is applied on the QTF, a shift of the oscillator frequency, proportional to the photoacoustic force, is created. This frequency shift depends on the phase between the photoacoustic force and the piezoelectric actuation force and is maximal when the two are in phase quadrature. Finally, a differential measurement is set by sequentially modifying the phase sign. While the laser modulation phase is changed, the drifts seen by the QTF are the same (temperature, pressure, ...), which should theoretically improve the sensor immunity to drifts and unwanted backgrounds. Therefore we propose to monitor the oscillator frequency in order to determine the applied photoacoustic force as we further explain in the next paragraphs.

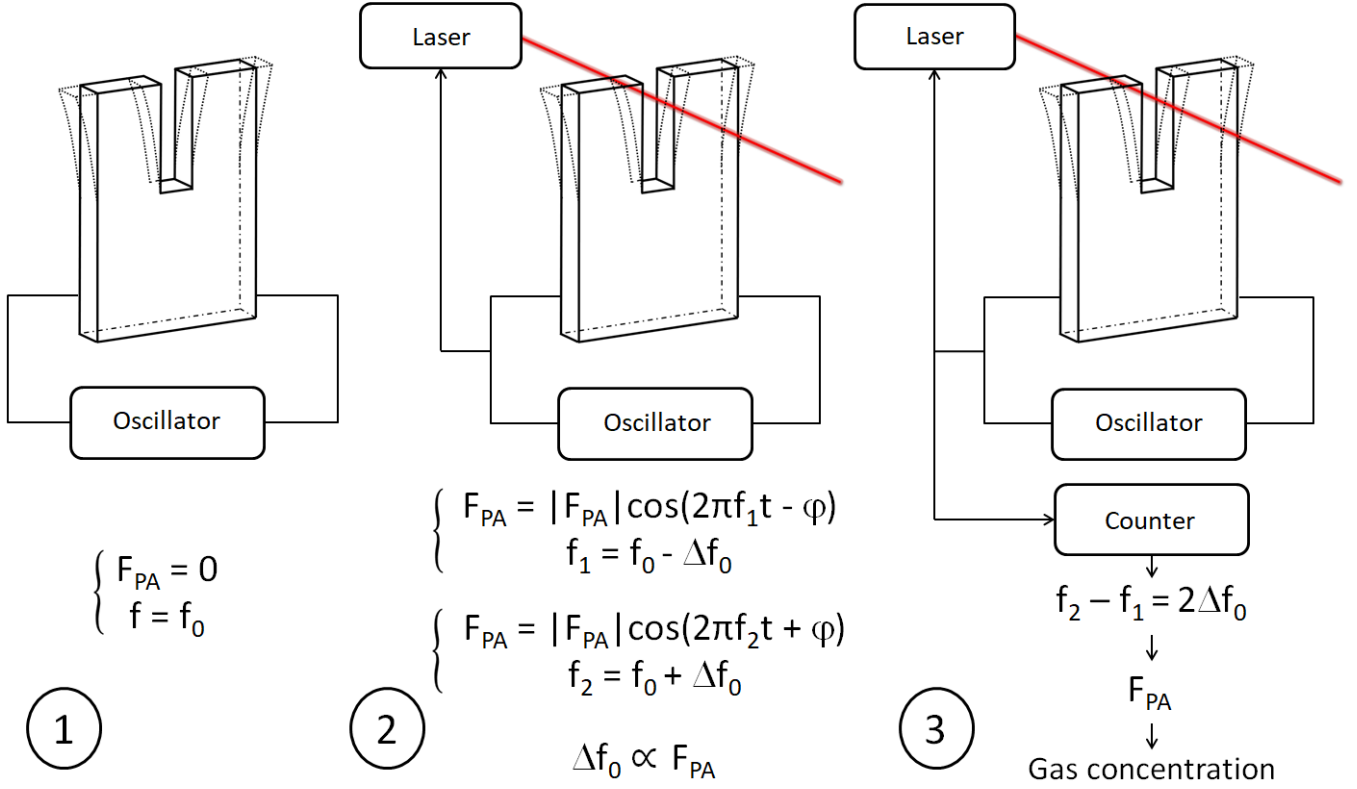


Figure 5.2: (1) The QTF is kept at resonance by means of an electrical oscillator. (2) The introduction of a supplementary photoacoustic force  $F_{PA}$  induces a frequency shift  $\Delta f_0$  which value depends on the phase  $\varphi$  of the modulated force. (3) Modifying the phase sign in time enables to set a differential measurement. The frequency shift value  $2\Delta f_0$  is monitored by means of a frequency counter and is proportional to the gas concentration.

## 5.2 Theoretical analysis of the method

In this section we present the analytical model used to describe our method. We first present how to obtain the generated signal, and in a second time the system noise. Finally, we derive the method signal-to-noise ratio by using the Allan deviation.

### 5.2.1 Signal generation

#### 5.2.1.1 Variation of frequency with phase

The tuning fork can be modelled as a second harmonic oscillator as discussed in Chapter 2. Let  $W(t)$  be the displacement of a second order harmonic resonator of mass  $M$ , vibrating at the frequency  $f_0$  and of damping ratio  $\xi$ . This resonator is driven by an external force  $F_{tot}$  satisfying the following differential equation:

$$\frac{d^2 W(t)}{dt^2} + 4\pi\xi f_0 \frac{dW(t)}{dt} + (2\pi f_0)^2 W(t) = \frac{1}{M} F_{tot}. \quad (5.1)$$

The applied force is sinusoidal and can be written as  $F_{tot} = |F_{tot}| \cos(2\pi f t)$ . One can show that the steady state solution is sinusoidal with the same period and an additional phase shift  $\varphi$ :

$$W(t) = \frac{\frac{1}{M} |F_{tot}|}{(2\pi)^2 \sqrt{(f_0^2 - f^2)^2 + 4\xi^2 f_0^2 f^2}} \cos(2\pi f t - \varphi), \quad (5.2)$$

with,

$$\varphi = \arctan \left( \frac{2f f_0 \xi}{f_0^2 - f^2} \right). \quad (5.3)$$

In brief, the application of a sinusoidal force makes the resonator oscillate with a phase shift  $\varphi$  between resonator motion and actuation force. The phase shift can be directly related to the oscillation frequency as shown by the transfer function of the oscillator (Figure 5.3). For convenience, we will work with the frequency and we will express the relation between the two in the next paragraphs.

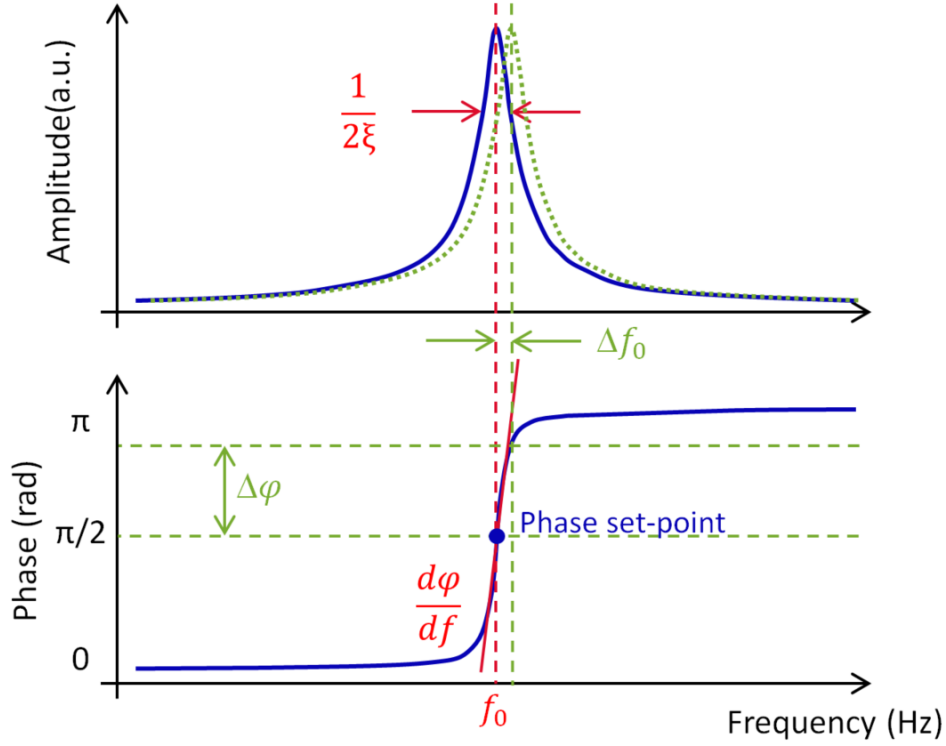


Figure 5.3: Oscillator amplitude and phase representation over frequency (blue curve). When applying an external force, a variation of the phase  $\Delta\varphi$  is obtained and corresponds to a frequency shift  $\Delta f_0$  (green curve).

The frequency shift corresponding to a phase shift around the resonance can be computed by taking the oscillator phase derivative  $\frac{d\varphi}{df}$ . One can easily demonstrate the following equation:

$$\frac{d\varphi}{df} = \frac{2f_0 \xi (f^2 + f_0^2)}{(f_0^2 - f^2)^2 + 4f^2 f_0^2 \xi^2}. \quad (5.4)$$

When  $f = f_0$  the equation becomes:

$$\left. \frac{d\varphi}{df} \right|_{f_0} = \frac{1}{f_0 \xi}. \quad (5.5)$$

At this point the quality factor  $Q$  of the resonator can be introduced through the definition of the damping ratio  $\xi = \frac{1}{2Q}$ . Finally, we obtain the equation expressing the variation of frequency with phase variation around resonance for a second harmonic oscillator:

$$\Delta f_0 = \frac{f_0}{2Q} \Delta\varphi. \quad (5.6)$$

This expression is valid for small variations of the frequency compared to the resonator bandwidth, i.e.  $\Delta f_0 \ll \frac{f_0}{Q}$ . It can be noted that the lowest the quality factor is, the highest the frequency variation will be, which can be understood by looking at the phase slope near resonance. Indeed, the phase slope near resonance increases with  $Q$  which in turn reduces the frequency variation on the resonance curve.

### 5.2.1.2 Phase variation induced by force application

We now have to express the phase variation around resonance  $\Delta\varphi$  induced by the photoacoustic force, in order to quantify the frequency variations of our system, i.e. the signal. We present the principle block diagram in Figure 5.4 and present the parameters in the following.

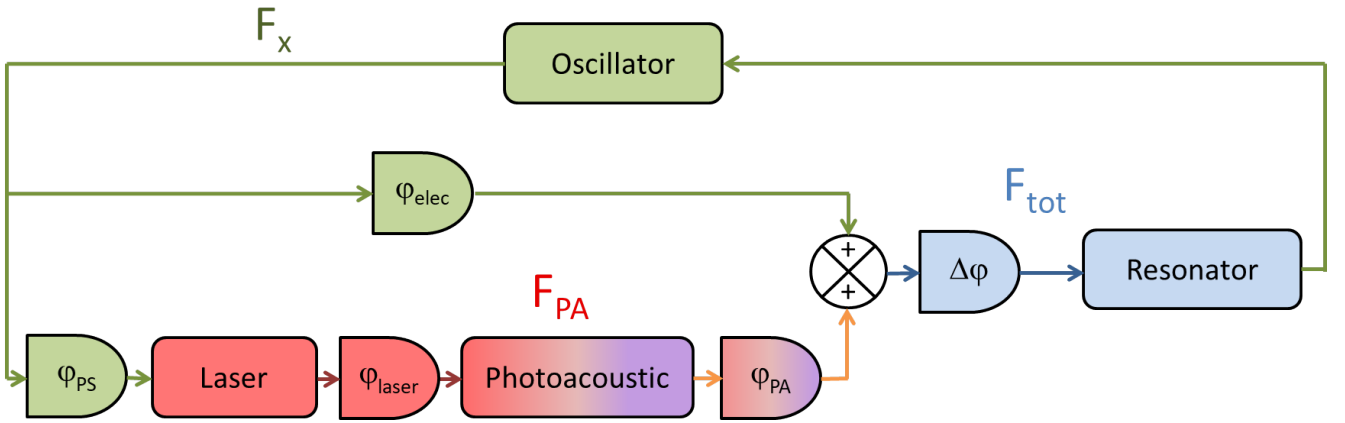


Figure 5.4: Block diagram of the method principle showing the different forces and phase shifts.

The resonator is simultaneously driven by an electrical oscillator inducing a force  $F_X$  and by the photoacoustic force  $F_{PA}$ ; these two forces are harmonic of frequency  $f_0$ . The total force acting on the resonator can be expressed as the sum of the two:  $F_{tot} = F_X + F_{PA}$  that we express as the real part of its complex form  $F_{tot} = Re\{|F_{tot}|e^{j(2\pi f_0 t - \Delta\varphi)}\}$  with  $\Delta\varphi$  the phase shift induced by applying  $F_{PA}$ .

In order to express  $F_{tot}$  it is necessary to introduce the different phase shifts of the system.

The first,  $\varphi_{laser}$ , is the phase delay due to the laser propagation between the source and the detector. Let  $d$  the distance between the laser and the detector, at the first order one can write:

$$\varphi_{laser} = \frac{2\pi d}{\lambda_L}, \quad (5.7)$$

with  $\lambda_L$  the optical wavelength in the medium.

The second is the photoacoustic phase shift  $\varphi_{PA}$ . It is the delay between the excitation and the photoacoustic signal due to gas relaxation. Its value can be derived from the generated heat expressed in Section 2.1.2 and depends on the gas relaxation time  $\tau_{V-T}$  and on the system detection frequency  $f_0$ .

$$\varphi_{PA} = -\arctan(2\pi f_0 \tau_{V-T}) \quad (5.8)$$

The third,  $\varphi_{elec}$ , is the delay introduced by the electrical circuit between the electrical oscillator driving force and the photoacoustic force. This delay takes into account the phase shifts of the circuit, due to noises or to phase shifters.

Finally, we introduce a supplementary adjustable phase shift  $\varphi_{PS}$  between the driving force and the photoacoustic force. As detailed in the next paragraphs, this phase shift is modified in order to set a quadrature between

the forces and perform differential measurements.

The piezoelectric force  $F_X$  phase is taken as the phase reference while the photoacoustic force  $F_{PA}$  acts with a phase shift depending on the total phase shift of the system. This total phase shift between the forces can be expressed by summing up all of the previous contributions:

$$\varphi_{\text{tot}} = \varphi_{\text{laser}} + \varphi_{\text{PA}} + \varphi_{\text{elec}} + \varphi_{\text{PS}}. \quad (5.9)$$

The forces can now be expressed as the real part of their complex form:

$$F_X = \text{Re}\left\{|F_X|e^{j2\pi f_0 t}\right\}, \quad (5.10)$$

$$F_{PA} = \text{Re}\left\{|F_{PA}|e^{j(2\pi f_0 t - \varphi_{\text{tot}})}\right\}. \quad (5.11)$$

Therefore, one can identify the modulus and argument of the total force by summing up the two previous expressions.

$$F_{\text{tot}} = F_X + F_{PA} = \text{Re}\left\{\left(|F_X| + |F_{PA}|e^{-j\varphi_{\text{tot}}}\right)e^{j2\pi f_0 t}\right\} = \text{Re}\left\{|F_{\text{tot}}|e^{j(2\pi f_0 t - \Delta\varphi)}\right\} \quad (5.12)$$

$$|F_{\text{tot}}| = \sqrt{\left(|F_X| + |F_{PA}|\cos(\varphi_{\text{tot}})\right)^2 + \left(|F_{PA}|\sin(\varphi_{\text{tot}})\right)^2} \quad (5.13)$$

$$\Delta\varphi = \arg(F_{\text{tot}}) = -\arctan\left(\frac{|F_{PA}|\sin(\varphi_{\text{tot}})}{|F_X| + |F_{PA}|\cos(\varphi_{\text{tot}})}\right) + 2n\pi \text{ with } n \in \mathbb{Z} \quad (5.14)$$

Usually, the electrical driving force is orders of magnitude higher than the photoacoustic force, allowing us to simplify the total force phase into:

$$\Delta\varphi \approx -\frac{|F_{PA}|}{|F_X|}\sin(\varphi_{\text{tot}}) + 2n\pi \text{ with } n \in \mathbb{Z}. \quad (5.15)$$

Eventually, one can derive the photoacoustic force as the real part of its complex form:

$$F_{\text{tot}} \approx |F_X|\cos\left(2\pi f_0 t + \frac{|F_{PA}|}{|F_X|}\sin(\varphi_{\text{tot}})\right). \quad (5.16)$$

### 5.2.1.3 Frequency variation induced by force application

The electrical driving force amplitude  $|F_X|$  is considered to be constant, therefore a change in the photoacoustic force modulus  $|F_{PA}|$  induces a linear variation of the oscillator phase with a proportionality factor that depends on the phase shift  $\varphi_{\text{tot}}$ . As shown previously in Equation 5.6, this phase shift can be converted into a frequency shift and thus one can write:

$$\Delta f_0 \approx \frac{f_0}{2Q}\Delta\varphi \approx \frac{f_0}{2Q}\left(2n\pi - \frac{|F_{PA}|}{|F_X|}\sin(\varphi_{\text{tot}})\right) \text{ with } n \in \mathbb{Z}. \quad (5.17)$$

The modification of oscillator frequency  $f_0$  is then directly proportional to the photoacoustic force magnitude as long as the condition  $|F_{PA}| \ll |F_X|$  is satisfied. Otherwise, it will be necessary to study the method linearity when the driving force becomes of the same order of magnitude as the photoacoustic one. Also, for the oscillation condition to remain valid, the frequency shift must be kept small compared to the resonator bandwidth i.e.

$\Delta f_0 \ll \frac{f_0}{Q}$ . In addition, by carefully choosing the value of the phase shift  $\varphi_{PS}$  we introduce in the circuit, it is possible to maximise the value of the frequency shift.

$$|\sin(\varphi_{\text{tot}})| = 1 \iff \varphi_{\text{tot}} = \frac{\pi}{2} + n\pi \text{ with } n \in \mathbb{Z} \quad (5.18)$$

The frequency shift  $\Delta f_0$  is thus maximised when a force quadrature is established between the electric and the photoacoustic forces. This quadrature is set when the tunable phase shift  $\varphi_{PS}$  compensates for the other phase shifts of the oscillator loop. This also means that studying the phase shifts of the oscillator loop allows for determining the gas relaxation rate  $\tau_{V-T}$ .

Finally, through sequential injection of the phase shifts,  $\varphi_{PS} = \{\varphi_{PS,\text{min}} + 2n\pi; \varphi_{PS,\text{max}} + 2n\pi, \text{ with } n \in \mathbb{Z}\}$  minimising and maximising the frequency shift, it is possible to carry out a differential measurement. By measuring the frequency of the oscillator at these phases one can obtain the differential frequency shift:

$$\Delta f_{0,\text{diff}} = |(f_0 + \Delta f_0) - (f_0 - \Delta f_0)| \approx \frac{1}{Q} f_0 \frac{|F_{PA}|}{|F_X|}. \quad (5.19)$$

Measuring a frequency difference provides immunity against time variation of the resonator frequency due, for example, to temperature or pressure modifications. Also, one can expect an improvement of the immunity of the sensor against acoustic or vibratory background signals.

## 5.2.2 Frequency noise description using Leeson's equation

After expressing the signal generated by our new method as a differential frequency shift, we now have to identify which noise does limit the system. We here expect the frequency noise of the oscillator to be the ultimate noise of our system, if we are able to detect it. In order to express the frequency noise, we use the model described by Leeson in 1966 through the heuristic study of oscillator loops [186].

Let us consider a system composed of a loop containing a resonator driven by a gain amplifier (Figure 5.5).

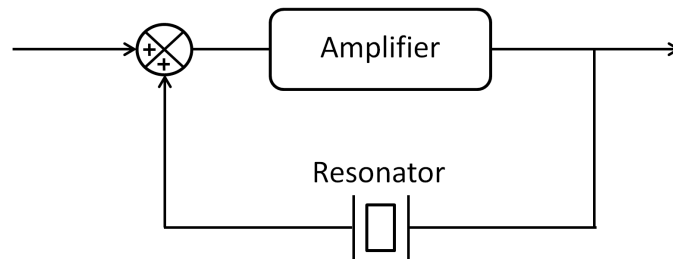


Figure 5.5: Oscillator loop containing a gain amplifier and a resonator being a tuning fork in our case.

One can write the phase noise spectral density  $S_{\Phi}(\delta f)$  of this oscillator thanks to the Leeson-Cutler equation [186]:

$$S_{\Phi}(\delta f) = \frac{Fk_B T}{P_0} \left[ 1 + \frac{1}{\delta f^2} \left( \frac{f_0}{2Q} \right)^2 \right] \left( 1 + \frac{f_c}{\delta f} \right). \quad (5.20)$$

$S_{\Phi}(\delta f)$  is in  $\text{rad}^2 \cdot \text{Hz}^{-1}$  and is computed along  $\delta f$ , the distance from the carrier frequency in Hz. This equation can be plotted as a curve with three different slopes. The first represents the phase noise floor  $\frac{Fk_B T}{P_0}$ ,

where  $F$  is the oscillator noise factor,  $P_0$  is the power dissipated within the oscillator in  $W$ ,  $k_B$  is the Boltzmann constant and  $T$  the temperature in  $K$ . The two other slopes depend on the position of the corner frequency  $f_c$ , between white and Flicker noise, with respect to Leeson's frequency  $f_L = \frac{f_0}{2Q}$  as shown in Figure 5.6.

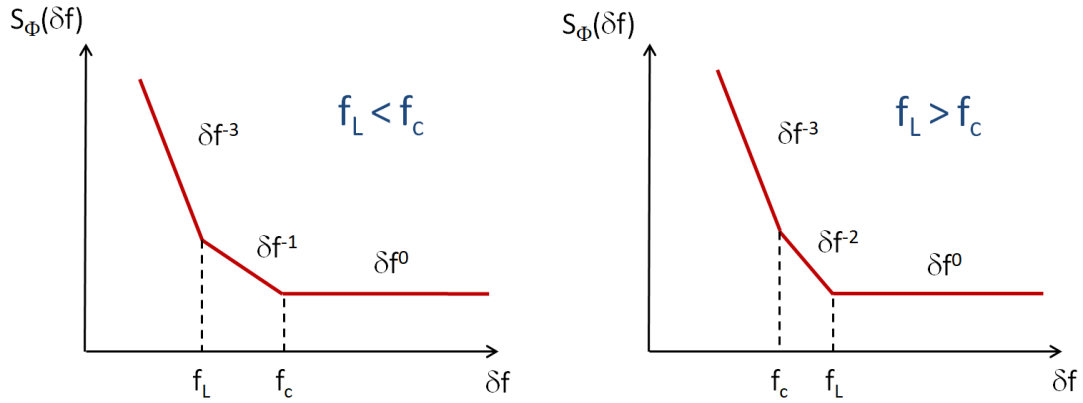


Figure 5.6: Leeson's model for phase noise depending on the value of the corner frequency with respect to the Leeson's frequency.

The corner frequency  $f_c$  and the oscillator noise factor  $F$  depend on the amplifier noises. These have to be determined experimentally for each system, a task we will accomplish in the next sections.

The phase noise can be considered to be a frequency noise and conversely. For convenience, we work with frequency and so the frequency noise spectral density in  $\text{Hz}^2 \cdot \text{Hz}^{-1}$  can be expressed as follows:

$$S_F(\delta f) = \delta f^2 S_\Phi(\delta f). \quad (5.21)$$

Eventually, to compute the signal-to-noise ratio, one can use the Allan deviation  $\sigma_F(\tau)$  in  $\text{Hz}$  of the oscillator frequency. It can be computed by integrating the product of the variance transfer function with the frequency noise power spectral density [187, 154] over a bandwidth from 0 to the high corner frequency  $f_{H1}$ . This bandwidth is adjusted by the oscillator filter.

$$\sigma_F(\tau) = f_0 \sqrt{2 \int_0^{f_H} S_F(\delta f) \frac{\sin^4(\pi \delta f \tau)}{(\pi \delta f \tau)^2} d(\delta f)} \quad (5.22)$$

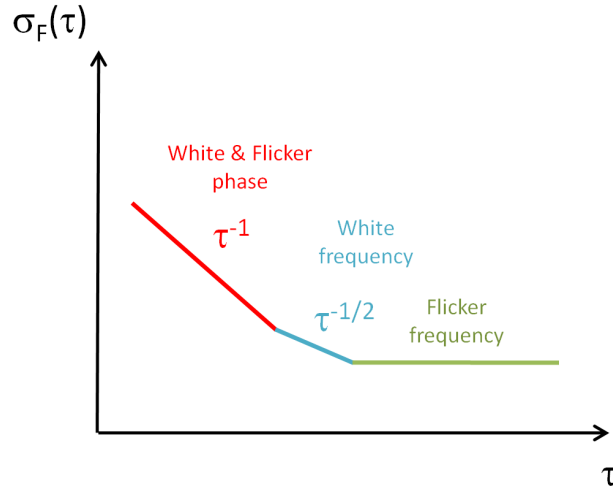


Figure 5.7: Model of the Allan deviation representing the different slopes and corresponding noises.

A solution of this integral can be given. We choose to limit our study so that we do not consider the oscillator random walk and further drifts inducing a rise of the Allan deviation for longer integration times. This solution describes three different slopes of the Allan deviation as represented in Figure 5.7. The first one, proportional to  $\tau^{-1}$ , represents the white and Flicker phase noises. The second one, proportional to  $\tau^{-1/2}$ , represents the white frequency noise. The last one is the frequency Flicker noise floor.

$$\sigma_F(\tau) = f_0 \sqrt{\left( \frac{b_0}{f_0^2} \frac{3f_H}{4\pi^2} + \frac{b_{-1}}{f_0^2 4\pi^2} \left( 1 + 3 \ln(2\pi f_{H1} \tau) \right) \right) \frac{1}{\tau^2} + \frac{b_0}{8Q\tau} + \frac{\ln(2)b_{-1}}{2Q^2}} \quad (5.23)$$

$$b_0 = \frac{Fk_B T}{P_0} \quad b_{-1} = f_c b_0 \quad (5.24)$$

One can finally compute the theoretical SNR for an integration time  $\tau$  as:

$$\text{SNR}(\tau) = \frac{\Delta f_{0,\text{diff}}}{\sigma_F(\tau)}. \quad (5.25)$$

## 5.3 Experimental validation of the analytical model

In this section we will strive to validate the analytical model we have presented through an experimental analysis of the method. We will present how this method was implemented, as well as the analysis of the noise and signal depending on system parameters.

### 5.3.1 Implementation

In order to study the method we have used QTF C2 presented in this manuscript. This QTF has a fundamental frequency of 21.5 kHz and a quality factor of approximately 8,000 in air at atmospheric pressure. Its electrodes pattern was slightly modified by using an electrode for the excitation and the other electrodes for signal collection (see Table 5.2).

#### 5.3.1.1 Proximity electronics

As for the open loop detection scheme, the QTF signal was amplified before processing. In addition, a suppression of the parasitic capacitance  $C_0$  effect has been set to enhance the oscillator stability. For this purpose a



subtracting circuit is used in parallel of the resonator and in which a capacitance  $C'_0$  is placed. Its value is chosen as close as possible to  $C_0$  and the gain of the amplifier is set so as to compensate for the effect of this capacitance at the QTF resonance. This signal is then amplified owing to a transimpedance amplifier followed by a voltage amplifier (Figure 5.8).

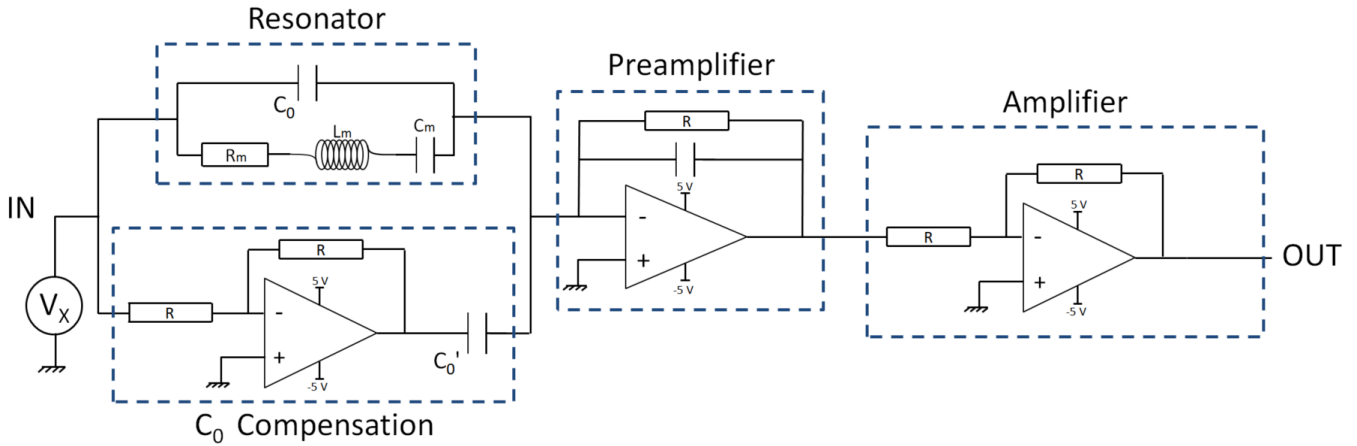


Figure 5.8: Schematic of the proximity circuit for amplification of the QTF signal and compensation of the parasitic capacitance  $C_0$ . The triangular components are classic operational amplifiers.

### 5.3.1.2 Oscillator

In order to make the resonator oscillate, we have demonstrated the possibility to use an analog oscillator as shown in [185]. However, to study the influence of the system parameters and to improve the SNR we used a HF2LI lock-in amplifier (Zurich Instruments). This commercial LIA is capable of oscillating a resonator through the use of two phase-locked loops. In addition, it is capable of performing signal and noise analysis through Fourier transform. Finally, this instrument is easily remotely controlled by means of Python scripts.

## 5.3.2 Noise measurements

In the theoretical section, we presented the oscillator phase noise as the ultimate noise of this system. In this section, we will strive to verify which noise does actually limit the system. Moreover, we will study the influence of parameters such as excitation voltage or motional resistance on the oscillator phase noise power spectral density (PSD).

### 5.3.2.1 Experimental setup

We placed the QTF and its proximity electronics within a metallic enclosure acting as a Faraday cage to shield from the electromagnetic environment (Figure 5.9).

Firstly, the QTF spectrum is swept across in order to find its resonance frequency, quality factor and phase set-point at resonance (see Figure 5.3). The oscillation is then set based on these values by means of a phase-locked loop (PLL 1) (Figure 5.10).

A PLL is a loop composed of three main components. The first is a voltage controlled oscillator (VCO) that generates a harmonic signal, the second is a phase detector which measures the difference of phase between the VCO and the input signal. This measure is then fed to a PID controller enabling control of the phase difference by adjustment of the generated signal frequency.

The resulting oscillator (QTF + oscillating circuit) is characterised by its driving power  $P_0$ , by its noise factor  $F$ , and Flicker corner frequency  $f_c$ , both depending on the electrical design of the amplifiers. Oscillator power

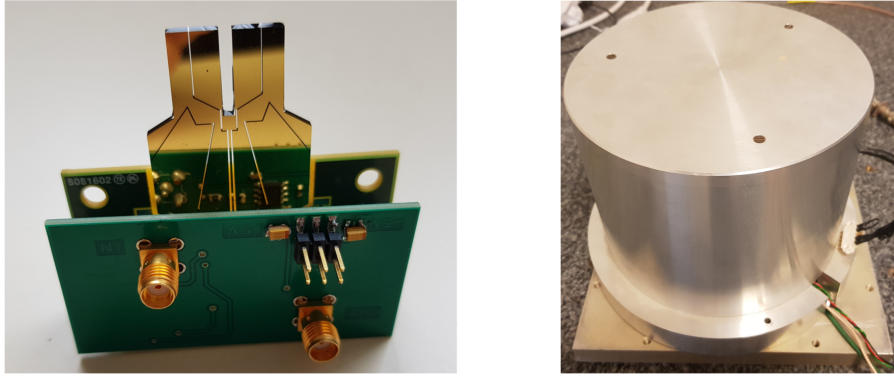


Figure 5.9: C2 QTF and its electronics for parasitic capacitance compensation (left). Metallic enclosure inside which the QTF is placed for noise measurements (right).

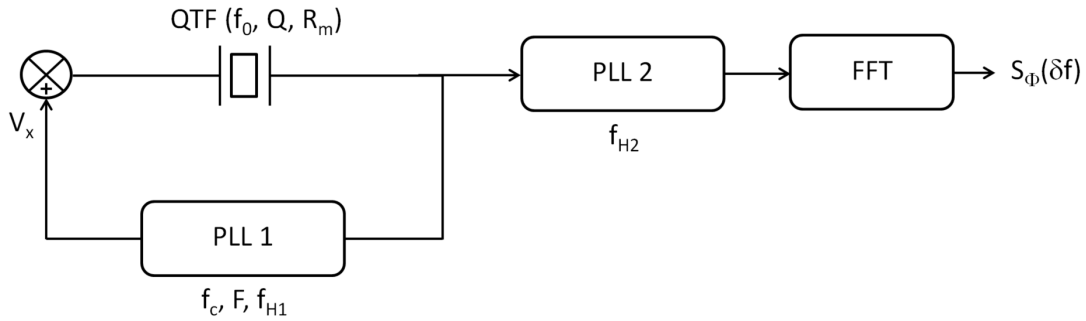


Figure 5.10: Differential photoacoustic noise measurement scheme. The QTF is oscillated with a PLL, then a second PLL filters the long term drifts and a Fourier transform is performed giving the phase noise PSD.

depends on the excitation voltage  $V_X$  and on the QTF motional resistance  $R_m$  as described in Equation 5.26. Finally,  $R_m$  itself depends on the QTF features and on the excitation electrode in a non-trivial way.

$$P_0 = \frac{V_X^2}{R_m} \quad (5.26)$$

The first PLL sets the oscillation and a low-pass of bandwidth  $f_{H1}$  is used to reduce noises and increase the oscillator stability. After the oscillation is started, a second PLL follows the frequency of the first. Its bandwidth  $f_{H2}$  is chosen to be very small, typically inferior to 1 Hz, in order to keep static phase variations and filter long term phase drifts. The phase comparator inside the second PLL computes the difference between the output of the first PLL and the second PLL signal. This difference yields the phase noise of the oscillator. Finally, a Fourier transform of the second PLL output is performed and provides the oscillator phase noise power spectral density  $S_\Phi(\delta f)$ .

### 5.3.2.2 Determination of the limiting noise

A first measurement was carried out in order to determine the limiting noise. The parameters values are given in Table 5.1 and the measurement is presented in Figure 5.11.

Data at frequencies below  $f_{H1}$  account for long term drifts and should not be taken into account. Data beyond  $f_{H2}$  are filtered by the second PLL, reason why the noise is decreasing, and should not be taken into account either. These areas have been greyed out in Figure 5.11.

A least-square fit was made based on the theoretical model of the phase noise PSD (Equation 5.20) with the input parameters presented in Table 5.1. The fit output gave the parameters  $F$  and  $f_c$  of the oscillator amplifier

QTF		Oscillator	
$f_0$ (Hz)	21,509	$V_X$ (mV <sub>pk</sub> )	1
$Q$	8,000	$f_{H1}$ (Hz)	100
$R_m$ (M $\Omega$ )	1	$f_{H2}$ (mHz)	100

Table 5.1: Measurement parameters.

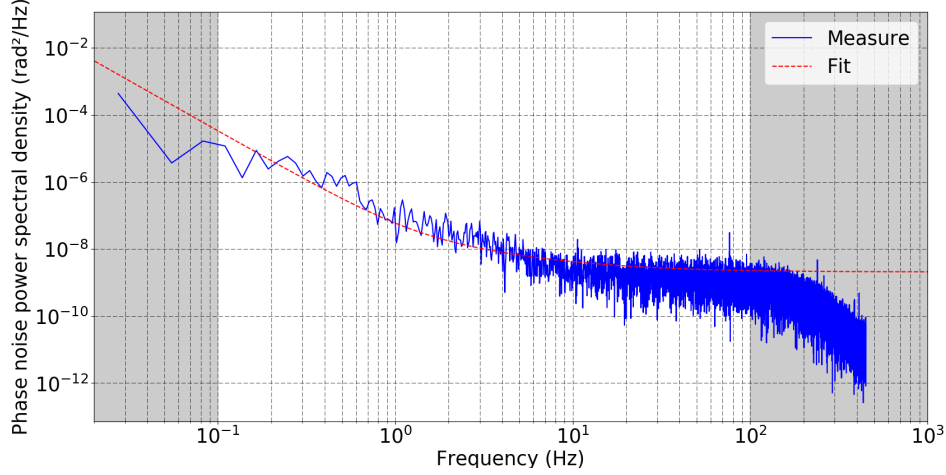


Figure 5.11: Measured phase noise power spectral density for  $f_{H1} = 100$  Hz,  $f_{H2} = 100$  mHz (blue). The first point is the FFT resolution, here 7 mHz. Data are fitted so as to obtain the values of  $F$  and  $f_c$  (red).

All other fit parameters are known from prior computations.

(constituted of the proximity electronics and of the HF2LI). The oscillator noise factor  $F$  was computed to be around 1 while the Flicker corner frequency  $f_c$  was computed to be around 10 Hz. These values are typical for quartz oscillators ( $F = 1$ ,  $f_c = 24$  Hz for a 60 kHz QTF with a quality factor of 12,000 in [188]).

The good agreement between the measured phase noise PSD and its theoretical fit using Equation 5.20 enables us to state that this noise is actually limiting in our system, as we expected. From now on, we will use the values determined by the fit to model the phase noise.

### 5.3.2.3 Influence of excitation voltage

In order to further validate our noise model, we studied the influence of several parameters on the phase noise PSD. One of them is the voltage  $V_X$  used to excite the QTF. According to Equations 5.20 and 5.26 the noise PSD should be inversely proportional to  $V_X^2$ .

To perform these measurements, we chose identical parameters as the ones presented in Table 5.1 and we varied the excitation voltage. The results are presented in Figure 5.12.

The resulting PSD matches the theoretical model for excitation voltages from 100  $\mu$ V<sub>pk</sub> to 10 mV<sub>pk</sub>. Indeed, the noise PSD decreases by a factor 100 when increasing the excitation voltage by 10. However, data does not match with the model for 100 mV<sub>pk</sub> (below 1 Hz) and 1 V<sub>pk</sub>. This can be explained by the presence of other noises in the system. In fact, by increasing the voltage we decreased the noise amplitude and reached the limiting noise of the system. This system noise can hardly be attributed to any specific source but could come from the amplifiers or from the phase measurement itself.

By performing these measurements we confirmed that we should work with the lowest excitation voltage available. Indeed, the SNR is not modified with the excitation voltage as both the signal and noise are scaled with it. Using the lowest excitation allows for the phase noise PSD to become the limiting noise of the system before

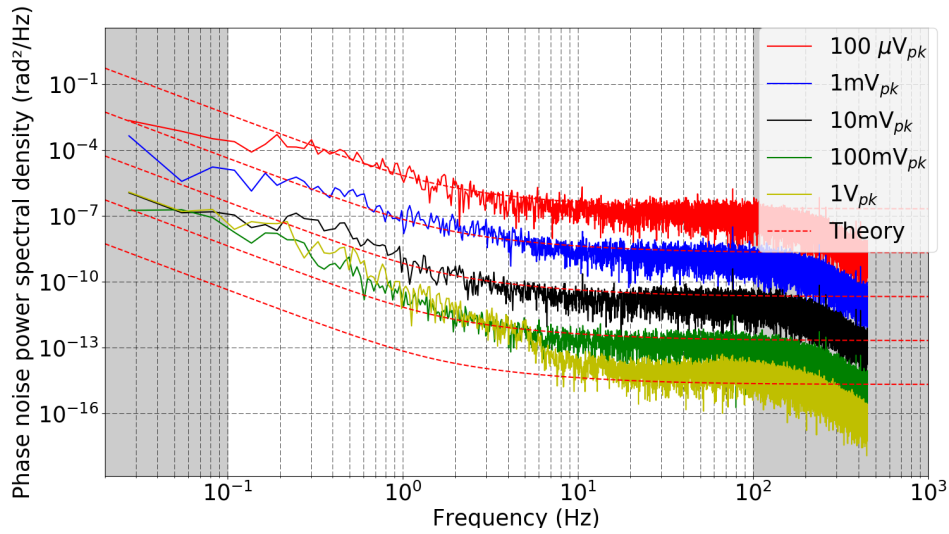
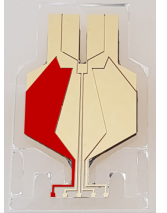
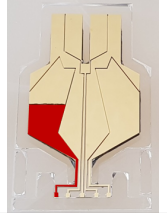


Figure 5.12: Measured phase noise power spectral density for different excitation voltages. The measurement parameters are the ones presented in Table 5.1. For each value of  $V_X$ , the resulting PSD is compared with the theory from Equation 5.20 without any adjustment of the fitting parameters determined in Figure 5.11.

other noise sources.

#### 5.3.2.4 Influence of motional resistance

QTF	"Full"	"Half"
Photography		
$f_0$ (Hz)	21,509	21,909
$Q$	8,000	7,500
$R_m$ (M $\Omega$ )	1	3

Oscillator	
$V_X$ (mV <sub>pk</sub> )	10
$f_{H1}$ (Hz)	100
$f_{H2}$ (mHz)	200

Table 5.2: Measurement parameters for two C2 QTFs with different electrode schemes. The electrode colored red is used for excitation of the QTF while the others are used for signal recovery.

A second parameter whose influence was studied is the QTF motional resistance  $R_m$ . It depends on the QTF features (geometry,  $Q$ , charge distribution, etc.) and on the excitation electrode efficiency. In order to perform comparative measurements, we used two different C2 QTFs and modified their electrode pattern. The first of them, we call "Full", is excited by a full electrode and is the one we used during all previous experiments. For the other one, called "Half", we used a Cr-Au etchant to perform an electrical cutting of the same electrode. The frequency, quality factor and motional resistance were computed after a sweep of the resonance frequency using the HF2LI lock-in amplifier. The motional resistance can be obtained through the amplitude of the resonance. These parameters are presented in Table 5.2. By performing such a cutting, we increased the motional resistance up to 3 times the one of the QTF "Full" and 13 times the one of the QTF with a classic electrode scheme. This increase should theoretically allow for increasing the phase noise PSD which is proportional to  $R_m$  in the same

way as what we achieved by decreasing the excitation voltage.

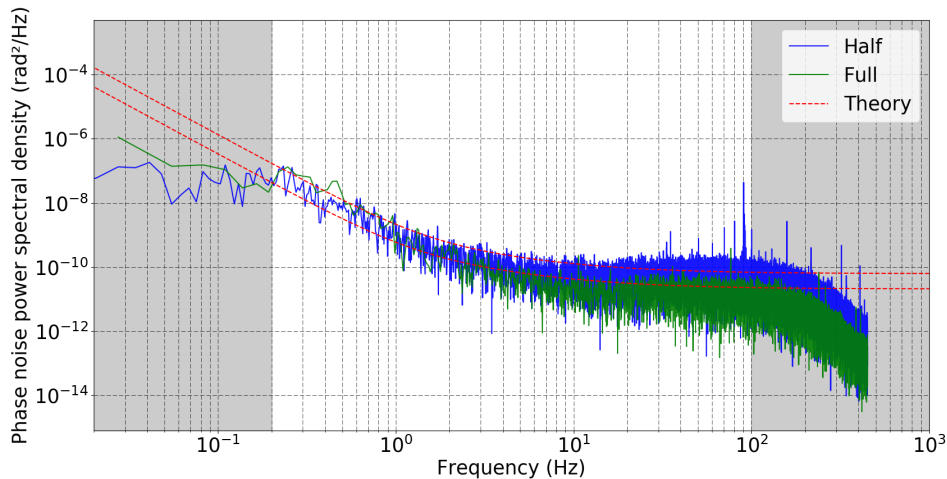


Figure 5.13: Measured phase noise power spectral density for C2 QTFs presenting different electrode patterns. The measurement parameters are the ones presented in Table 5.1. Each PSD is compared with the theory from Equation 5.20 without any adjustment of the parameters, only  $R_m$  is varied according to the values reported in Table 5.2.

As seen in Figure 5.13, results show that the phase noise PSD matches the theoretical curves. As expected, the noise PSD was increased by a factor approximately 3 when using QTF "Half" compared to QTF "Full". In the same way as what we achieved through modifying the excitation voltage, it is thus possible to increase the noise when reducing the motional resistance. This increase could allow us to make sure that this noise is limiting in the system and provides an alternative solution to the decrease of the excitation voltage.

### 5.3.3 Photoacoustic measurements

After having studied the oscillator noise and proving it is the system limiting noise, we will hereafter keep on studying our new method through photoacoustic measurements.

#### 5.3.3.1 Experimental setup

In a very similar way to noise measurements, the experimental setup consists in oscillating the QTF with PLL 1. Then, the second PLL follows the first while imposing a phase shift  $\varphi_{PS}$  that we will use in order to set the differential measurement as presented before. This phase shifted signal is used to modulate the amplitude of the laser diode thanks to a Mach-Zehnder modulator, giving a modulated laser power of 6 mW. The telecom laser diode temperature was set and stabilised to reach the  $6,490.02 \text{ cm}^{-1}$  absorption line of  $\text{C}_2\text{H}_2$  yielding an absorption of  $1.88 \cdot 10^{-7} \text{ cm}^{-1}$  for 1 ppmv. Finally, the cell was evacuated and filled with a certified mixture of 1,000 ppmv  $\text{C}_2\text{H}_2$  in  $\text{N}_2$  at atmospheric pressure.

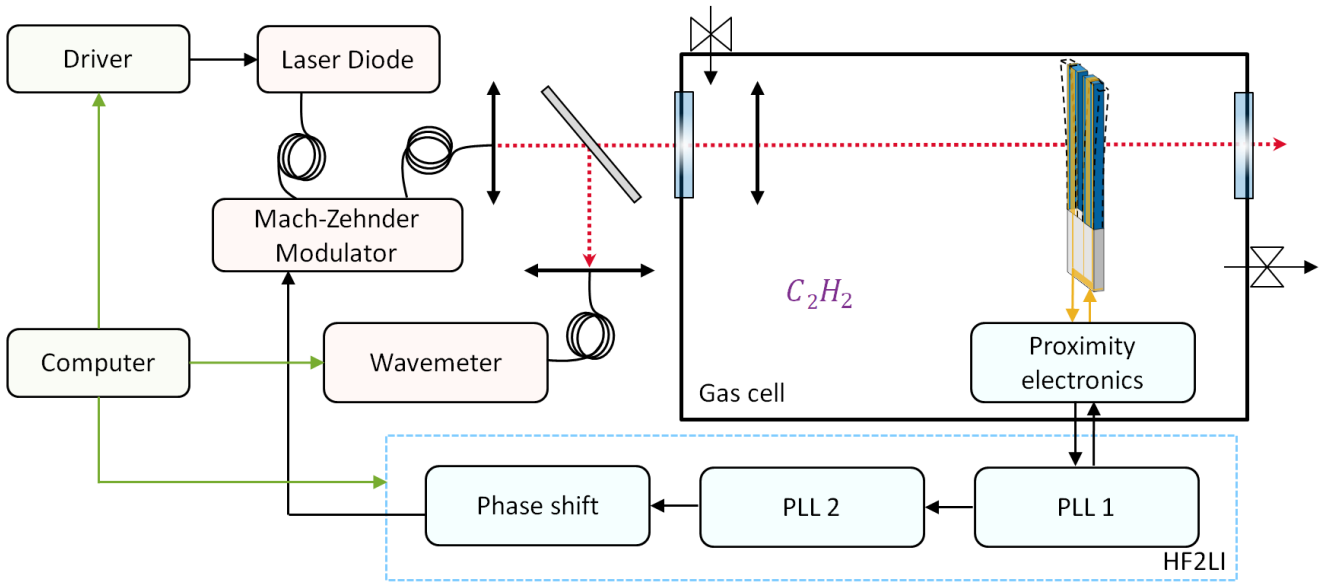


Figure 5.14: Differential photoacoustic measurement experimental setup. The QTF is driven by an oscillator whose frequency is used to modulate the laser amplitude. A phase shift stage is added so as to perform differential measurements.

### 5.3.3.2 Principle validation

In order to perform the differential frequency measurement, we started the oscillator and programmed the measurement by means of a Python script. Parameters of the oscillator are presented in Table 5.3.

QTF "Full"		Oscillator	
$f_0$ (Hz)	21,509	$V_X$ (mV <sub>pk</sub> )	10
$Q$	8,000	$f_{H1}$ (Hz)	1
$R_m$ (M $\Omega$ )	1	$f_{H2}$ (Hz)	1

Table 5.3: Measurement parameters for principle validation.

The first step is to perform a measurement of the oscillator frequency while varying phase shift  $\varphi_{PS}$ . This measurement allows for finding the values,  $\varphi_{PS,min}$  and  $\varphi_{PS,max}$ , respectively minimising and maximising the frequency shift. As explained in Section 5.2.1, these values enable a quadrature to be set between the piezoelectric force and the photoacoustic force. They depend on the circuit, laser propagation, as well as gas relaxation time and detection frequency.

We obtained  $\varphi_{PS,min} = 122^\circ$  and  $\varphi_{PS,max} = -55^\circ$  as seen in Figure 5.15. Also, as we described in Equation 5.6, the frequency shift  $\Delta f_0$  is sinusoidal with the applied phase shift.

By measuring the phase shift of the circuit, one could deduce the photoacoustic phase shift, hence the gas relaxation time. This could allow to correct measurements for gases with a slow relaxation time varying in time.

After finding the phase shift values leading to the frequency shift extrema, the corresponding values were stored and sent sequentially in order to carry out the differential measurement. First,  $\varphi_{PS,max}$  was set, then we measured the oscillator frequency, then we waited a certain time  $t_{wait}$  and repeated this step with  $\varphi_{PS,min}$ . After this measurement was performed we computed the difference between the maximal and minimal frequencies  $\Delta f_{0,diff}$ .

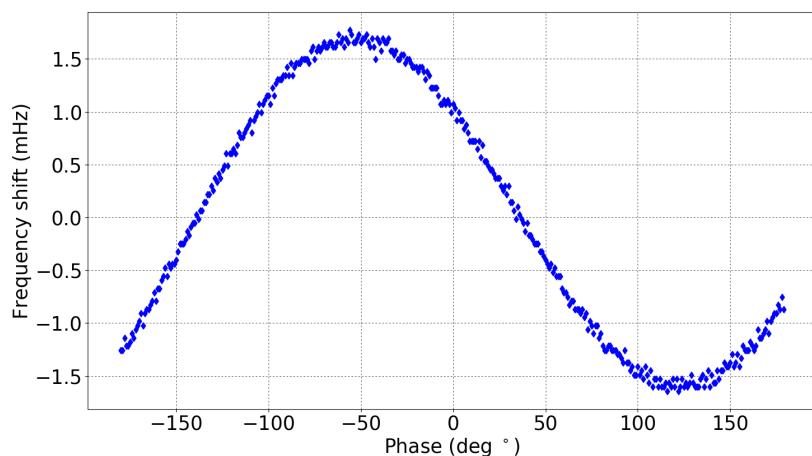


Figure 5.15: Determination of the optimum phase shifts  $\varphi_{PS,min}$  and  $\varphi_{PS,max}$  used to perform differential measurements.

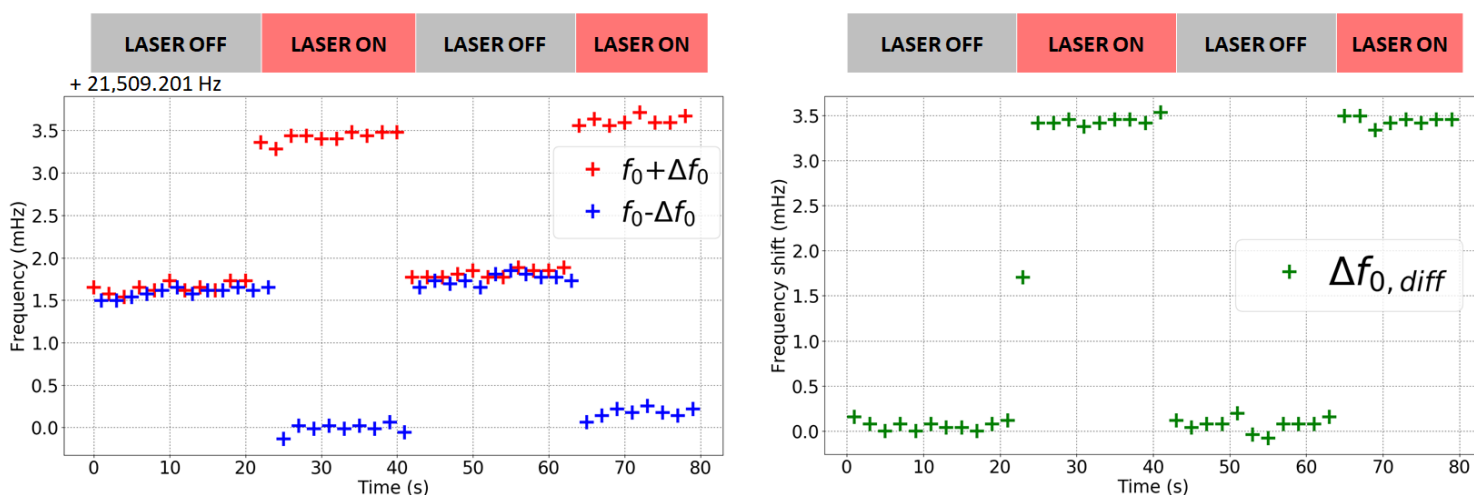


Figure 5.16: Principle validation of the differential measurement. The optimum phase shifts are sent sequentially with a wait time  $t_{wait}$  of 1s, resulting in extrema of the frequency shift. A frequency drift over time can be observed (left). The differential allows to cancel the frequency drift (right).

An example is presented in Figure 5.16. During this demonstrative measurement, we switch on and off the laser in order to show the background signal and the oscillator frequency drift. Indeed, on the left part of the figure, we can see a slight drift of the oscillator frequency with time. This drift is mainly caused by temperature changes seen by the QTF. On the right, we demonstrated a cancellation of this drift thanks to the differential scheme, which shall improve the signal stability in temperature fluctuating gases. A signal of 3.4 mHz was obtained for 1,000 ppmv of  $C_2H_2$  at  $6,490.02\text{ cm}^{-1}$ . This signal is 4 times inferior to the one predicted by theory. This discrepancy still needs to be explained and varies from one measurement to another, however it did not impact the SNR. Further study should focus on the investigation of this issue in order to have a model that can quantitatively describe the signal amplitude.

Eventually, we performed a calculation of the Allan deviation of the differential signal, as presented in Figure 5.17. One can observe a typical averaging of the QTF phase Flicker and white noise, followed by an averaging of white frequency noise. The minimal detection limit of 10  $\mu\text{Hz}$  is reached around an integration time of 200 s. Beyond 300 s random walk frequency noise is seen.

In order to verify its validity, we fitted the Allan deviation plot with our model. For this purpose, we com-

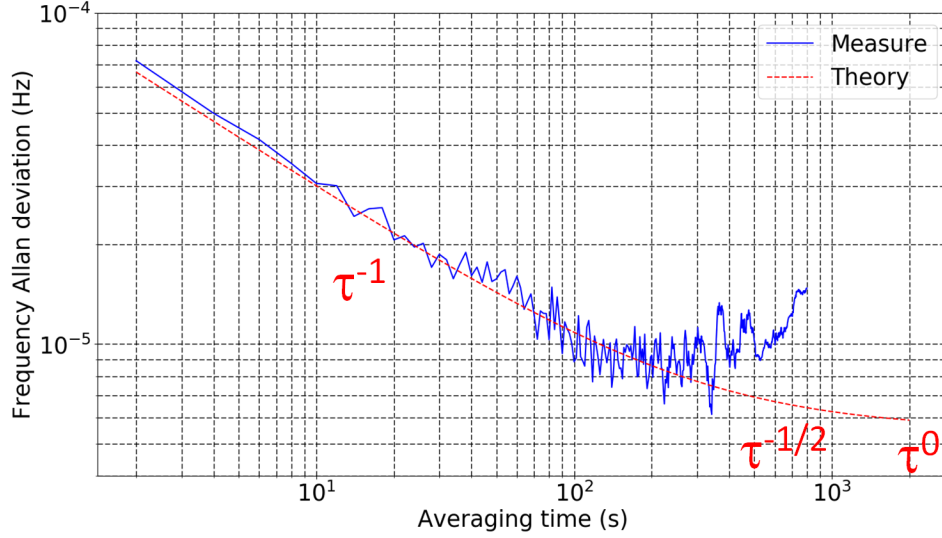


Figure 5.17: Allan deviation of the differential photoacoustic measurement. The averaging of the phase Flicker and white noise is seen (proportional to  $\tau^{-1}$ ) followed by averaging of the white frequency noise ( $\tau^{-1/2}$ ). The signal drifts around 300 s before reaching the frequency Flicker noise floor.

puted the photoacoustic force using our analytical model (PYRATS) and obtained a force of  $5.16 \times 10^{-10}$  N for a laser power of 6 mW. The piezoelectric force acting on the actively driven QTF was determined through simulation. A 1 V voltage was defined on the excitation electrode and the coefficient  $c_X$  giving the force per voltage was computed (Equation 5.27). We obtained  $c_X = 8.33 \times 10^{-6}$  N.V<sup>-1</sup>, representing a piezoelectric force  $F_X$  of  $1.18 \times 10^{-7}$  N.

$$|F_X| = c_X V_X \quad (5.27)$$

We obtained a good fit by slightly modifying the photoacoustic force from  $5.16 \times 10^{-10}$  N to  $6.16 \times 10^{-10}$  N which is a rather good estimate considering this force was evaluated analytically. However, one can observe that the signal drifts before reaching the analytical frequency Flicker noise floor shown by the fitted deviation beyond 1,000 s.

While we predicted an enhancement of the stability over time thanks to the differential measurement, drifts inevitably happen. The nature of this long term drift is hard to determine, nonetheless it usually corresponds to frequency drift due to temperature or pressure changes, vibrations or even laser wavelength and power stability. Additional experiments should be conducted in order to determine the drift nature. Nonetheless, we expect that reducing the large wait time,  $t_{\text{wait}} = 1$  s, between each measurement of the frequency will lead to stability enhancement. Limiting the system drifts will allow for longer averaging of the signal and improvement of the detection limit.

### 5.3.3.3 Influence of excitation voltage

The same study as the one we led on the phase noise PSD was carried out on the signal and Allan deviation while modifying the QTF excitation voltage. For this purpose, the optimal phase shifts were determined for each value of the excitation voltage. In the same time, the PLL parameters were adapted to match the new phase set-point of the resonance, which slightly changes with excitation. For each voltage, we measured the differential signal and performed an Allan deviation calculation. These results are presented in Figure 5.18 and the parameters are the same as in Table 5.3.



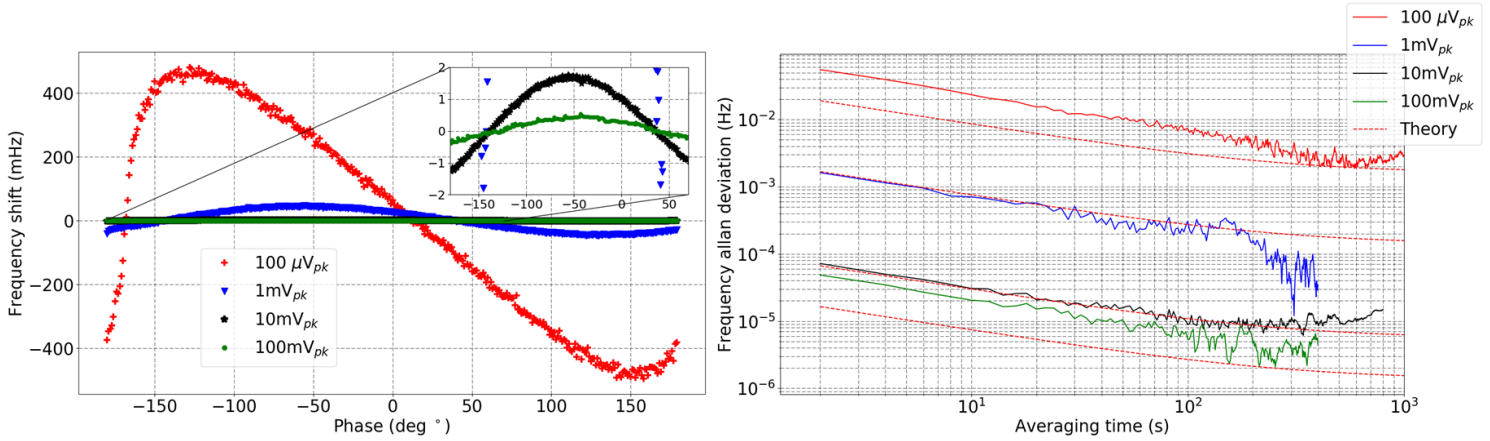


Figure 5.18: Influence of excitation voltage on the frequency shift  $\Delta f_0$  (left) and on the Allan deviation (right). Theoretical Allan deviations are plotted for comparison.

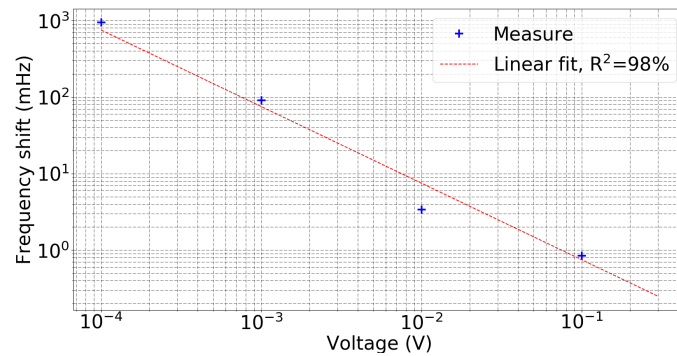


Figure 5.19: Influence of excitation voltage on the frequency shift  $\Delta f_{0,diff}$ . After taking the logarithm, a linear fit was made, showing that the signal is inversely related to the voltage as expected from Equations 5.6 and 5.27.

Concerning the signal one can see that a dependence on the inverse of the excitation voltage is found with a coefficient  $R^2$  of 98% (Figure 5.19). This is described by Equations 5.6 and 5.27, the piezoelectric force being proportional to the voltage. A discrepancy can be observed for a voltage of 10 mV<sub>pk</sub> and still needs to be explained. Moreover, one can note that the curve shape for  $V_X = 100 \mu\text{V}_{pk}$  deviates from a sine function in contrast to the others. For this case, the differential frequency can be computed to be nearly equal to 1 Hz which is close to the QTF bandwidth ( $f_0/Q \approx 2.7$  Hz). Therefore the hypothesis we made in Equation 5.6 no longer holds, thus causing a distortion of the sine wave. Furthermore, for frequency shifts this big compared to the QTF bandwidth, there is a risk to unlock the oscillator, which should be avoided by adapting the excitation to the photoacoustic force. The signal for a 1 V<sub>pk</sub> excitation could not be determined because it was too weak compared to the signal background noise.

In the same way, Allan deviation is the highest when excitation is the lowest. It is well described by the theoretical fit in most cases. However, for 100 mV<sub>pk</sub> the Allan deviation seems to have reached the system noise limitation. This also could be seen on the phase noise PSD in Figure 5.12. For 100  $\mu\text{V}_{pk}$ , the same can be observed despite the good match of the noise PSD. A possible explanation is the stability of the voltage source for such a weak signal and the influence of electromagnetic background on it. It is also possible that having a big frequency shift compared to the QTF bandwidth increased the oscillator instability. The SNR can be considered constant with a modification of the excitation voltage, except in cases where the noise is limited by the system rather than by the oscillator. Voltage should then be chosen the lowest possible

while satisfying the condition  $\Delta f_{0,\text{diff}} \ll \frac{f_0}{Q}$ . This parameter enables to choose the sensor dynamic range or to adapt it to the current signal level, expanding the dynamic range from the limit of detection to 100% gas concentrations.

### 5.3.3.4 Influence of motional resistance

We applied the same method to study the influence of motional resistance. The same parameters were applied for each QTF and are presented in Table 5.4. Theoretically, this resistance value modifies the oscillator power  $P_0$  and the piezoelectric force  $F_X$ . The piezoelectric force value was determined by simulation for both QTFs.

QTF	"Full"	"Half"
$f_0$ (Hz)	21,509	21,909
$Q$	8,000	7,500
$R_m$ (M $\Omega$ )	1	3
$c_X$ (N.V <sup>-1</sup> )	$8.33 \cdot 10^{-6}$	$1.82 \cdot 10^{-6}$

Oscillator	
$V_X$ (mV <sub>pk</sub> )	10
$f_{H1}$ (Hz)	1
$f_{H2}$ (Hz)	1,000

Table 5.4: Measurement parameters for two C2 QTFs with different electrode schemes.

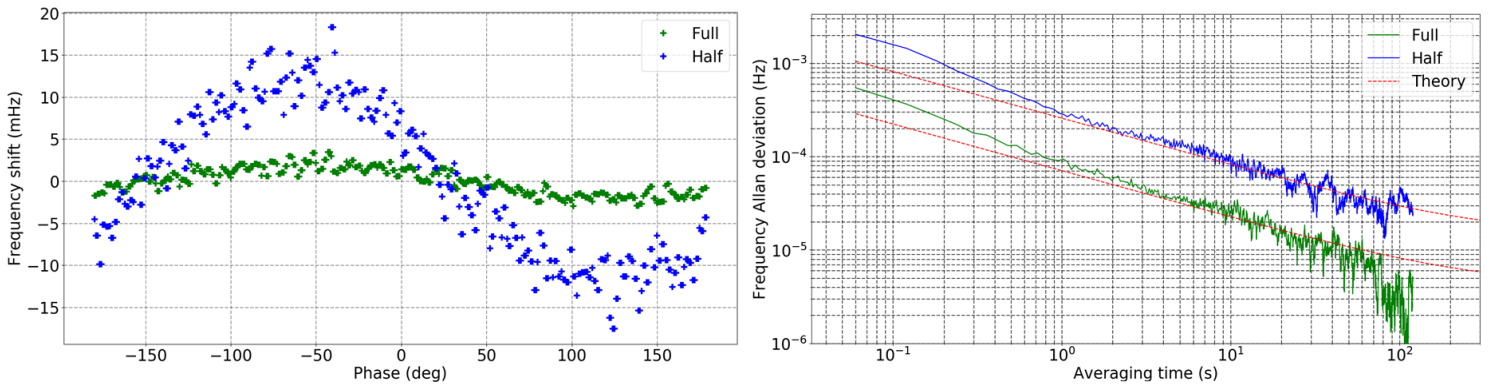


Figure 5.20: Influence of motional resistance on the frequency shift  $\Delta f_{0,\text{diff}}$  (left) and Allan deviation (right).

As shown in Figure 5.20 the differential frequency was increased by a factor approximately 6 when using the QTF "Half" compared to QTF "Full". This factor corresponds to the simulated decrease of the piezoelectric force. On the other hand the Allan deviation was increased by a factor 3 to 4 while, according to theory, it should have increased by the square root of the resistance increase i.e.  $\sqrt{3}$  when passing from 1 to 3 M $\Omega$ . This discrepancy could not be explained and further studies should try to understand this result. Nonetheless, the result clearly shows that increasing the motional resistance induces increasing the system frequency shift and noise.

### 5.3.3.5 Linearity with gas concentration

While photoacoustic techniques are generally linear with the gas concentration for weak absorptions, we propose to study the linearity of our method. The differential signal depends on the ratio of the photoacoustic force on the piezoelectric force, potentially creating non-linearities if the two forces are of the same order of magnitude. We showed that modifying excitation voltage and motional resistance could be used to scale the piezoelectric force. Nonetheless, here we choose to study the linearity for a same excitation voltage of 1 mV<sub>pk</sub>. We measured

the linearity of our method by diluting a mix of 1,000 ppmv of  $C_2H_2$  in  $N_2$  in ambient air. Results are presented in Figure 5.21. Parameters are the same as in Table 5.3.

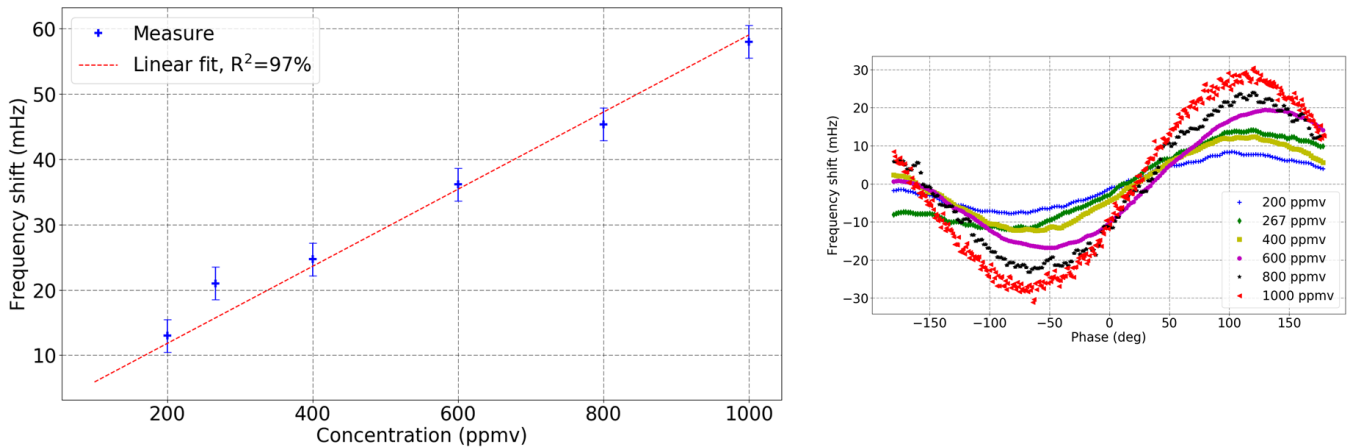


Figure 5.21: Linearity of the technique with gas concentration. Linear fit of the data (left). Raw data (right).

Measurements could be made for concentrations from 200 to 1,000 ppmv. Unfortunately, an electromagnetic background induced a varying signal of a few mHz, making measurements impossible at lower concentrations. After studying our system we saw that this background came from the laser modulation coming out of the HF2LI towards the Mach-Zehnder modulator. This signal, modulated at the detection frequency, presents an amplitude of a few volts and its influence was observed on the background signal. We could not efficiently cancel this electromagnetic background, however several solutions are possible. Indeed, it could be possible to use a wavelength modulation scheme so that this parasitic signal frequency is no more coincident with the detection frequency. Also, by integrating this measurement in a packaged sensor it should be possible to shield it from electromagnetic interference.

This background also induced uncertainties represented by the error bars on the figure. Nonetheless, we were able to fit the signal with a linear curve with a coefficient  $R^2$  of 97%. We believe that a reduction of the signal background will lead to an improvement of the signal linearity over concentration.

We can also observe on Figure 5.21(right), that the noise appears to be increasing with the gas concentration. This results from the increase of measurement integration time to measure the smallest concentrations.

### 5.3.3.6 Comparison with open loop detection

Finally, we compared our new closed-loop method to classic open-loop detection in terms of sensitivity and stability. For proper comparison we used the same HF2LI lock-in amplifier and set it to be used in classic open-loop detection. We measured the signal from the C2 QTF by employing the exact same experimental setup (gas, wavelength, etc.). The lock-in time constant in open-loop detection was set to 10 ms (corresponding to a bandwidth of 16 Hz) while the measurement rate of closed-loop detection was set to 10 Hz.

For comparison we computed the force equivalent Allan deviations by multiplying the deviation by the measured scale factors, these are shown in Figure 5.22. Both deviations show the averaging of the QTF noise and of the oscillator noise until system drifts occur near 200 s. This means that our new method is at least as stable as the classic one. The drifts occurring after 200 s could be due to QTF frequency drift caused by temperature changes or by stability of the experimental setup (laser wavelength stability, environment, etc.). As such we hope for our new method that further reduction of the differential frequency measurement time will allow for longer integration time, hence improving the sensor limit of detection.

Concerning the amplitude, a factor around 2.2 is observed between the two curves, which can mainly be attributed to the fact that the closed-loop measurement is differential (the same force induces two times more

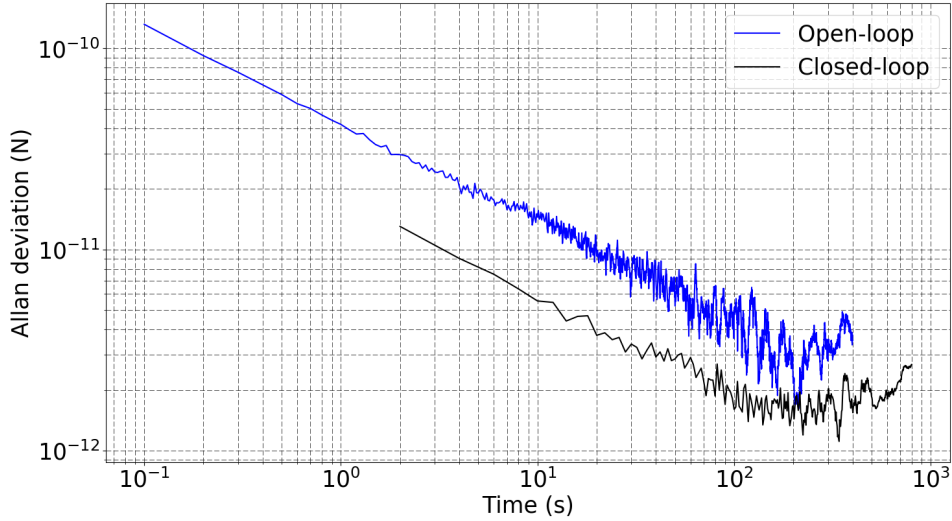


Figure 5.22: Comparison of the force equivalent Allan deviation of our new method (black curve) and of classic open-loop lock-in detection (blue curve).

signal).

It is finally possible to compare both method sensitivities. The Allan deviation of closed-loop detection presents a noise floor of 10  $\mu$ Hz for an integration time of 100 s (i.e. a bandwidth of 1/100 Hz), while the differential signal was 3.4 mHz, leading to a minimum detection limit of 3 ppmv of  $C_2H_2$  and a NNEA of:

$$NNEA = \frac{6 \cdot 10^{-3} \times 1.9 \cdot 10^{-4}}{\frac{3.4 \cdot 10^{-3}}{1 \cdot 10^{-5}} \times \sqrt{1/100}} \approx 3.35 \cdot 10^{-8} \text{ W.cm}^{-1} \cdot \text{Hz}^{-1/2}. \quad (5.28)$$

This NNEA was not degraded compared to the one obtained in classic open-loop lock-in detection (see Chapter 3). Eventually, this new method presents other advantages as summed up in the following.

## 5.4 Conclusion and perspectives

To conclude, we presented a new measurement method for photoacoustics employing quartz tuning forks (or any mechanical resonator used at resonance). This method takes advantage of the oscillation of the resonator by means of an electrical oscillator, in phase quadrature with the force to detect. Contrarily to open-loop detection the measurement is made on the QTF frequency rather than on its amplitude.

We also analytically modelled this new method signal and noise through the analysis of the system phase shifts and Leeson's phase noise model. The method was further implemented by using a commercial HF2LI lock-in amplifier and homemade electronics. We confirmed that our system limiting noise was the described Leeson's phase noise. Finally, we studied the influence of different parameters on the system in order to validate our analytical model. In every case we demonstrated a good agreement between measurements and theory which will facilitate the design of such systems in the future.

The new method has a similar sensitivity and is as stable as classic detection while presenting unique advantages. We demonstrated that our method could perform faster measurements than classic detection down to 60 ms. Indeed, the QTF displacement at resonance is immediate while the response time of classic QEPAS detection is a multiple of the QTF  $Q$  over  $f_0$  (typically a few seconds). This fast response time should allow for precisely measuring fast varying gas concentrations.

Also by monitoring the QTF frequency and quality factor it should be possible to correct the measurement of

gases presenting higher viscosity or adsorbing on the QTF (water vapor for example). Yet another possible correction consists in monitoring in real time the gas relaxation rate through determination of the system optimal phase shifts.

We also were capable of setting differential measurements in an amplitude modulation scheme. The differential should enable cancellation of frequency drifts over time due to temperature modifications for example. In addition, an improvement on the sensitivity to acoustical, vibratory or optical environment should be expected, further enhancing the stability of QEPAS and allowing the use of photoacoustic systems in industrial environments. Using such a method should benefit to the use of amplitude modulation scheme which is sometimes mandatory depending on the nature of the laser source (single pulsed mode of operation for example) and for molecules presenting wide absorption lines. Otherwise, the principle could also be adapted to wavelength modulation method by adding a simple frequency divider to the laser modulation.

Yet another advantage is the replacement of lock-in detection by frequency counting, which should facilitate the implementation in embedded systems and reduce memory size requirements.

In the future, efforts should be focused on the integration of our method on a FPGA platform, with which several advantages are foreseen: reduction of the electromagnetic background, automated adjustment of the dynamic range, reduction of the measurement time down to a few milliseconds and thus stability improvement of the technique compared to the classic one. Proof of stability should be given, for example through comparing the influence of temperature changes on the signal deviation.





# Conclusion

## Summary of our work

In this manuscript, we investigated the use of new quartz tuning forks configurations for photoacoustic spectroscopy, and compared them to other detection techniques. We aimed in particular at a better understanding of the phenomena at play to determine if sensitivity improvements are still possible.

To this end, we first performed a review of the different photoacoustic technologies and developments presented in the literature. Combined with previous works at ONERA, we showed that sensitivity performances were scattered over a wide range, leading to a difficult interpretation of this spread.

To tackle this issue, we then laid out theoretical tools to compare photoacoustic sensors, covering the different variants such as QEPAS, CEPAS or MPAS. It consists in an analytical model for photoacoustic sensors from the laser source to the useful signal-to-noise ratio, able to predict their NNEA. We showed how to refine the analytical results thanks to a finite element tool that could accurately simulate the complex vibroacoustic effects occurring within photoacoustic sensors.

Our generalised model allows to unravel the physical phenomena at stake for any photoacoustic sensor. This model introduces different factors that are the heat deposition, pressure generation and amplification, acoustic-mechanic overlap, vibroacoustic efficiency and normalised SNR.

In a third part, we analysed experimental results of different sensors we worked with or representative from the literature. We obtained NNEA values in good agreement with the model, giving us a good confidence to exploit the theory intermediate estimates obtained with our unified model.

In the fourth part, we highlighted the differences between the techniques MPAS, CEPAS and QEPAS in terms of sensitivity, frequency, immunity to the environment and compactness. We estimated the unified model factors for the different studied sensors and proposed improvements to the different techniques with a focus on QEPAS. Two improvements for QEPAS were carried out experimentally. Firstly, we showed that the use of the in-plane configuration instead of the classical on-beam configuration allowed to increase the acoustic-mechanic overlap  $\eta_s$ , leading to a four time more sensitive sensor. Secondly, we introduced the first acoustic radial resonator coupled to a QTF in QEPAS. The latter QTF was particularly adapted to be coupled to acoustic resonators by design, and we showed experimentally the highest acoustic-mechanic overlap among our different systems and literature to the best of our knowledge. In addition, this resonator presents a good trade-off between pressure amplification and quality factor, which has resulted in a sensitivity close to the state-of-the-art. Most importantly, it presents unique advantages compared to small tubes, as a facilitated laser beam alignment, machining and positioning. Indeed, a similar sensitivity is reached while the laser has to be focused in a 2 mm large and deep space, compared to a 1 cm long tube of diameter 500  $\mu\text{m}$ .

In terms of sensitivity, we found that QEPAS state-of-the-art sensitivity is one order of magnitude worse than the other techniques, due to the poor acoustic overlap between the mechanical and acoustical resonators, and the decrease of the quality factor.

Eventually, we presented a new signal processing method for QEPAS. Instead of measuring the signal in open-loop scheme as traditionally achieved, our new method oscillates the QTF. We modelled it analytically and



obtained a good agreement with experiments in most cases and a sensitivity comparable to the one measured in open-loop. The measurement is faster, of the order of a few milliseconds compared to a few seconds traditionally and could be improved in the future. Also, as the frequency, quality factor and gas relaxation rate can be monitored, the raw signal can be further processed to be unaffected by the gas matrix fluctuations of pressure or temperature.

In the following we will open the discussion to the interest of using quartz tuning forks in photoacoustic spectroscopy and future improvements.

## Tuning forks in photoacoustic spectroscopy

As a common thread of this work, we also investigated the interest of using tuning forks in photoacoustic spectroscopy.

Contrarily to what can be stated in some works in the literature, we demonstrated that quartz tuning forks techniques do not demonstrate better sensitivities compared to MPAS and CEPAS. Even if the bare QTFs can indeed present a better mechanical detection, conveyed by a better  $\text{SNR}_{1\text{Pa}}$ , their overall sensitivity is degraded by their coupling to the acoustic source, conveyed by a low acoustic-mechanic overlap  $\eta_s$ . Bare QTFs sensitivities are similar to the ones of the best microphones and cantilevers without acoustic cell. In turn, they are indeed more sensitive than MEMs microphones in free space. The advantage of using bare QTFs is then their better sensitivity in free space compared to MEMs microphones, and their piezoelectric detection compared to cantilevers.

Furthermore, when coupled to acoustic resonators, the sensitivity of QTFs is also worse by one order of magnitude than the one provided by MPAS and CEPAS. This is caused again by a low acoustic-mechanic overlap and by the decrease of their quality factor when coupled to low quality factor acoustic resonators. While in the literature it is usually said that QTFs present a reduced size, we showed that MPAS and CEPAS sensors could present the same size and sensitivity. For example, Mirsense's cell we presented and recent developments on fibered CEPAS setups present similar sensitivities and sizes as a watch tuning fork with tubes.

To balance these observations, the main advantage of QEPAS may be a greater immunity to the environment sounds and vibrations. Thanks to their higher resonance frequency, quality factor and their quadrupolar nature, QTFs might be less sensitive to the environment which is a major limitation of traditional photoacoustic devices. Nonetheless, apart from these first considerations, this immunity to the environment has not been proven yet and will be primordial to demonstrate the interest of using QEPAS in photoacoustics.

## Perspectives

Based on our work, we highlighted possible improvements for the different photoacoustic techniques.

In order to develop the QEPAS technique, we have proposed several improvements.

Firstly, the use of the in-plane configuration to improve the acoustic-mechanic overlap and so the sensitivity. Secondly, the development of acoustic resonators better coupled to the QTF, presenting a compromise between quality factor and pressure amplification. We illustrated this new paradigm with the design of a radial resonator particularly well coupled to its QTF. The demonstration of this resonator paves the way towards new resonators for QEPAS that could improve the state-of-the-art sensitivity or enable other advantages such as easier alignment or machining.

Also, we highlighted the possible use of intracavity setups with C2 and its radial resonator, that could improve the state-of-the-art sensitivity of intracavity QEPAS.

Eventually, it would be interesting to consider the use of QTFs at higher frequencies, that could present an even

better compromise between size and sensitivity for gases presenting fast relaxation rates.

## **Personal perspectives**

On a personal point of view, I will be working in the field of QEPAS one supplementary year at ONERA. I recently applied to a POC'Up project financed by the SATT Paris-Saclay that selected my project. The aim will be to mature a QEPAS sensor and the signal processing we described in Chapter 5 so as to evaluate and industrialise this technology.



# Bibliography

- [1] S. M. Cristescu, S. T. Persijn, S. Te Lintel Hekkert, and F. J. M. Harren. Laser-based systems for trace gas detection in life sciences. *Applied Physics B: Lasers and Optics*, 92(3 SPECIAL ISSUE):343–349, 2008. [Cited in pages 1 and 2]
- [2] A. Berrou, M. Raybaut, A. Godard, and M. Lefebvre. High-resolution photoacoustic and direct absorption spectroscopy of main greenhouse gases by use of a pulsed entangled cavity doubly resonant OPO. *Applied Physics B: Lasers and Optics*, 98(1):217–230, 2010. [Cited in page 1]
- [3] G. V. L. Alves, W. C. Dos Santos, W. R. Waldman, J. G. Oliveira, H. Vargas, and M. G. Da Silva. A photoacoustic technique applied to detection of ethylene emissions in edible coated passion fruit. *Journal of Physics: Conference Series*, 214, 2010. [Cited in page 1]
- [4] C. M. Lee, K. V. Bychkov, A. I. Karapuzikov, I. V. Sherstov, and V. A. Vasiliev. High-sensitivity laser photoacoustic leak detector. *Optical Engineering*, 46(June 2007):1–8, 2007. [Cited in page 1]
- [5] C. K. N. Patel. Laser photoacoustic spectroscopy helps fight terrorism: High sensitivity detection of chemical Warfare Agent and explosives. *European Physical Journal: Special Topics*, 153(1):1–18, 2008. [Cited in pages 1 and 2]
- [6] S. Mengali, I. Elmi, L. Masini, F. Bonafé, F. Tamarri, M. Sanmartin, R. Viola, N. Liberatore, and S. Zampolli. GC-QEPAS: A MEMs-enabled portable trace chemical sensor for safety & security applications. In *2019 20th International Conference on Solid-State Sensors, Actuators and Microsystems & Eurosensors XXXIII (TRANSDUCERS & EUROSENSORS XXXIII)*, pages 1365–1368. IEEE, 2019. [Cited in page 2]
- [7] D. C. Dumitras, M. Petrus, and A. M. Bratu. Applications of near infrared photoacoustic spectroscopy for analysis of human respiration: A review. *Molecules*, 25, 2020. [Cited in page 2]
- [8] M. F. Kircher, A. De La Zerda, J. V. Jokerst, C. L. Zavaleta, P. J. Kempen, E. Mittra, K. Pitter, R. Huang, C. Campos, F. Habte, R. Sinclair, C. W. Brennan, I. K. Mellinshoff, E. C. Holland, and S. S. Gambhir. A brain tumor molecular imaging strategy using a new triple-modality MRI-photoacoustic-Raman nanoparticle. *Nature Medicine*, 18(5):829–834, 2012. [Cited in page 2]
- [9] L. Dong, F. K. Tittel, C. Li, N. P. Sanchez, H. Wu, C. Zheng, Y. Yu, A. Sampaolo, and R. J. Griffin. Compact TDLAS based sensor design using interband cascade lasers for mid-IR trace gas sensing. *Optics express*, 24(6):A528–A535, 2016. [Cited in page 2]
- [10] G. Durry, J. S. Li, I. Vinogradov, A. Titov, L. Joly, J. Cousin, T. Decarpenterie, N. Amarouche, X. Liu, B. Parvitte, et al. Near infrared diode laser spectroscopy of C<sub>2</sub>H<sub>2</sub>, H<sub>2</sub>O, CO<sub>2</sub> and their isotopologues and the application to TDLAS, a tunable diode laser spectrometer for the martian PHOBOS-GRUNT space mission. *Applied Physics B*, 99(1):339–351, 2010. [Cited in page 2]
- [11] T.-V. Dinh, I.-Y. Choi, Y.-S. Son, and J.-C. Kim. A review on non-dispersive infrared gas sensors: Improvement of sensor detection limit and interference correction. *Sensors and Actuators B: Chemical*, 231:529–538, 2016. [Cited in page 2]

- [12] M. Nowakowski, J. Wojtas, Z. Bielecki, and J. Mikolajczyk. Cavity enhanced absorption spectroscopy sensor. *Acta Physica Polonica-Series A General Physics*, 116(3):363, 2009. [Cited in page 3]
- [13] D. A. Long, A. J. Fleisher, S. Wojtewicz, and J. T. Hodges. Quantum-noise-limited cavity ring-down spectroscopy. *Applied Physics B*, 115(2):149–153, 2014. [Cited in pages 3 and 145]
- [14] W. Gurlit, R. Zimmermann, C. Giesemann, T. Fernholz, V. Ebert, J. Wolfrum, U. Platt, and J. P. Burrows. Lightweight diode laser spectrometer CHLD (compact high-altitude in-situ laser diode) for balloonborne measurements of water vapor and methane. *Applied optics*, 44(1):91–102, 2005. [Cited in page 3]
- [15] P. R Griffiths and J. A. De Haseth. *Fourier transform infrared spectrometry*, volume 171. John Wiley & Sons, 2007. [Cited in page 3]
- [16] H. J. Yoon, J. H. Yang, Z. Zhou, S. S. Yang, M. M.-C. Cheng, et al. Carbon dioxide gas sensor using a graphene sheet. *Sensors and Actuators B: Chemical*, 157(1):310–313, 2011. [Cited in page 3]
- [17] R. Mavrodineanu, C. T. J. Alkemade, R. Bleekrode, J. C. Burger, C. C. Butler, P. G. Cath, V. A. Fassel, P. T. Gilbert, W. Gillies, R. Herrmann, et al. *Analytical flame spectroscopy*. Macmillan International Higher Education, 1970. [Cited in page 3]
- [18] G. A. Eiceman, Z. Karpas, and H. H. Hill Jr. *Ion mobility spectrometry*. CRC press, 2013. [Cited in page 3]
- [19] H. M. McNair, J. M. Miller, and N. H. Snow. *Basic gas chromatography*. John Wiley & Sons, 2019. [Cited in page 3]
- [20] S. Zampolli, S. Mengali, N. Liberatore, I. Elmi, L. Masini, M. Sanmartin, and R. Viola. A mems-enabled deployable trace chemical sensor based on fast gas-chromatography and quartz enhanced photoacoustic spectroscopy. *Sensors*, 20(1):120, 2020. [Cited in page 3]
- [21] A. Miklós, P. Hess, and Z. Bozóki. Application of acoustic resonators in photoacoustic trace gas analysis and metrology. *Review of scientific instruments*, 72(4):1937–1955, 2001. [Cited in pages 3, 19, 20, 21, 46, 47, 49, 77, and 141]
- [22] J. Hodgkinson and R. P. Tatam. Optical gas sensing: a review. *Measurement Science and Technology*, 24(1):012004, 2012. [Cited in pages 3 and 144]
- [23] A. G. Bell. *Upon the production of sound by radiant energy*. Gibbson brothers, 1881. [Cited in pages 5 and 40]
- [24] E. L. Kerr and J. G. Atwood. The laser illuminated absorptivity spectrophone: A method for measurement of weak absorptivity in gases at laser wavelengths. *Applied Optics*, 7(5):915, 1968. [Cited in page 5]
- [25] T. L. Cottrell and J. C. McCoubrey. *Molecular energy transfer in gases*. Butterworths, 1961. [Cited in pages 5 and 42]
- [26] G. Aoust. *Développements de sources infrarouges et de résonateurs en quartz pour la spectroscopie photoacoustique*. PhD thesis, Ecole Polytechnique, Université Paris-Saclay, 2016. [Cited in pages 5, 7, 29, 36, 39, 42, 43, 44, 52, 53, 55, 58, 61, 87, 89, 93, 94, 95, 99, 108, and 140]
- [27] T. Laurila, H. Cattaneo, V. Koskinen, J. Kauppinen, and R. Hernberg. Diode laser-based photoacoustic spectroscopy with interferometrically-enhanced cantilever detection: erratum. *Optics express*, 14(9):4195, 2006. [Cited in page 6]
- [28] A. A. Kosterev, Y. A. Bakhirkin, R. F. Curl, and F. K. Tittel. Quartz-enhanced photoacoustic spectroscopy. *Optics letters*, 27(21):1902–1904, 2002. [Cited in pages 6, 25, 29, 32, 54, 60, 87, 95, 125, and 127]

- [29] L. Bizet, R. Vallon, B. Parvitte, M. Brun, G. Maisons, M. Carras, and V. Zeninari. Multi-gas sensing with quantum cascade laser array in the mid-infrared region. *Applied Physics B*, 123(5):145, 2017. [Cited in page 7]
- [30] M. Carras, G. Aoust, G. Maisons, M. Brun, O. Spitz, and F. Grillot. Quantum cascade laser technology and applications at mirSense, from spectroscopy to chaotic communication. In *8th Annual World Congress of Advanced Materials*, Osaka, Japan, July 2019. [Cited in page 7]
- [31] R. Levy, G. Papin, O. Le Traon, D. Janiaud, and J. Guerard. Nonlinear regime operation for a high resolution vibrating beam UGS seismometer. *Analog Integrated Circuits and Signal Processing*, 82(3):621–626, 2015. [Cited in page 7]
- [32] A. Parent, O. Le Traon, S. Masson, and B. Le Foulgoc. A coriolis vibrating gyro made of a strong piezoelectric material. In *SENSORS, 2007 IEEE*, pages 876–879. IEEE, 2007. [Cited in page 7]
- [33] T. Perrier, R. Levy, B. Bourgeteau-Verlhac, P. Kayser, J. Moulin, and S. Paquay. Optimization of an MEMS magnetic thin film vibrating magnetometer. *IEEE Transactions on Magnetics*, 53(4):1–5, 2016. [Cited in page 7]
- [34] B. Hardy, A. Berrou, S. Guilbaud, M. Raybaut, A. Godard, and M. Lefebvre. Compact, single-frequency, doubly resonant optical parametric oscillator pumped in an achromatic phase-adapted double-pass geometry. *Optics letters*, 36(5):678–680, 2011. [Cited in page 7]
- [35] E. Cadiou, D. Mammez, J.-B. Dherbecourt, G. Gorju, J. Pelon, J.-M. Melkonian, A. Godard, and M. Raybaut. Atmospheric boundary layer CO<sub>2</sub> remote sensing with a direct detection LIDAR instrument based on a widely tunable optical parametric source. *Optics letters*, 42(20):4044–4047, 2017. [Cited in page 7]
- [36] M. L. Viengerov. New method of gas analysis based on tyndall-roentgen optoacoustic effect. *Doklady Akademii Nauk SSSR*, 19(687):8, 1938. [Cited in page 17]
- [37] F. Cerini and S. Adorno. Flexible simulation platform for multilayer piezoelectric MEMS microphones with signal-to-noise ratio (SNR) evaluation. In *Multidisciplinary Digital Publishing Institute Proceedings*, volume 2, page 862, 2018. [Cited in pages 18, 19, and 57]
- [38] S. C. Thompson, J. L. LoPresti, E. M. Ring, H. G. Nepomuceno, J. J. Beard, W. J. Ballard, and E. V. Carlson. Noise in miniature microphones. *The Journal of the Acoustical Society of America*, 111(2):861–866, 2002. [Cited in pages 18, 19, and 72]
- [39] <https://www.infineon.com/>. Accessed: 2020-05-28. [Cited in page 18]
- [40] A. Dehé, M. Wurzer, M. Földner, and U. Krumbein. The infineon silicon MEMS microphone. In *AMA conferences*, volume 2013, pages 14–16. Citeseer, 2013. [Cited in page 18]
- [41] <https://www.bksv.com/>. Accessed: 2020-05-28. [Cited in pages 18 and 200]
- [42] D. Homentcovschi and R. N. Miles. An analytical-numerical method for determining the mechanical response of a condenser microphone. *The Journal of the Acoustical Society of America*, 130(6):3698–3705, 2011. [Cited in page 19]
- [43] K. F. Luft. Über eine neue methode der registrierenden gasanalyse mit hilfe der absorption ultraroter strahlen ohne spektrale zerlegung. *Z. tech. Phys*, 24:97–104, 1943. [Cited in page 19]
- [44] C. F. Dewey Jr, R. D. Kamm, and C. E. Hackett. Acoustic amplifier for detection of atmospheric pollutants. *Applied Physics Letters*, 23(11):633–635, 1973. [Cited in page 19]

- [45] L.-G. Rosengren. Optimal optoacoustic detector design. *Applied optics*, 14(8):1960–1976, 1975. [Cited in pages 19 and 21]
- [46] V. Zeninari, B. Parvitte, D. Courtois, V. A. Kapitanov, and Y. N. Ponomarev. Methane detection on the sub-ppm level with a near-infrared diode laser photoacoustic sensor. *Infrared physics & technology*, 44(4):253–261, 2003. [Cited in pages 19, 21, 22, 47, 72, 79, 80, 81, 82, 85, 111, 114, 137, and 141]
- [47] M. R. Moldover, J. P. M. Trusler, T. J. Edwards, J. B. Mehl, and R. S. Davis. Measurement of the universal gas constant R using a spherical acoustic resonator. *Physical review letters*, 60(4):249, 1988. [Cited in page 19]
- [48] S. Schäfer, A. Miklós, and P. Hess. Quantitative signal analysis in pulsed resonant photoacoustics. *Applied optics*, 36(15):3202–3211, 1997. [Cited in page 19]
- [49] J.-P. Besson, S. Schilt, and L. Thévenaz. Multi-gas sensing based on photoacoustic spectroscopy using tunable laser diodes. *Spectrochimica Acta Part A: Molecular and Biomolecular Spectroscopy*, 60(14):3449–3456, 2004. [Cited in pages 20, 22, 47, 48, 74, 75, and 76]
- [50] C. Brand, A. Winkler, P. Hess, A. Miklós, Z. Bozóki, and J. Sneider. Pulsed-laser excitation of acoustic modes in open high-Q photoacoustic resonators for trace gas monitoring: results for C<sub>2</sub>H<sub>4</sub>. *Applied optics*, 34(18):3257–3266, 1995. [Cited in page 20]
- [51] A. Miklós and A. Lörincz. Windowless resonant acoustic chamber for laser-photoacoustic applications. *Applied Physics B*, 48(3):213–218, 1989. [Cited in page 20]
- [52] D. K. Havey, P. A. Bueno, K. A. Gillis, J. T. Hodges, G. W. Mulholland, R. D. van Zee, and M. R. Zachariah. Photoacoustic spectrometer with a calculable cell constant for measurements of gases and aerosols. *Analytical chemistry*, 82(19):7935–7942, 2010. [Cited in pages 20 and 22]
- [53] M. E. Webber, M. Pushkarsky, and C. K. N. Patel. Fiber-amplifier-enhanced photoacoustic spectroscopy with near-infrared tunable diode lasers. *Applied optics*, 42(12):2119–2126, 2003. [Cited in pages 20 and 22]
- [54] F. G. C. Bijnen, J. Reuss, and F. J. M. Harren. Geometrical optimization of a longitudinal resonant photoacoustic cell for sensitive and fast trace gas detection. *Review of Scientific Instruments*, 67(8):2914–2923, 1996. [Cited in pages 20, 21, 22, 56, 72, 74, 75, 76, 77, 111, 114, 137, 138, and 139]
- [55] M. Zhang, B. Zhang, K. Chen, M. Guo, S. Liu, Y. Chen, Z. Gong, Q. Yu, Z. Chen, and M. Liao. Miniaturized multi-pass cell based photoacoustic gas sensor for parts-per-billion level acetylene detection. *Sensors and Actuators A: Physical*, page 112013, 2020. [Cited in page 20]
- [56] B. Zhang, K. Chen, Y. Chen, B. Yang, M. Guo, H. Deng, F. Ma, F. Zhu, Z. Gong, W. Peng, et al. High-sensitivity photoacoustic gas detector by employing multi-pass cell and fiber-optic microphone. *Optics Express*, 28(5):6618–6630, 2020. [Cited in pages 20 and 22]
- [57] Y. Ma, S. Qiao, Y. He, Y. Li, Z. Zhang, X. Yu, and F. K. Tittel. Highly sensitive acetylene detection based on multi-pass retro-reflection-cavity-enhanced photoacoustic spectroscopy and a fiber amplified diode laser. *Optics Express*, 27(10):14163–14172, 2019. [Cited in page 21]
- [58] Y. Ma and H. Dang. Corner cube prism-enhanced photoacoustic spectroscopy based gas sensing. *Infrared Physics & Technology*, page 103386, 2020. [Cited in page 21]
- [59] X. Yin, L. Dong, H. Wu, H. Zheng, W. Ma, L. Zhang, W. Yin, S. Jia, and F. K. Tittel. Sub-ppb nitrogen dioxide detection with a large linear dynamic range by use of a differential photoacoustic cell and a 3.5 W blue multimode diode laser. *Sensors and Actuators B: Chemical*, 247:329–335, 2017. [Cited in pages 21 and 22]

- [60] J. Rouxel. *Conception et réalisation de cellules photoacoustiques miniaturisées pour la détection de traces de gaz*. PhD thesis, Reims, 2015. [Cited in pages 21, 22, and 63]
- [61] V. Zeninari, A. Grossel, L. Joly, T. Decarpenterie, B. Grouiez, B. Bonno, and B. Parvitte. Photoacoustic spectroscopy for trace gas detection with cryogenic and room-temperature continuous-wave quantum cascade lasers. *Central European Journal of Physics*, 8(2):194–201, 2010. [Cited in pages 22 and 49]
- [62] E. L. Holthoff, D. A. Heaps, and P. M. Pellegrino. Development of a MEMS-scale photoacoustic chemical sensor using a quantum cascade laser. *IEEE Sensors Journal*, 10(3):572–577, 2010. [Cited in page 22]
- [63] J. P. Lima, H. Vargas, A. Miklos, M. Angelmahr, and P. Hess. Photoacoustic detection of NO<sub>2</sub> and N<sub>2</sub>O using quantum cascade lasers. *Applied Physics B*, 85(2-3):279–284, 2006. [Cited in page 22]
- [64] K. Wilcken and J. Kauppinen. Optimization of a microphone for photoacoustic spectroscopy. *Applied spectroscopy*, 57(9):1087–1092, 2003. [Cited in pages 23 and 72]
- [65] J. Kauppinen, K. Wilcken, I. Kauppinen, and V. Koskinen. High sensitivity in gas analysis with photoacoustic detection. *Microchemical journal*, 76(1-2):151–159, 2004. [Cited in page 23]
- [66] M. Saarinen. *Cantilever enhanced gas sensing using photoacoustic spectroscopy*. PhD thesis, Aalto University, 2010. [Cited in pages 23, 55, 72, and 73]
- [67] K. Chamassi, W. Trzopil, R. Arinero, R. Rousseau, A. Vicet, and M. Bahriz. Capacitive silicon micro-electromechanical resonator for enhanced photoacoustic spectroscopy. *Applied Physics Letters*, 115(8):081106, 2019. [Cited in pages 23 and 25]
- [68] T. Lauwers, A. Glière, and S. Basrour. Resonant optical transduction for photoacoustic detection. In *Photonic Instrumentation Engineering VII*, volume 11287, page 112870P. International Society for Optics and Photonics, 2020. [Cited in page 23]
- [69] H. Lhermet, T. Verdot, A. Teulle, A. Berthelot, A. Glière, B. Desloges, F. Souchon, M. Fournier, J.-M. Fédéli, and J.-G. Coutard. Micro-photoacoustic cell with integrated microphone for sub-ppm gas sensing. In *2019 20th International Conference on Solid-State Sensors, Actuators and Microsystems & Eurosensors XXXIII (TRANSDUCERS & EUROSENSORS XXXIII)*, pages 68–71. IEEE, 2019. [Cited in pages 23, 24, and 25]
- [70] N. Ledermann, P. Mural, J. Baborowski, M. Forster, and J.-P. Pellaux. Piezoelectric Pb (Zr<sub>x</sub>, Ti<sub>1-x</sub>) O<sub>3</sub> thin film cantilever and bridge acoustic sensors for miniaturized photoacoustic gas detectors. *Journal of Micromechanics and Microengineering*, 14(12):1650, 2004. [Cited in pages 23 and 24]
- [71] V. Koskinen, J. Fonsen, K. Roth, and J. Kauppinen. Progress in cantilever enhanced photoacoustic spectroscopy. *Vibrational spectroscopy*, 48(1):16–21, 2008. [Cited in pages 24 and 25]
- [72] K. Chen, M. Guo, S. Liu, B. Zhang, H. Deng, Y. Zheng, Y. Chen, C. Luo, L. Tao, M. Lou, et al. Fiberoptic photoacoustic sensor for remote monitoring of gas micro-leakage. *Optics express*, 27(4):4648–4659, 2019. [Cited in pages 24 and 25]
- [73] P. Karioja, K. Keränen, K. Kautio, J. Ollila, M. Heikkinen, I. Kauppinen, T. Kuusela, B. Matveev, M. E. McNie, R. M. Jenkins, et al. LTCC-based differential photo acoustic cell for ppm gas sensing. In *Optical Sensing and Detection*, volume 7726, page 77260H. International Society for Optics and Photonics, 2010. [Cited in page 24]
- [74] V. Koskinen, J. Fonsen, K. Roth, and J. Kauppinen. Cantilever enhanced photoacoustic detection of carbon dioxide using a tunable diode laser source. *Applied Physics B*, 86(3):451–454, 2007. [Cited in pages 24, 25, 35, 56, 72, 73, 74, 77, 78, 111, 114, 137, 138, 140, and 141]



- [75] J. Uotila et al. *Use of the optical cantilever microphone in photoacoustic spectroscopy*. PhD thesis, University of Turku, 2009. [Cited in page 25]
- [76] K. Chen, H. Deng, M. Guo, C. Luo, S. Liu, B. Zhang, F. Ma, F. Zhu, Z. Gong, W. Peng, et al. Tube-cantilever double resonance enhanced fiber-optic photoacoustic spectrometer. *Optics & Laser Technology*, 123:105894, 2020. [Cited in pages 25, 73, 74, 77, 78, and 111]
- [77] K. Chen, Z. Yu, Z. Gong, and Q. Yu. Lock-in white-light-interferometry-based all-optical photoacoustic spectrometer. *Optics letters*, 43(20):5038–5041, 2018. [Cited in page 25]
- [78] S. Zhou and D. Iannuzzi. A fiber-tip photoacoustic sensor for in situ trace gas detection. *Review of Scientific Instruments*, 90(2):023102, 2019. [Cited in page 25]
- [79] N. Petra, J. Zweck, A. A. Kosterev, S. E. Minkoff, and D. Thomazy. Theoretical analysis of a quartz-enhanced photoacoustic spectroscopy sensor. *Applied Physics B*, 94(4):673–680, 2009. [Cited in pages 25, 26, 44, 45, 54, and 118]
- [80] L. Dong, A. A. Kosterev, D. Thomazy, and F. K. Tittel. QEPAS spectrophones: design, optimization, and performance. *Applied Physics B*, 100(3):627–635, 2010. [Cited in pages 26, 29, 30, 32, 55, 87, 95, 97, 98, 100, 105, and 109]
- [81] P. Patimisco, A. Sampaolo, L. Dong, M. Giglio, G. Scamarcio, F. K. Tittel, and V. Spagnolo. Analysis of the electro-elastic properties of custom quartz tuning forks for optoacoustic gas sensing. *Sensors and Actuators B: Chemical*, 227:539–546, 2016. [Cited in pages 26, 27, 87, and 88]
- [82] P. Patimisco, A. Sampaolo, M. Giglio, S. Dello Russo, V. Mackowiak, H. Rossmadl, A. Cable, F. K. Tittel, and V. Spagnolo. Tuning forks with optimized geometries for quartz-enhanced photoacoustic spectroscopy. *Optics Express*, 27(2):1401–1415, 2019. [Cited in pages 26, 27, 28, and 29]
- [83] A. Sampaolo, P. Patimisco, L. Dong, A. Geras, G. Scamarcio, T. Starecki, F. K. Tittel, and V. Spagnolo. Quartz-enhanced photoacoustic spectroscopy exploiting tuning fork overtone modes. *Applied Physics Letters*, 107(23):231102, 2015. [Cited in pages 27 and 28]
- [84] H. Wu, X. Yin, L. Dong, K. Pei, A. Sampaolo, P. Patimisco, H. Zheng, W. Ma, L. Zhang, W. Yin, et al. Simultaneous dual-gas QEPAS detection based on a fundamental and overtone combined vibration of quartz tuning fork. *Applied Physics Letters*, 110(12):121104, 2017. [Cited in pages 27 and 28]
- [85] H. Zheng, Y. Liu, H. Lin, B. Liu, X. Gu, D. Li, B. Huang, Y. Wu, L. Dong, W. Zhu, et al. Quartz-enhanced photoacoustic spectroscopy employing pilot line manufactured custom tuning forks. *Photoacoustics*, 17:100158, 2020. [Cited in pages 27 and 29]
- [86] A. Sampaolo, P. Patimisco, M. Giglio, M. S. Vitiello, H. E. Beere, D. A. Ritchie, G. Scamarcio, F. K. Tittel, and V. Spagnolo. Improved tuning fork for terahertz quartz-enhanced photoacoustic spectroscopy. *Sensors*, 16(4):439, 2016. [Cited in pages 27, 87, and 95]
- [87] P. Patimisco, A. Sampaolo, L. Dong, F. K. Tittel, and V. Spagnolo. Recent advances in quartz enhanced photoacoustic sensing. *Applied Physics Reviews*, 5(1):011106, 2018. [Cited in pages 27 and 95]
- [88] H. Zheng, L. Dong, A. Sampaolo, P. Patimisco, W. Ma, L. Zhang, W. Yin, L. Xiao, V. Spagnolo, S. Jia, et al. Overtone resonance enhanced single-tube on-beam quartz enhanced photoacoustic spectrophone. *Applied Physics Letters*, 109(11):111103, 2016. [Cited in pages 27, 28, 29, 87, and 94]
- [89] S. Zhou, L. Xu, L. Zhang, T. He, N. Liu, Y. Liu, B. Yu, and J. Li. External cavity quantum cascade laser-based QEPAS for chlorodifluoromethane spectroscopy and sensing. *Applied Physics B*, 125(7):125, 2019. [Cited in pages 27 and 29]

- [90] U. Willer, M. Köhring, M. Mordmüller, and W. Schade. Photoacoustic sensing with micro-tuning forks. In *Next-Generation Spectroscopic Technologies VIII*, volume 9482, page 94820B. International Society for Optics and Photonics, 2015. [Cited in pages 28 and 33]
- [91] P. Patimisco, A. Sampaolo, M. Giglio, V. Mackowiak, H. Rossmadl, B. Gross, A. Cable, F. K. Tittel, and V. Spagnolo. Octupole electrode pattern for tuning forks vibrating at the first overtone mode in quartz-enhanced photoacoustic spectroscopy. *Optics Letters*, 43(8):1854–1857, 2018. [Cited in page 28]
- [92] M. Giglio, A. Elefante, P. Patimisco, A. Sampaolo, F. Sgobba, H. Rossmadl, V. Mackowiak, H. Wu, F. K. Tittel, L. Dong, et al. Quartz-enhanced photoacoustic sensor for ethylene detection implementing optimized custom tuning fork-based spectrophone. *Optics express*, 27(4):4271–4280, 2019. [Cited in pages 28, 29, 30, and 32]
- [93] S. Li, L. Dong, H. Wu, A. Sampaolo, P. Patimisco, V. Spagnolo, and F. K. Tittel. Ppb-level quartz-enhanced photoacoustic detection of carbon monoxide exploiting a surface grooved tuning fork. *Analytical chemistry*, 91(9):5834–5840, 2019. [Cited in page 28]
- [94] A. K. Y. Ngai, S. T. Persijn, I. D. Lindsay, A. A. Kosterev, P. Groß, C. J. Lee, S. M. Cristescu, F. K. Tittel, K.-J. Boller, and F. J. M. Harren. Continuous wave optical parametric oscillator for quartz-enhanced photoacoustic trace gas sensing. *Applied Physics B*, 89(1):123, 2007. [Cited in page 29]
- [95] H. Zheng, L. Dong, A. Sampaolo, H. Wu, P. Patimisco, X. Yin, W. Ma, L. Zhang, W. Yin, V. Spagnolo, et al. Single-tube on-beam quartz-enhanced photoacoustic spectroscopy. *Optics letters*, 41(5):978–981, 2016. [Cited in pages 29, 30, 95, and 100]
- [96] H. Lin, Z. Huang, R. Kan, H. Zheng, Y. Liu, B. Liu, L. Dong, W. Zhu, J. Tang, J. Yu, et al. Application of micro quartz tuning fork in trace gas sensing by use of quartz-enhanced photoacoustic spectroscopy. *Sensors*, 19(23):5240, 2019. [Cited in page 29]
- [97] H. Wu, A. Sampaolo, L. Dong, P. Patimisco, X. Liu, H. Zheng, X. Yin, W. Ma, L. Zhang, W. Yin, et al. Quartz enhanced photoacoustic H<sub>2</sub>S gas sensor based on a fiber-amplifier source and a custom tuning fork with large prong spacing. *Applied Physics Letters*, 107(11):111104, 2015. [Cited in pages 29, 30, 32, and 100]
- [98] G. Aoust, R. Levy, M. Raybaut, A. Godard, J.-M. Melkonian, and M. Lefebvre. Theoretical analysis of a resonant quartz-enhanced photoacoustic spectroscopy sensor. *Applied Physics B*, 123(2):63, 2017. [Cited in pages 29, 36, 37, 55, and 97]
- [99] D. V. Serebryakov, I.V. Morozov, A. A. Kosterev, and V. S. Letokhov. Laser microphotoacoustic sensor of ammonia traces in the atmosphere. *Quantum Electronics*, 40(2):167, 2010. [Cited in pages 29, 95, 97, and 100]
- [100] L. Dong, V. Spagnolo, R. Lewicki, and F. K. Tittel. Ppb-level detection of nitric oxide using an external cavity quantum cascade laser based QEPAS sensor. *Optics Express*, 19(24):24037–24045, 2011. [Cited in page 29]
- [101] H. Yi, W. Chen, S. Sun, K. Liu, T. Tan, and X. Gao. T-shape microresonator-based high sensitivity quartz-enhanced photoacoustic spectroscopy sensor. *Optics express*, 20(8):9187–9196, 2012. [Cited in pages 29, 31, 32, and 95]
- [102] M. Giglio, A. Sampaolo, P. Patimisco, H. Zheng, H. Wu, L. Dong, F. K. Tittel, and V. Spagnolo. Single-tube on beam quartz-enhanced photoacoustic spectrophones exploiting a custom quartz tuning fork operating in the overtone mode. In *Quantum Sensing and Nano Electronics and Photonics XIV*, volume 10111, page 1011107. International Society for Optics and Photonics, 2017. [Cited in page 30]

- [103] R. Rousseau, Z. Loghmari, M. Bahriz, K. Chamassi, R. Teissier, A. N. Baranov, and A. Vicet. Off-beam QEPAS sensor using an 11- $\mu\text{m}$  DFB-QCL with an optimized acoustic resonator. *Optics express*, 27(5):7435–7446, 2019. [Cited in pages 31, 32, and 95]
- [104] M. Helman, H. Moser, A. Dudkowiak, and B. Lendl. Off-beam quartz-enhanced photoacoustic spectroscopy-based sensor for hydrogen sulfide trace gas detection using a mode-hop-free external cavity quantum cascade laser. *Applied Physics B*, 123(5):141, 2017. [Cited in page 31]
- [105] H. Yi, W. Chen, A. Vicet, Z. Cao, X. Gao, T. Nguyen-Ba, M. Jahjah, Y. Rouillard, L. Nähle, and M. Fischer. T-shape microresonator-based quartz-enhanced photoacoustic spectroscopy for ambient methane monitoring using 3.38- $\mu\text{m}$  antimonide-distributed feedback laser diode. *Applied Physics B*, 116(2):423–428, 2014. [Cited in pages 31 and 32]
- [106] L. Dong, H. Wu, H. Zheng, Y. Liu, X. Liu, W. Jiang, L. Zhang, W. Ma, W. Ren, W. Yin, et al. Double acoustic microresonator quartz-enhanced photoacoustic spectroscopy. *Optics letters*, 39(8):2479–2482, 2014. [Cited in pages 31 and 100]
- [107] H. Zheng, L. Dong, P. Patimisco, H. Wu, A. Sampaolo, X. Yin, S. Li, W. Ma, L. Zhang, W. Yin, et al. Double antinode excited quartz-enhanced photoacoustic spectrophone. *Applied Physics Letters*, 110(2):021110, 2017. [Cited in page 31]
- [108] S. Borri, P. Patimisco, I. Galli, D. Mazzotti, G. Giusfredi, N. Akikusa, M. Yamanishi, G. Scamarcio, P. De Natale, and V. Spagnolo. Intracavity quartz-enhanced photoacoustic sensor. *Applied Physics Letters*, 104(9):091114, 2014. [Cited in pages 31 and 32]
- [109] J. Wojtas, A. Gluszek, A. Hudzikowski, and F. K. Tittel. Mid-infrared trace gas sensor technology based on intracavity quartz-enhanced photoacoustic spectroscopy. *Sensors*, 17(3):513, 2017. [Cited in pages 31, 32, and 141]
- [110] H. Wu, L. Dong, X. Liu, H. Zheng, X. Yin, W. Ma, L. Zhang, W. Yin, and S. Jia. Fiber-amplifier-enhanced QEPAS sensor for simultaneous trace gas detection of  $\text{NH}_3$  and  $\text{H}_2\text{S}$ . *Sensors*, 15(10):26743–26755, 2015. [Cited in page 32]
- [111] V. Spagnolo, L. Dong, A. A. Kosterev, D. Thomazy, J. H. Doty, and F. K. Tittel. Modulation cancellation method (MOCAM) in modulation spectroscopy. In *Optical Sensors 2011; and Photonic Crystal Fibers V*, volume 8073, page 807313. International Society for Optics and Photonics, 2011. [Cited in page 32]
- [112] H. Zheng, L. Dong, Y. Ma, H. Wu, X. Liu, X. Yin, L. Zhang, W. Ma, W. Yin, L. Xiao, et al. Scattered light modulation cancellation method for sub-ppb-level  $\text{NO}_2$  detection in a LD-excited QEPAS system. *Optics express*, 24(10):A752–A761, 2016. [Cited in pages 32, 33, and 40]
- [113] H. Wu, L. Dong, H. Zheng, X. Liu, X. Yin, W. Ma, L. Zhang, W. Yin, S. Jia, and F. K. Tittel. Enhanced near-infrared QEPAS sensor for sub-ppm level  $\text{H}_2\text{S}$  detection by means of a fiber amplified 1582 nm DFB laser. *Sensors and Actuators B: Chemical*, 221:666–672, 2015. [Cited in page 33]
- [114] R. Rousseau, N. Maurin, W. Trzpił, M. Bahriz, and A. Vicet. Quartz tuning fork resonance tracking and application in Quartz enhanced photoacoustics spectroscopy. *Sensors*, 19(24):5565, 2019. [Cited in pages 33, 35, and 148]
- [115] M. Mordmüller, M. Köhring, W. Schade, and U. Willer. An electrically and optically cooperated QEPAS device for highly integrated gas sensors. *Applied Physics B*, 119(1):111–118, 2015. [Cited in pages 33 and 34]

- [116] M. Mordmueller, W. Schade, and U. Willer. QEPAS with electrical co-excitation for photoacoustic measurements in fluctuating background gases. *Applied Physics B*, 123(8):224, 2017. [Cited in pages 33, 34, and 147]
- [117] M. Mordmueller, S. Edelmann, M. Knestel, W. Schade, and U. Willer. Phase optimized photoacoustic sensing of gas mixtures. *Applied Sciences*, 10(2):438, 2020. [Cited in pages 34 and 148]
- [118] H. Wu, L. Dong, H. Zheng, Y. Yu, W. Ma, L. Zhang, W. Yin, L. Xiao, S. Jia, and F. K. Tittel. Beat frequency quartz-enhanced photoacoustic spectroscopy for fast and calibration-free continuous trace-gas monitoring. *Nature communications*, 8(1):1–8, 2017. [Cited in pages 34 and 35]
- [119] <http://www.pranalytica.com/products-services/nitrolux.php>. Accessed: 2020-05-28. [Cited in pages 35 and 36]
- [120] <http://mirsense.com/>. Accessed: 2020-05-28. [Cited in pages 35 and 36]
- [121] <https://www.gasera.fi/product/gaseraone/>. Accessed: 2020-05-28. [Cited in pages 35 and 36]
- [122] [https://www.thorlabs.com/newgrouppage9.cfm?objectgroup\\_id=11241&pn=ADM01](https://www.thorlabs.com/newgrouppage9.cfm?objectgroup_id=11241&pn=ADM01). Accessed: 2020-05-28. [Cited in page 36]
- [123] T. Wei, H. Wu, L. Dong, and F. K. Tittel. Acoustic detection module design of a quartz-enhanced photoacoustic sensor. *Sensors*, 19(5):1093, 2019. [Cited in page 36]
- [124] G. Aoust, R. Levy, B. Verlhac, and O. Le Traon. Optimal quality factor for tuning forks in a fluid medium. *Sensors and Actuators A: Physical*, 243:134–138, 2016. [Cited in pages 36, 37, and 87]
- [125] G. Aoust, R. Levy, B. Verlhac, and O. Le Traon. Ultra high quality factor resonators operated in fluids. *Sensors and Actuators A: Physical*, 269:569–573, 2018. [Cited in pages 36, 37, 38, 87, 101, 102, and 104]
- [126] G. Aoust, R. Levy, M. Raybaut, J.-M. Melkonian, B. Bourgeteau, J.-B. Dherbecourt, A. Godard, and M. Lefebvre. Experimental and numerical analysis of commercial and homemade tuning forks for QEPAS. In *2015 Conference on Lasers and Electro-Optics (CLEO)*, pages 1–2. IEEE, 2015. [Cited in page 37]
- [127] E. L. Kerr and J. G. Atwood. The laser illuminated absorptivity spectrophone: a method for measurement of weak absorptivity in gases at laser wavelengths. *Applied optics*, 7(5):915–921, 1968. [Cited in page 40]
- [128] M. Giglio, A. Zifarelli, A. Sampaolo, G. Menduni, A. Elefante, R. Blanchard, C. Pfluegl, M. F. Witinski, D. Vakhshoori, H. Wu, et al. Broadband detection of methane and nitrous oxide using a distributed-feedback quantum cascade laser array and quartz-enhanced photoacoustic sensing. *Photoacoustics*, 17:100159, 2020. [Cited in page 40]
- [129] A. Miklós, C.-H. Lim, W.-W. Hsiang, G.-C. Liang, A. H. Kung, A. Schmohl, and P. Hess. Photoacoustic measurement of methane concentrations with a compact pulsed optical parametric oscillator. *Applied Optics*, 41(15):2985–2993, 2002. [Cited in page 40]
- [130] L. S. Rothman, I. E. Gordon, Y. Babikov, A. Barbe, D. C. Benner, P. F. Bernath, M. Birk, L. Bizzocchi, V. Boudon, L. R. Brown, et al. The HITRAN2012 molecular spectroscopic database. *Journal of Quantitative Spectroscopy and Radiative Transfer*, 130:4–50, 2013. [Cited in pages 41, 83, and 91]
- [131] G. Wysocki, A. A. Kosterev, and F. K. Tittel. Influence of molecular relaxation dynamics on quartz-enhanced photoacoustic detection of CO<sub>2</sub> at  $\lambda = 2 \mu\text{m}$ . *Applied Physics B*, 85(2-3):301–306, 2006. [Cited in pages 42 and 43]
- [132] J. Saarela, J. Toivonen, A. Manninen, T. Sorvajärvi, and R. Hernberg. Wavelength modulation waveforms in laser photoacoustic spectroscopy. *Applied optics*, 48(4):743–747, 2009. [Cited in pages 42 and 44]

- [133] S. Schilt, L. Thevenaz, and P. Robert. Wavelength modulation spectroscopy: combined frequency and intensity laser modulation. *Applied optics*, 42(33):6728–6738, 2003. [Cited in page 42]
- [134] T. Iguchi. Modulation waveforms for second-harmonic detection with tunable diode lasers. *JOSA B*, 3(3):419–423, 1986. [Cited in page 44]
- [135] B. Parvitte, C. Risser, R. Vallon, and V. Zéninari. Quantitative simulation of photoacoustic signals using finite element modelling software. *Applied Physics B*, 111(3):383–389, 2013. [Cited in pages 46, 47, and 63]
- [136] B. Baumann, B. Kost, H. Groninga, and M. Wolff. Eigenmode analysis of photoacoustic sensors via finite element method. *Review of scientific instruments*, 77(4):044901, 2006. [Cited in page 47]
- [137] A. Karbach and P. Hess. High precision acoustic spectroscopy by laser excitation of resonator modes. *The Journal of chemical physics*, 83(3):1075–1084, 1985. [Cited in page 48]
- [138] G. Aoust, R. Levy, B. Bourgeteau, and O. Le Traon. Acoustic damping on flexural mechanical resonators. *Sensors and Actuators A: Physical*, 238:158–166, 2016. [Cited in pages 51, 52, and 53]
- [139] C. Zener. Internal friction in solids. I. theory of internal friction in reeds. *Physical review*, 52(3):230, 1937. [Cited in page 51]
- [140] R. Lifshitz and M. L. Roukes. Thermoelastic damping in micro-and nanomechanical systems. *Physical review B*, 61(8):5600, 2000. [Cited in page 51]
- [141] P. Patimisco, A. Sampaolo, V. Mackowiak, H. Rossmadl, A. Cable, F. K. Tittel, and V. Spagnolo. Loss mechanisms determining the quality factors in quartz tuning forks vibrating at the fundamental and first overtone modes. *IEEE transactions on ultrasonics, ferroelectrics, and frequency control*, 65(10):1951–1957, 2018. [Cited in pages 51 and 52]
- [142] K. Naeli and O. Brand. Dimensional considerations in achieving large quality factors for resonant silicon cantilevers in air. *Journal of applied Physics*, 105(1):014908, 2009. [Cited in page 52]
- [143] F. Lochon, I. Dufour, and D. Rebiere. Influence of losses on microcantilever-based chemical sensors design. In *Euroensors XIX*, page x, Barcelone, Spain, September 2005. NC. [Cited in page 52]
- [144] O. Le Traon, S. Masson, C. Chartier, and D. Janiaud. LGS and GaPO<sub>4</sub> piezoelectric crystals: New results. *Solid state sciences*, 12(3):318–324, 2010. [Cited in page 52]
- [145] X. Zhang and W. C. Tang. Viscous air damping in laterally driven microresonators. In *Proceedings IEEE Micro Electro Mechanical Systems An Investigation of Micro Structures, Sensors, Actuators, Machines and Robotic Systems*, pages 199–204. IEEE, 1994. [Cited in page 52]
- [146] M. Duquesnoy, G. Aoust, J.-M. Melkonian, R. Lévy, M. Raybaut, and A. Godard. Quartz enhanced photoacoustic spectroscopy based on a custom quartz tuning fork. *Sensors*, 19(6):1362, 2019. [Cited in pages 53, 55, 87, 105, and 142]
- [147] T. Rück. *Development, characterization and miniaturization of a trace gas detection system for NO<sub>2</sub> in air based on photoacoustic spectroscopy*. PhD thesis, Fakultät für Chemie und Pharmazie der Universität Regensburg, 2019. [Cited in pages 55 and 114]
- [148] R. D. Grober, J. Acimovic, J. Schuck, D. Hessman, P. J. Kindlemann, J. Hespanha, A. S. Morse, K. Karrai, I. Tiemann, and S. Manus. Fundamental limits to force detection using quartz tuning forks. *Review of Scientific Instruments*, 71(7):2776–2780, 2000. [Cited in pages 56 and 93]

- [149] <https://www.mouser.fr/datasheet/2/720/DS37-1.01%20AKU143%20Datasheet-552974.pdf>. Accessed: 2020-10-12. [Cited in page 57]
- [150] <https://www.infineon.com/cms/en/product/sensor/mems-microphones/im69d130/>. Accessed: 2020-10-12. [Cited in page 57]
- [151] <https://en.wikipedia.org/wiki/A-weighting>. Accessed: 2020-10-12. [Cited in page 57]
- [152] <https://www.bksv.com/media/doc/bp0389.pdf>. Accessed: 2020-10-09. [Cited in pages 58, 59, and 72]
- [153] <https://www.zhinst.com/europe/resources/principles-of-lock-in-detection>. Accessed: 2020-10-09. [Cited in page 60]
- [154] W. J. Riley. *Handbook of frequency stability analysis*. US Department of Commerce, National Institute of Standards and Technology., 2008. [Cited in pages 60 and 154]
- [155] M. Giglio, P. Patimisco, A. Sampaolo, G. Scamarcio, F. K. Tittel, and V. Spagnolo. Allan deviation plot as a tool for quartz-enhanced photoacoustic sensors noise analysis. *IEEE Transactions on Ultrasonics, Ferroelectrics, and Frequency Control*, 63(4):555–560, 2015. [Cited in page 60]
- [156] <https://www.open-engineering.com/>. Accessed: 2020-10-09. [Cited in page 61]
- [157] Y. Ma, Y. Hu, S. Qiao, Y. He, and F. K. Tittel. Trace gas sensing based on multi-quartz-enhanced photothermal spectroscopy. *Photoacoustics*, 20:100206, 2020. [Cited in page 61]
- [158] S. D. Russo, A. Zifarelli, P. Patimisco, A. Sampaolo, T. Wei, H. Wu, L. Dong, and V. Spagnolo. Light-induced thermo-elastic effect in quartz tuning forks exploited as a photodetector in gas absorption spectroscopy. *Optics Express*, 28(13):19074–19084, 2020. [Cited in page 61]
- [159] <https://www.comsol.fr/>. Accessed: 2020-10-12. [Cited in page 63]
- [160] <https://www.comsol.com/blogs/how-to-model-thermoviscous-acoustics-in-comsol-multiphysics/>. Accessed: 2020-10-12. [Cited in pages 64, 85, and 130]
- [161] [https://rion-sv.com/download/catalog/UC%e3%83%bbNH\\_SERIES#UC%e3%83%bbNH\\_SERIES](https://rion-sv.com/download/catalog/UC%e3%83%bbNH_SERIES#UC%e3%83%bbNH_SERIES). Accessed: 2020-09-10. [Cited in pages 72 and 204]
- [162] <https://www.distrelec.be/fr/element-de-microphone-sennheiser-ke4-211/p/13010100>. Accessed: 2020-12-07. [Cited in pages 72, 200, and 201]
- [163] <https://eu.mouser.com/ProductDetail/Knowles/SPU0409HD5H-PB?qs=ZBAH5PeHI6u8%2FbIfWDJEYw%3D%3D>. Accessed: 2020-12-07. [Cited in pages 72, 201, and 202]
- [164] <https://eu.mouser.com/ProductDetail/Akustica/AKU143?qs=X7720quulpWZdE4DSOQInA%3D%3D>. Accessed: 2020-12-07. [Cited in pages 72, 83, and 202]
- [165] <https://eu.mouser.com/ProductDetail/Knowles/EK-23024-000?qs=iTHNLyg2fuVZNPHS3WD9hA%3D%3D>. Accessed: 2020-12-07. [Cited in pages 72, 202, and 203]
- [166] K. K. Park, H. J. Lee, P. Crisman, M. Kupnik, O. Oralkan, and B. T. Khuri-Yakub. Optimum design of circular CMUT membranes for high quality factor in air. In *2008 IEEE Ultrasonics Symposium*, pages 504–507. IEEE, 2008. [Cited in page 72]
- [167] C. B. Hirschmann. *Cantilever-enhanced photoacoustic spectroscopy in the analysis of volatile organic compounds*. PhD thesis, Oulu Graduate School, 2012. [Cited in pages 72, 73, 74, 77, 78, 111, 114, and 137]

- [168] F. G. C. Bijnen, F. J. M. Harren, J. H. P. Hackstein, and J. Reuss. Intracavity CO laser photoacoustic trace gas detection: cyclic CH<sub>4</sub>, H<sub>2</sub>O and CO<sub>2</sub> emission by cockroaches and scarab beetles. *Applied Optics*, 35(27):5357–5368, 1996. [Cited in pages 74, 76, 77, 82, and 111]
- [169] J.-P. Besson, S. Schilt, and L. Thévenaz. Sub-ppm multi-gas photoacoustic sensor. *Spectrochimica Acta Part A: Molecular and Biomolecular Spectroscopy*, 63(5):899–904, 2006. [Cited in page 76]
- [170] P. R. Scheeper, B. Nordstrand, J. O. Gullv, B. Liu, T. Clausen, L. Midjord, and T. Storgaard-Larsen. A new measurement microphone based on MEMS technology. *Journal of Microelectromechanical systems*, 12(6):880–891, 2003. [Cited in page 77]
- [171] V. Zeninari, V. A. Kapitanov, D. Courtois, and Y. N. Ponomarev. Design and characteristics of a differential Helmholtz resonant photoacoustic cell for infrared gas detection. *Infrared physics & technology*, 40(1):1–23, 1999. [Cited in page 77]
- [172] B. D. Adamson, J. E. Sader, and E. J. Bieske. Photoacoustic detection of gases using microcantilevers. *Journal of Applied Physics*, 106(11):114510, 2009. [Cited in page 77]
- [173] C. Risser, B. Parvitte, R. Vallon, and V. Zeninari. Optimization and complete characterization of a photoacoustic gas detector. *Applied Physics B*, 118(2):319–326, 2015. [Cited in pages 79, 80, 81, and 111]
- [174] J. Rouxel, J.-G. Coutard, S. Gidon, O. Lartigue, S. Nicoletti, B. Parvitte, R. Vallon, V. Zéninari, and A. Glière. Miniaturized differential Helmholtz resonators for photoacoustic trace gas detection. *Sensors and Actuators B: Chemical*, 236:1104–1110, 2016. [Cited in page 79]
- [175] D. Hofstetter, M. Beck, J. Faist, M. Nägele, and M. W. Sigrist. Photoacoustic spectroscopy with quantum cascade distributed-feedback lasers. *Optics Letters*, 26(12):887–889, 2001. [Cited in page 80]
- [176] <https://www.euroquartz.co.uk/products/2x6mm-watch-crystal>. Accessed: 2020-10-23. [Cited in page 87]
- [177] J. Rodriguez, S. A. Chandorkar, G. M. Glaze, D. D. Gerrard, Y. Chen, D. B. Heinz, I. B. Flader, and T. W. Kenny. Direct detection of anchor damping in MEMS tuning fork resonators. *Journal of Microelectromechanical Systems*, 27(5):800–809, 2018. [Cited in page 88]
- [178] <https://www.bd.com/en-us/offering/capabilities/syringes-and-needles/conventional-syringes-and-needles/conventional-needles>. Accessed: 2020-11-28. [Cited in page 99]
- [179] A. A. Kosterev, L. Dong, D. Thomazy, F. K. Tittel, and S. Overby. QEPAS for chemical analysis of multi-component gas mixtures. *Applied Physics B*, 101(3):649–659, 2010. [Cited in page 100]
- [180] Y. Ma, S. Qiao, P. Patimisco, A. Sampaolo, Y. Wang, F. K. Tittel, and V. Spagnolo. In-plane quartz-enhanced photoacoustic spectroscopy. *Applied Physics Letters*, 116(6):061101, 2020. [Cited in pages 125 and 127]
- [181] M. L. Kuntzman, C. T. Garcia, A. G. Onaran, B. Avenson, K. D. Kirk, and N. A. Hall. Performance and modeling of a fully packaged micromachined optical microphone. *Journal of Microelectromechanical Systems*, 20(4):828–833, 2011. [Cited in page 139]
- [182] M. A. Shah, I. A. Shah, D.-G. Lee, and S. Hur. Design approaches of MEMS microphones for enhanced performance. *Journal of Sensors*, 2019, 2019. [Cited in page 143]

- [183] <https://abracon.com/Support/Tuning-Fork-Crystals-and-Oscillator.pdf>. Accessed: 2020-09-10. [Cited in page 148]
- [184] H. Wu, H. Zheng, Y. Yu, W. Ma, L. Zhang, W. Yin, L. Xiao, S. Jia, F. K. Tittel, and L. Dong. Beat frequency quartz-enhanced photoacoustic spectroscopy for fast and calibration-free continuous trace-gas monitoring. *Nature Communications*, 8(June):1–8, 2017. [Cited in page 148]
- [185] R. Levy, M. Duquesnoy, J.-M. Melkonian, M. Raybaut, and G. Aoust. New signal processing for fast and precise QEPAS measurements. *IEEE Transactions on Ultrasonics, Ferroelectrics, and Frequency Control*, 67(6):1230–1235, 2019. [Cited in pages 148 and 156]
- [186] D. B. Lesson. A simple model of feedback oscillator noise spectrum. *proc. IEEE*, 54(2):329–330, 1966. [Cited in page 153]
- [187] G. Papin. *Analyse des limites de résolution fréquentielle des capteurs vibrants de type MEMS*. PhD thesis, Université Paris-Est, 2014. [Cited in page 154]
- [188] R. Levy and V. Gaudineau. Phase noise analysis and performance of the vibrating beam accelerometer. In *2010 IEEE International Frequency Control Symposium*, pages 511–514. IEEE, 2010. [Cited in page 158]
- [189] B. J. James. A new measurement of the basic elastic and dielectric constants of quartz. In *Proceedings of the 42nd Annual Frequency Control Symposium, 1988.*, pages 146–154. IEEE, 1988. [Cited in page 196]
- [190] <https://eu.mouser.com/ProductDetail/Knowles/EK-23133-000?qs=iTHNlyg2fuWOGultbTzkIQ%3D%3D>. Accessed: 2020-12-07. [Cited in pages 203 and 204]





# List of publications

## Articles

M. Duquesnoy, G. Aoust, J.-M. Melkonian, R. Lévy, M. Raybaut, and A. Godard. Quartz enhanced photoacoustic spectroscopy based on a custom quartz tuning fork. *Sensors*,19(6):1362, 2019.

M. Duquesnoy, J.-M. Melkonian, R. Levy, M. Raybaut, J.-B. Dherbecourt, and A. Godard. Comprendre. détection de gaz par spectroscopie photoacoustique: principe et mise en œuvre. *Photoniques*, (94):38–44, 2018.

R. Levy, M. Duquesnoy, J.-M. Melkonian, M. Raybaut, and G. Aoust. New signal processing for fast and precise QEPAS measurements. *IEEE Transactions on Ultrasonics, Ferro-electrics, and Frequency Control*, 67(6):1230–1235, 2019.

M. Duquesnoy, G. Aoust, J.-M. Melkonian, R. Lévy, M. Raybaut, and A. Godard. QEPAS sensor using a radial resonator. Being written.

## Communications

M. Duquesnoy, G. Aoust, J.-M. Melkonian, R. Lévy, M. Raybaut, and A. Godard. Quartz enhanced photoacoustic spectroscopy based on a custom quartz tuning fork. In *EUROSENSORS 2018*, Austria (Oral).

R. Levy, M. Duquesnoy, J.-M. Melkonian, M. Raybaut, and G. Aoust. New signal processing for fast and precise QEPAS measurements. In: *IEEE Transactions on Ultrasonics, Ferro-electrics, and Frequency Control*, 2019, Japan (Oral).

M. Duquesnoy, G. Aoust, J.-M. Melkonian, R. Lévy, M. Raybaut, and A. Godard. Photoacoustic sensor with radial and longitudinal acoustic resonators. In *Laser Applications to Chemical, Security and Environmental Analysis* (pp. LTh4F-5), 2020, Canada (Oral).

M. Duquesnoy, R. Lévy, J.-M. Melkonian, G. Aoust, M. Raybaut, and A. Godard. Fast and stable photoacoustic gas spectroscopy by frequency tracking of a quartz tuning fork in closed loop detection. In *Laser Applications to Chemical, Security and Environmental Analysis* (pp. LTh4F-5), 2020, Canada (Poster).

M. Duquesnoy, R. Lévy, J.-M. Melkonian, G. Aoust, M. Raybaut, and A. Godard. QEPAS Sensor Based on the Tracking of the Photoacoustic Induced Frequency Shift of a Tuning Fork Maintained in Self-Sustained Oscillation by Electrical Excitation. In: *CLEO 2021* (Presentation to be accepted).

## Patents

R. Levy, M. Duquesnoy, J.-M. Melkonian, M. Raybaut et V. Gaudineau. « Détecteur photoacoustique ». Being deposited (2020).

Patents deposited during the previous PhD thesis, concerning the recovery cavity and the new detection scheme, upon which part of our work is based:

G. Aoust, R. Levy, B. Bourgeteau et O. Le Traon. « Dispositif de récupération de l'énergie acoustique ». Patent number FR3054666 (2016).

R. Levy, G. Aoust, B. Bourgeteau, J. Guérard, O. Le Traon et V. Gaudineau. « Méthode de mesure électronique ». Patent number FR3057078 (2016).

# List of Figures

1	Needs for gas detection . . . . .	1
2	Spectra of different target molecules in the MIR . . . . .	4
3	QCL and OPO principle . . . . .	5
4	Principle of photoacoustics . . . . .	6
5	Mirsense's products . . . . .	7
1.1	Microphone principle . . . . .	18
1.2	Examples of condenser microphones . . . . .	18
1.3	Acoustic resonators first modes . . . . .	19
1.4	Acoustic simple resonators . . . . .	20
1.5	Acoustic differential resonators . . . . .	21
1.6	Acoustic differential Helmholtz resonators . . . . .	22
1.7	Cantilevers . . . . .	23
1.8	Principle of CEPAS detection . . . . .	24
1.9	CEPAS cells . . . . .	24
1.10	Watch QTF and on-beam configuration . . . . .	26
1.11	Custom QTFs in the literature . . . . .	27
1.12	Overtone QTF mode . . . . .	28
1.13	QEPAS different configurations . . . . .	30
1.14	Resonant QEPAS examples . . . . .	30
1.15	Intracavity QEPAS . . . . .	31
1.16	MOCAM technique . . . . .	33
1.17	Alternate electrical excitation . . . . .	34
1.18	Beat frequency QEPAS . . . . .	35
1.19	ONERA's custom QTFs . . . . .	37
1.20	ONERA's custom acoustic resonator . . . . .	38
2.1	Analytical model description . . . . .	40
2.2	Laser intensity profile . . . . .	40
2.3	Gas absorption profile . . . . .	41
2.4	Heat source in wavelength modulation . . . . .	43
2.5	Heat source in wavelength modulation depending on modulation depth . . . . .	44
2.6	Pressure distribution over laser axis . . . . .	45
2.7	Acoustic resonator parameters . . . . .	46
2.8	Cylinder cell quality factor versus radius and length . . . . .	48
2.9	Cylinder cell constant versus radius and length . . . . .	50
2.10	Geometrical parameters of cantilevers and QTFs . . . . .	50
2.11	Pressure on watch QTF faces . . . . .	54
2.12	Theoretical coupling of acoustical and mechanical resonators . . . . .	55
2.13	Microphone typical sensitivity with frequency . . . . .	57
2.14	Microphone spectral noise density example . . . . .	57

2.15	Resonator electrical equivalent model . . . . .	58
2.16	Open-loop amplifier circuit . . . . .	59
2.17	Lock-in amplifier principle . . . . .	59
2.18	Modal analysis of the mechanical resonator . . . . .	62
2.19	Cylindrical acoustic source simulation . . . . .	63
2.20	Physical phenomena occurring in a photoacoustic sensor . . . . .	65
2.21	Heat density scheme . . . . .	65
2.22	Pressure generation scheme . . . . .	66
2.23	Pressure amplification scheme . . . . .	66
2.24	Pressure overlap scheme . . . . .	67
2.25	Vibroacoustic efficiency scheme . . . . .	68
2.26	SNR1Pa scheme . . . . .	68
3.1	Photoacoustic experimental setup for Mirsense's cell characterisation . . . . .	82
3.2	Absorption spectra for the Mirsense's cell characterisation bench . . . . .	83
3.3	Experimental Mirsense's cell resonance . . . . .	83
3.4	Experimental water vapor spectrum using Mirsense's cell . . . . .	84
3.5	Absorption spectra for the tuning fork characterisation bench . . . . .	91
3.6	Photoacoustic experimental setup for QTF characterisation . . . . .	92
3.7	ONERA's photoacoustic cell for QTF characterisation . . . . .	92
3.8	Noise measurements for bare QTFs . . . . .	93
3.9	Euroquartz with dual-tube resonators scheme . . . . .	96
3.10	FEM results for Euroquartz when varying the tubes length . . . . .	97
3.11	FEM modelling of Euroquartz with dual-tube resonators . . . . .	97
3.12	Photograph of experimental setup: Euroquartz with dual-tube resonators . . . . .	99
3.13	Experimental results for Euroquartz when varying the tubes length . . . . .	99
3.14	FEM simulation of C2 acoustic emission . . . . .	101
3.15	C2 with acoustic recovery cavity scheme . . . . .	102
3.16	FEM modelling of C2 with recovery cavity . . . . .	103
3.17	Photograph of experimental setup: C2 with acoustic recovery cavity . . . . .	104
3.18	C2 with acoustic recovery cavity and tubes scheme . . . . .	106
3.19	FEM modelling of C2 with recovery cavity and dual-tubes . . . . .	106
3.20	Experimental determination of the best coupling for C2 with dual tube resonators . . . . .	107
3.21	Photograph of experimental setup: C2 with acoustic recovery cavity and tubes . . . . .	108
4.1	Evolution of the static overlap . . . . .	117
4.2	Evolution of the static pressure amplification . . . . .	118
4.3	Illustration of the quadrupolar emission of a QTF . . . . .	119
4.4	Illustration of the pressure field amplitude for the studied QTFs . . . . .	120
4.5	Evolution of the vibroacoustic efficiency . . . . .	121
4.6	Evolution of the model factors for the coupling of Euroquartz with dual tubes . . . . .	122
4.7	Scheme of in-plane configuration . . . . .	125
4.8	Experimental study of in-plane configuration with U1 . . . . .	126
4.9	C2 with radial resonator scheme . . . . .	128
4.10	FEM results for C2 when varying the resonator radius . . . . .	129
4.11	FEM modelling of C2 with radial resonator . . . . .	129
4.12	Photograph of C2 with radial resonator . . . . .	132
4.13	Experimental measurement of the radial resonator quality factor . . . . .	133
4.14	Experimental noise PSD for C2 with radial resonator . . . . .	133
4.15	Experimental results for C2 when varying the resonator radius . . . . .	134

4.16	NNEA values reported in the literature . . . . .	136
4.17	Immunity to acoustic background with the recovery cavity . . . . .	142
4.18	Comparison of the SNR and size of mechanical detectors . . . . .	143
4.19	Comparison of the detectors NNEA and laser interaction length . . . . .	144
4.20	Sensitivity comparison of gas sensing methods . . . . .	145
5.1	Influence of temperature on frequency . . . . .	148
5.2	Schematic principle of our new signal processing . . . . .	149
5.3	Phase variation with frequency on the oscillator transfer function . . . . .	150
5.4	Block diagram of the method . . . . .	151
5.5	Oscillator loop scheme . . . . .	153
5.6	Leeson's phase noise model scheme . . . . .	154
5.7	Allan deviation model . . . . .	155
5.8	Electrical circuit scheme for CO compensation . . . . .	156
5.9	Experimental setup for phase noise PSD measurements . . . . .	157
5.10	Schematic of the setup for phase noise PSD measurements . . . . .	157
5.11	Phase noise PSD fit . . . . .	158
5.12	Influence of excitation voltage on phase noise PSD . . . . .	159
5.13	Influence of motional resistance on phase noise PSD . . . . .	160
5.14	Photoacoustic closed-loop experimental setup . . . . .	161
5.15	Determination of optimal phase shifts . . . . .	162
5.16	Differential measurement principle validation . . . . .	162
5.17	Allan deviation fit . . . . .	163
5.18	Influence of excitation voltage on signal and Allan deviation . . . . .	164
5.19	Influence of excitation voltage on the scale factor . . . . .	164
5.20	Influence of motional resistance on Allan deviation . . . . .	165
5.21	Linearity with gas concentration . . . . .	166
5.22	Allan deviation comparison between open and closed-loop . . . . .	167
B.1	Microphone BK4179 datasheet . . . . .	200
B.2	Microphone KE4-211-2 datasheet . . . . .	200
B.3	Microphone SPU0409HD5H datasheet . . . . .	201
B.4	Microphone AKU143 datasheet . . . . .	202
B.5	Microphone EK 23133 datasheet . . . . .	202
B.6	Microphone EK 23024 datasheet . . . . .	203
B.7	Microphone Rion UC 57 datasheet . . . . .	204
C.1	ONERA's white room . . . . .	205
C.2	Quartz resonator realisation process . . . . .	206

## List of Tables

1	Comparison of different gas detection methods . . . . .	3
1.1	MPAS sensitivities . . . . .	22

1.2	CEPAS sensitivities	25
1.3	Custom QTFs parameters	27
1.4	Bare QTF sensitivities	29
1.5	Intracavity QEPAS sensitivities	31
1.6	Resonant QEPAS sensitivities	32
1.7	Photoacoustic instruments in the industry	36
1.8	ONERA's custom QTFs parameters	37
3.1	Determination of different microphones SNR	72
3.2	Determination of different cantilevers SNR	73
3.3	Cantilevers analytical frequency and quality factor contributions	73
3.4	Acoustic resonators cases to study	74
3.5	Experimental results on the use of cylindrical acoustic resonators with microphones	76
3.6	Experimental results on the use of cylindrical acoustic resonators with cantilevers	78
3.7	Differential acoustic resonators cases to study	79
3.8	Analytical determination of differential resonators performances	80
3.9	Experimental results on the use of differential acoustic resonators	81
3.10	Experimental results on the use of Mirsense's cell	85
3.11	Bare QTF cases to study	87
3.12	Comparison of tuning forks fundamental frequencies through analytical, FEM and experimental results	88
3.13	Tuning forks analytical quality factor contributions	89
3.14	Analytical determination of tuning forks sensitivities	90
3.15	Experimental comparison between AM and WM modulation schemes	93
3.16	Experimental results in WM modulation for bare QTFs	94
3.17	Euroquartz with dual-tube resonators: resonators parameters	96
3.18	Euroquartz with dual-tube resonators: FEM results	98
3.19	Euroquartz with dual-tube resonators: experimental results	100
3.20	C2 with recovery cavity: quality factor comparison	102
3.21	C2 with recovery cavity: FEM results	104
3.22	C2 with recovery cavity: experimental results	105
3.23	C2 with recovery cavity and dual-tubes: FEM results	107
3.24	C2 with recovery cavity and dual-tubes: experimental results	109
3.25	Sensitivity comparison of the different detectors	110
3.26	Sensitivity comparison of the different sensors	111
4.1	Model factors for MPAS and CEPAS	114
4.2	Limiting cases definition for the acoustic-mechanic overlap	115
4.3	Analytical model factors for QTFs in free space	116
4.4	FEM results for static operation of QTFs	118
4.5	FEM model factors for QTFs in free space	120
4.6	Comparison of the analytical and FEM NNEA	121
4.7	FEM model factors for Euroquartz with dual-tubes	123
4.8	FEM model factors for C2 with acoustic resonators	124
4.9	Analytical determination of tuning forks sensitivities in in-plane configuration	125
4.10	Experimental results of in-plane configuration	127
4.11	C2 with radial resonator: FEM results	130
4.12	FEM model factors for C2 with radial resonator	131
4.13	C2 with radial resonator: experimental results	135
4.14	Comparison of the mechanical detectors ultimate SNR	137

4.15	Comparison of cell constant values between photoacoustic techniques . . . . .	137
4.16	Comparison of state-of-the-art MPAS, CEPAS and QEPAS sensors . . . . .	138
5.1	Phase noise PSD fit parameters . . . . .	158
5.2	Measurement parameters for different motional resistances . . . . .	159
5.3	Principle validation parameters . . . . .	161
5.4	Photoacoustic measurement parameters for different motional resistances . . . . .	165
A.1	Hook coefficients . . . . .	197
A.2	Parameters of Quartz material . . . . .	197
A.3	Parameters of Silicon material . . . . .	197
A.4	Parameters of Stainless steel material . . . . .	197
A.5	Parameters of air material . . . . .	198
B.1	Microphone BK4179 parameters . . . . .	200
B.2	Microphone KE4-211-2 parameters . . . . .	201
B.3	Microphone SPU0409HD5H parameters . . . . .	201
B.4	Microphone AKU143 parameters . . . . .	202
B.5	Microphone EK 23133 parameters . . . . .	203
B.6	Microphone EK 23024 parameters . . . . .	204
B.7	Microphone UC 57 parameters . . . . .	204





# Appendices

## Appendix A

# Material parameters

### Quartz piezoelectric coefficients

For analytical or finite element simulations of piezoelectric materials such as Quartz, one can describe the material through the piezoelectric constitutive equations. For a stress charge these equations are:

$$\begin{cases} T = c^E S - e^T E \\ D = e S + \varepsilon_0 \varepsilon_S E \end{cases} \quad (\text{A.1})$$

with T the stress components in N.m<sup>-2</sup>, S the strain components, E the electric field components in V.m<sup>-1</sup> and D the electric displacement components in C.m<sup>-2</sup>.  $\varepsilon_0$  is the vacuum electric permittivity in F.m<sup>-1</sup>.

These are linked by the stiffness tensor  $c^E$ , the piezoelectric tensor e and the relative permittivity  $\varepsilon_S$ .

For modelling Quartz, which belongs to the Trigonal 32 group, one can define the previous coefficients using the Voigt notation as follows:

$$\left\{ \begin{array}{l} c^E = \begin{pmatrix} C_{11} & C_{12} & C_{13} & C_{14} & 0 & 0 \\ C_{12} & C_{11} & C_{13} & -C_{14} & 0 & 0 \\ C_{13} & C_{13} & C_{33} & 0 & 0 & 0 \\ C_{14} & -C_{14} & 0 & C_{44} & 0 & 0 \\ 0 & 0 & 0 & 0 & C_{44} & C_{14} \\ 0 & 0 & 0 & 0 & C_{14} & (C_{11} - C_{12})/2 \end{pmatrix} \\ e = \begin{pmatrix} e_{11} & -e_{11} & 0 & e_{14} & 0 & 0 \\ 0 & 0 & 0 & 0 & -e_{14} & -e_{11} \\ 0 & 0 & 0 & 0 & 0 & 0 \end{pmatrix} \\ \varepsilon_S = \begin{pmatrix} \varepsilon_{11}^S & 0 & 0 \\ 0 & \varepsilon_{11}^S & 0 \\ 0 & 0 & \varepsilon_{33}^S \end{pmatrix} \end{array} \right. \quad (\text{A.2})$$

The values we used for these coefficients are given in Table A.1 [189].

$C_{11}$	86.79	$C_{12}$	6.7901	$C_{13}$	12.009
$C_{14}$	18.116	$C_{33}$	105.79	$C_{44}$	58.212
$e_{11}$	0.1711	$e_{14}$	0.0406		
$\varepsilon_{11}$	39.92	$\varepsilon_{33}$	41.04		

Table A.1: Matrix coefficients. Stiffness tensor coefficients are given in GPa, stress piezoelectric coupling coefficients in  $C.m^{-2}$  and dielectric permittivity coefficients in  $pC.V^{-1}.m^{-1}$ . These coefficients are given at  $25^{\circ}C$ .

Other general parameters of Quartz material are given in the following table.

Mass density $\rho_q$ ( $kg.m^{-3}$ )	2,648.4
Young modulus $E$ (GPa)	78.6
Thermal conductivity $\kappa$ ( $W.m^{-1}.K^{-1}$ )	11.8
$C_p$ ( $J.kg^{-1}.K^{-1}$ )	750
Linear thermal expansion $\alpha$ ( $K^{-1}$ )	$1.377 \cdot 10^{-5}$

Table A.2: Parameters of Quartz material at  $25^{\circ}C$ .

Parameters for other materials are given in the next paragraphs.

## Silicon

Mass density $\rho_q$ ( $kg.m^{-3}$ )	2,330
Young modulus $E$ (GPa)	160
Thermal conductivity $\kappa$ ( $W.m^{-1}.K^{-1}$ )	150
$C_p$ ( $J.kg^{-1}.K^{-1}$ )	710
Linear thermal expansion $\alpha$ ( $K^{-1}$ )	$2.5 \cdot 10^{-6}$

Table A.3: Parameters of Silicon material at  $25^{\circ}C$ .

## Stainless steel

Mass density $\rho_q$ ( $kg.m^{-3}$ )	7,850
Young modulus $E$ (GPa)	190
Thermal conductivity $\kappa$ ( $W.m^{-1}.K^{-1}$ )	30
$C_p$ ( $J.kg^{-1}.K^{-1}$ )	502
Linear thermal expansion $\alpha$ ( $K^{-1}$ )	$17 \cdot 10^{-6}$

Table A.4: Parameters of Stainless steel material at  $25^{\circ}C$ .

## Air

Mass density $\rho_f$ ( $\text{kg.m}^{-3}$ )	1.225
Sound speed $v$ ( $\text{m.s}^{-1}$ )	340
Laplace coefficient $\gamma$	1.4
$C_p$ ( $\text{J.kg}^{-1}.\text{K}^{-1}$ )	1,005.42
Thermal conductivity $\kappa$ ( $\text{W.m}^{-1}.\text{K}^{-1}$ )	$2.58 \cdot 10^{-2}$
Dynamic viscosity $\mu$ ( $\text{Pa.s}$ )	$1.81 \cdot 10^{-5}$

Table A.5: Parameters of air material at atmospheric conditions (25°C and 101,325 Pa).

## Appendix B

# Determination of microphone parameters from datasheets

### Method

In order to determine the microphones  $SNR_{1Pa}$  we found the equivalent input noise (EIN) from datasheets. This noise is usually given in dB(A) (A-weighted decibels), meaning that the noise is weighted over its entire frequency range to match the Human hearing perception. As we do not have the noise spectrum, we could not convert this value to dB. We thus assumed that these levels were equivalent, which should be a good approximation working near 1 kHz (which is the reference frequency generally used in datasheets).

The  $SNR_{1Pa}$  can then be derived by taking the standard pressure level of 1 Pa corresponding to 94 dB and removing the equivalent input noise,  $SNR_{1Pa} = 94 - EIN$ . This value corresponds to the entire microphone frequency range and is after derived in the bandwidth we consider (1/16 Hz):  $SNR_{1Pa}(\Delta_f = 1/16) = SNR_{1Pa}(\Delta_{f1}) \times \sqrt{\frac{\Delta_{f1}}{1/16}}$  with  $\Delta_{f1}$  the microphone working range.

### Microphone BK4179

For this microphone different parameters are given. Either the noise density in  $\mu Pa \cdot Hz^{-1/2}$  or the equivalent noise is dB(A). However, these values do not lead to the same microphone  $SNR_{1Pa}$ . Using the first, we obtain  $127 \text{ dB} \cdot Pa^{-1}$ , while using the second we find  $151 \text{ dB} \cdot Pa^{-1}$ .

We could not determine which value is correct and as we do not possess the microphone we could not measure it.

Cartridge data valid at 23°C, 975 mbar, 50% RH unless specifically stated otherwise.

**FREQUENCY RESPONSE:**  
 In accordance with IEC 651, Type 1:  
 14Hz to 4kHz  $\pm 1$  dB\*\*  
 10 Hz to 10 kHz  $\pm 2$  dB\*\*  
 7 Hz to 12.5 kHz  $\pm 2$ , -3dB\*\*  
 Cartridge Lower Limiting Frequency:  
 -3dB point at 5 to 7 Hz, determined by pressure equalization system (side vented)

**SENSITIVITY:**  
 System: nominally 1 V/Pa (0 dB re 1 V/Pa)  
 Cartridge: **nominally 100 mV/Pa at 250 Hz** (-20dB re 1 V/Pa)  
 Preamplifier Gain: 20dB  $\pm 0,1$ dB

**INHERENT NOISE:**  
 Cartridge **Thermal Noise: 0,14  $\mu$ Pa/ $\sqrt{\text{Hz}}$**   
 A-weighted\*: -5,5 dB(A) including  $R_n$ \*\*  
 Lin. **20 Hz to 20 kHz** -3,6 dB including  $R_n$ \*\*  
 Preamplifier Equivalent Input Noise:  
 Typically 1,1  $\mu$ V A-weighted with 50 pF connected to preamplifier input  
 Total System Noise: See Fig.2  
 A-weighted: -2,5 dB  
 Lin. 20 Hz to 20 kHz: 2,6 dB

Figure B.1: Microphone BK4179 datasheet.


Microphone	BK4179 [41]
Photograph	
Working range (Hz)	20-20k
Sensitivity $R_M$ (mV.Pa <sup>-1</sup> )	100
Noise level ( $\mu$ Pa.Hz <sup>-1/2</sup> )	0.14
Noise level (dB(A))	-2.5
SNR (dB(A))	96.5
SNR <sub>1Pa</sub> (dB.Pa <sup>-1</sup> ) in 1/16 Hz	151

Table B.1: Microphone BK4179 parameters.

## Microphone Sennheiser KE4-211-2

**Technical Data**

Transducer type ..... back-electret condenser capsule  
 (pressure receiver)

Pick-up pattern ..... omni-directional

**Frequency response ..... 20 to 20,000 Hz  $\pm 3$  dB**  
 40 to 15,000 Hz  $\pm 2.5$  dB

**Sensitivity (free field, no load, 1 kHz) ..... 10 mV/Pa  $\pm 2.5$  dB**  
 - 40 dB ref 1 V/Pa  $\pm 2.5$  dB

Phase relation of output signal  
 (free field, no load, 1 kHz):  
 Impedance transformer configuration  
 (source follower) ..... non-inverting  
 Amplifier configuration (source circuit) ..... inverting

Impedance at 1 kHz ..... approx. 1 k $\Omega$   
 Minimum terminating impedance ..... 4.7 k $\Omega$   
 Maximum SPL (THD<sub>total</sub> K2) ..... 130 dB (THD = 1 %),  
 (140 dB, THD = 3 %, V > 7.5 V; R = 18 k $\Omega$ )

**Equivalent noise level:**  
**db(A)<sub>1Pa</sub> ..... 27 dB**  
 CCIR 468-2, peak value ..... 38 dB

Figure B.2: Microphone KE4-211-2 datasheet [162].


Microphone	Sennheiser KE4-211-2 [162]
Photograph	
Working range (Hz)	20-20k
Sensitivity $R_M$ (mV.Pa <sup>-1</sup> )	10
Noise level (dB(A))	27
SNR (dB(A))	67
SNR <sub>1Pa</sub> (dB.Pa <sup>-1</sup> ) in 1/16 Hz	122

Table B.2: Microphone Sennheiser KE4-211-2 parameters.

## Microphone SPU0409HD5H

TEST CONDITIONS: 23 ±2°C, 55±20% R.H.,  $V_{DD}(\min) < V_{DD} < V_{DD}(\max)$ , no load, unless otherwise indicated

Parameter	Symbol	Conditions	Min	Typ	Max	Units
Supply Voltage <sup>1</sup>	$V_{DD}$		1.5	-	3.6	V
Supply Current <sup>1,2</sup>	$I_{DD}$		-	145	190	μA
Sensitivity <sup>1</sup>	S	94 dB SPL @ 1 kHz	-45	-42	-39	dBV/Pa
Signal to Noise Ratio	SNR	94 dB SPL @ 1 kHz, A-weighted	-	59	-	dB(A)
Total Harmonic Distortion	THD	94 dB SPL @ 1 kHz, S = Typ, $R_{load} > 2 \text{ k}\Omega$	-	-	1	%
Acoustic Overload Point	AOP	10% THD @ 1 kHz, S = Typ, $V_{DD} = 3.6\text{V}$ , $R_{load} > 2 \text{ k}\Omega$	115	-	-	dB SPL
DC Output		$V_{DD} = 1.5\text{V}$	-	0.84	-	V
Output Impedance	$Z_{OUT}$	@ 1 kHz	-	-	100	Ω
Directivity			Omnidirectional			
Polarity		Increasing sound pressure	Decreasing output voltage			

<sup>1</sup> 100% tested.

Figure B.3: Microphone SPU0409HD5H datasheet [162].


Microphone	SPU0409HD5H [163]
Photograph	
Working range (Hz)	100-10k
Sensitivity $R_M$ (mV.Pa <sup>-1</sup> )	7.94
Noise level (dB(A))	35
SNR (dB(A))	59
SNR <sub>1Pa</sub> (dB.Pa <sup>-1</sup> ) in 1/16 Hz	111

Table B.3: Microphone SPU0409HD5H parameters.



# Microphone AKU143

Parameter	Test Conditions	Min.	Typ.	Max.	Unit
Directivity		Omni-directional			
Signal to Noise Ratio (SNR)	$f_{in} = 1\text{kHz}$ , A-weighted, 20Hz-10kHz		65		dB
Low Frequency Corner <sup>1</sup>	-3dB from 1kHz sensitivity value		50	100	Hz
Upper Frequency Corner	+3dB from 1kHz sensitivity value		11.5		kHz
Sensitivity <sup>1</sup>	1kHz, 94dB SPL	-43	-42	-41	dBV/Pa

Figure B.4: Microphone AKU143 datasheet [164].

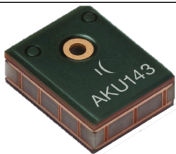
Microphone	AKU143 [163]
Photograph	
Working range (Hz)	20-10k
Sensitivity $R_M$ (mV.Pa <sup>-1</sup> )	7.94
Noise level (dB(A))	29
SNR (dB(A))	65
SNR <sub>1Pa</sub> (dB.Pa <sup>-1</sup> ) in 1/16 Hz	117

Table B.4: Microphone AKU143 parameters.

# Microphone EK 23133

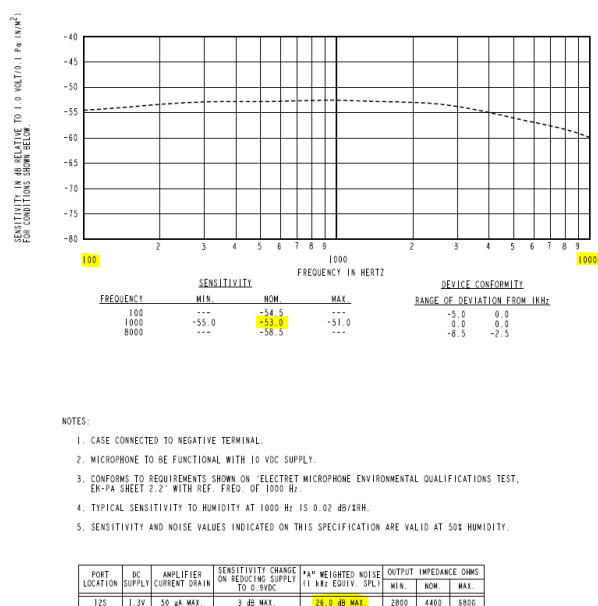


Figure B.5: Microphone EK 23133 datasheet [165].




Microphone	EK 23024 [190]
Photograph	
Working range (Hz)	100-10k
Sensitivity $R_M$ (mV.Pa <sup>-1</sup> )	2.2
Noise level (dB(A))	26
SNR (dB(A))	68
SNR <sub>1Pa</sub> (dB.Pa <sup>-1</sup> ) in 1/16 Hz	120

Table B.6: Microphone EK 23024 parameters.

## Microphone Rion UC 57

Model	UC-57 <sub>CE</sub>
Suitable preamplifier	NH-17/ 17A/22A
Nominal diameter	
Frequency response	Field
Frequency range (Hz)	10 to 16 000
Bias voltage (V)	0
Sensitivity level (dB re 1 V/Pa) *1	-22
Capacitance (pF)	14
Maximum input sound pressure level (dB) (Linearity error ±0.3 dB)	132 *4
A-weighted Inherent noise (dB)	13
Temperature coefficient (dB/°C)	±0.45 dB (at 250 Hz) *5
Diaphragm	
Dimensions (mm)	13.2 (dia) x 13.5

Figure B.7: Microphone Rion UC 57 datasheet [161].


Microphone	UC 57 [161]
Photograph	
Working range (Hz)	10-16k
Sensitivity $R_M$ (mV.Pa <sup>-1</sup> )	79.4
Noise level (dB(A))	13
SNR (dB(A))	81
SNR <sub>1Pa</sub> (dB.Pa <sup>-1</sup> ) in 1/16 Hz	135

Table B.7: Microphone UC 57 parameters.

## Appendix C

# Realisation of custom quartz resonators at ONERA

As presented in the introduction, the context of this thesis was favorable. Working at Mirsense and ONERA provided for an expertise in laser based spectroscopy and photoacoustics. Another expertise of ONERA is the realisation of quartz resonators that we will detail hereafter. For this purpose ONERA has its own white room as presented in Figure C.1.

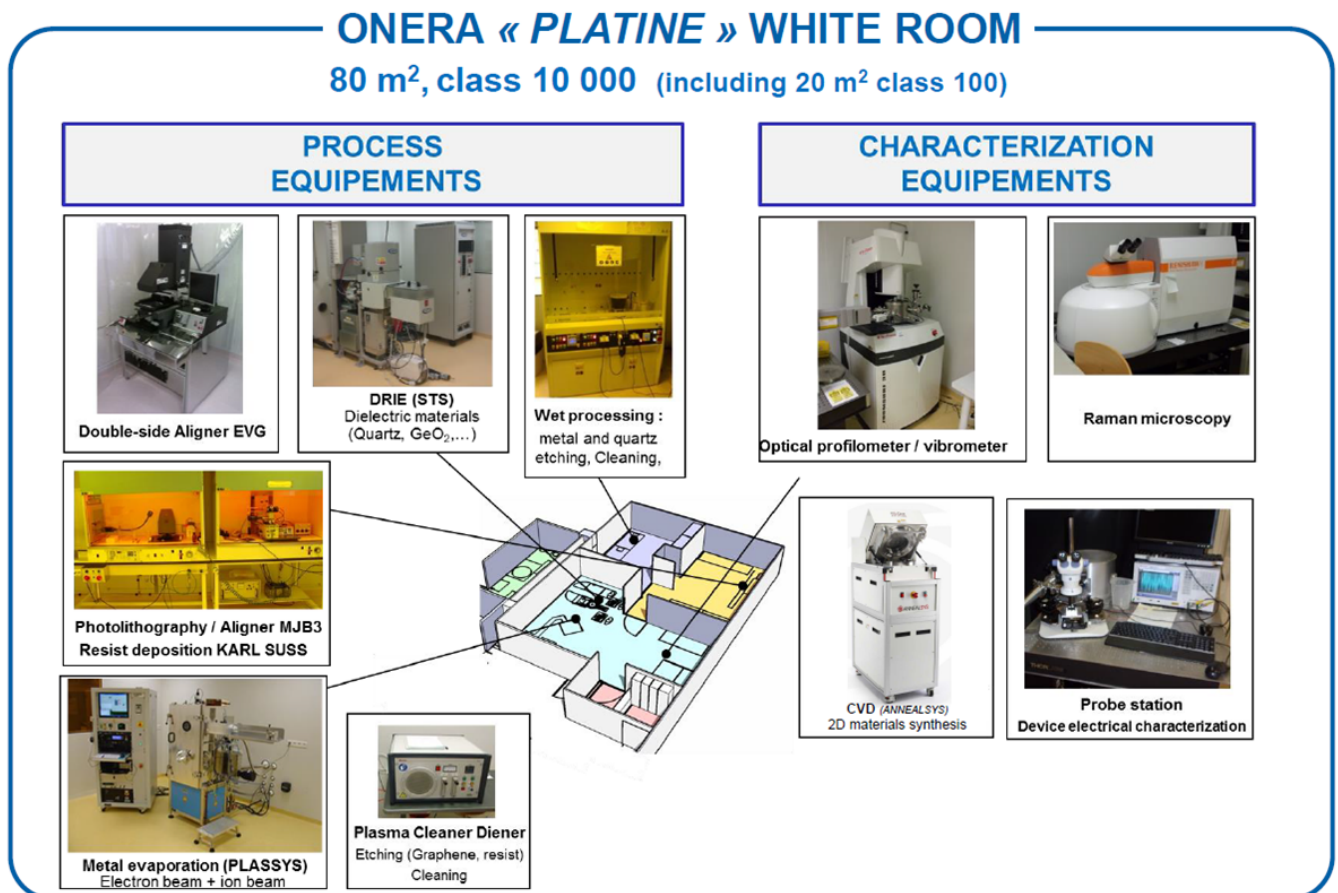


Figure C.1: ONERA's white room for quartz resonator processing.

## Design

The first step towards custom resonators is their design. Thanks to analytical and finite element models presented in this manuscript for photoacoustics, the resonator prong geometry is determined. For this resonator, the anchor losses are minimised through FEM and the electrodes are adapted to collect the charges in the most efficient way. Then, the masks for photo-lithography are created and the realisation process is determined.

## Process

For quartz resonators used in QEPAS, the process is usually simple. It consists in several steps of photo-lithography for quartz and electrode design by wet chemical etching as follows:

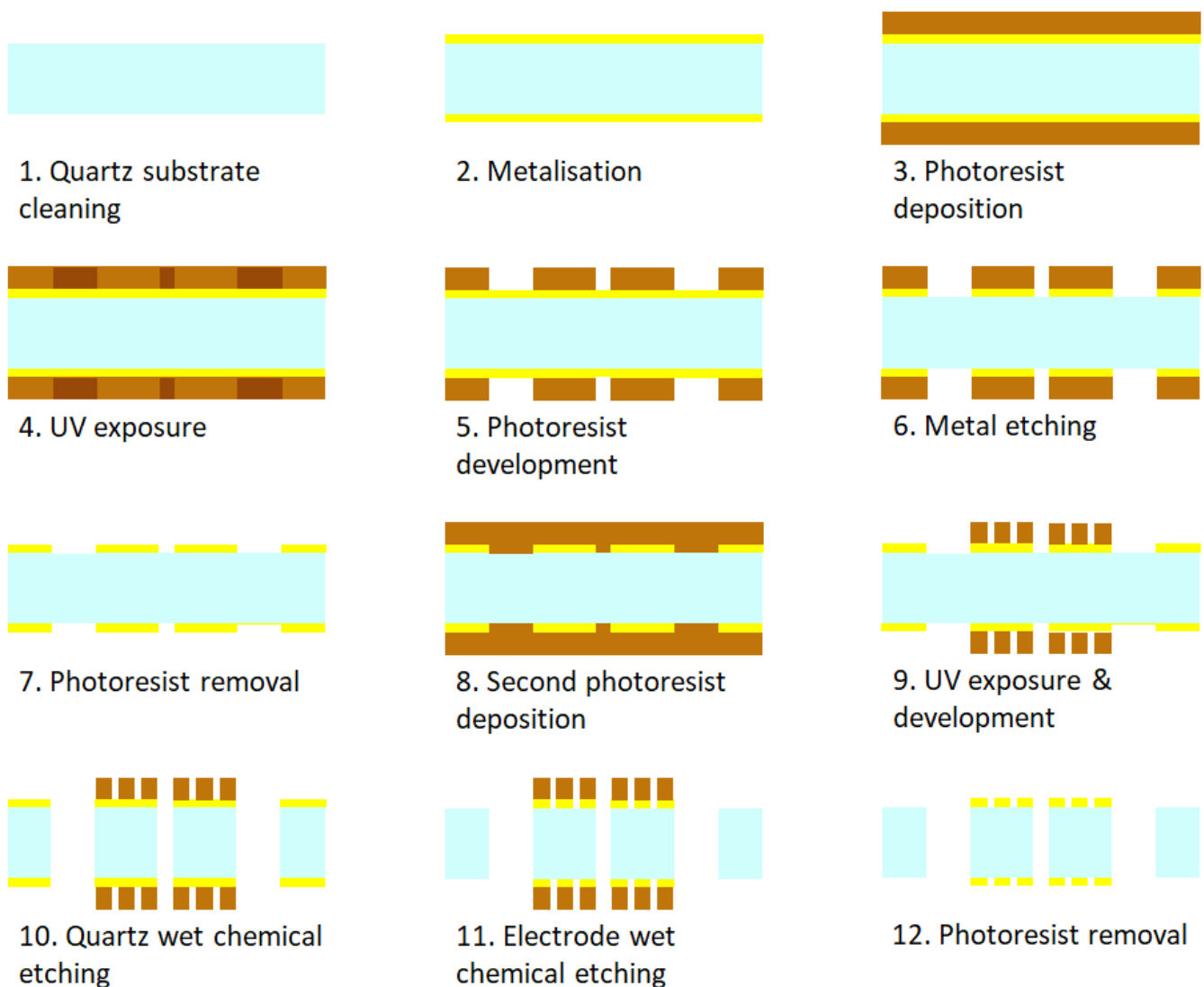


Figure C.2: Sectional view schematic of the process used to make typical quartz resonators. The quartz is represented in cyan, the gold electrodes in yellow and the photoresist in brown.

Eventually, the resonator resonance is characterised electrically, using an impedance analyser. The resonator is then glued on its support and the electrodes are connected to the electrical circuit, ready for measurements.



**Titre:** Mise en œuvre de diapasons en spectroscopie photoacoustique : Étude comparative et nouveaux développements

**Mots clés:** Photoacoustique, spectroscopie, QEPAS, laser, résonateur, quartz

**Résumé:** La spectroscopie photoacoustique est une technique de détection possédant une forte capacité multi-gaz. La détection est effectuée dans le domaine acoustique au moyen de microphones plutôt que dans le domaine optique à l'aide de photodétecteurs, rendant la détection indépendante de la longueur d'onde optique. En vue d'améliorer la détection acoustique, des résonateurs mécaniques ont récemment été employés et peuvent être couplés à des résonateurs acoustiques. Le but de cette thèse est d'étudier l'utilisation de ces résonateurs en vue de comprendre les phénomènes physiques mis en jeu. Plus particulièrement, l'objectif est d'estimer la limite de sensibilité de diapasons en quartz seuls ou couplés à des résonateurs acoustiques et de les comparer aux autres capteurs photoacoustiques existants. Dans ce manuscrit, un état de l'art exhaustif des différentes techniques photoacoustiques est mené. Un modèle analytique et éléments finis pouvant décrire les différents résonateurs acoustiques ou mécaniques est présenté. Ce modèle est validé expérimentalement et démontre un bon accord sur les nombreux systèmes évalués. Dans le but d'améliorer la QEPAS (Quartz-Enhanced PhotoAcoustic Spectroscopy), l'utilisation d'un nouveau résonateur radial couplé à un diapason est présentée et démontre une sensibilité similaire à l'état de l'art avec des contraintes de mises en œuvre fortement réduites. Ensuite, un schéma de détection innovant en boucle fermée est décrit et modélisé, permettant la mise en place d'une mesure différentielle en un temps nettement inférieur aux schémas conventionnels. Enfin, un chapitre est consacré à la description et la compréhension des différents phénomènes existant dans les capteurs photoacoustiques au travers de la définition d'un nouveau modèle. Un positionnement des techniques photoacoustiques en est extrait, permettant de déterminer l'intérêt respectif de chaque technique et les perspectives d'améliorations du QEPAS en particulier.

**Title:** Tuning forks in photoacoustic spectroscopy: Comparative study and new developments

**Keywords:** Photoacoustics, spectroscopy, QEPAS, laser, resonator, quartz

**Abstract:** Photoacoustic spectroscopy is a detection method enabling a strong multi-gas capacity. Instead of using photodetectors, the detection is realised in the acoustic domain by using microphones, making the detection independent from the optical wavelength. In order to improve the acoustical detection, mechanical resonators such as quartz tuning forks have been used, alone or coupled to acoustical resonators. The aim of this PhD thesis is to study these systems so as to better understand the phenomena at play. Particularly, the main objective is to determine the limit of sensitivity those systems can reach and to compare them with other techniques. For that purpose, this manuscript first presents a comprehensive state-of-the-art review. Thereafter, an analytical and finite element method model, capable of describing the different sensors is described and further validated through the experimental study of various systems. In order to improve QEPAS (Quartz-enhanced photoacoustic spectroscopy), the use of a new radial resonator coupled to a tuning fork is presented and demonstrates a sensitivity similar to the state-of-the-art one as well as a facilitated implementation. In addition, an innovative closed-loop detection scheme is presented and modelled, and further compared to experiments, enabling a differential measurement with a reduced time compared to the conventional detection. Ultimately, a chapter is dedicated to the description and understanding of the physical phenomena at play in photoacoustics through the definition of a new model. From these, a clear positioning is made for the photoacoustic techniques allowing to determine the relevance of their use, particularly concerning QEPAS and their improvement perspectives.

